A Holistic Approach to Multi-Scale, Coupled Modeling of Hydrologic Processes, Flow Dynamics, Erosion, and Sediment Transport

by

Jongho Kim

A dissertation submitted in partial fulfillment
of the requirements for the degree of
Doctor of Philosophy
(Civil Engineering)
in the University of Michigan
2013

Doctoral Committee:

Assistant Professor Valeriy Y. Ivanov, Chair
Assistant Professor Mark G. Flanner
Professor Nikolaos D. Katopodes
Professor Steve J. Wright

DEDICATION

With great pleasure, I dedicate this to my wife, Eun Go.

ACKNOWLEDGEMENTS

Over the last four and half years as a graduate student, this dissertation work has been supported by the Graham Environmental Sustainability Institute at the University of Michigan through the grant, the Rackham International Student Fellowship at the University of Michigan, the Graduate Fellowship of the Department of Civil and Environmental Engineering at the University of Michigan, and the NSF Grant EAR 1151443 .

The first unutterable appreciation is devoted to my advisor, Prof. Valeriy Y. Ivanov who truly deserves to be admirable and support me throughout this long journey by offering me motivation and encouragement. He always struggles with me every time we met challenging problems, provides relevant and in-depth advice and guidance about complicated issues, and motivates me to investigate many unresolved curious problems scattered in an interdisciplinary area and to make a progress toward the higher scientific goal and vision. Other than the academic assistances, he sincerely expresses encouragement rather than disappointment with a generous, thoughtful, nice attitude when I am in a state of chaos and thus insufficiency of progress.

I am also very appreciative of their invaluable advice from my Ph.D. Committee members: Prof. Nikolaos D. Katopodes, Prof. Steve J. Wright, and Prof. Mark G. Flanner. In particular, I am very grateful to Dr. Katopodes for his organized remark and clear explanation on research of flow dynamics; to Dr. Wright for his sharp opinion and insight coming out of his

long-term experience on research of sediment transport; and to Dr. Flanner for his unforeseen angles of view on research I have never considered.

Successful and satisfactory journey of dissertation cannot be attained without their helps. I would like to thank to Dr. Brett Sanders for his help with the overland flow code and for sharing his experience for the numerical difficulties; to Dr. D.S.L. Lawrence for her help with experimental data used for verifying the upscaled regression equation developed in vegetated area; and to my Italian friend, Dr. Simone Fatichi for sharing his wisdom in stochastic downscaling to project future climate conditions. Furthermore, I would like to thank to all of the other members in environmental water resources group including Prof. Aline Cotel and my colleagues and friends, Antonio Francipane, April Warnock, Lingli He, Sara Rimer, Jenahvive Morgan, Chase Dwelle, Frank Sedlar, and TaoTao for sharing their expertise and friendship. Thanks for having a wonderful Ann Arbor life together to my Korean brothers: Sukhoon Pyo, Seungjun Ahn, Joon-Oh Seo, Jun-Hyuk Kwon, and Hyon-Sohk Ohm.

To the greatest extent, this dissertation is devoted to my parents, Ilkyun Kim and Duckja Im who always trust me every time I need to decide and express their unconditional love toward us; and to my sister and brother, Eunja Kim and Hyun-Chul Kim who have been of great role in our family to the part that I should do while I leave. Thank you very much.

Lastly, none of any conventional words can describe my love and gratitude to my wife, Eun Go. The satisfactory completion of doctoral program cannot be attained without her sacrifices and support. Her optimistic, pleasurable characteristics make me relieve any stress, and enable to refresh myself to continue to work. Although any earthly deeds cannot compensate her support, I will promise to keep me appreciate and remember it for the rest of my life.

TABLE OF CONTENTS

LIST OF TABLES

LIST OF FIGURES

LIST OF APPENDICES

ABSTRACT

Watershed systems supply services and goods to human society. They should be sustainable, maintain natural structure and function, and continue to meet societal needs in the long-term. Numerous efforts investigated the effects of climate change on watershed components. However, comprehensive studies of climate impacts relevant to the scale of human decisions have been extremely limited. One of the goals of this dissertation is to develop a holistic, multi-scale watershed model that describes essential physical processes. A coupling framework between hydrologic processes, hydrodynamics, and soil erosion and sedimentation is developed and presented. A previously existing model describing hydrological processes (tRIBS) has been integrated with a solution of the Saint-Venant shallow water equations (OFM) and the Hairsine-Rose formulation of erosion and deposition processes (HRM). The system of equations is resolved using the finite volume method based on the Roe's approximate Riemann solver on an unstructured grid. The resultant tRIBS-OFM-HRM model is one of the most comprehensive, process-scale tools required for evaluations of climate signals that propagate through a non-linear hydrological system.

The model has been used in several basic science applications. First, it has been applied to address the problem of roughness upscaling for areas covered by partially submerged obstacles, such as vegetated hillslopes. Two approaches, "Equivalent Roughness Surface" and the "Equivalent Friction Slope", for computing the upscaled Manning roughness coefficient are

proposed. Predictive equations with several prognostic variables are developed to quantify the additional resistance caused by partially submerged vegetation. The effects of all independent variables are quantitatively investigated.

Second, the coupled model has been used to address a possible mechanism leading to the non-uniqueness of soil erosion. It is attributed to two major conflicting effects: erosion enhancement, due to supply of highly erodible sediment, and erosion impediment, due to formation of a shielding layer that constrains the availability of lighter particles overlain by heavier sediment. Two characteristic time scales, the time to peak and the time to steady-state, are shown to separate three characteristic periods that correspond to flow-limited, source-limited, and steady-state regimes. These time scales are demonstrated to be log-linearly and negatively related to the spatially averaged Shields parameter.

CHAPTER I

Introduction

1.1 Motivation of a holistic, multi-scale, coupled approach

1.1.1 Climate change and human activity in watershed systems

Human societies require services and goods supplied by watershed systems, which should be sustainable, maintain natural structure and function, and continue to meet societal needs in the long-term [*Meyer and Pulliam*, 1992]. However, the world is undergoing a period of rapid climate change, rarely experienced in the past [*IPCC (Intergovernmental Panel on Climate Change)*, 2001; 2007]. Its impacts, in concert with other human pressures, such as the accelerated rates of water re-allocation and consumption, promise to alter the character and services of watershed systems. Global-scale climate change and local-scale human impacts on landuse inevitably affect the state of the atmosphere, surface and subsurface processes, streamflow, erosion and sedimentation. They may lead to a variety of undesirable implications. Figure 1.1 shows one striking example of such changes through aerial photographs of the Muskegon River estuary [*Baird*, 2001]. This region has been highly affected by climate change due to shorter and warmer winters, and warmer summer temperatures and extreme precipitation

events, resulting in a remarkable change of the estuary morphology over the period of the past thirty years. Little information however exists to quantify the exact causes of this change, and predicting how the current state will evolve further. Focused efforts are required to address the short- and long-term effects of climate change on erosion, sediment transport and morphology in earth-science disciplines.

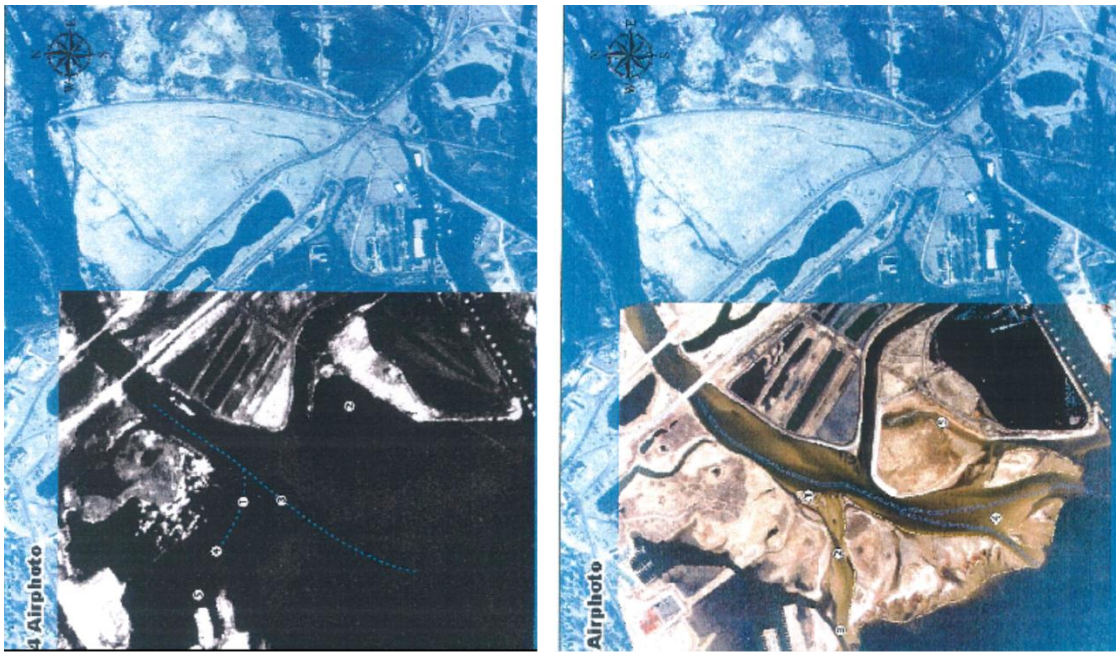

Figure 1.1: Aerial photographs of the Muskegon River estuary (after *Baird*, 2001)

1.1.2 Significance and challenges of a multi-scale coupled approach

The processes of erosion and sedimentation originate at the watershed level: the watershed-scale, hydrologic disturbances propagate into streamflow and alter the flow regime; the flow process leads to erosion processes that modify landscape morphology. When considered

in the context of long-term effects of climate change on such important drivers as precipitation and temperature, perturbations at larger scale impact local-scale hydrological signals, especially evaporation and runoff, which subsequently affect streamflow variations. The flow motion ultimately leads to an effect on sediment transport and erosion rates, and modifies the morphology of the surface; the resultant morphologic change in turn affects the flow dynamics. Therefore, modeling the impacts of climate change on landscape evolution, catchment morphology and sediment yields requires a holistic approach, involving many significant components such as hydrology, hydraulics, vegetation dynamics, erosion and sedimentation.

Any assessment of potential impact of climate change should consider all related processes that occur different spatial and temporal scales, and employ an integrated approach capable of simulating all involved process components simultaneously. Models including individual components or a subset of coupled processes (e.g., hydrology-erosion or hydraulics-erosion) have been previously developed with moderate-to-satisfactory success. However, models including all critical process components have not yet been proposed. The likely reason is the complexity of coupling, in which related processes operate at a range of temporal and spatial scale. For example, climate change and morphologic variations are characteristic of global spatial and long-term temporal scales; hydrologic processes are conveyed at the watershed scale, over relatively short-term temporal scales; hydraulic and erosion processes are concerned with a river-reach or a hillslope spatial, and short-term temporal scales (see Figure 1.2). Another reason why fully coupled models have not been developed is because relevant processes extend across several disciplines. The connection between hydrology and hydraulics in overland flow modeling, and the effects of channel and hillslope erosion processes on the total sediment budget in watershed erosion modeling have not been fully considered at the relevant level of detail.

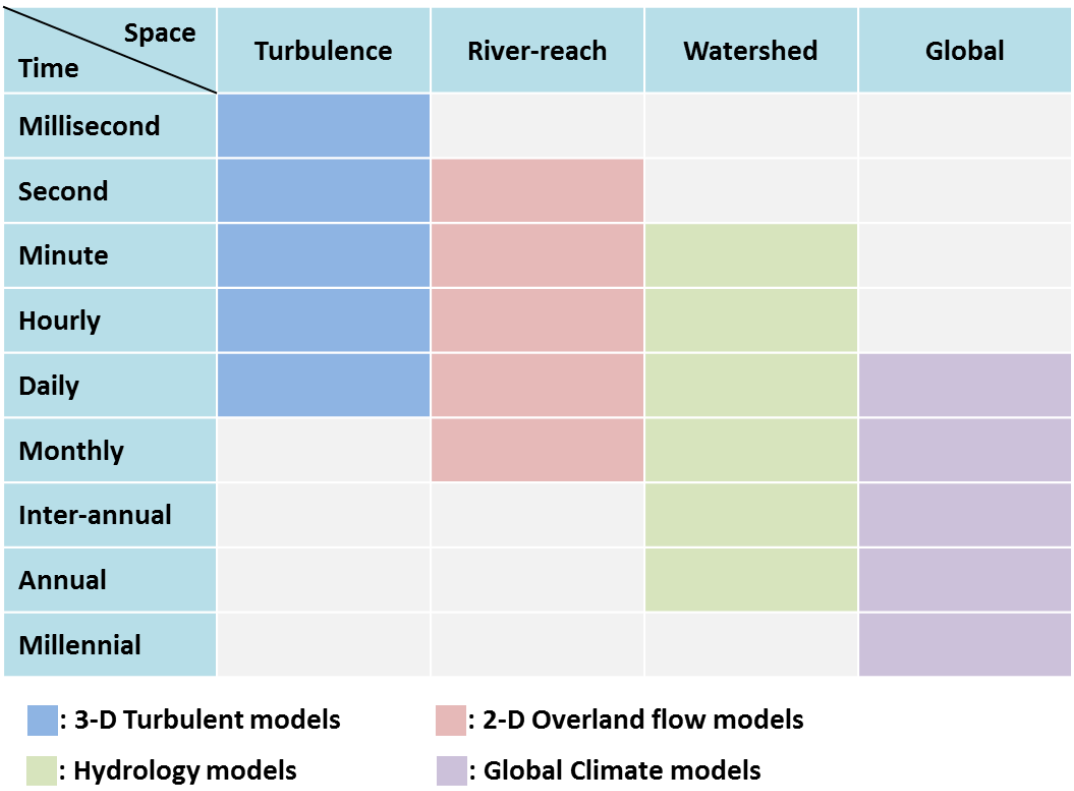

Figure 1.2: A space-time diagram showing characteristic ranges of modeling approaches.

1.1.3 Characteristics of watershed systems: connectivity and non-linearity

A critical feature of watershed systems is their connectivity [*Michaelides and Chappell*, 2009], i.e., hydrologically mediated transfer of mass, momentum, energy, or organisms within or between basin compartments. Disturbances arising at any scale will necessarily propagate downstream, e.g., large-scale climate perturbations will affect local-scale hydrologic processes, flow regime, erosion, and stream sedimentation. The local-scale effects can be responsible for damages to aquatic habitats and disruption of ecological services [*Mooney et al.*, 2009]. Due to the tremendous disparity of involved spatiotemporal scales, we currently lack assessment tools that explicitly consider connectivity of watershed processes (and are also relevant to the "scales

of human decisions" and ecosystem services). Further, watersheds are non-linear systems; their dynamics depend on 'convective' and 'dissipative' characteristics of involved processes. The latter are inevitably time- and space- varying and depend on forcings, and initial and boundary conditions. Physically-based, "process-scale" approaches considering both connectivity and non-linearity of watershed systems are required for robust assessments of non-linear effects. Compensation and mitigation of climate impacts are also limited due to the difficulty of evaluation of climate signals that propagate through a non-linear hydrological system.

1.1.4 The need for a holistic, multi-scale, coupled model

Comprehensive studies of climate impacts relevant to the scale of human decisions, such as an agricultural field, a stream reach, or a flood-control structure, have been extremely limited. For example, global and regional scale studies have examined the impact of projected climate change on a number of large-scale hydrologic variables [*Barnett et al.*, 2005; *Milly et al.*, 2005]. They however lacked the propagation of this information through watershed systems to seek a more detailed level of flow characteristics (i.e., those that extend beyond the traditional metrics of bulk, area-integrated runoff) that can be directly responsible for major impacts on water quality and aquatic habitat characteristics. At the other end of research spectrum, hydraulic engineers carried out stream-reach scale studies addressing flow regimes and details of flow dynamics. However, by assuming artificial boundary conditions these studies have failed to connect to catchment- and larger-scale (e.g., climate) information. This has essentially "disengaged" channel flow from watershed processes [*Milly et al.*, 2002; *Arnell*, 2003; *Cherkauer and Sinha*, 2010]. As a result, at present we entirely lack assessments of climate impacts on spatially-distributed flow characteristics, water quality, and aquatic systems through a

holistic, multi-scale approach. Understanding and predicting the corresponding shifts across a range of space-time scales is one of the most fundamental, yet poorly quantified challenges facing society today.

1.2 Research scope

A new holistic, coupled model that considers hydrological processes, flow dynamics, and erosion and sediment transport is developed and presented in detail in the following chapters.

Chapter II of this dissertation addresses a coupling framework between a hydrologic model and a hydrodynamic model. The resultant coupled model, tRIBS-OFM, considers spatially-distributed, physically-based hydrologic processes over the land-surface and subsurface by using tRIBS (Triangulated irregular network – based, Real time Integrated Basin Simulator); the hydrodynamic component is the Overland Flow Model (OFM), which solves the two-dimensional Saint-Venant (shallow-water) equations using Roe's approximate Riemann solver on an unstructured grid. The original OFM formulation targeted hydraulic applications and did not provide an accurate solution for partially-submerged mesh cells. Modifications of the hydrodynamic model are proposed in this chapter by applying a new method of reconstruction of variables. Several comparisons with analytical solutions, observed data, and other numerical models, and two applications to a synthetic domain and a real-world basin, the Peacheater Creek watershed located near Christie, OK, U.S.A., are also presented.

Chapter III outlines a novel, two-dimensional, physically-based model of soil erosion and sediment transport. The Hairsine-Rose formulation of erosion and deposition processes is used to account for size-selective sediment transport and differentiate bed material into original and

deposited soil layers. The formulation has been integrated within the framework of the hydrologic and hydrodynamic model tRIBS-OFM. The resultant model explicitly couples the hydrodynamic formulation with the advection-dominated transport equations for sediment of multiple particle sizes. The finite volume method based on Roe's approximate Riemann solver on an unstructured grid is described with the system of equations including both the Saint-Venant and the Hairsine-Rose equations. The chapter also provides verifications with analytical solutions and empirical data for two benchmark cases; two sensitivity tests to grid resolution and the number of particle sizes; and an application at the catchment scale for the Lucky Hills watershed located in southeastern Arizona, U.S.A. Additionally, spatial output has been analyzed and the driving role of topography in erosion processes is discussed.

The developed coupled model has been used in several basic science applications. In Chapter IV the developed model is used to numerically investigate the characteristics of upscaling the Manning resistance coefficient for areas covered by partially submerged vegetation elements, such as shrub or tree stems. A number of high-resolution hydrodynamic simulations corresponding to scenarios with different domain slopes, inflow rates, bed roughness, and vegetation cover fractions are carried out. Using simulations performed at fine space-time scales, two methods are developed for computing the upscaled Manning coefficient, called "Equivalent Roughness Surface (ERS)" and "Equivalent Friction Slope (EFS)". Further, the effects of four independent variables on the total Manning coefficient are discussed. A regression relation that includes all four variables and the additional resistance due to partially submerged vegetation representing the sum of the form and wave resistances is presented. The upscaled values computed from the developed regression relation are validated through a comparison with

estimates reported in five different empirical studies. The simulated wave resistance coefficients are also compared with those predicted from an equation proposed in a previous study.

Chapter V addresses possible reasons leading to non-uniqueness of soil erosion susceptibility; specifically, the role of shielding layer in multi-size particle dynamics are discussed. To obtain relevant insights, 95 numerical simulations using synthetic storms of varying intensity, duration, and lag time between successive events (to obtain different runoff conditions in a zero-order catchment) are presented. The design targets to generate flow and 'perturb' soil substrate by a first rainfall event, creating the initial conditions of flow and sediment prior to the onset of a subsequent rainfall event. Due to the affected particle size distribution, a shielding layer composed of larger particles is formed in some cases. The results indicate that unless the initial condition of flow and sediment spatial distribution is identical, the same volume of runoff can generate different total sediment yields even in conditions of identical rainfall forcing. The reasons for non-uniqueness are attributed to two major conflicting effects occurring during the erosion process: erosion enhancement, because of supply of highly erodible sediment from upstream areas, and erosion impediment, because of formation of a shielding layer that constrains the availability of lighter particles due to heavier sediment. Long-term simulations with continuous rainfall also show that a peculiar feature of sediment yield series is the existence of maximum before the steady-state is reached. Two characteristic time scales, the time to peak and the time to steady-state, are eventually presented to separate three characteristic periods that correspond to flow-limited, source-limited, and steady-state regimes

Chapter VI summarizes this dissertation and addresses perspectives for ongoing and future studies. Major conclusions and critical assumptions of conducted research, and a feasibility study for national assessment of soil loss are presented. The latter objective focuses on

investigating interactions among the components of agricultural farming such as tillage, conservative practices, and landuse management. It is conjectured that through extensive observations of USLE (Universal Soil Loss Equation) database, the developed model can be further verified, and representative parameter sets for complex conditions can be obtained to carry out relevant assessments. Lastly, the uncertainty and non-linearity of processes of erosion and sedimentation related to climate projections and hydrological conditions such as extreme precipitation and dynamically varying vegetation state during growing and dormant seasons is argued to be a fruitful research agenda that will be addressed in future.

CHAPTER II

Coupled modeling of hydrologic and hydrodynamic processes including overland and channel flow: "tRIBS-OFM"

2.1 Introduction

A description of overland and channel flow processes plays a crucial role in a variety of hydrologic, hydraulic, agricultural, and ecological problems, such as rainfall-runoff modeling, flood routing, sedimentation and erosion, irrigation and drainage, and environmental change of aquatic habitats. In particular, the consequences of flow-related events were recently addressed in the light of abnormal meteorological phenomena occurring possibly due to climate change [*Chen et al.*, 2008; *Makkeasorn et al.*, 2008; *L H Li et al.*, 2010], i.e., more violent storms with higher precipitation intensities, leading to extreme flooding events [*Dankers and Feyen*, 2008; *Kay et al.*, 2009; *Mantua et al.*, 2010]. Such abnormal events may have numerous undesirable implications for human life and damage of property, as well as ecological consequences. Therefore, a number of studies have investigated the rainfall-runoff mechanism and ways to diminish human and property damages from floods by using physically-based hydrologic and hydraulic models for predictions [*Hunter et al.*, 2007].

Overland flow can be regarded as the propagation of shallow water waves, which can be mathematically represented by the Saint-Venant equations, the so called "dynamic wave" formulation, or by their simplified versions, e.g., the inertia-free and kinematic approximations [*Katopodes*, 1982]. In the dynamic wave model, the momentum equation is balanced among inertial, pressure, gravitational, frictional, and momentum source terms, while in the inertia-free model, the local and convective acceleration terms are neglected; in the kinematic wave model, not only these but the pressure term is also neglected. Researchers and engineers have historically developed hydrologic models based on simplified approximations that can be applicable for problems of flood wave propagation in steep terrain because of their computational efficiency or simplicity [*Parlange et al.*, 1981; *Hromadka et al.*, 1985; *Hromadka and Nestlinger*, 1985; *Govindaraju et al.*, 1990; *Keskin and Agiralioglu*, 1997; *Odai*, 1999; *Moramarco and Singh*, 2000; *Wang et al.*, 2002; *Downer and Ogden*, 2004; *Panday and Huyakorn*, 2004; *Tsai and Yang*, 2005; *Howes et al.*, 2006; *Kollet and Maxwell*, 2006a; *Du et al.*, 2007; *Alonso et al.*, 2008; *Prestininzi*, 2008; *Goderniaux et al.*, 2009; *J K Huang and Lee*, 2009]. However, simplified models have several limitations for applications in cases of flow over flat slopes, flow into large reservoirs, flow reversals, and strong backwater conditions. These limitations may seriously constrain the applicability of simplified models to a range of practical problems as well as conditions of the changing world.

In order to enhance the applicability and accuracy of simplified models, several dynamic wave models have been previously developed for simulating overland flow by calculating the full version of the momentum equations in the Saint-Venant equations [*Akanbi and Katopodes*, 1988; *DiGiammarco et al.*, 1996; *Katopodes and Bradford*, 1999; *Horritt*, 2002; *Begnudelli and Sanders*, 2006; *Gottardi and Venutelli*, 2008]. However, the dynamic wave model formulation

requires detailed watershed topographic and channel cross sectional data and poses serious challenges for the numerical solution when applied continuously over storm-interstorm periods. Additionally, such models neglect a detailed description of crucial components of the hydrologic processes, such as evapotranspiration, interception, infiltration, and groundwater dynamics. These models treat these processes implicitly through "well-defined" inputs or assumptions to compute the components of flow regime in terms of the maximum water depth, discharge and velocities of flow as well as the maximum inundation area.

Runoff generation, the crucial process for simulating overland and channel flow, is highly affected by the spatial variability of antecedent moisture and hydrologic processes of infiltration and percolation, groundwater recharge/discharge, and evapotranspiration, as determined by the spatial distribution of meteorological forcing. Because of the strong interdependence between surface hydraulics and the subsurface hydrology, there has been an increased interest in recent years in the development of coupled surface and subsurface models [*Bixio et al.*, 2000; *VanderKwaak and Loague*, 2001; *Morita and Yen*, 2002; *Panday and Huyakorn*, 2004; *Kollet and Maxwell*, 2006a; *Goderniaux et al.*, 2009; *Camporese et al.*, 2010; *Rihani et al.*, 2010; *Shen and Phanikumar*, 2010]. All of these studies represent the flow processes in the variably saturated zone by solving the Richards equation. The surface flow phenomenon is also considered by solving different approximations of the Saint-Venant equations: the inertia-free formulation is used most often, while the kinematic [*Kollet and Maxwell*, 2006b; *Rihani et al.*, 2010] and dynamic [*Morita and Yen*, 2002] forms were also proposed. The numerical simulation of the coupled surface and subsurface equations is carried out using either an unstructured triangular mesh [*VanderKwaak and Loague*, 2001; *Goderniaux et al.*, 2009] or a rectangular grid (the rest of the studies cited above). With the exception of the studies by *Rihani et al.* [2010] and

Shen and Phanikumar [2010], most of the above cited model developments focus on the subsurface phenomena, simplistically describing above-surface processes (e.g., evapotranspiration). Energy exchanges between the subsurface and the atmosphere are neglected. However, if one intends to take into account the spatiotemporal structure of runoff production and the related effect on the flow regime, both a spatially-distributed, comprehensive hydrologic model that considers all relevant processes, and a hydrodynamic model solving the full dynamic equations have to be considered to accurately predict flow characteristics (e.g., depth, velocity vectors, vorticities, shear stress, etc.).

A coupled model, tRIBS-OFM is introduced in this Chapter. The key features of the tRIBS-OFM include 1) the generality of the dynamic wave formulation that can deal with various boundary conditions and its numerical implementation based on an unstructured triangular mesh; 2) the capability of applying the model for challenging hydrological situations, such as a partially wetted domain and low-flow conditions; and 3) coupling of the hydrodynamic component with a hydrological model, which provides a seamless transition from the hydrometeorologic boundary conditions to those that are required by the hydrodynamic simulation at the catchment scale.

The overarching objective of the coupled framework is to quantitatively predict the spatial and temporal hydrologic response to imposed scenarios of climate change, land-use variations, soil, and vegetation types in small- to large-scale basins. First, model backgrounds are provided and modifications necessary for the coupled model are described. These modifications are stressed because in large domains with both steep and flat slopes, the typical shallow water solver developed for hydraulic applications does not accurately capture the flow regime in a large number of partially-submerged cells of an unstructured grid. Next, model verifications are

carried out in which the simulation results are compared with analytical solutions, observed data, and other numerical models; a one-dimensional plane and a V-shaped domain are used. The effects of inertia and pressure terms in the momentum equation are investigated for the V-shaped catchment. The results of using both the kinematic and dynamic formulations are also presented. Lastly, applications to both a synthetic domain and the Peacheater Creek watershed (64 km^2) located near Christie, OK, are performed to illustrate the model multi-scale capabilities and the feasibility of various aspects of watershed streamflow simulation: runoff production occurrences and rates, streamflow, flow depth, velocities, and a reservoir problem.

2.2 Description of the coupled model

2.2.1 Model heritage: tRIBS

The coupled model presented in this study consists of a hydrologic model and a hydrodynamic model. The hydrologic model, the TIN (Triangulated Irregular Network) - Based Real Time Integrated Basin Simulator (tRIBS), has the capability to explicitly utilize a variety of data, such as topography, soil type, land use, and vegetation. The tRIBS model is forced with meteorological series that consist of precipitation, radiation, metrics of atmospheric turbulence, temperature and humidity. The model simulates in a spatially-explicit manner a number of hydrologic processes such as rainfall interception, evapotranspiration, infiltration with continuous soil moisture accounting, lateral moisture transfer in the unsaturated and saturated zones, and one-dimensional channel runoff routing. In particular, the model stresses the role of topography in lateral soil moisture redistribution, accounting for the effects of spatially heterogeneous and anisotropic soil in a simplified manner. The model computational basis, structure, and the description of process parameterizations are detailed by *Ivanov et al.* [2004a].

A brief outline of the implemented process parameterizations is provided in the following and summarized in Table 2.1.

- For simulating precipitation interception, the Rutter canopy water balance model [*Rutter et al.*, 1971; *Rutter et al.*, 1975] is used. Canopy water dynamics is species dependent such that the parameters can vary for different vegetation types.
- For estimating surface energy budget, shortwave and longwave radiation components are simulated, accounting for geographic location, time of year, aspect and slope of the element surface [*Bras*, 1990]. The combination equation [*Penman*, 1948; *Monteith*, 1965], gradient [*Entekhabi*, 2000], and force-restore [*Lin*, 1980; *Z Hu and Islam*, 1995] methods are used to estimate the latent, sensible, and ground heat fluxes at the land surface. An optimum is sought in terms of the surface temperature that leads to the energy balance. Soil water content in the root zone and top soil layer constrains evapotranspiration from vegetated surfaces and bare soil. A species-dependent parameterization of stomatal conductance allows for the diurnal variation of transpiration flux.
- Latent heat energy is partitioned into evaporation from wet canopy, vegetation transpiration, and bare soil evaporation; the latter two are limited by available moisture in the soil zone, depending on vegetation fractional coverage of an element and canopy state.
- For simulating the process of infiltration, an assumption of gravity-dominated flow in a sloped column of heterogeneous, anisotropic soil is used, so that the effect of capillary forces is approximated [*Cabral et al.*, 1992; *Ivanov et al.*, 2004a]. All soil parameters described in Table 2.2 are allowed to vary in space over a heterogeneous basin area; there are specific assumptions about changes in the soil saturated hydraulic conductivity that are detailed in *Ivanov et al.* [2004a]. By considering the evolution of the wetting and top

fronts and the fluctuation of the water table in any given element, the vadose zone is conceptualized with five states: initial, unsaturated, perched, surface saturated, and completely saturated [*Ivanov et al.,* 2004a]. The first three states are defined for cases where the soil infiltration capacity is not constrained by the conductivity at the surface, while the surface saturated state is generated when the soil's infiltration capacity is constrained by the entire saturated profile that exhibits a decay of conductivity with depth. In the unsaturated state, only the wetting front is present, while in the perched (surface saturated) state, the top front is shallower than the wetting front (located at the soil surface). For the fully saturated state, the soil infiltration capacity is zero. The unsaturated and saturated zones are coupled, accounting for the interaction of the moving infiltration front with a time-varying water table. Topography and soil control the magnitude of lateral moisture transfer in the unsaturated zone. Continuous soil moisture accounting allows the representations of both storm and interstorm conditions, thus permitting long-term simulation over a range of hydrometeorological forcings.

- For simulating the groundwater dynamics, a model based on the Boussinesq's equation under the Dupuit-Forchheimer assumptions is used, allowing for a lateral water redistribution in the saturated zone and its dynamic interactions with the unsaturated zone. The lateral exchanges between contiguous elements are calculated by using the depth-averaged aquifer transmissivity, and the local slope of water table.
- Runoff generation is made possible via four mechanisms: saturation excess [*Dunne and Black*, 1970], infiltration excess [*Horton*, 1933; *Loague et al.,* 2010], perched subsurface stormflow [*Weyman*, 1970], and groundwater exfiltration [*Hursh and Brater*, 1941]. Runoff is generated by representing the movement of infiltration fronts, water table

fluctuations, and lateral moisture fluxes in the unsaturated and saturated zones. The runoff computed in this hydrologic module is used as input to the hydrodynamic overland flow model.

- A snowpack dynamic model has been recently added [*Rinehart et al.*, 2008] that permits the simulation of energy and mass budgets of snow-covered areas.

Table 2.1: A summary of processes considered in the hydrologic model tRIBS.

Processes	Governing equations and methods
Rainfall interception	Rutter canopy water balance model [*Rutter et al.*, 1971; *Rutter et al.*, 1975]
Surface energy balance	The combination equation method for latent heat flux [*Penman*, 1948; *Monteith*, 1965], gradient method for sensible heat flux [*Entekhabi*, 2000], and force-restore method for ground water flux [*Lin*, 1980; *Z Hu and Islam*, 1995]
Evapotranspiration	The bare soil evaporation [*Deardorff*, 1978], canopy evaporation, and transpiration [*Eltahir and Bras*, 1993]
Infiltration	Gravity-dominated unsaturated flow [*Cabral et al.*, 1992; *Ivanov et al.*, 2004a]
Groundwater dynamics	Quasi-3D Boussinesq's equation under the Dupuit-Forchheimer assumptions [*Ivanov et al.*, 2004a]
Runoff generation	Saturation excess [*Dunne and Black*, 1970], infiltration excess [*Horton*, 1933], perched stormflow [*Weyman*, 1970], and groundwater exfiltration [*Hursh and Brater*, 1941]
Snowpack dynamics	Snowpack dynamic model [*Rinehart et al.*, 2008]

Table 2.2: The soil hydraulic and thermal parameters used in calibration for Peacheater Creek.

Case	Area	K_s	θ_s	θ_R	m	φ_B	f	A_s	A_u	η'	k_s	C_s
1	cropland/pasture	14.5	0.4	0.05	2.0	-400	0.0005	300	300	10	1	50000
	Forested soil	30.0	0.4	0.05	2.0	-300	0.0005	300	300	10	1	50000
2	cropland/pasture	17.5	0.4	0.05	2.0	-400	0.0005	200	400	10	1	50000
	Forested soil	30.0	0.4	0.05	2.0	-300	0.0007	200	400	10	1	50000
3	cropland/pasture	14.5	0.4	0.05	2.0	-400	0.0005	300	200	10	1	50000
	Forested soil	30.0	0.4	0.05	2.0	-300	0.0007	300	200	10	1	50000
4	cropland/pasture	16.5	0.4	0.05	2.0	-400	0.0005	300	300	10	1	50000
	Forested soil	30.0	0.4	0.05	2.0	-300	0.0005	300	300	10	1	50000
5	cropland/pasture	16.5	0.4	0.05	2.0	-400	0.0005	400	400	10	1	50000
	Forested soil	30.0	0.4	0.05	2.0	-300	0.0005	400	400	10	1	50000
6-12	cropland/pasture	16.5	0.4	0.05	2.0	-400	0.0005	300	300	10	1	50000
	Forested soil	30.0	0.4	0.05	2.0	-300	0.0005	300	300	10	1	50000
13	cropland/pasture	50.0	0.4	0.05	2.0	-400	0.0005	300	300	10	1	50000
	Forested soil	50.0	0.4	0.05	2.0	-300	0.0005	300	300	10	1	50000
14	cropland/pasture	50.0	0.4	0.05	2.0	-400	0.000005	300	300	10	1	50000
	Forested soil	50.0	0.4	0.05	2.0	-300	0.000005	300	300	10	1	50000

K_s: Saturated hydraulic Conductivity [mm/hr], θ_s: Volumetric soil moisture at saturation [m^3 m^{-3}], θ_R: volumetric residual soil moisture [m^3 m^{-3}], *m*: Pore-size distribution index [-], φ_B: Air entry bubbling pressure [mm], *f*: Conductivity decay parameter [mm^{-1}], A_s: Anisotropy ratio in the saturated zone [-], A_u: Anisotropy ratio in the unsaturated zone [-], η' : Bedrock depth [m], k_s: Volumetric heat conductivity [J/m/s/K], C_s: Soil heat capacity [J/m^3K]. For details, refer to *Ivanov et al.* [2004b].

2.2.2 Model heritage: OFM

The hydrodynamic Overland Flow Model (OFM) is a high resolution, depth-averaged, two-dimensional finite volume model that solves the Saint-Venant equations on the basis of an unstructured triangular grid. Early contributions to the numerical solution of the Saint-Venant equations were made by *Leendertse* [1967], *Liggett* [1968], and *Abbott* [1974]. In this study, Roe's approximate Riemann solver [*Roe*, 1981] is used to compute fluxes. The hydrodynamic model was originally developed by *Bradford and Katopodes* [1999] to simulate turbidity currents and was later used to model surface irrigation [*Bradford and Katopodes*, 2001]. It has been previously successfully applied to a wide range of hydrodynamic scenarios [*Bradford and Sanders*, 2002] and extended to an unstructured triangular mesh [*Begnudelli and Sanders*, 2006]. In order to enhance the run-time efficiency, a Local Time Stepping (LTS) scheme was developed that showed an increased performance by 50 to 70 %, without a loss of accuracy or mass conservation [*Sanders*, 2008]. The OFM is able to compute the depth of flow, the velocity field, and the location and elevation of the free surface. A detailed outline of the governing equations, Roe's approximate Riemann solver implemented in the model, boundary conditions, etc. are provided in the Chapter III.

2.2.3 OFM modification

The original OFM was designed for hydraulic applications such as flooding and dam break problems. In order to adapt the design to hydrologic applications, several modifications have been made for calculating the flux, bottom slope, and friction slope terms by applying a different reconstruction method of variables. Before describing these changes in the tRIBS-OFM

framework, the method for identifying partially-submerged cells, a situation frequently occurring in hydrologic applications, is explained in the following.

The standard OFM design classifies the computational cells (i.e., triangles of unstructured triangular mesh) into three different groups corresponding to fully-submerged (wet), partially-submerged, and non-submerged (dry) conditions. The model first checks conditions at all cell vertices. Similar to the published studies by *Jones et al.* [2008] and *Camporese et al.* [2010], the model identifies "wet nodes" by comparing the depth at each vertex with a very small, pre-defined tolerance value (e.g., 10^{-7} m). The model then labels cells as "wet", only if all vertices have depths larger than the tolerance value. Cells under any other conditions are defined as "dry cells". Once a cell is identified as a "wet" cell, the model solves both the continuity and momentum equations for this cell, yielding the *x*- and *y*- components of velocity of the flow. However, if a cell has been identified as "dry", the model sets the flow velocity to zero, and therefore does not compute the momentum equations. This procedure prevents the numerical instability that would be otherwise generated because of unrealistically high velocities that would result from dividing the volume fluxes by very small depths. The condition of numerical instability is the "classical" but critical problem of applying a fully dynamic model to a hydrologic simulation with small runoff production.

The first difference in dealing with partially-submerged cells in hydrologic vs. hydraulic applications concerns the existence of dry or "partially wet" cells. Hydraulic applications such as flood propagation and wave runup involve a large number of initially wet cells (river or ocean) and a distinct wet and dry boundary (floodplain or coastline). Several approaches have been developed to track wet and dry fronts and handle the phenomenon by using information of neighboring wet cells [*Titov and Synolakis*, 1995; *Bradford and Sanders*, 2002; *Xia et al.*, 2010]

and by modifying the bed level difference [*Brufau and Garcia-Navarro*, 2003; *Brufau et al.*, 2004]; for a more detailed review, the reader is referred to *Zokagoa and Soulaimani* [2010]. However, such hydraulic approaches have not considered the conditions of neighboring dry cells, which frequently occur in hillslopes with small runoff production rates, as described in the following.

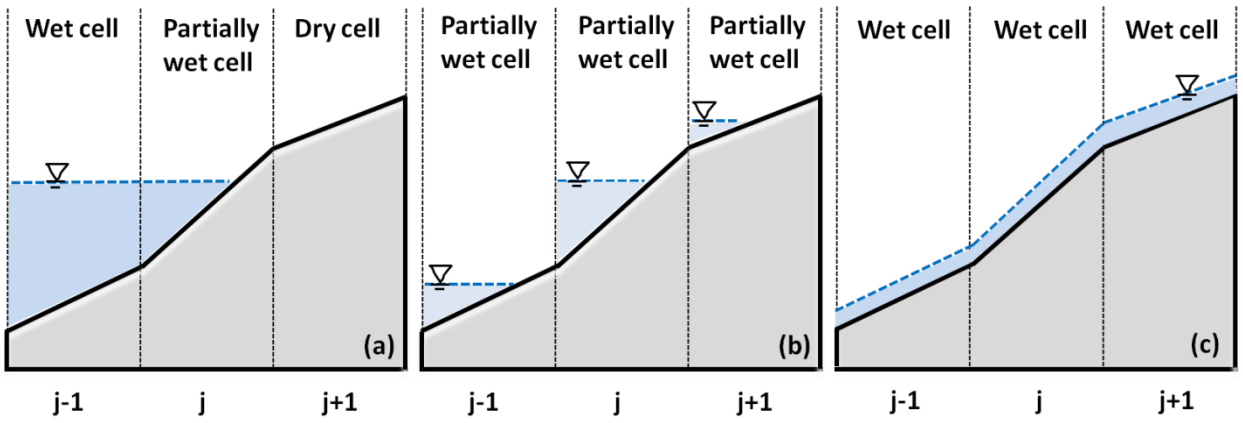

Figure 2.1: Flow regimes near the wet and dry boundary on a sloped bed: (a) the quiescent flow regime characteristic of hydraulic applications, such as flooding and wave runup; (b) an incorrect representation of flow regime using the concept (a) for hydrological applications; and (c) the sheet flow representation of a flow regime for hydrological applications with low runoff on a steeply sloped bed.

The water profile in Figure 2.1-(a) corresponds to hydraulic applications with both wet and dry cells. Partially-submerged cells near this boundary need reconstructions of the flow depth and velocity to balance the pressure fluxes and bed slope terms on a sloping bed [*Bradford and Sanders*, 2002]. Many researchers have employed variables in a partially-submerged cell extrapolated from those of a fully-submerged neighbor cell. For example, flow variables on the right side of cell interface, *j-1/2* use the information of the neighboring cell, *j-1* instead of the cell

j. This extrapolation method has yielded good results in terms of accuracy and stability [*Titov and Synolakis*, 1995; *Bradford and Sanders*, 2002]. However, in most hydrologic, watershed-scale applications that have steeply sloped cells with dry conditions encountered throughout the simulation, the domain is represented by a large number of partially-submerged cells, shown in Figure 2.1-(b). This is due to the fairly coarse resolution of topography and typically small magnitude of hillslope runoff that is insufficient for submerging initially dry cells on a steeply sloped bed. For partially-submerged cells, proper values of depth and velocity cannot be attained from neighboring cells. Such extrapolation can neither represent an appropriate regime of flow nor reconstruct an accurate depth for both sides of the cell interface. As an acceptable flow regime on natural hillslopes, the sheet-flow concept as shown in Figure 2.1-(c) is usually used for modeling purposes [*De Roo et al.*, 1989; *Morgan et al.*, 1998]. In this study, the sheet flow approximation of flow regime within one cell is employed locally. In this fashion, a reconstruction of variables at cell interfaces is easily obtained by using the cell-centered information of each cell.

Another difference of the presented adaptation from a traditional hydraulic model is that the latter typically defines the free surface elevation (ζ) as the sum of elevation and depth. For partially-submerged cells under the quiescent flow regime (c.f. Figure 2.1-(a)), the cell-averaged depth is badly represented by the depth at the centroid. The cell-averaged depth wets all faces of partially-submerged cells, which induces the unwanted spreading of water into adjacent dry cells and causes a numerical error [*Bradford and Sanders*, 2002]. In order to avoid these problems, the free surface elevation at the centroid is obtained by using the volume-free-surface relationship (VFR) calculating the ratio of the fluid volume to the cell area [*Begnudelli and Sanders*, 2006]. However, in hydrological problems, the use of the free surface elevation is inappropriate. This is

because the free surface elevation in partially-submerged cells is nearly always smaller than the bed elevation of cell interfaces, and thus, their corresponding flow depths at interfaces are set to zero. For example, on the left side of each cell interface, the free surface elevation is less than the bed elevation at the interface, so that its flow depth has a zero value, as shown in Figure 2.1-(b). Fluxes cannot be properly calculated in such cells with this type of representation. On the other hand, the sheet flow approximation does not need to perform an additional calculation of the free surface elevation in the cell interfaces. Cell depths at cell interfaces are attained as flow depths at the centroid, shown in Figure 2.1-(c).

One of the consequences of the original OFM extrapolation or free surface elevation estimation of partially-submerged cells in overland flow is the development of a "no-flow phenomenon". This refers to a situation when runoff is stored within a cell without the possibility to flow out. So, the generated runoff fills up the cell until it becomes fully inundated, i.e. "wet", according to the accepted definition. At this time, the momentum flux is computed and water starts flowing to a downstream cell. Note that this numerical problem is very critical in domains characterized by high bed slopes and low flow conditions (e.g., hillslope areas of the watershed), where most of the cells correspond to partially-submerged cells. On the other hand, we found that the local sheet flow approximation using the depth at the cell center instead of free surface elevations allows one to avoid all of the aforementioned problems.

2.2.4 Information exchange between the hydrologic and hydrodynamic models

This work couples the hydrologic and hydrodynamic models described previously by using a built-in mapping procedure to exchange information between the computational

architectures of the two models. The mapping procedure is needed because tRIBS calculates physical processes such as interception, infiltration, evapotranspiration as well as runoff, in elements using the dual diagram of the Triangulated Irregular Network (TIN) - the Voronoi Polygon Network (VPN) [*Ivanov et al.*, 2004a]. The OFM model computes the flow variables, including the water depth and velocities, using the TIN [*Begnudelli and Sanders*, 2006]. The VPN-based variables obtained after taking into account physical hydrologic processes must be transferred to the triangle-based variables that will be used in the hydrodynamic model. To do that, it is assumed that the VPN-based quantities are uniformly distributed inside each Voronoi cell. Thus, a triangle-based quantity is calculated by spatially-weighting the hydrologic quantities using the areal fractions of the three Voronoi polygons that compose any given triangle. In this way, any exchanged quantity is fully conserved.

Three areal Voronoi fractions in each TIN triangle (see Figure 2.2) are calculated with the ratio as specified in Eq. (2.1). The triangle-based variable at each TIN triangle is computed by summing the three values using Eq. (2.2). For example, a transformed variable of runoff is used as the source term in the continuity equation; this transformation of information plays a crucial role in integrating the two models. As another example of how the mapping procedure is used, the spatially-variable Manning coefficient given in vertex-based form can be seamlessly transferred to the cell-based form through the following mapping procedure

$$VF_{i,j} = \frac{Fraction\ Area(i,j)}{Voronoi\ Area(i,j)} \quad i = 1,2,3 \cdots N_{TIN}\ and\ j = 1,2,3 \tag{2.1}$$

$$Variable_i^{TIN} = \sum_{j=1}^{3} \left(VF_{i,j} \times Variable_{i,j}^{VPN} \right) \tag{2.2}$$

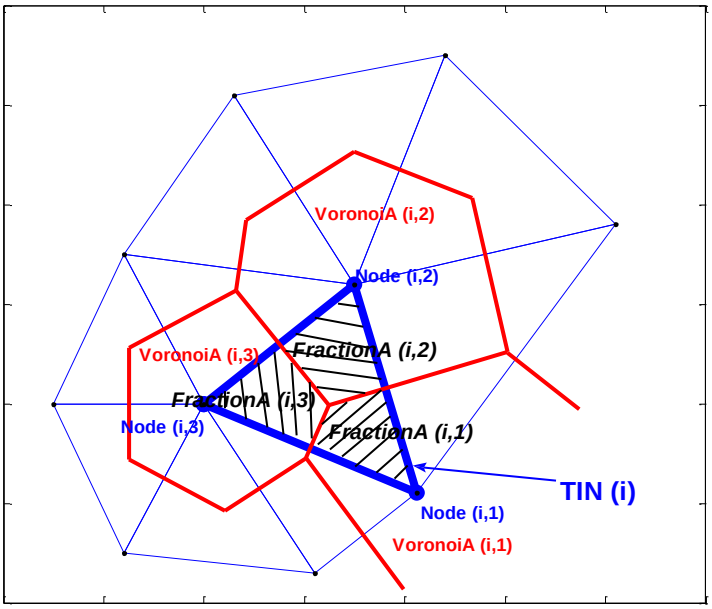

Figure 2.2: A schematic diagram of the mapping procedure.

The time step for the hydrodynamic computation is constrained due to the Courant-Friedrichs-Lewy (CFL) condition, while the model of hydrologic processes operates at fixed time steps, which are typically much larger. tRIBS-OFM therefore uses two different time steps: a small time step for the surface flow and a relatively larger one for the subsurface flow. This indicates that the total run-time efficiency depends on the calculations of the explicit Saint-Venant equations. An adaptive time stepping scheme that satisfies a local stability criterion can be used in the hydrodynamic module to reduce the total run-time [*Sanders*, 2008]. The higher level of the local time stepping implies a larger local time step (by a factor of two) for a given cell, provided the stability condition is satisfied. The runoff produced during a larger time step of the hydrological scheme is assumed to occur at the same rate over that time step. This runoff is then specified as a source term for the hydrodynamic module. The flow process however does not affect runoff generation, implying that flowing water cannot re-infiltrate. Note that such a

one-way exchange of information between modules implies that the coupling between the surface and subsurface is executed in a "loose" fashion [*Sulis et al.*, 2010].

2.3 OFM verification

The numerical results of the coupled model are compared with an analytical solution, experimental data, and results obtained by previously developed numerical models. The analytical solution can be calculated using the kinematic-wave theory only if a domain is of simple geometry. An impervious soil surface condition is assumed for the verifications, implying that all precipitation is allowed to become runoff.

2.3.1 One dimensional flow problem over mild-sloped plane

One dimensional flow along an inclined plane with a unit width and a length of 200 m is simulated. The plane has a bottom slope of 0.001 and a Manning's roughness coefficient of 0.03 $s/m^{1/3}$. The forcing is a spatially uniform rainfall of 60 mm/hr continuous intensity over the duration of 1 hour. From the analytical solution of the kinematic-wave problem, the time of concentration is 31.6 min, the uniform (normal) depth is 0.0316 m, the equilibrium discharge is 0.0033 m^2/s, and the kinematic-wave number, $KFr^2 = S_0 L_0/H_0$ (where S_0 is the bottom slope, L_0 is the channel length, and H_0 is the uniform depth) is 6.25, and the Froude number is 0.188. The kinematic wave number in this example is small and very close to the threshold value for $Fr \leq 0.5$ of 5.0 above which the kinematic approximation is appropriate [*Morris and Woolhiser*, 1980]. Also, some internal points have the kinematic-wave number less than 5, meaning that the dynamic wave method is a better option for the solution. The mesh spacing is 0.5 m, the number

of nodes and triangular cells is 1203 and 1600, respectively. The time step used during the simulation is 0.1 sec. Figure 2.3-(a) shows the hydrograph at the downstream boundary as well as a comparison with the kinematic analytical solution and the kinematic and inertia-free numerical solutions by *Gottardi and Venutelli* [2008]. The numerical solution by *Gottardi and Venutelli* [2008] of the kinematic-wave approximation is consistent with the analytical solution, but neither kinematic solutions show any attenuation effects in the rising limb. There is also an almost exact agreement between the numerical solution of the inertia-free formulation of *Gottardi and Venutelli* [2008] and the presented solution by tRIBS-OFM. Overall, the timing and magnitude of the rising and falling limbs are satisfactory.

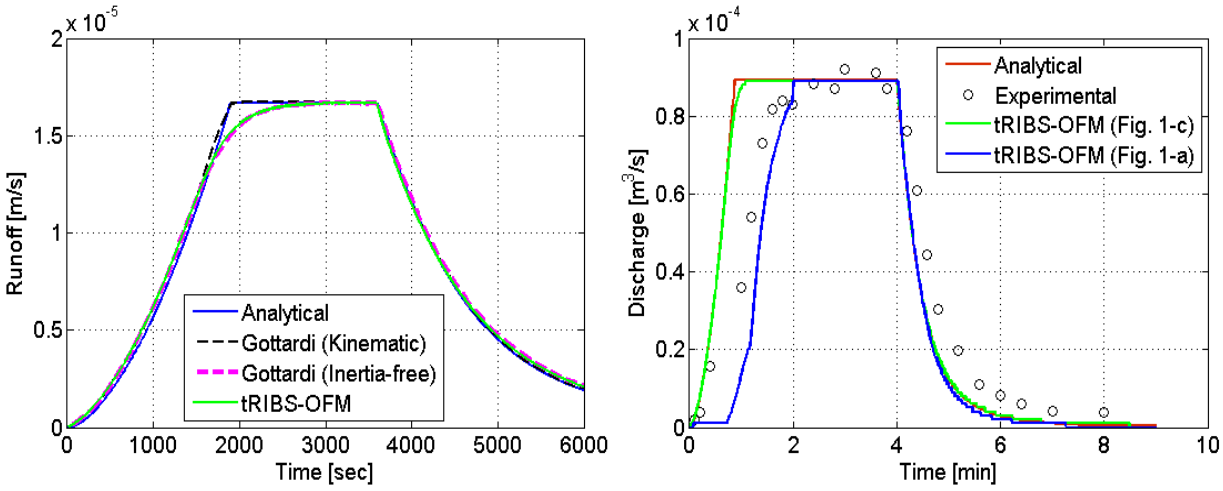

(a) Shallow-sloped plane (b) Steep plane

Figure 2.3: Two comparisons of the simulated hydrographs with: (a) the kinematic analytical solution, and numerical simulations by *Gottardi and Venutelli* [2008]; (b) the experimental data of *Schreiber and Bender* [1972] and the analytical solution. The calculated results of (b) (green and blue lines) are based on the dynamic wave method.

2.3.2 One dimensional flow over steeply sloped plane

A sloped plane that has the length of 4.88 m and the width of 2.44 m is used for a comparison with the experimental data presented in the study of *Kawahara and Yokoyama* [1980] and *Schreiber and Bender* [1972]. The characteristics of the domain used in their experiment are as follows: the bottom slope is 0.0465 (along the flow direction) and 0 (perpendicular to the flow direction), and the Manning coefficient is 0.0125 $s/m^{1/3}$. The authors used a rainfall intensity of 27 mm/hr with the duration of 4 min. From the analytical solution of the kinematic-wave model, the time of concentration is 52.6 min, the uniform depth is 0.0003945 m, the uniform discharge is 0.0000366 m^2/s, and the kinematic wave number is 575, and the Froude number is 1.492. Unlike the previous verification example, the kinematic-wave number calculated in this example is much larger than the threshold value for $Fr \geq 0.5$ of 20.0 [*Morris and Woolhiser*, 1980]. Therefore, both the kinematic and the dynamic wave methods can be used in this case, and it is found that the resulting hydrographs are essentially identical. The size of the mesh is 0.305 m, the number of nodes and cells are 161 and 272, respectively, and the time step used during the simulation time of 9 min is 0.1 sec. In Figure 2.3-(b), the hydrograph at the downstream boundary shows a huge deviation of the tRIBS-OFM results that are based on an old reconstruction method. The "no-flow phenomenon" can be easily detected at the simulation start because water is numerically retained within cells until they are sufficiently filled and "allow" water flux downstream. Conversely, an overall excellent agreement with the analytical solution is observed for the simulation results of the modified tRIBS-OFM.

2.3.3 Two dimensional flow problem in V-shaped catchment domain

A flow routing problem over a tilted V-shaped catchment [*DiGiammarco et al.*, 1996; *Panday and Huyakorn*, 2004] is considered. The V-shaped catchment is perfectly symmetrical and is divided into two parts: two hillslopes and one channel, with different bottom slopes (S_x and S_y) and roughness coefficients (n). The specific dimensions are illustrated in Figure 2.4. The rainfall intensity of 10.8 mm/hr over the duration of 90 min is used for simulations. The number of nodes and cells are 16513 and 32600, respectively. The results obtained in this study are compared with the results of four different numerical models developed by *DiGiammarco et al.* [1996], *Panday and Huyakorn* [2004], US Environmental Protection Agency [*Johanson et al.*, 1980], and US Army Corps Engineers [*HEC*, 1998]. *DiGiammarco et al.* [1996] developed an inertia-free model using a locally conservative finite element method; *Panday and Huyakorn* [2004] also developed an inertia-free model; a Hydrologic Simulation Program-Fortran, HSPF [*Johanson et al.*, 1980] model was developed on the basis of the storage routing and the kinematic wave methods; and a Hydrologic Engineering Center, HEC-1 [*HEC*, 1998] model was developed using routing schemes such as Muskingum-Cunge and the kinematic wave methods. Two different boundary conditions, that is, critical and zero depth gradient boundary conditions, can be specified at the downstream boundary. However, only a zero depth gradient boundary condition was specified in the HEC-1 model and only a critical boundary condition was specified in the HSPF and *DiGiammarco et al.* [1996] models due to the limited possible options of boundary conditions with these methods.

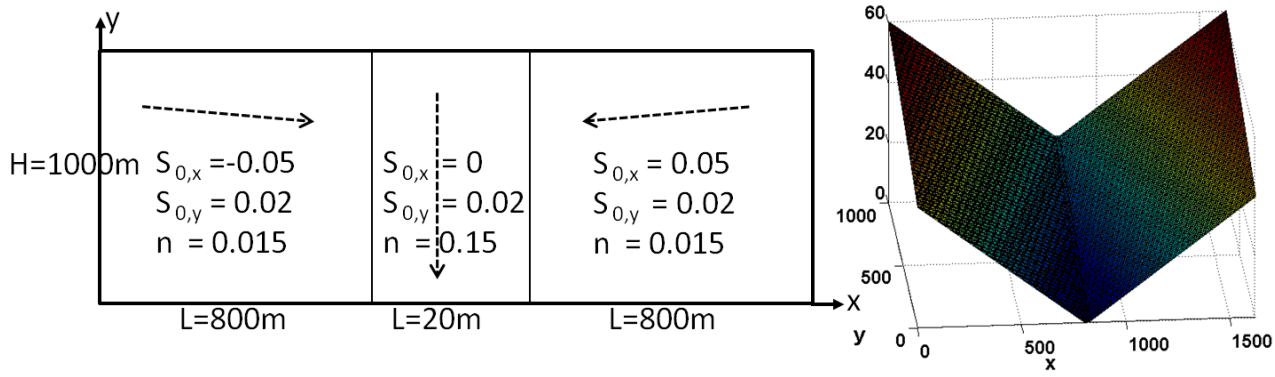

Figure 2.4: A V-shaped catchment: a plan view (left; not to scale) and a 3-D representation (right).

In Figure 2.5, the hydrograph of each model shows a somewhat different time of concentration, but all models demonstrate a good consistency with respect to the peak discharge. Note again the occurrence of the "no-flow phenomenon" (green dashed line) exhibited by the simulation results with the old method of reconstruction of variables. For the other two tRIBS-OFM cases that use either the kinematic or the dynamic wave methods, the hydrograph characteristics generally agree with those of the other models. As seen, the wave speed of the kinematic-wave model is slightly faster than that of the dynamic wave (e.g., see the rising limb). One may further investigate the actually simulated wave speeds for the kinematic case ($(5/3)\ u_k$) and the dynamic case ($u_d + \sqrt{gh}$), where u_k and u_d are the velocities of the kinematic and dynamic cases, respectively; g is the acceleration constant due to gravity; and h is flow depth. For example, at a location in the upper region of the hillslope, the kinematic-wave solution leads to a depth of 0.00017 m, a flow velocity of 0.0542 m/s, and a wave speed of 0.0903 m/s. For the same location and time, the dynamic case has a depth of 0.000173 m, a velocity of 0.0479 m/s, and a wave speed of 0.0891 m/s. At another location in the lower region of the hillslope, the

kinematic-wave solution leads to a depth of 0.004852 m, a velocity of 0.5055 m/s, and a wave speed of 0.8425 m/s, while the dynamic case has the depth of 0.004955 m, the velocity of 0.4495 m/s, and the wave speed of 0.6699 m/s. The difference in the characteristics of the propagation of two wave types is thus consistent across the hillslope.

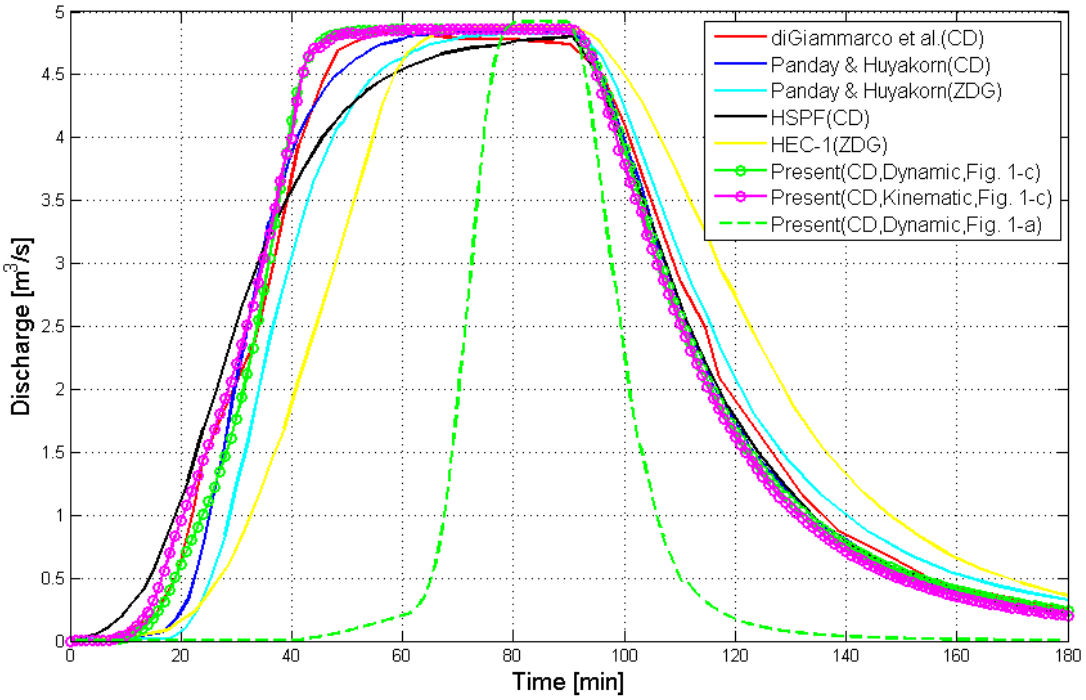

Figure 2.5: A comparison of hydrographs simulated by the presented model with numerical results of four different models. “CD” implies the critical depth boundary condition and “ZDG” stands for the zero depth gradient boundary condition.

Figure 2.6 shows the evolution of cell-centered flow depth and velocity magnitude ($=\sqrt{u^2+v^2}$) along the channel (the *x* coordinate is equal to 805 m). Twelve longitudinal profiles are plotted, corresponding to the intervals of 5 min during the first 60 min of simulation. The gradients of flow depth and velocity in the Figure 2.6 are high in the first 400 m of the channel

and small throughout the rest. Abrupt changes at the outlet occur due to the imposed critical flow boundary condition. One may note that the overall shape of the flow depth evolution is similar to the formulation of a kinematic wave that uses the combined sheet and rill flow conceptualization [see *Sulis et al.*, 2010].

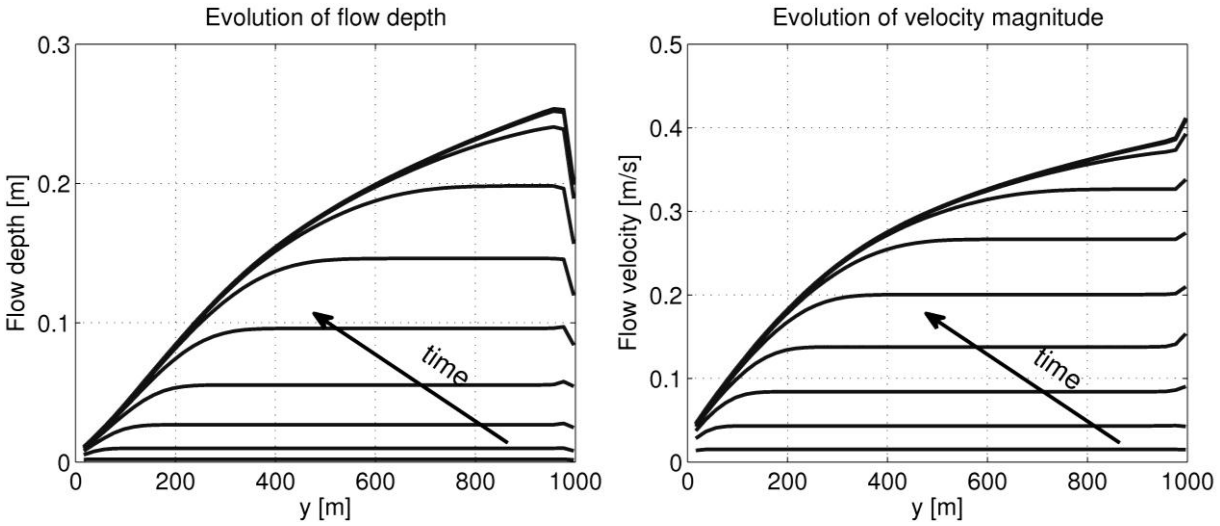

Figure 2.6: The evolution of cell-centered flow depth (left plot) and velocity (right plot) along the channel (x = 805 m). The outlet of the domain is at y = 1000 m. Each line shows a profile for every 5 min during the first 60 min of simulation. The last four profiles, corresponding to times 45, 50, 55 and 60 min, are overlapped because the steady state was reached.

Figure 2.7 illustrates transverse-profiles of flow depth and velocity taken at every 3 min during the first 30 min of the same simulation (the *y* coordinate is equal to 503.3 m). The channel is defined as the segment between coordinates x = 800 and 820 m, while the rest of the region can be regarded as hillslopes. A tendency of increasing flow depth and velocity can be noticed in Figure 2.7, when one moves downslope along hillslopes. The corresponding magnitudes are very small and thus the kinematic approximation is reasonable in the hillslopes because of a high

kinematic wave number. However, the channel with the shallow slope has a larger flow depth and a smaller velocity magnitude, which leads to a small kinematic wave number. This may warrant using the dynamic wave formulation. Overall, as seen from the above examples, flow in various parts of the domain should be modeled with different levels of approximation of the governing equations.

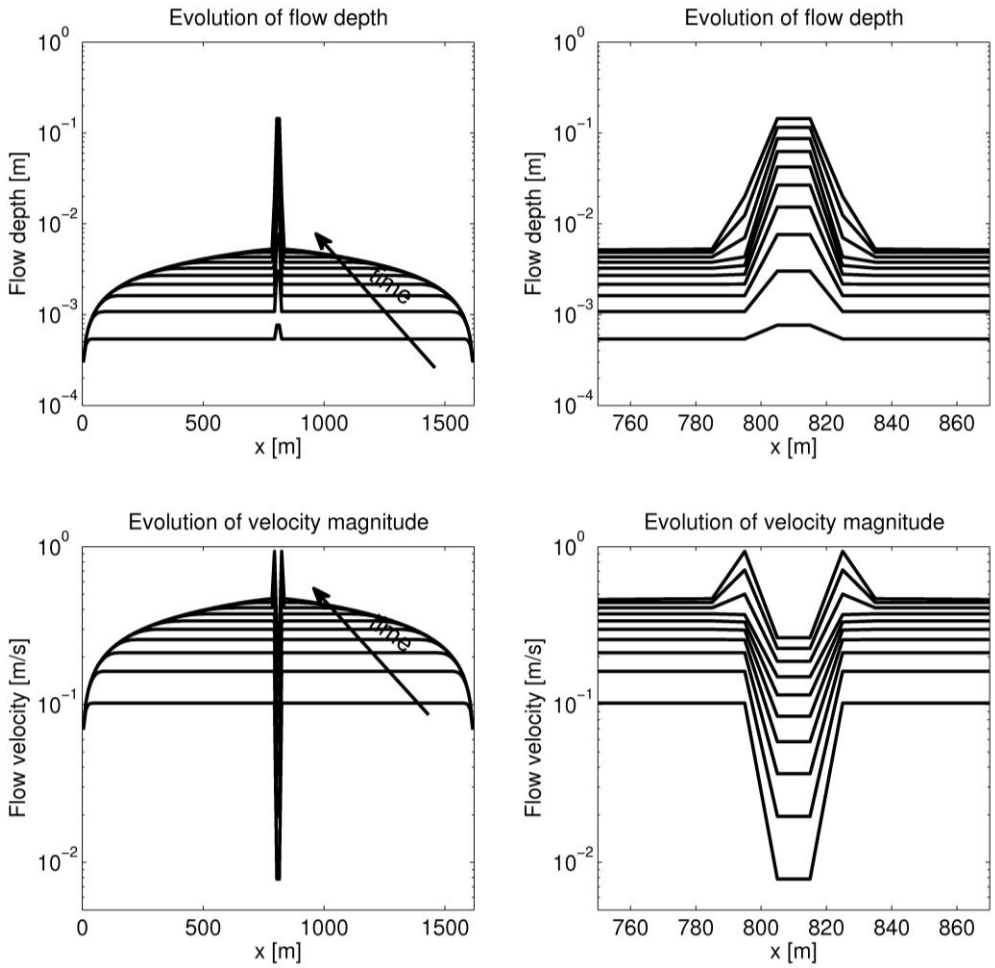

Figure 2.7: The evolution of cell-centered flow depth (upper subplots) and velocity (lower subplots) along the hillslope. The transverse profiles were taken at y = 503.3 m. The channel is located between coordinates 800 and 820 m, while the rest of the region can be regarded as hillslopes. Each profile is shown for every 3 minutes during the first 30 minutes of simulation. The zoomed in figures of the channelized area are shown on the right.

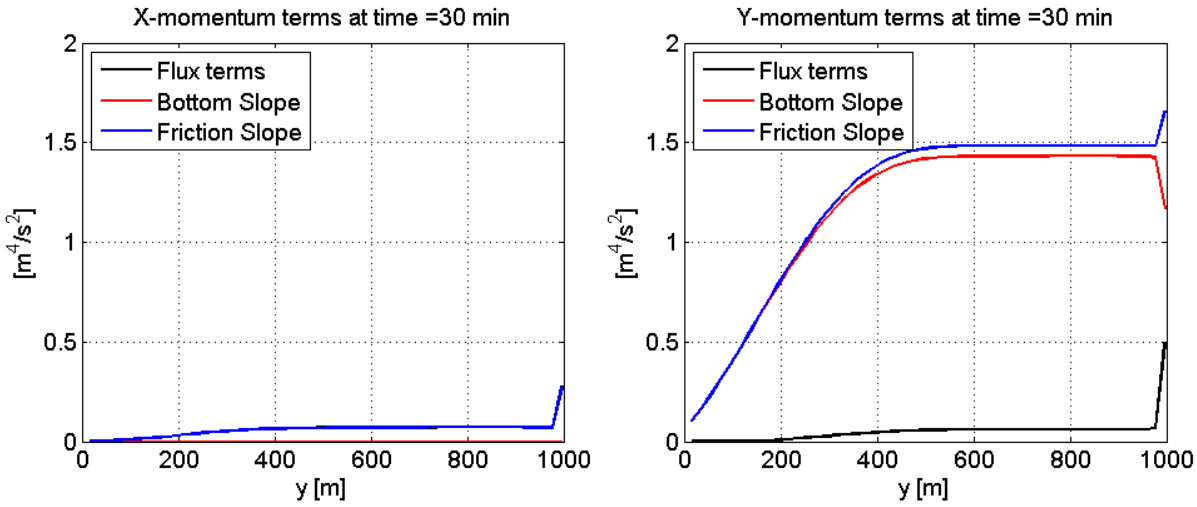

Figure 2.8: The flux, the bottom slope, and the friction slope terms in the *x*- (left plot) and *y*- (right plot) momentum equations along the channel (corresponding to the coordinate x = 805 m) at time of 30 min. The domain outlet is at y = 1000 m. In the left figure, the black line is identical to the blue line.

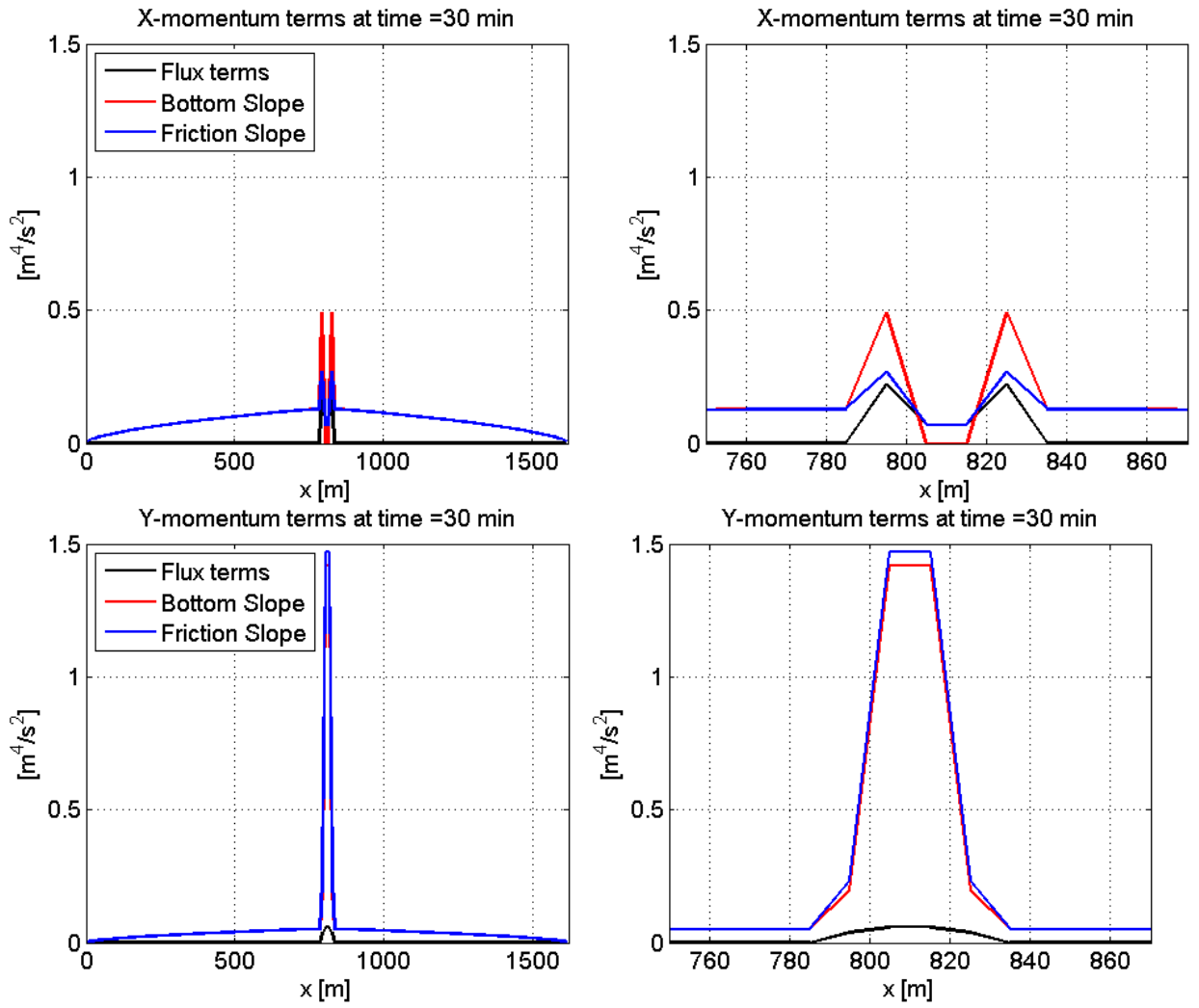

Figure 2.9: The longitudinal profiles of the flux, the bottom slope, and the friction slope terms in the *x*- (upper plots) and *y*- (lower plots) momentum equations (*y* = 503.3 m) at time of 30 min. The channel is between coordinates 800 and 820 m. The zoomed in figures near the channel area are shown on the right.

In order to illustrate the above notion more explicitly, the effects of the inertia and pressure in the momentum equations are presented for different profiles in Figures 2.8 and 2.9. The flux terms are calculated as the line integral of fluxes in each cell, which include the convective acceleration and pressure terms. The bottom slope and the friction terms are calculated as the areal integrals of the first and second source terms in each cell, which represent

gravity and bed resistance, respectively. As an example, for the *x*-direction, the flux, the bottom slope, and the friction slope terms are calculated as follows

$$Flux\ term = \oint_{\partial\Omega} -\left(huu_{\perp} + \frac{1}{2}gh^2\cos\emptyset + \frac{1}{24}g\Delta h^2\cos\emptyset\right)ds \tag{2.3}$$

$$Bottom\ slope\ term = \iint_{\Omega} -gh\frac{\partial z_b}{\partial x}d\Omega \tag{2.4}$$

$$Friction\ slope\ term = \iint_{\Omega} -C_D u\sqrt{u^2+v^2}d\Omega \tag{2.5}$$

where h is flow depth; u and v are the x- and y- components of the velocity, respectively; g is the gravitational acceleration constant; z_b is the bed elevation; C_D is the bed drag coefficient that is parameterized by using Manning's coefficient, n, as $C_D = gn^2h^{-1/3}$; $u_{\perp}$ denotes the velocity normal to the cell interface, computed as $u_{\perp} = u\,cos\,\emptyset + v\,sin\,\emptyset$; $\emptyset$ is an angle between the face normal vector and the x axis; and Δh is the variation of h along the cell face. The last term in equation (2.3) represents a hydrostatic thrust correction suggested by *Bradford and Sanders* [2002], which is necessary to balance the bed slope terms in the still water condition. All terms have units of $[m^4/s^2]$ and the absolute values are used for a comparison. Figure 2.8 shows the magnitude of the flux terms and the bottom and friction slope terms in the x- and y- momentum equations along the channel, corresponding to the coordinate x = 805 m. In the x- momentum equation, the bottom slope is zero due to the flat bottom along the channel, and the flux terms are identical to the friction slope term. The latter implies that the pressure and inertia are balanced by the resistance force, and thus the kinematic wave approximation is not appropriate on a flat plane even though the x- components of flow are practically negligible. On the other hand, in the y-momentum equation, the flux terms are relatively small and the bottom slope term is almost the

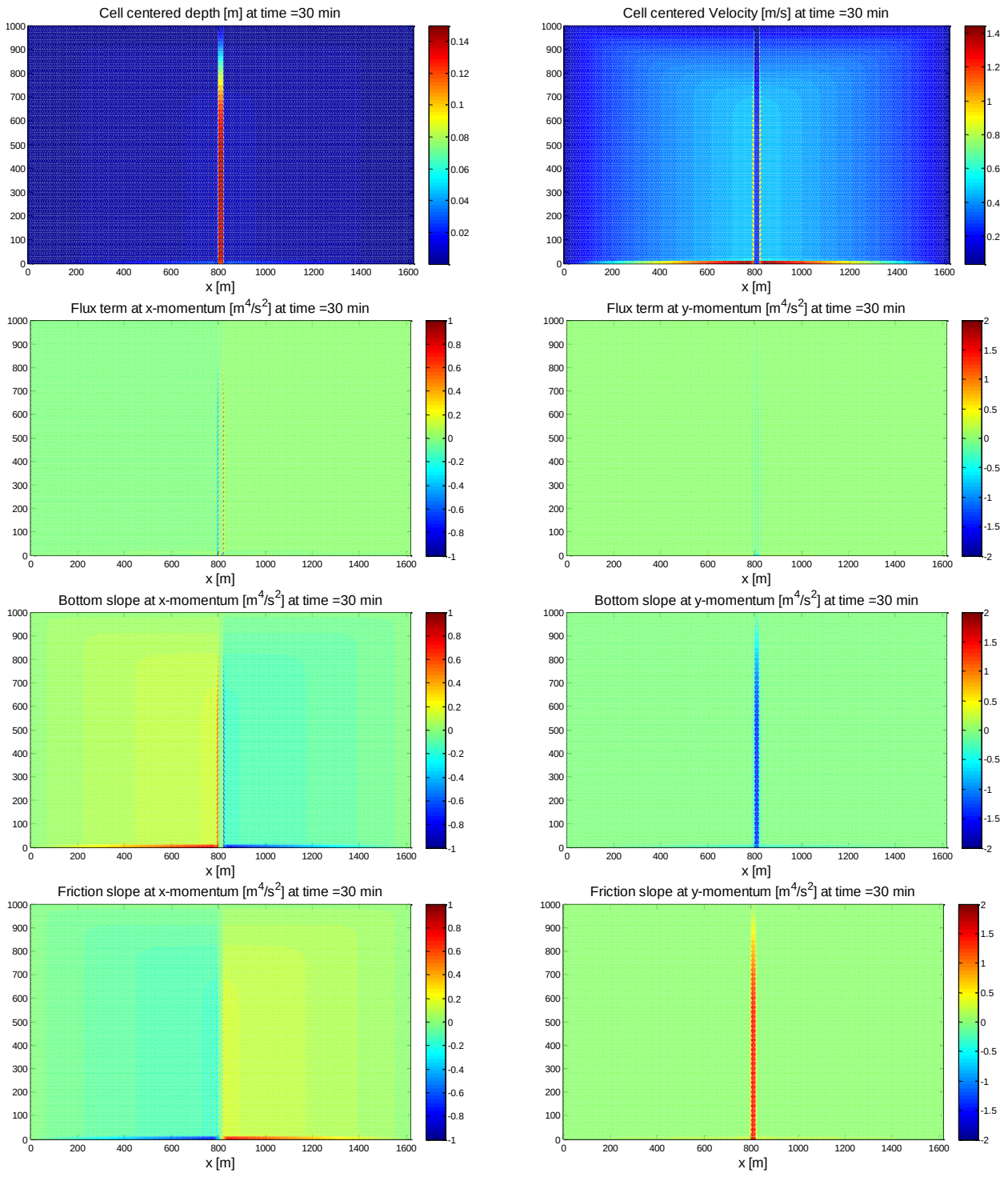

Figure 2.10: The spatial distributions of cell-centered variables at time of 30 minutes: the flow depth and velocity magnitude, as well as flux, the bottom slope and the friction slope terms in the x- and y- momentum equations.

same with the friction slope term. Still, one can expect small errors (less than 5 %) to occur if the kinematic wave method is used for this flow situation.

The importance of the flux terms in the channel area is highlighted in Figure 2.9, which provides longitudinal profiles (i.e., along the *x*- axis). The flux terms are nearly zero, and the two other terms are almost the same in the hillslope region. Thus, the kinematic wave approximation for both directions is a natural simplification. However, in the transitional area between the hillslope and the channel (e.g., $780 < x < 800$ m), the flux terms become significant and their magnitudes are of the same order as the other terms. Consequently, the "dynamic" effects are generally minor for a simple hillslope but should be considered for a consistent description of the flow situation where topography is characterized by flat slopes or where vastly varying slopes exist.

The spatial distributions of cell-centered variables such as the flow depth, the velocity, and the terms of the momentum equation (in both the *x*- and *y*- directions) at time equal to 30 min are shown in Figure 2.10. The figure allows one to appreciate the spatial variability of flow situations that can be described with various degrees of approximation of the Saint-Venant equations. It illustrates the differences between the channel and hillslopes as well as the symmetry of simulated variables for both hillslopes. The flow depth is less than few centimeters in the hillslopes, but it is larger by one order of magnitude in the channel. The flow velocity in the hillslopes is higher than that in the channel and it is generally less than 0.5 m/s. In terms of the spatial distribution of the momentum terms, the same conclusions can be made, i.e., the relative importance of the inertia and pressure terms is not very high and the kinematic approximation is appropriate for the hillslope areas. However, the influence of inertia and pressure increases when an abrupt change of topography occurs near the channel. The preceding

example convincingly illustrates that even for this particular case, which can be described by "kinematic wave conditions", the relative magnitudes of various terms vary across the landscape.

2.3.4 A hydraulic jump problem for steep-to-mild slope transition

A steep-to-mild slope transition, in which water at a high velocity enters a zone of tranquil flow, is used for illustrating the capability of the model to reproduce the occurrence of a hydraulic jump. A rectangular domain of total length of 2000 m and width of 2 m consists of two stream reaches, each of which has length of 1000 m. The upstream reach has a hydraulically steep slope (10%), while the downstream reach has a mild slope (0.1%). No rainfall and no infiltration conditions are assumed. The Manning coefficient for both reaches is 0.02 $s/m^{1/3}$ and the upstream inflow discharge is 20 m^3/s. Critical depth condition is imposed as the downstream boundary condition. The size of the mesh elements is 1 m, the number of nodes and cells are 6005 and 8004, respectively, and the time step used is 0.002 sec. In order to compare the numerical results with an analytical solution, a gradually-varied flow equation at steady state is used. From the analytical calculations, the normal depths for the steep and mild stream segments are 0.7597 and 3.0243 m, respectively, while the critical depth is 2.1685 m. The upstream conjugate depth is 1.538 m and a hydraulic jump occurs in the mild reach, which is established by comparing the specific momentum forces in both reaches. Figure 2.11 shows the depth profiles along the flow direction (left-to-right) for the analytical solution and the dynamic wave simulation by tRIBS-OFM. The kinematic wave "solution" is also presented but it cannot capture the hydraulic jump due to inherent nature of its assumptions; it simply calculates the normal depths for each of the stream segments. The latter solution is incorrect because a hydraulic jump

must occur at the downstream reach and the flow depth has to gradually increase before or after the jump. As seen in the figure, the dynamic wave solution correctly simulates the drawdown (M2) and the tailwater (M3) profiles and captures the location of the hydraulic jump. The drawdown profile occurs because the downstream reach cannot approach the normal flow condition due to an insufficient reach length and because of the critical boundary condition specified at the domain outlet. The large difference between the kinematic and dynamic wave solutions in the area between 1000 and 1200 m emphasizes that the dynamic wave method is needed when abrupt slope transitions occur.

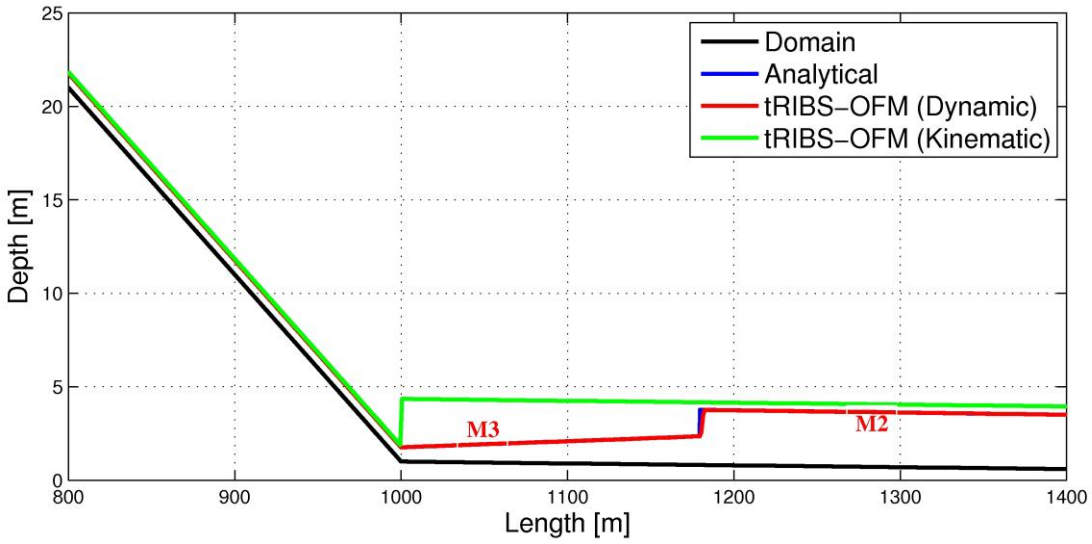

Figure 2.11: Flow depth profiles for a steep-to-mild slope transition. The tailwater (M3) profile followed by a hydraulic jump and the drawdown (M2) profile are all very well simulated by the dynamic wave solution (the analytical profile cannot be clearly seen because it coincides with the simulated profile).

2.4 Model application

2.4.1 Model application to a synthetic watershed

The presented model shows a good performance when compared to other model results for the cases of simple domain topography and rainfall input. In order to investigate the rainfall-runoff phenomenon under more complicated conditions, a synthetic domain is used with three different inputs of precipitation and four mesh types. The synthetic domain selected for the simulations represents a wide range of geometric characteristics, such as slope magnitudes and flow drainage directions. The three different inputs of precipitation correspond to uniform intensities of 10, 50 and 100 mm/hr. The domain is 2 km × 2 km and the dimension of a typical TIN element in the coarsest mesh is about 30 m × 40 m (the elements are of triangular shape). Figure 2.12-(a) and 2.12-(d) show the three-dimensional topographic representations of the coarser and finer mesh illustrating both valleys and hillslopes. The four different mesh types shown in Figure 2.12-(a) to 2.12-(d) are used to evaluate the sensitivity of the hydrograph simulation to mesh resolution. The domain shown in Figure 2.12-(a) has a uniform coarse resolution, where each cell has an area of 600 m^2. The domain shown in Figure 2.12-(d) is resolved at a finer scale, with cells that are 9 times smaller. The domains shown in Figure 2.12-(b) and 2.12-(c) have nested regions resolved at a finer scale (same as Figure 2.12-(d)). This mesh generation is performed by refining the region where the flow concentration is anticipated according to the convergence of surface contributing areas. For example, Figure 2.12-(b) and 2.12-(c) are refined in the region where the surface contributing area of each Voronoi cell (defined using the steepest drainage direction approach, e.g., *Ivanov et al.* [2004a]) is greater than 10 and 1 percent of the total contributing area of the domain, respectively. The total contributing area at the outlet of all domains is 4 km^2. In total, 2601, 4717, 7918 and 22801

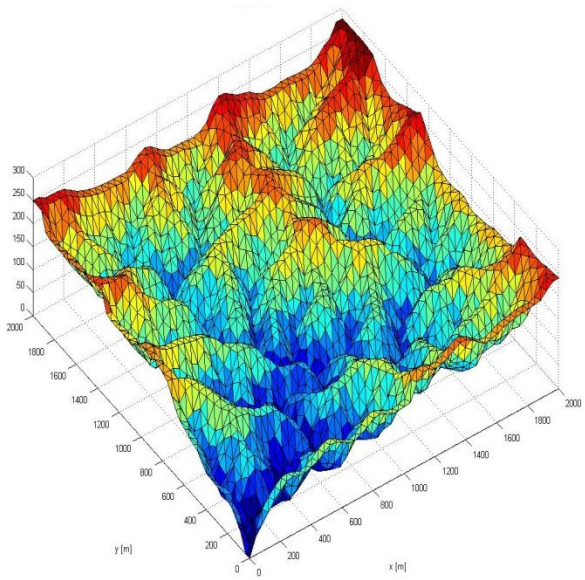

(a) Coarser mesh (cell area = 600 m^2)

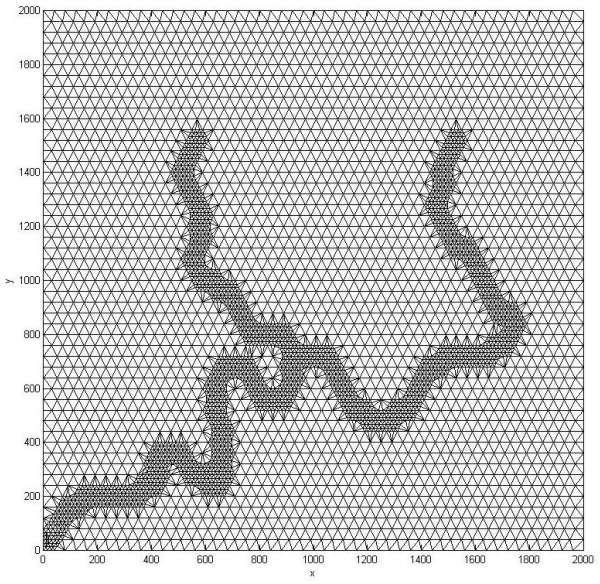

(b) Refined mesh (CA 10%)

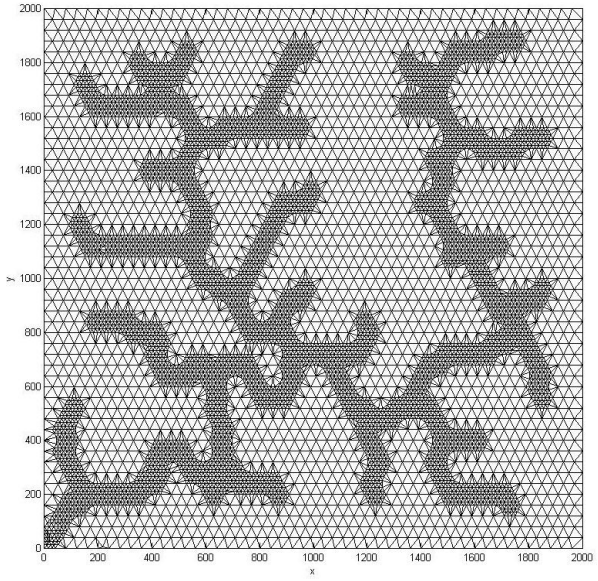

(c) Refined mesh (CA 1%)

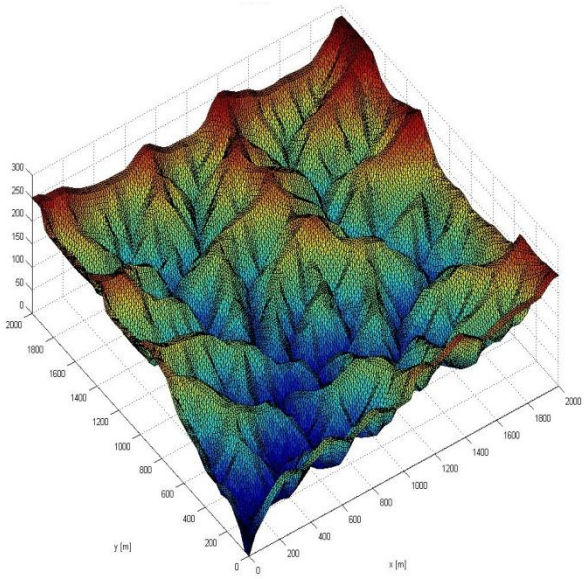

(d) Finer mesh (cell area = 66.7 m^2)

Figure 2.12: Four different meshes used in simulations: (a) and (d) show the three-dimensional representation of the synthetic domain, and have a uniform resolution. The cell size of the domain in (d) is 9 times smaller than that of the domain in (a); (b) and (c) have refined cell resolution defined according to the convergence of surface contributing area (CA), which are refined in the region, where the surface contributing area of each Voronoi cell is greater than 10 and 1 percent of the total contributing area of basin, respectively.

computational nodes and 5000, 9226, 15628 and 45000 computational TIN triangular cells are used to represent the meshes shown in Figure 2.12-(a) to 2.12-(d). Impervious surface is assumed and thus all precipitation becomes surface runoff. Such a design facilitates the investigation of the surface flow without considering subsurface flow phenomena.

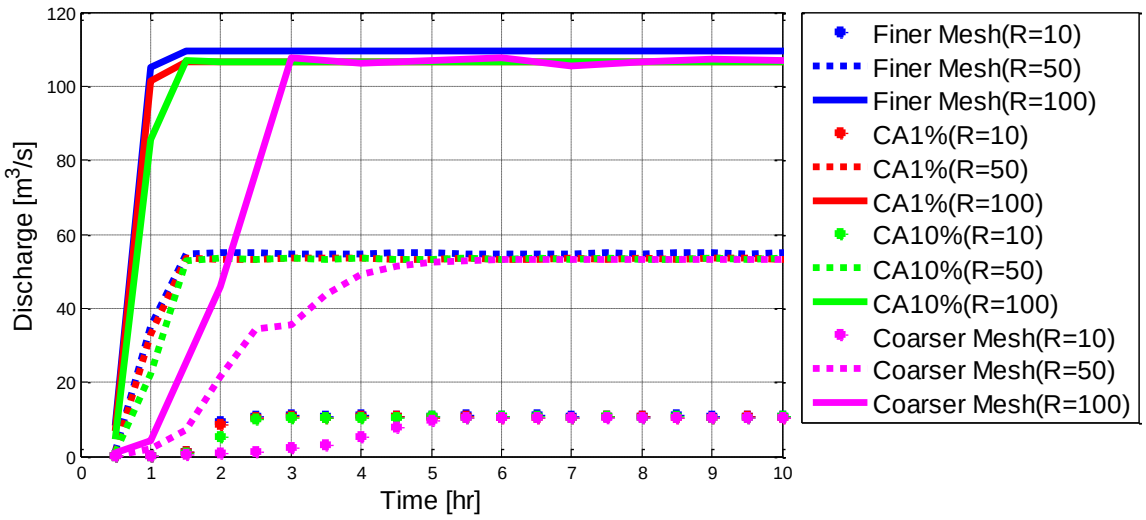

Figure 2.13: The outlet hydrographs for four different input meshes and three precipitation scenarios. Only the dynamic model formulation was used. “CA” is contributing area and “R” is rainfall rate.

Figure 2.13 shows the outlet hydrographs for each of the domains when the dynamic formulation is used. One may note that one of the characteristics of the simulation for the domain with the coarser mesh is a delay of response to the rainfall event (e.g., until after about 3 hours for the rainfall rate of 100 mm/hr), even though runoff is generated all the time. If it rains only for a short period of time (e.g., less than 3 hours in the above example), no outflow occurs and all storm runoff is stored in the domain. In contrast, the hydrographs corresponding to the finer

mesh cases exhibit non-zero outflow at the outlet shortly after 1.5 hours. All domains show similar values of peak discharge after a steady state is achieved because the same magnitude of precipitation is used (the minor difference in magnitudes is due to slightly different total runoff production because the runoff outside of Voronoi cells located along the boundaries is assumed to be zero). For the lower rate of precipitation (see also Figure 2.13), a similar effect of the dependence of the time of concentration on mesh resolution can be observed. These results imply that the model behavior is resolution-dependent.

In previous research by *Begnudelli and Sanders* [2007], *Yu and Lane* [2006] and *Sulis et al.* [2011], similar results were achieved, in terms of the effect of grid resolution on the flow. *Begnudelli and Sanders* [2007] applied their model to simulate the St. Francis dam break problem with different Manning's coefficients and with different mesh resolutions. According to their results, an increase in the mesh resolution had a significant effect on the flood behavior: the time of concentration was smaller for a finer mesh than for a coarser mesh due to the higher speed of the flood in the former case. *Begnudelli and Sanders* [2007] explained this phenomenon by stating that "a poorly resolved grid behaves similarly to a grid with an unrealistically large resistance parameter".

To provide a deeper insight for such an effect, slope characteristics of four mesh types were examined. In the channel network, slopes are typically small, with magnitudes lower than 1 degree. In the hillslope, slopes can be very steep, larger than 40 degrees. Such a high slope magnitude results in a significant elevation difference among the triangle vertices, particularly for a coarse mesh. Therefore, using a refined mesh near the channel can contribute to different delineations of channel and floodplain. A coarser mesh represents a much wider channel width than a mesh with a finer resolution. The implication is that a wider channel width influences the

conveyance ability, leading to a lower velocity of the flow in the channel. Figure 2.14 shows the spatial distribution of the flow velocity at the same location for the cases of the coarser mesh and the refined mesh (CA 10%). The simulation shows that water is concentrated only in the colored portion of the map, which corresponds to the channelized flow. The computed flow for the refined mesh is faster than that for the coarser mesh. This confirms the previous observation that finer meshes lead to a faster response to rainfall at the outlet. Thus, the computational results indicate that a finer resolution is required to differentiate the channel regions from the rest of the domain. However, one may also infer from Figure 2.13 that the simulation is insensitive to the increased resolution of the entire watershed area. This indicates that only channel/floodplain areas need to be represented at a higher level of detail to alleviate the resolution effects of reduction of conveyance ability.

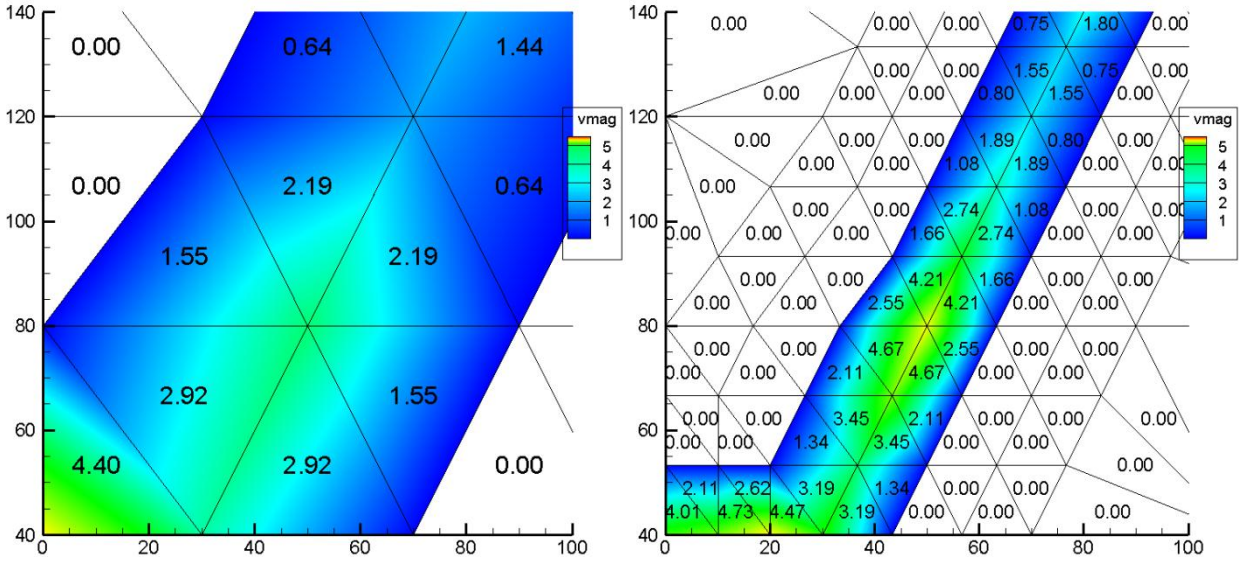

Figure 2.14: The spatial distribution of velocity in coarser mesh (left plot) and a refined mesh (for CA 10%; right plot). The same location is illustrated in both plots. The numerical values and figure legends denote the simulated velocities in [m/s].

2.4.2 Model application to a natural watershed

2.4.2.1 A description of the Peacheater Creek watershed

The cases of the model application to the synthetic domain and three verification cases focus on the dynamics of overland flow and do not consider hydrological processes that include runoff generation processes. This section presents cases where a full rainfall-runoff phenomenon is reproduced for a real-world, mid-size watershed with complex terrain and land-surface conditions. The Peacheater Creek watershed, with its outlet located near Christie, OK, (see Figure 2.15) was selected as a case study for investigating the surface flow phenomena with the coupled hydrology-overland flow model. The area of the watershed is 64 km^2 and the predominant soils are gravelly silt loams. The basin exhibits typical slopes of 2-5% and steeper slopes of 15-40%. About 36% of the area is occupied by deciduous and evergreen forest in the southern region of the catchment, while about 54% is occupied by pasture and agricultural crop lands in its northern region (Figure 2.15). Basic topographic and hydrologic characteristics of the basin and spatial distributions of soil and land use are described in *Ivanov et al.* [2004b]. This watershed was selected because it was one of the experimental watersheds in the Distributed Model Intercomparison Project, DMIP [*M B Smith et al.*, 2004] and DMIP-2 [*M B Smith et al.*, 2006]. The hydrologic component of the presented model, tRIBS, was among twelve models used in DMIP. Streamflow simulations were compared to observations and were shown to attain a reasonable performance [*Ivanov et al.*, 2004b]. Unfortunately, the only data available for the model assessment and verification are streamflow series. Nevertheless, this simulation case of the DMIP study represents an appropriate scenario because it further demonstrates how spatially-distributed information on precipitation and watershed properties can affect simulation results. In

this study, we used the same parameter values and the same initial condition, except those used for the flow routing and soil parameterization.

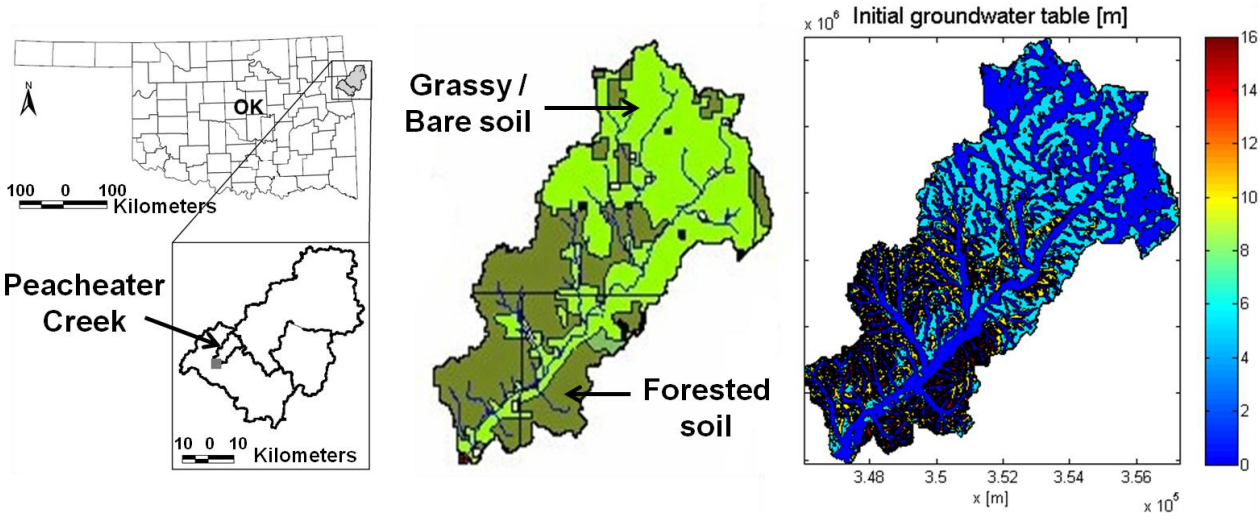

Figure 2.15: The location (left plot), landuse (middle plot), and initial groundwater depth distribution (right plot) of the Peacheater Creek watershed.

The representation of catchment topography is based on a USGS 50-m resolution DEM: the number of nodes and triangular cells is 25531and 51030, respectively. Information about vegetation cover and soil type was obtained from the USGS Land Use and Land Cover (LULC) and the Soil Conservation Service (SCS) State Soil Geographic Database (STATSGO). The NWS Next-Generation Weather Radar (NEXRAD) data are used as rainfall estimates obtained at the resolution of one hour from the Arkansas-Red River Forecasting Center (ABRFC) from 1993 to 2001 (for a description, see*M B Smith et al.* [2004] *M B Smith et al.* [2004]). Meteorological data including atmospheric and vapor pressures, cloud cover, wind speed, and air temperature (see *M B Smith et al.* [2004]) are used for the computation of energy flux partition. The

interception and evapotranspiration parameters are obtained from the literature and previous calibration efforts [*Ivanov et al.,* 2004a]. The simulations are carried out in a continuous fashion and include the representation of subsurface and surface dynamics. The time step used for hydrologic processes is 3.75 min, and the time step used for hydraulic routing is 0.5 sec, which can be adaptively increased according to the local CFL condition.

2.4.2.2 Calibration of channel and hillslope routing parameters

Hydrologic models consider spatially distributed data, such as topography, vegetation cover, soil type, and surface properties, and thus can describe a distributed basin response to atmospheric forcing in a long-term simulation. Although hydrologic models have shown a credible performance in predicting the overall trends of streamflow, they have difficulties associated with parameterizations. Therefore calibration is typically required for a reliable simulation [*Ivanov et al.,* 2004b]. These difficulties are inevitable due to the large number of assumptions and parameters required. For example, in channel flow, the original formulation of tRIBS assumes a rectangular channel cross sectional shape with regional geomorphological relationships of the form: $b = f(A_c)$, where the channel width b is represented by a power law function of the contributing area (A_c) [*Orlandini and Rosso*, 1998]. In addition, for every hillslope path, the velocity is calculated according to the velocity-discharge relationship of the form: $V = f(Q/A_c)$, where the velocity (V) is described as a power law function of discharge (Q) and contributing area (A_c). Each assumption needs a reasonable estimation or calibration of two parameters (a coefficient and an exponent) representing characteristics of the channel network. These four routing parameters are primary in the calibration effort because they control the shape

and timing of the hydrograph in response to rainfall and results exhibit fairly high sensitivity [*Ivanov et al.*, 2004b]. Therefore, their determination plays a crucial role in routing the generated runoff in both hillslope and channel flow pathways. However, if a hydrodynamic model is used, the model fully solves the governing equations without using the above assumptions. Thus, the former parameter calibration is no longer needed, except for the Manning's coefficient that quantifies bed resistance to flow. Overall, one might expect the model to produce more reliable results.

2.4.2.3 Soil parameter calibration

Manual calibration has been performed using the outlet streamflow of the Peacheater catchment by changing the soil parameters that affect runoff production. The calibration was carried out for a single rainfall event, starting on September 24, 1996, with the total simulation duration of 200 hours. The soil distribution in the watershed was divided into two distinct regions: cropland and pasture in the northern part, and forested soil in the southern part [*Ivanov et al.*, 2004b]. Therefore, two soil parameter sets were used. In this study, five calibration cases of soil parameters with various conditions are presented. They were derived based on a comparison of the simulated runoff volume with the observed total streamflow volume. Specifically, soil parameters were calibrated to satisfy the conditions that the simulated peak discharge needs to be consistent with the observed one (e.g., Case 2, 4); and the simulated total runoff volume needs to be consistent with the observed volume (e.g., Case 1, 4). The soil parameter values and descriptions used in the calibration are described in the Table 2.2. Figure 2.16 shows the observed and simulated streamflow hydrographs, as well as the simulated instantaneous runoff production rate (expressed in the same units as streamflow). The latter,

influenced by soil parameters, is an output of hydrologic processes and used as an input to the model of hydrodynamic routing. Overall, small discrepancies between hydrographs can be detected, as shown in Figure 2.16. But for Cases 2 and 4, the peak discharge agrees well with the observed value and hydrographs exhibit a similar shape. Based on various error indices, Case 4 shows the best fit with the observed data (See Table 2.4).

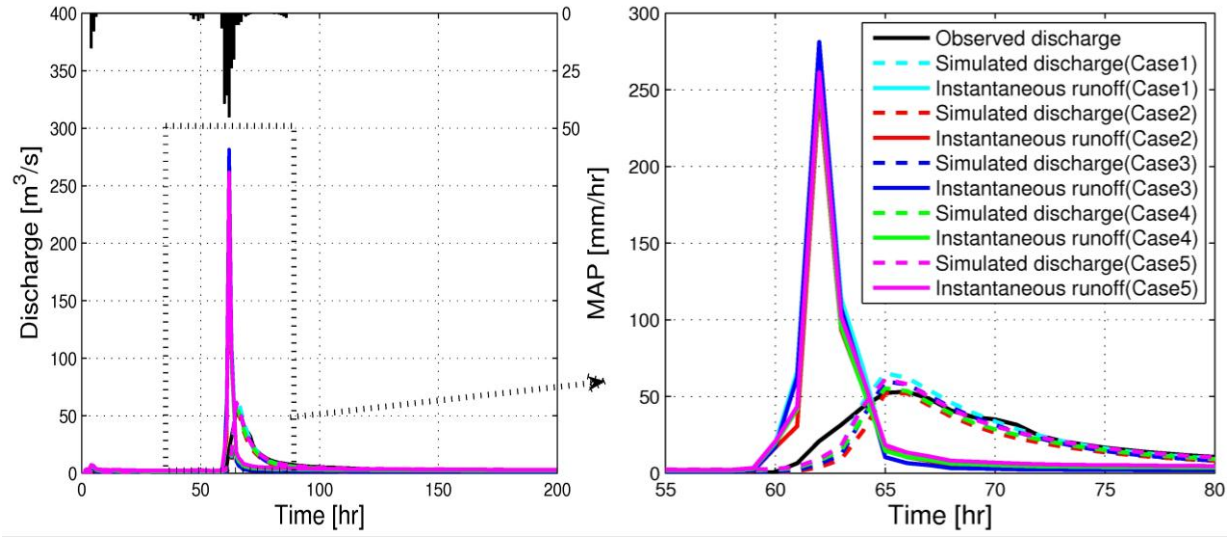

Figure 2.16: The effect of soil parameters on streamflow; mean areal precipitation (upper and right axis) and hydrographs (lower and left axis) of the observed discharge and simulated runoff and discharge. The illustrated cases have the same, spatially two different values of Manning's coefficient (See Table 2.3 and 2.4).

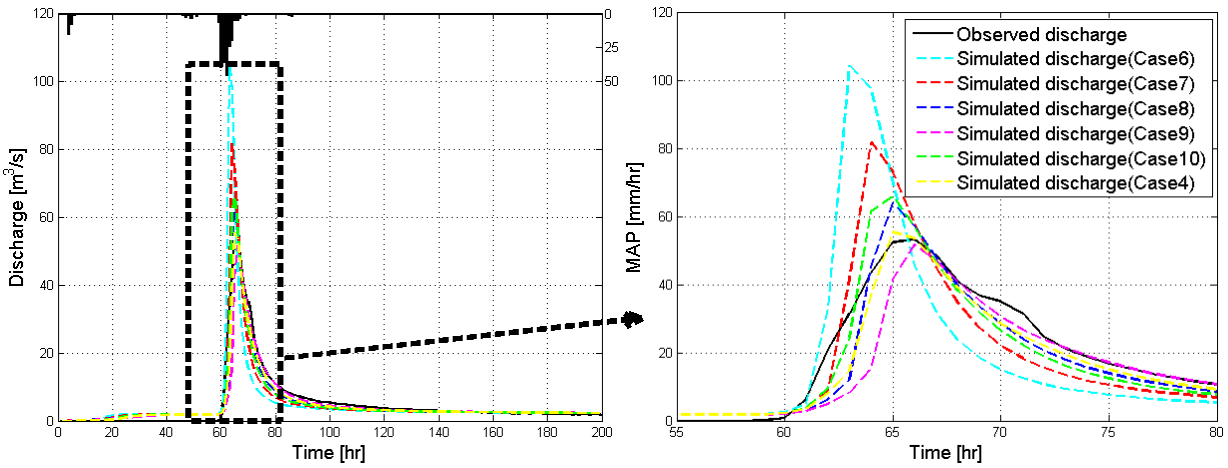

Figure 2.17: The effect of the Manning's coefficient scenario on streamflow simulation. The mean areal precipitation (upper and right axis) and observed (black line) and simulated (dash lines) hydrographs are illustrated. The cases shown have the same soil parameters as the Case 4 of the soil scenarios.

2.4.2.4 Parameterization of the hydrodynamic routing model

The Saint-Venant equations are fundamental physics-based equations describing flow motion using mass and momentum conservation laws. Therefore, all parameters used in the equations can be theoretically measurable. For example, many researchers have parameterized the bed drag coefficient (C_D) by using Manning's, Chezy's, or Darcy-Weisbach coefficients, to calculate the friction terms. These coefficients can be obtained by measuring the roughness height over the flow surface, but it is quite impossible to get measured data for every computational element due to the spatial heterogeneity. As an alternative approach to this problem, calibration of the roughness coefficient can be performed in the hydrodynamic routing problem. In this study, two different cases were used due to insufficient information about the roughness in this watershed. First, a spatially uniform Manning coefficient and second, two values of the coefficient corresponding to the hillslope and channel flow paths were used (See

Table 2.3). In order to assess the sensitivity of hydrographs at the basin outlet to this coefficient, several values within a physically realistic range, i.e., between n = 0.015 and n = 0.06 s/m$^{1/3}$, were used. Figure 2.17 shows the effects of Manning's coefficient on streamflow with the same soil parameters as for Case 4, with six different combinations of Manning's coefficient. Since the results of Cases 11 and 12 are similar to those of Cases 10 and 4, respectively, these results are not shown to avoid cluttering of the figure. Significant differences among the hydrographs can be noticed. As Manning's coefficient gets smaller, the hydrographs have a higher peak discharge, the time of concentration becomes shorter, and the slope of both the rising and the recession limbs becomes steeper. This is consistent with the expected sensitivity but, overall, it is difficult to assess whether any particular parameter set is more suitable for the simulation. The corresponding error statistics are described in Table 2.4.

Table 2.3: The Manning roughness coefficients [s/m$^{1/3}$] used in calibration for Peacheater Creek.

Case	Hillslope	Channel
1-5	0.060	0.015
6	0.015	0.015
7	0.030	0.030
8	0.045	0.045
9	0.060	0.060
10	0.045	0.015
11	0.045	0.030
12	0.060	0.030
13-14	0.060	0.015

Table 2.4: The error indices of the simulation results for Peacheater Creek.

Case	Rainfall Volume [$10^3 m^3$]	Generated runoff [m^3]	Simulated outflow [m^3]	Peak flow [m^3/s]	Peak flow error [%]	Phase error [h]	Volume error [%]	RMSE [m^3/s]	RSR[-]	NSE [-]	CC [-]	EV [%]	PBIAS [%]
1	13,821	3,876,953	3,589,900	65.21	-22.53	1	2.59	2.04	0.23	0.95	0.99	94.89	-2.59
2	13,821	2,659,270	2,437,000	52.09	2.13	1	30.36	2.94	0.33	0.89	0.98	92.07	30.36
3	13,821	2,945,697	2,716,500	59.80	-12.37	1	22.37	2.44	0.27	0.93	0.99	94.17	22.37
4	13,821	3,629,601	3,340,500	55.38	-4.06	1	4.54	2.01	0.22	0.95	0.99	95.09	4.54
5	13,821	4,219,435	3,899,900	61.21	-15.03	1	11.45	1.92	0.21	0.95	0.99	95.85	-11.45
6	13,821	3,629,601	3,404,400	104.1	-95.65	3	2.71	7.61	0.84	0.29	0.88	29.01	2.71
7	13,821	3,629,601	3,383,900	81.76	-53.63	2	3.29	4.08	0.45	0.80	0.96	79.64	3.29
8	13,821	3,629,601	3,360,900	63.89	-20.05	1	3.95	2.39	0.26	0.93	0.98	93.04	3.95
9	13,821	3,629,601	3,333,800	51.67	2.91	0	4.73	3.07	0.34	0.88	0.97	88.47	4.73
10	13,821	3,629,601	3,362,900	65.88	-23.80	1	3.89	2.57	0.28	0.92	0.98	91.97	3.89
11	13,821	3,629,601	3,360,200	65.10	-22.34	1	3.97	2.46	0.27	0.93	0.98	92.62	3.97
12	13,821	3,629,601	3,335,800	53.18	0.08	0	4.67	2.36	0.26	0.93	0.99	93.24	4.67

The generated runoff is the total volume of generated runoff, while the simulated outflow is what flows out of the domain over the simulation period of 200 hours. RMSE: root mean square error; RSR: RMSE-observations standard deviation ratio; NSE: Nash-Sutcliffe efficiency; CC: coefficient of correlation; EV: explained variance; PBIAS: percent bias (See Appendix A).

2.4.2.5 Simulation results

In order to compare the simulated hydrographs presented in the previous section, several error statistics typically used in calibration and verification are presented here. Specifically, nine different error indices are computed by using the observed and simulated outlet discharge. Relevant equations are provided in Appendix A. Guidelines for the quantification of accuracy were evaluated by using reported performance ratings and range values [*Moriasi et al.*, 2007]. As one example, model simulation results are considered as "very good" if $0.75 < NSE < 1.0$, $0.0 <$

RSR < 0.5 and PBIAS < $\pm$10 %. According to these criteria, most simulation cases can be evaluated as “very good”, even though few of them (for the Cases 2, 3, 5 and 6) exhibit small discrepancies. Cases 4, 9 and 12 show particularly good results in terms of the peak flow error and volume error. Therefore, Case 4 is used for comparisons throughout the rest of the manuscript.

Figure 2.18 shows the spatial distribution of the frequency of runoff occurrence as the fraction of the total simulation time (equal to 200 hours). The pattern of infiltration excess runoff in the northern region of the basin is due to the particular structure of storm (as inferred from 4 km x 4km radar images) that passed the watershed area. Saturation excess runoff does not exhibit a particular dependence on the soil type because the infiltration capacity and lateral rates of moisture redistribution are high. This runoff mechanism, on the other hand, is highly influenced by topography. Therefore, it frequently occurs near the stream network of the watershed with large contributing areas and flat slopes of the terrain. The perched return runoff and the groundwater exfiltration runoff are also mainly generated near the stream network.

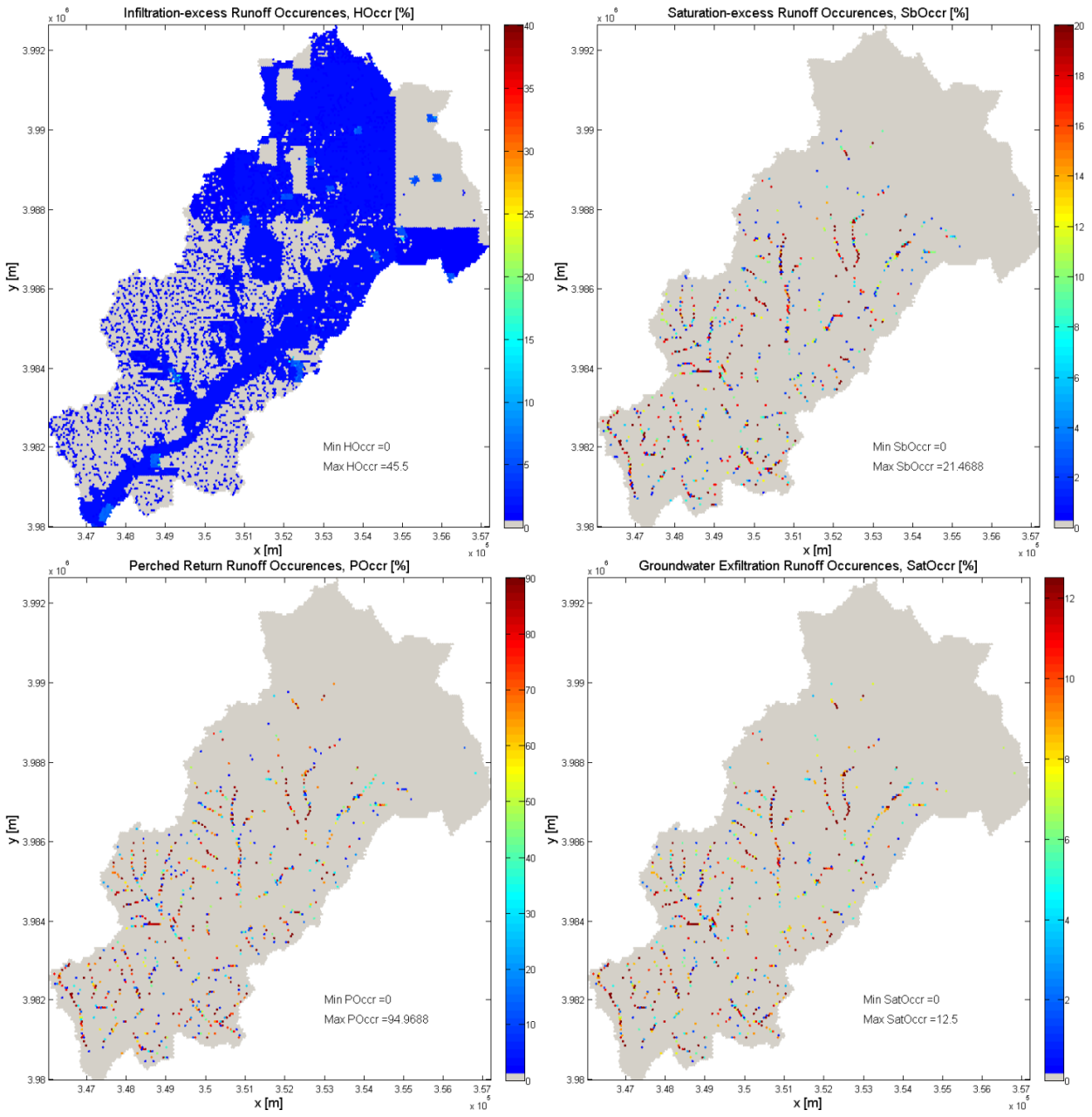

Figure 2.18: The frequency of runoff occurrence as the percentage of the total simulation time over 200 hours (for Case 4). Infiltration excess runoff (upper-left), saturation excess runoff (upper-right), perched return flow runoff (lower-left), and groundwater exfiltration runoff (lower-right) are shown.

In Figure 2.19, several hydrologic metrics, such as evapotranspiration and runoff, averaged over the entire watershed as well as the hydrographs by tRIBS (that uses a kinematic wave approximation for rectangular channels, *Ivanov et al.* [2004a]) and tRIBS-OFM are illustrated. Cases 4, 13, and 14 are used (Table 2.2). Note that Cases 13 and 14 are entirely synthetic with larger K_s and smaller f values. They were imposed to illustrate how a change in the predominant runoff generation process affects surface processes of flow as well as the consistency of coupling between the subsurface and surface flow processes. Specifically, a larger K_s increases infiltration that subsequently reduces infiltration-excess runoff for the same imposed precipitation events (Case 13). A smaller f value leads to more rapid groundwater dynamics that results in return flow emerging near the channel areas where the initial water table is shallow (Case 14). This results in high saturation-excess runoff that is generated in the early period of the simulation (starting around hour 5). This fairly large runoff volume is entirely due to the initialization of the groundwater (see Figure 2.15) and is a reflection of a synthetic nature of the experiment.

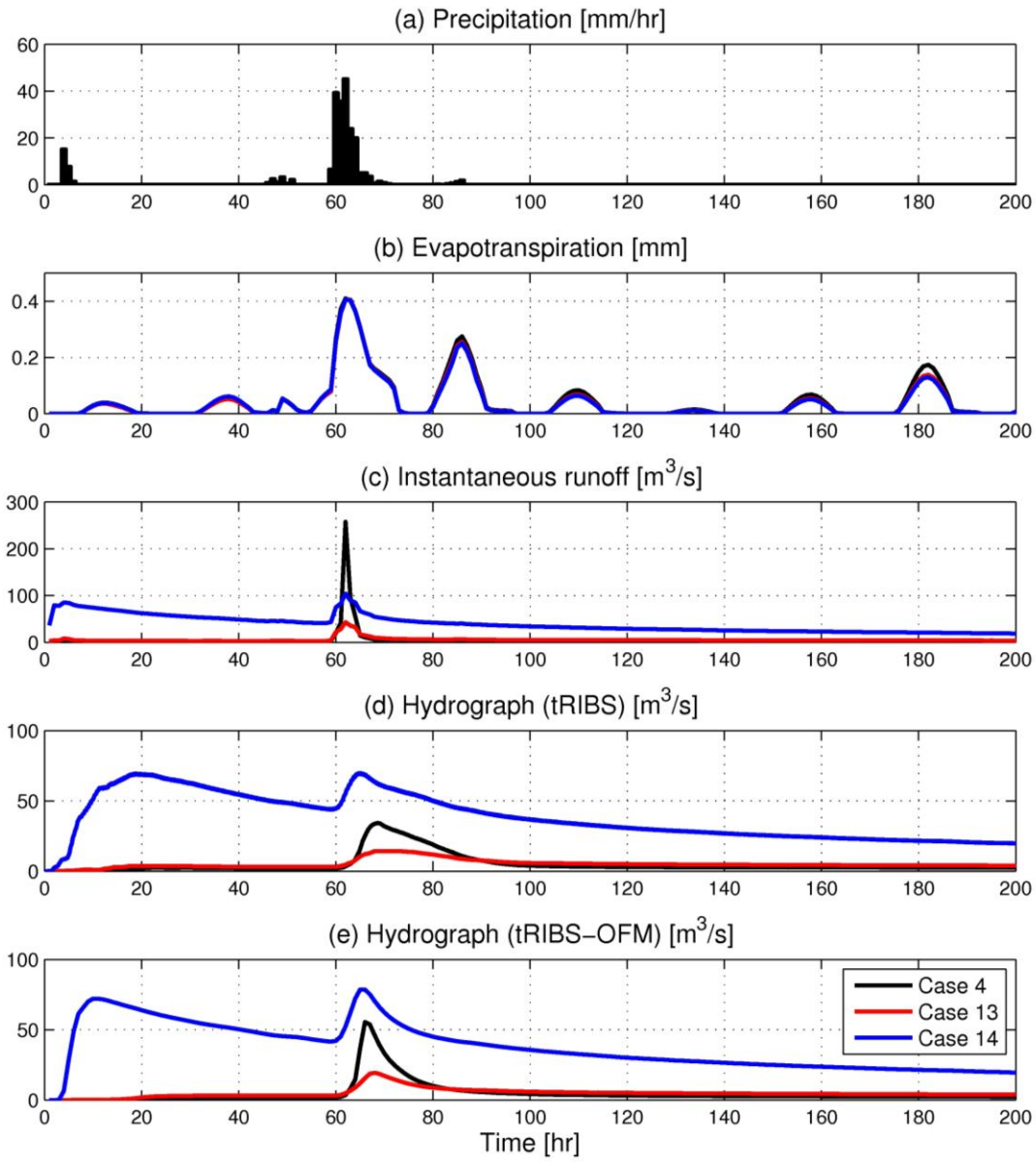

Figure 2.19: An illustration of spatially mean (a) precipitation, (b) evapotranspiration, and (c) instantaneous runoff production as well as the simulated hydrographs by (d) tRIBS (that uses a kinematic wave approximation for rectangular channels) and (e) tRIBS-OFM.

In order to illustrate the difference between the original tRIBS simulation and changes introduced by the coupled tRIBS-OFM model, two sets of simulation results are shown in the subplots (d) and (e) of Figure 2.19. Note that for the flow routing parameters described in the section 2.4.2.2, a single set of parameters was specified for the tRIBS simulation. Since a calibrated set of routing parameters used in the DMIP study [*Ivanov et al.*, 2004b] corresponds to the kinematic wave approximation, certain differences in hydrographs between tRIBS (subplot (d)) and tRIBS-OFM (subplot (e)) simulations can be observed. But, the presented comparison argues that an added value of the tRIBS-OFM coupled framework is a reduced uncertainty of the simulation: the computed flow series shown in the subplot (e) are unique, given the specified surface resistance of the watershed. Conversely, the series in the subplot (d) can be considered as a single realization of a large ensemble of possible series due to uncertainties in the parameterization of overland flow in the original tRIBS model of *Ivanov et al.* [2004a].

2.4.2.6 Hydrology-hydrodynamics coupling

As one contribution of the coupled model, a number of hydraulic variables can be explicitly simulated in a fully-distributed manner in time and space. First, instantaneous spatial distributions of depth and velocity ($\sqrt{u^2 + v^2}$) at two different times are shown in Figure 2.20. Each time represents a particular point on the simulated hydrograph, corresponding to the flow peak or recession flow. Depth and velocities in the hillslopes are very small as compared to the channel. Throughout most of the stream network, the flow has a depth of less than 1.0 m and a velocity magnitude of less than 1.0 m/s. At hour 65, near the observed peak, the flow depth is increasing, channel width is becoming wider, the channel network is more pronounced, and the

flow velocity is higher than at other times. Next, detailed information on the direction and magnitude of the two-dimensional velocity at hour 65 is shown in Figure 2.21. Most of the velocity vectors are directed toward the channel from hillslopes, reflecting water accumulation. On the other hand, only small vectors with the streamwise direction exist within the stream network because the adopted size of grid cells (50 m resolution) is not sufficiently fine to represent the channel network. This detailed velocity information is necessary for obtaining other "derivative" metrics of flow conditions, such as shear stress and vorticity. These variables are required for investigating the effects of climate and watershed hydrology on soil erosion, sediment transport, and impacts on fish habitats.

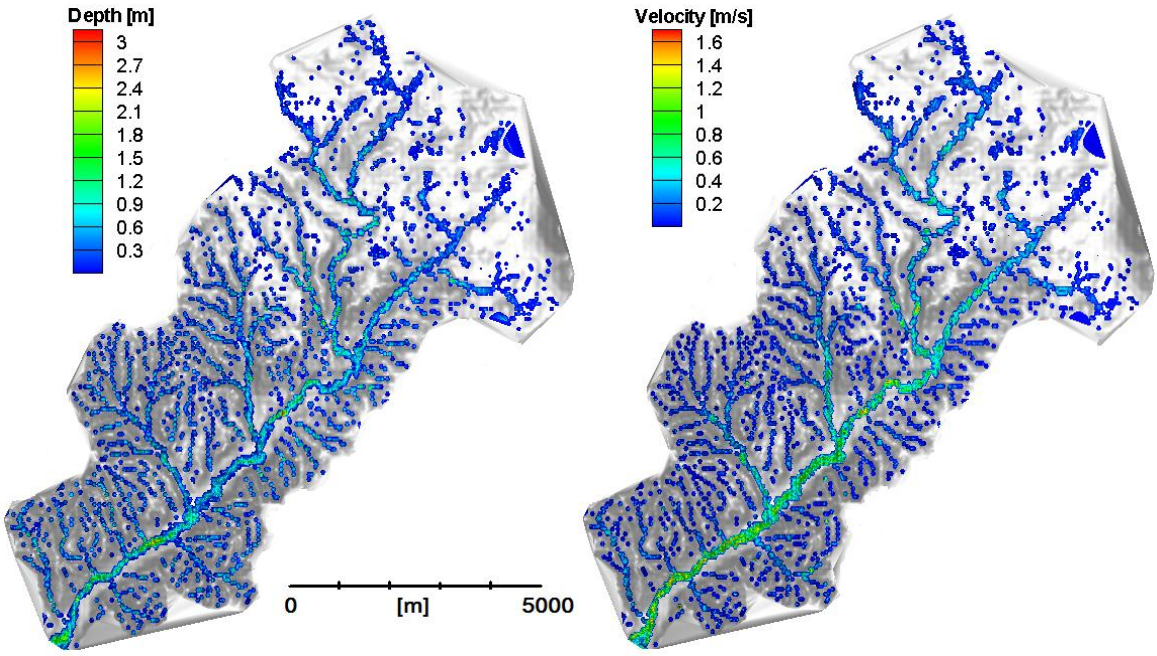

(a) Hour 65 (near observed peak)

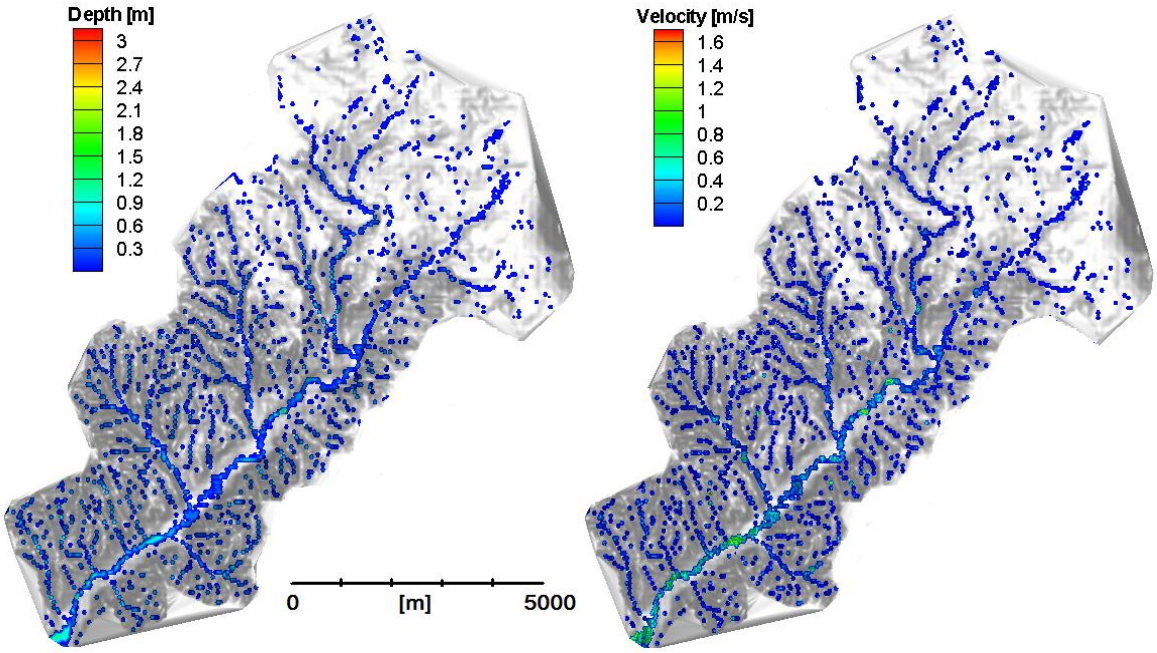

(b) Hour 120 (the recession curve)

Figure 2.20: The spatial distributions of flow depth (left plots) and velocity magnitude (right plots) for the soil scenario Case 4. The light and shade effects represent topography; the lighter shade implies a flat area, while the shaded areas imply steep terrain.

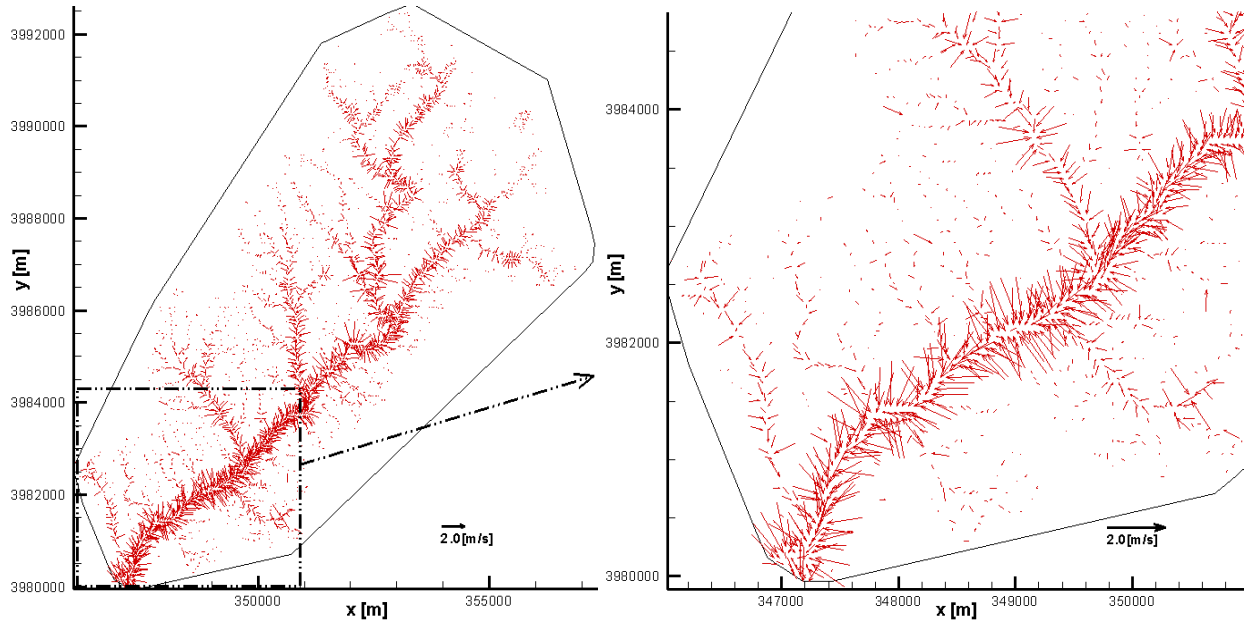

Figure 2.21: A two-dimensional representation of velocity vectors at hour 65. The soil scenario Case 4 was used.

Finally, a synthetic example is presented in the following that illustrates the model flexibility to incorporate various boundary conditions that may arise in a river basin either due to human activity or, more generally, due to the presence of complex boundaries such as lakes, tidal regimes, etc. Specifically, the impact of a downstream control on the streamflow hydrograph due to a non-regulated dam is discussed (Figure 2.22). It should be noted that other hydrologic routing techniques and kinematic wave approximations do not recognize downstream controls and backwater effects. These methods are therefore not appropriate for this situation. Using the parameter values for the Case 4, a virtual dam is constructed at the outlet of Peacheater Creek with different heights of 1.5, 3.0, and 4.5 m. As compared to the previous simulation of Case 4 (without a dam), Figure 2.22 shows major changes in terms of the hydrograph shape and timing related to the effect of flow retardation: an attenuation of the peak discharge, a larger time of

concentration, and a gradual change of the recession limb, as the height of the dam increases. Although this is a hypothetical simulation that can not be compared with observations, it indicates that the coupled tRIBS-OFM model can be used for more general scenarios of flow conditions and for studying the impacts of human activity on flow regimes of natural watersheds.

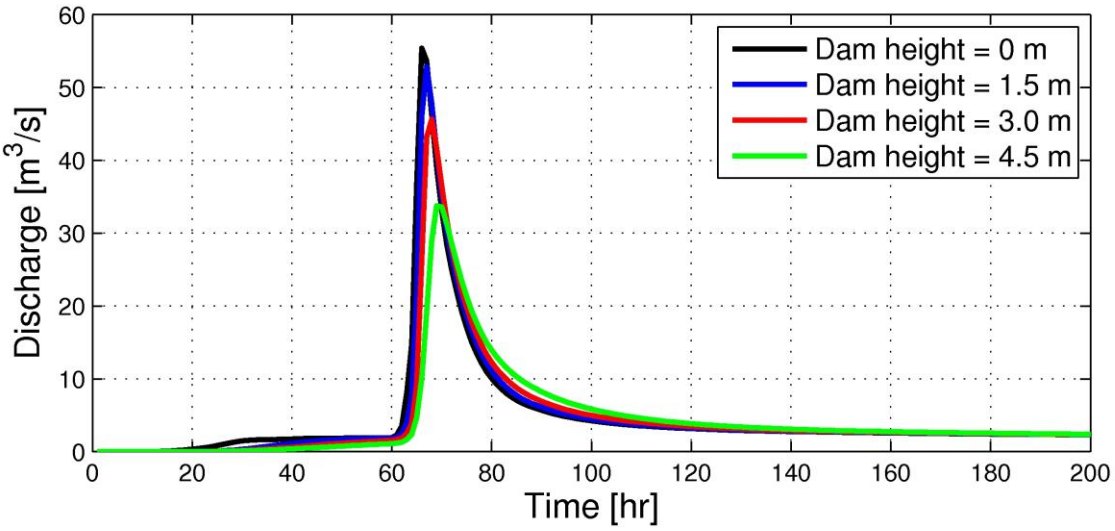

Figure 2.22: The effects of a hypothetical dam "constructed" in the outlet region of Peacheater Creek on the flow hydrograph. The soil scenario Case 4 was used.

2.5 Conclusions

A spatially-distributed, fully-coupled model of hydrologic and hydrodynamic processes resolved on an unstructured, multiple resolution triangular mesh is presented in this Chapter. The tRIBS-OFM considers both a physically-based formulation of hydrologic processes in the above-surface and subsurface domains, and also includes the solution of the two-dimensional Saint-Venant equations for overland flow. As compared to the previously developed shallow water models for simulating flow in rivers, tRIBS-OFM employs a sheet flow regime for the calculation of fluxes and source terms. This modification drastically enhances the accuracy and

consistency of the formulation avoiding the numerical "no-flow phenomenon" in the partially-submerged cells that occurs in steeply sloped areas with low runoff production rates.

As a consistent outcome of the illustrated applications, the flow model confirms its sensitivity with respect to surface roughness coefficients and mesh resolution. Specifically, mesh resolution, especially near the channel and floodplain regions, affects the speed of wave propagation in the drainage network and thus a coarser mesh has a larger time of concentration. Insufficient information about roughness characteristics of the domain gives rise to significant uncertainties associated with flow routing.

The popular kinematic wave assumption may be inappropriate in some parts of the flow domain. In contrast, the dynamic wave routing method shows more accurate, physically-consistent results, especially in the areas of confluence of channel and hillslope and the regions where abrupt transitions of terrain slope occur. Thus, the developed coupled model is an appropriate tool to use for cases with time-varying flow conditions.

The work of this Chapter expands previous research by adapting a hydrodynamic model to watershed-scale simulations, which makes it suitable for providing a more coherent and comprehensive description of runoff phenomena and flow characteristics. The essential strengths of the coupled model are as follows. 1) The model can solve the overland flow problem in all situations that cannot be addressed with traditional hydrologic models. These include hydraulic jumps, backwater conditions, and control structure effects. In particular, tRIBS-OFM is one of a few existing comprehensive hydrologic-hydrodynamic models that can be used for simulating flow converging-diverging effects due to microtopographic disturbances and vegetation features at both micro (cm) and macro (km) scales. 2) The model reduces the uncertainty associated with

parameterizations used by traditional hydrologic routing procedures. 3) The model can be used to obtain detailed information about flow regime characteristics, i.e. the flow depth and velocity. 4) The model is especially valuable in hydraulic problems related to stream or river domains (e.g., flood inundation), where upstream or downstream boundary conditions of a river cannot be easily specified and need to be computed independently with a hydrologic model. According to the definition of a drainage watershed, all surface water located within the watershed ultimately converges to an outlet. Therefore, the coupled model needs only two types of "known" boundary conditions, i.e., non-transmissible (wall) for all boundaries except for an outlet or transmissible (open) boundary conditions for an outlet. 5) Finally, if further combined with other geoscience and engineering models, such as those representing erosion and sediment transport, or a model of aquatic habitat, the proposed model will be useful for addressing a range of scientific questions, for example, how meteorological and hydrological signals affect streamflow regimes, morphological variability, and quality of aquatic habitats.

CHAPTER III

Hairsine-Rose erosion equations coupled with hydrological processes and overland flow at watershed scale: "tRIBS-OFM-HRM"

3.1 Introduction

Soil erosion and excessive sedimentation are among the most important threats to sustainable agriculture and watershed management worldwide [*Oldeman et al.*, 1991; *Bai et al.*, 2008]. Erosion leads to significant soil loss [*Buringh*, 1981; *Brown*, 1984] and imposes substantial social costs [*Pimentel et al.*, 1995; *Noel*, 2001]. Major problems and concerns related to soil erosion are as follows. (1) Rainfall- and runoff-induced erosion from watersheds and farm fields produce major non-point source pollutants for many significant environmental resources [*Hogarth et al.*, 2004b]. (2) River bank erosion and the associated rise of channel bed can lead to a diminished flow capacity and higher vulnerability to floods. (3) Land degradation caused by acceleration of agricultural activities, deforestation, and urbanization remove fertile topsoil, resulting in a decrease of agricultural productivity [*Fiener et al.*, 2008]. (4) Streamflow characteristics and erosion processes are critical in determining stream physical habitat properties and can be responsible for undesired ecological impacts on biotic composition [*Poff and Allan*, 1995; *Bunn and Arthington*, 2002; *Poff and Zimmerman*, 2010].

In order to enhance the understanding of the erosion mechanism and investigate how to reduce social costs, a number of continuing efforts have been undertaken to simulate the erosion process over the last few decades. Depending on what model is given an emphasis in an overall approach, studies can be conceptually divided into two classes. First, hydrologically-based erosion models can be categorized either as empirical or mechanistic. Empirical models are usually derived by processing data observed at a plot-scale with further application of statistical or stochastic scaling techniques that extract general characteristics for parsimonious estimation of soil erosion. These models have been widely used due to their simplicity and reduced computational cost and data requirements. However, empirical models are limited in their capabilities: they use lumped parameters that cannot be directly measured in the field and ignore non-linearities, thus limiting transferability of parameters from one watershed to another. Conversely, mechanistic or sometimes referred to as "physically based" models originate from conservation laws with parameters that bear physical meaning. These models enforce mass conservation and simplified versions of momentum conservation for flow, as well as mass conservation for sediment that is present in both the flow and stream bed. For a detailed review of the most commonly used hydrologically-based erosion models, the reader is referred to *Merritt et al.* [2003] and *Aksoy and Kavvas* [2005].

As another type of approach to erosion and sediment transport modeling, hydraulics-based erosion models focus on accurate solutions of flow mechanisms and coupling sediment motions to the flow dynamics. These models generally do not consider hydrological processes, assuming artificial or "known" boundary conditions. They solve various simplified forms of the Saint-Venant or shallow-water equations combined with advection-dominated sediment transport equations. Among this type of models that have been recently developed are those reported in

Cao et al. [2004], *Nord and Esteves* [2005], *Simpson and Castelltort* [2006], *Murillo et al.* [2008], *Heng et al.* [2009], and *Papanicolaou et al.* [2010]. All these studies represent modeling of flow and sediment processes in a spatially distributed (one- or two-dimensional) manner for a continuous, unsteady flow with the possibility of including multiple, consecutive rainfall events. They can calculate sediment concentrations and bed morphological changes as well as flow variables such as depth and velocity. Table 3.1 summarizes the essential features of these models.

Table 3.1: Hydraulics-based erosion and sediment transport models.

Study	Hydrology	GE	Method	Size-Selectivity	Mesh
Cao et al. [2004]	-	1-D	FVM	Single	-
Nord and Esteves [2005]	Green-Ampt	2-D	FDM	Single	Rectangular
Simpson and Castelltort [2006]	-	2-D	FVM	Single	Rectangular
Murillo et al. [2008]	-	2-D	FVM	Single	Triangular
Heng et al. [2009]	-	1-D	FVM	Multi	-
Papanicolaou et al. [2010]	-	1-D	FVM	Multi	-
This work	tRIBS	2-D	FVM	Multi	Triangular

FVM = Finite Volume Method; FDM = Finite Difference Method; GE = Governing Equation

The performance of the aforementioned erosion models may vary depending on whether the models can credibly take into account predominant factors controlling soil erosion. Soil erosion is strongly affected by many external factors such as meteorological forcing, subsurface water pore pressure, flow conditions, vegetation cover and land use, topography, and human

activities. It is also influenced by the soil's inherent properties such as erodibility, cohesiveness, and particle size distribution. Among the external factors, meteorological forcing, land use, and topographic data are typically given as input to an erosion model, and the last two are usually known at sufficiently high accuracy. Given appropriate meteorological input, the performance of a model depends mainly on the capability to reproduce the remaining factors: hydrological dynamics, including subsurface and above-surface phenomena, and hydrodynamic flow motions caused by complex topography at the watershed scale. Similarly, while soil erodibility and cohesiveness are considered in many erosion models as parameters, sediment particle size distribution is not generally included and a single sediment size is used. Overall, among external and internal factors, hydrological and hydraulic characteristics and particle size distribution are arguably the three most crucial elements in modeling erosion because of several reasons: (1) the partition of rainfall into runoff and "losses" (e.g. infiltration) strongly influences the overall magnitude of sediment erosion; for example, the sensitivity to this partition is very high in semi-arid areas, where more than 90 percent of precipitation is lost to infiltration [*Nearing et al.*, 2007]; (2) the two-dimensional spatial variability of hydraulic or sediment state variables due to precipitation, topography or man-made infrastructures can affect the capability of accurate prediction of detachment and deposition of sediment; and (3) size differences of bed material impact the load and spatiotemporal variability of sediment dynamics. From a practical point, it is particularly valuable to discern fine sediments because many materials that impair water quality tend to adhere to them.

None of the advanced hydraulics-based erosion studies listed in Table 3.1 consider all of the crucial factors and thus satisfy the aforementioned needs. Specifically, some of these studies employ the one-dimensional formulations of governing equations for flow and sediment; only a

few studies consider grain-size dependences. Moreover, most of these studies (with the exception of the study by *Nord and Esteves* [2005] that uses the Green-Ampt method for estimating runoff-loss partition) take little account of hydrologic processes at a relevant level of detail. It is especially of great importance in estimating runoff generation including saturation-excess runoff, perched and groundwater exfiltration as well as infiltration-excess runoff because it varies greatly depending on topography, climate, soil type, groundwater table, and initial conditions as well [*Noto et al.*, 2008]. Therefore, this work represents a first attempt to combine all necessary processes within a single framework.

Previously developed hydrologic and hydrodynamic models are coupled here with the Hairsine-Rose (H-R) formulation [*Hairsine and Rose*, 1991; 1992; *Sander et al.*, 2007a] to describe soil erosion and sediment transport. The H-R model can account for size-selective sediment transport based on particle size distribution. The formulation differentiates composition of the bed into original and deposited soil layers, recognizing whether material has an "intact" or a "loose" condition. Formulations of the governing equations and a description of the numerical model are provided in Sections 3.2 and 3.3. Model verification is subsequently carried out, in which simulation results are compared with analytical solutions and empirical data. Two benchmark laboratory cases dealing with rainfall-induced erosion and overland flow-induced erosion are used. The numerical model is further applied at catchment scale to the Lucky Hills watershed located in southeastern Arizona, U.S.A. Before calibration, we performed two sensitivity tests to a grid resolution and the number of particle size. Model confirmation is then carried out for the outlet using observed data for ten rainfall events with parameter values obtained through calibration for a single rainfall event. An analysis of spatially distributed size-dependent dynamics concludes this manuscript.

3.2 Governing equations

The present numerical model is comprised of three primary components: hydrology (tRIBS), flow dynamics (OFM), and erosion and sediment transport (H-R model). Governing equations or methods for the description of hydrologic processes considered in tRIBS are summarized in Table 2.1; for more detailed information, the reader is referred to *Ivanov et al.* [2004a]. Furthermore, the overland flow model was formerly developed by *Bradford and Katopodes* [1999] for simulating turbid underflows and was later extended to an unstructured triangular mesh [*Begnudelli and Sanders*, 2006]. It has been successfully used for a wide range of hydrodynamic applications of surface irrigation [*Bradford and Katopodes*, 2001], dam break- [*Begnudelli and Sanders*, 2007; *Begnudelli et al.*, 2008] or urban- [*Sanders et al.*, 2008] flooding phenomenon, and efficiency enhancement through a Local Time Stepping scheme [*Sanders*, 2008]. Most details of unstructured mesh formulation such as neighboring mapping functions are followed by the approach of *Begnudelli and Sanders* [2006].

For the purpose of attaining a numerical solution in the erosion and sediment transport problem, the two-dimensional (2-D) Saint-Venant equations coupled with a formulation of sediment mass conservation and bed morphology evolution are used. The 2-D Saint-Venant equations are based on the assumption of hydrostatic pressure distribution in the vertical, so they are appropriate for vertically-mixed water bodies. These equations, based on a vertical coordinate system, in conservative form are as follows

$$\frac{\partial h}{\partial t} + \frac{\partial (uh)}{\partial x} + \frac{\partial (vh)}{\partial y} = S_r \,, \tag{3.1}$$

$$\frac{\partial (uh)}{\partial t} + \frac{\partial (u^2 h + \frac{gh^2}{2})}{\partial x} + \frac{\partial (uvh)}{\partial y} = -gh\frac{\partial z_b}{\partial x} - C_D u\sqrt{u^2 + v^2} \,, \tag{3.2}$$

$$\frac{\partial(vh)}{\partial t}+\frac{\partial(uvh)}{\partial x}+\frac{\partial(v^2h+\frac{gh^2}{2})}{\partial y}=-gh\frac{\partial z_b}{\partial y}-C_D v\sqrt{u^2+v^2}\,, \tag{3.3}$$

where *x*, *y*, and *t* represent the Cartesian space and time; *h* is the flow depth; *u* and *v* are *x*- and *y*-directional depth-averaged velocities, respectively; *g* is the acceleration constant due to gravity; z_b is the bed elevation; C_D is the bed drag coefficient, which is parameterized by using Manning's coefficient, n, as $C_D = gn^2h^{-1/3}$; S_r is the net runoff production rate, which can also be negative (e.g. to represent an infiltrating surface). Four different types of runoff can be calculated by considering local hydrological processes of saturated-unsaturated flow [*Ivanov et al.*, 2004a]; the runoff rate is used as the source term in the mass conservation equation. In Eqs. (3.2) and (3.3), the first momentum source term represents gravity and the second term represents bottom friction.

The unsteady, two-dimensional equations of the Hairsine-Rose (H-R) model [*Hairsine and Rose*, 1991; 1992; *Sander et al.*, 2007a] for particle size class *i* are given by a mass conservation equation for suspended sediment and a bed evolution equation for the deposited layer. The H-R model was compared with experimental data and found to be able to satisfactorily represent erosion processes [*Proffitt et al.*, 1991; *Beuselinck et al.*, 1998; *C Huang et al.*, 1999; *Heng et al.*, 2011]. The 2-D H-R equations are

$$\frac{\partial(hc_i)}{\partial t}+\frac{\partial(uhc_i)}{\partial x}+\frac{\partial(vhc_i)}{\partial y}=e_i+e_{ri}+r_i+r_{ri}-d_i\,,\qquad i=1,2,\cdots I \tag{3.4}$$

$$\frac{\partial M_i}{\partial t}=d_i-e_{ri}-r_{ri}\,,\qquad i=1,2,\cdots I \tag{3.5}$$

$$(1-\beta)\rho_s\frac{\partial z_b}{\partial t}=\sum_{i=1}^{I}(d_i-e_i-e_{ri}-r_i-r_{ri}), \tag{3.6}$$

where c_i is the sediment concentration given as mass per unit volume [$\mathrm{M/L^3}$]; M_i is the sediment mass of the deposited layer formulated as mass per unit area [$\mathrm{M/L^2}$]; I is the number of sediment size classes; and $e_i, e_{ri}, r_i, r_{ri},$ and d_i respectively denote rainfall-driven detachment and redetachment rates, flow-induced entrainment and reentrainment rates, and the deposition rate formulated as mass per unit area per unit time [$\mathrm{M/L^2/T}$]. In equation (3.6), representing the conservation of soil mass, β is the porosity of original soil and ρ_s is the density of solids assumed to be uniform for all sediment classes.

To close the system of equations, the detachment and redetachment rates due to rainfall are calculated as [*Hairsine and Rose*, 1992]

$$e_i = F_w(1 - H)p_i a_0 P, \tag{3.7}$$

$$e_{ri} = F_w H \frac{M_i}{M_t} a_d P, \tag{3.8}$$

where p_i is the ratio of the amount of sediment of class i to that of the original soil; a_0 and a_d represent detachability of uneroded and deposited soil as mass per unit volume [$\mathrm{M/L^3}$]; P is rainfall intensity [$\mathrm{L/T}$]; and $M_t = \sum M_i$ is the total sediment mass in the deposited layer in mass per unit area [$\mathrm{M/L^2}$].

The rainfall-driven detachment and redetachment rates can be relatively small under conditions where the water depth is about three times greater than the raindrop diameter [*Proffitt et al.*, 1991]; this shield effect due to flowing water is known to affect soil detachment due to raindrop impact. Consequently, a shield factor, F_w, is included in equations (3.7) and (3.8). Several forms of this factor exist including exponential relations [*Laws and Parsons*, 1943;

Mutchler and McGregor, 1983] or a power law [*Proffitt et al.*, 1991]. Using the power law relation by *Proffitt et al.* [1991], the shield factor is formulated as

$$F_w = \begin{cases} 1, & h \le h_0 \\ (h_0/h)^b, & h > h_0 \end{cases} \tag{3.9}$$

where a threshold of $h_0 = 0.33\ D_R$ is used, where D_R is the mean raindrop size. An exponent b varies depending on the type of soil and can be obtained with a best fit using experimental data, e.g., for clay, b=0.66 [*Proffitt et al.*, 1991], and for loam, b=1.13 [*Mutchler and McGregor*, 1983].

The proportion of shielding of the deposited layer, H, is calculated as $H = min(M_t/(F_w M_t^*), 1)$, where M_t^* is a calibrated parameter denoting the mass of deposited sediment needed to completely sheild the original soil, given as mass per unit area [$\mathrm{M/L^2}$]. Note that the shield factor F_w is included in this relation using an analogy that the shield mass is expected to vary linearly with the rainfall redetachability, i.e., M_t^*/a_d is a constant. [*Heng et al.*, 2011].

The entrainment and reentrainment rates due to overland flow are evaluated as follows [*Hairsine and Rose*, 1992]

$$r_i = (1 - H) p_i \frac{F(\Omega - \Omega_{cr})}{J} \tag{3.10}$$

$$r_{ri} = H \frac{M_i}{M_t} \frac{F(\Omega - \Omega_{cr})}{(\rho_s - \rho_w) g h / \rho_s} \tag{3.11}$$

where Ω is the stream power [*Bagnold*, 1966] in units of [$\mathrm{M/T^3}$], computed as $\Omega = \rho_w g h S_f \sqrt{u^2 + v^2}$, where $S_f = n^2(u^2 + v^2)h^{-4/3}$; Ω_{cr} is the critical stream power, below which soil entrainment or reentrainment do not occur; F is the effective fraction of excess stream power

in entrainment or reentrainment, which is used to account for energy dissipation due to heat; *J* is the specific energy of entrainment, i.e. energy required for soil to be entrained per unit mass of sediment $[\mathrm{ML}^2/\mathrm{T}^2/\mathrm{M}]$; and ρ_w is the density of water.

Lastly, the deposition rate for a sediment class *i* is calculated as [*Hairsine and Rose*, 1992]

$$d_i = v_i c_i \tag{3.12}$$

where v_i represents the settling velocity of each sediment class $[\mathrm{L}/\mathrm{T}]$. Two implicit assumptions of Eq. (3.12) are the suspended load in the water column is completely mixed for the vertical direction [*Hairsine and Rose*, 1992], and infiltration rate is not incorporated with settling velocities [*Tromp-van Meerveld et al.*, 2008]. The former assumption cannot be avoided because 2-dimensional H-R erosion model coupled with the vertically-averaged S-V equations indeed cannot recognize the non-uniform vertical distribution, although the sediment concentration adjacent to the soil bed should be choosen for the computation of the deposition rate. The latter assumption is additionally employed in the application with infiltration at watershed scale because the deposition equation including infiltration rate may be currently not universal and can be appropriate in limited experimental conditions. This uncertainty was shown in the paper by *Tromp van-Meerveld et al.* [2008] in the form of introducing the "multiplication coefficient" (up to 9 times greater value for smaller particles while 0.35 times smaller value for larger particles) for the settling velocity. As they explained for the deviation of settling velocities, universal relationship at watershed scale where infiltration rate is really time-dependent and varies with soil moisture condition should be required.

The coupled system of the Saint-Venant and H-R equations is therefore

$$\frac{\partial \mathbf{U}}{\partial t} + \frac{\partial \mathbf{E}}{\partial x} + \frac{\partial \mathbf{G}}{\partial y} = \mathbf{S}, \qquad \frac{\partial \mathbf{M}}{\partial t} = \mathbf{D} \tag{3.13}$$

where **U** is the conservative variable vector, **E** and **G** are the *x*- and *y*- directional flux vectors, respectively, **S** is the source vector, **M** is a deposited mass vector, and **D** is the net deposition vector. These vectors are defined as

$$\mathbf{U} = \begin{pmatrix} h \\ uh \\ vh \\ c_1 h \\ \vdots \\ c_I h \end{pmatrix} \quad \mathbf{E} = \begin{pmatrix} uh \\ u^2 h + \frac{1}{2} g h^2 \\ uvh \\ c_1 uh \\ \vdots \\ c_I uh \end{pmatrix} \quad \mathbf{G} = \begin{pmatrix} vh \\ uvh \\ v^2 h + \frac{1}{2} g h^2 \\ c_1 vh \\ \vdots \\ c_I vh \end{pmatrix}$$

$$\mathbf{S} = \begin{pmatrix} S_r \\ -gh\frac{\partial z_b}{\partial x} - C_D u\sqrt{u^2+v^2} \\ -gh\frac{\partial z_b}{\partial y} - C_D v\sqrt{u^2+v^2} \\ e_1 + e_{r1} + r_1 + r_{r1} - d_1 \\ \vdots \\ e_I + e_{rI} + r_I + r_{rI} - d_I \end{pmatrix} \quad \mathbf{M} = \begin{pmatrix} M_1 \\ \vdots \\ M_I \end{pmatrix} \quad \mathbf{D} = \begin{pmatrix} d_1 - e_{r1} - r_{r1} \\ \vdots \\ d_I - e_{rI} - r_{rI} \end{pmatrix}. \tag{3.14}$$

The resultant system of equations thus couples the hydrodynamic formulation with the advection-dominated transport equations for grain-size dependent sediment. It expresses space-time dynamics of flow, erosion, and sediment transport.

3.3 Numerical model

The hydrologic model operates in a continuous fashion, simulating conditions of both storm and interstorm periods, propagating these conditions to both subsurface states and flow regimes. Consequently, hydrologic applications inevitably encounter flow conditions associated with low precipitation and runoff rates that result in many partially-submerged mesh cells [*Kim et al.*, 2012b]. Tracking and handling wet and dry fronts occurring in these cells has traditionally been of great interest and generally treated by using the information of neighboring wet cells [*Titov and Synolakis*, 1995; *Bradford and Sanders*, 2002; *Xia et al.*, 2010] and by modifying the bed level difference [*Brufau and Garcia-Navarro*, 2003; *Brufau et al.*, 2004]. However, such approaches were developed based on hydraulic applications such as flood propagation and wave runup, and were not targeted in hydrologic, watershed-scale applications that have steeply sloped cells with dry conditions encountered throughout the simulation. As a result, these cells can cause a numerical artifact so called "no-flow phenomenon" that hampers an accurate calculation of the flux, bottom slope, and friction slope terms [*Kim et al.*, 2012b]. This phenomenon refers to a situation when runoff is stored within a cell without the possibility to flow out. So, the generated runoff fills up the cell until it becomes inundated, i.e. "wet" cells. This numerical problem is very critical in domains characterized by high bed slopes and low flow conditions (e.g., hillslope areas of the watershed). Previously developed shallow water models for simulating flow in rivers have not addressed this numerical problem. The tRIBS-OFM model resolved it by using a representation of the sheet flow regime; this modification significantly enhanced the accuracy of calculation of fluxes and source terms. A more detailed description of the differences between the hydrologic and hydrodynamic approaches in dealing with wet/dry situations is provided in the Chapter 2.2.3.

The erosion and sediment transport equations are combined with the hydrologic and hydrodynamic formulation of tRIBS-OFM. Coupling the H-R equations to tRIBS-OFM is carried out by (i) solving them sequentially within a simulation time step for the system of equations (3.13) and (ii) updating the computed bed elevation at the end of the time step. For torrent flow conditions with high particle concentrations, where sediment cannot be considered to be a passive admixture, a simultaneous solution of the S-V equations and H-R equations is preferable [*Cao et al.*, 2002]. *Cao et al.* [2002] suggested an indicator as the relative time scale between the flow and deformation time scales and advocated that a coupled solution is required in cases of relative time scale smaller than the order of magnitude of 10^4. A possible flow and morphologic condition satisfying such criteria occurs in the Yellow River, China, where typical concentrations are very high, at approximately 10 percent, i.e., ~265 kg/m^3 [*Cao et al.*, 2002]. This study, however, assumes that sediment concentrations are small enough and do not affect the movement of the fluid; the assumption is acceptable because the relative time scale is always above 10^4, except for special cases (e.g. dam-break or debris flow).

The finite volume method on an unstructured grid is adopted to solve the system of equations (3.13). Regarding the existing finite volume techniques, as well as computational cells and neighboring mapping functions on unstructured grids, we closely follow the approach of *Begnudelli and Sanders* [2006]. Integrating Eq. (3.13) over an arbitrary two-dimensional computational element A with a boundary Γ, the governing equations expressed in conservation form are written as follows

$$\frac{\partial}{\partial t}\int_A \mathbf{U} dA + \oint_\Gamma \mathbf{F}\cdot\mathbf{n}\, d\Gamma = \iint_A \mathbf{S} dA\ , \tag{3.15}$$

where **F** is the flux vector; and **n** is the unit vector normal to boundary $\partial\Gamma$ and directed outward. The integrand $\mathbf{F}\cdot\mathbf{n} = \mathbf{F}_{\perp}$ is the numerical flux normal to each cell face and defined as

$$\mathbf{F}\cdot\mathbf{n} = \begin{pmatrix} hu_{\perp} \\ huu_{\perp} + \frac{1}{2}gh^2\cos\emptyset + \frac{1}{24}g\Delta h^2\cos\emptyset \\ hvu_{\perp} + \frac{1}{2}gh^2\sin\emptyset + \frac{1}{24}g\Delta h^2\sin\emptyset \\ hc_1u_{\perp} \\ \vdots \\ hc_Iu_{\perp} \end{pmatrix}, \tag{3.16}$$

where $u_{\perp}$ denotes the velocity normal to the cell interface and computed as $u_{\perp} = u\,cos\,\emptyset + v\,sin\,\emptyset$; $\emptyset$ is an angle between the face normal vector and the *x* axis; and Δh is a variation of *h* along the cell face. The last terms in the second and third rows of equation (3.16) are the hydrostatic thrust correction terms suggested by *Bradford and Sanders* [2002]. They are necessary to balance the bed slope terms for the still water condition.

Among a variety of possible schemes for calculating fluxes at a cell interface between two adjacent cells, Roe's approximate Riemann solver [*Roe*, 1981] is computed using the following equation:

$$\mathbf{F}_{\perp,f} = \frac{1}{2}\left(\mathbf{F}_{\perp,L} + \mathbf{F}_{\perp,R} - \widehat{\boldsymbol{R}}\left|\widehat{\boldsymbol{\Lambda}}\right|\Delta\widehat{\boldsymbol{V}}\right), \tag{3.17}$$

where the subscript *f* denotes the interface between two adjacent triangular cells; subscripts *L* and *R* denote left and right sides of the cell interface; and Δ denotes the finite difference across the interface. The terms $\hat{R}$ and $\hat{\Lambda}$ are the right eigenvector and the eigenvalue of the Jacobian of $\mathbf{F}_{\perp}$; and $\Delta\hat{V}$, defined as $\Delta\hat{V} = \hat{L}\Delta U$, denotes the wave strength, where $\hat{L}$ is the left eigenvector of the Jacobian of $\mathbf{F}_{\perp}$. Their mathematical representations are:

$$\hat{R} = \begin{pmatrix} 1 & 0 & 1 & 0 & \cdots & 0 \\ \hat{u} - \hat{a}\cos\emptyset & -\sin\emptyset & \hat{u} + \hat{a}\cos\emptyset & 0 & \cdots & 0 \\ \hat{v} - \hat{a}\sin\emptyset & \cos\emptyset & \hat{v} + \hat{a}\sin\emptyset & 0 & \cdots & 0 \\ \hat{c}_1 & 0 & \hat{c}_1 & 1 & \cdots & 0 \\ \vdots & \vdots & \vdots & \vdots & \ddots & \vdots \\ \hat{c}_I & 0 & \hat{c}_I & 0 & \cdots & 1 \end{pmatrix} \tag{3.18}$$

$$|\hat{\Lambda}| = \begin{pmatrix} |\hat{u}_\perp - \hat{a}| & & & & & \\ & |\hat{u}_\perp| & & & & \\ & & |\hat{u}_\perp + \hat{a}| & & & \\ & & & |\hat{u}_\perp| & & \\ & & & & \ddots & \\ & & & & & |\hat{u}_\perp| \end{pmatrix} \tag{3.19}$$

$$\Delta\hat{V} = \hat{L}\Delta U \; = \tag{3.20}$$

$$= \begin{pmatrix} \frac{h_R - h_L}{2} - \frac{((uh)_R - (uh)_L)\cos\emptyset + ((vh)_R - (vh)_L)\sin\emptyset - (\hat{u}\cos\emptyset + \hat{v}\sin\emptyset)(h_R - h_L)}{2\hat{a}} \\ ((vh)_R - (vh)_L)\cos\emptyset - ((uh)_R - (uh)_L)\sin\emptyset - (-\hat{u}\sin\emptyset + \hat{v}\cos\emptyset)(h_R - h_L) \\ \frac{h_R - h_L}{2} + \frac{((uh)_R - (uh)_L)\cos\emptyset + ((vh)_R - (vh)_L)\sin\emptyset - (\hat{u}\cos\emptyset + \hat{v}\sin\emptyset)(h_R - h_L)}{2\hat{a}} \\ (c_1 h)_R - (c_1 h)_L - \hat{c}_1(h_R - h_L) \\ \vdots \\ (c_I h)_R - (c_I h)_L - \hat{c}_I(h_R - h_L) \end{pmatrix},$$

where a denotes the celerity of a simple gravity wave; and $u_\parallel$ denote the velocity components parallel to the cell interface and are computed as $u_\parallel = -u\sin\emptyset + v\cos\emptyset$. The quantities denoted with a hat are Roe averages, which are calculated with the following relations:

$$\hat{h} = \sqrt{h_L h_R}, \qquad \hat{u} = \frac{\sqrt{h_L}u_L + \sqrt{h_R}u_R}{\sqrt{h_L} + \sqrt{h_R}}, \quad \hat{v} = \frac{\sqrt{h_L}v_L + \sqrt{h_R}v_R}{\sqrt{h_L} + \sqrt{h_R}}, \tag{3.21}$$

$$\hat{a} = \sqrt{\frac{g}{2}(h_L + h_R)}, \qquad \hat{c}_i = \frac{\sqrt{h_L}c_{i,L} + \sqrt{h_R}c_{i,R}}{\sqrt{h_L} + \sqrt{h_R}}.$$

Since Roe's method does not calculate the correct flux for critical flow, a local depression wave is introduced at critical flow locations by replacing the first and third eigenvalues with the following equation [*C Hirsch*, 1990]:

$$|\lambda|^* = \frac{\lambda^2}{\Delta\lambda} + \frac{\Delta\lambda}{4}, \tag{3.22}$$

where $\Delta\lambda = 4(\lambda_R - \lambda_L)$. This relation is used when $-\Delta\lambda/2 < |\lambda| < \Delta\lambda/2$ and the other eigenvalues, $\lambda = |\hat{u}_\perp|$, remain unmodified.

Under the assumption that all source terms in the flow and erosion equations are constant within a cell triangle, they are calculated as

$$\iint_A \mathbf{S} dA = \mathbf{S} \cdot A, \tag{3.23}$$

In the computation of the bottom slope, the gradient of z_b is obtained by applying Green's theorem to transform the area integral to the line integral. Thus, the integration of z_b along the cell boundaries gives

$$\frac{\partial z_b}{\partial x} = \frac{(y_2 - y_0)(z_1 - z_0) - (y_1 - y_0)(z_2 - z_0)}{(y_2 - y_0)(x_1 - x_0) - (y_1 - y_0)(x_2 - x_0)}, \tag{3.24}$$

where the subscripts 0, 1 and 2 are three counter-clockwise vertices of a cell triangle. All variables used for computations of source terms are evaluated at the cell center.

Finally, Eq. (3.13) and Eq. (3.6) are solved by using the following update equation

$$\mathbf{U}_j^{t+\Delta t} = \mathbf{U}_j^t + \Delta t \left[-\frac{1}{A_j} \sum_{k=1}^{3} \mathbf{F}_{\perp j,k} l_{j,k} m_{j,k} \right]^t + \Delta t \cdot \mathbf{S}_j^{t*}, \tag{3.25}$$

$$\mathbf{M}_j^{t+\Delta t} = \mathbf{M}_j^t + \Delta t \cdot \mathbf{D}_j^t \,, \tag{3.26}$$

$$z_{b_j}{}^{t+\Delta t} = z_{b_j}{}^t + \frac{\Delta \mathrm{t}}{(1-\beta)\rho_s}\left[\sum_{i=1}^{I}\left(d_{i,j} - e_{i,j} - e_{ri,j} - r_{i,j} - r_{ri,j}\right)\right]^t, \tag{3.27}$$

where *j* and *k* are cell and face indexes, respectively, $l_{j,k}$ is the length of the *k*-th face of the *i*-th cell, and $m_{j,k}$ is a function that takes on values of 1 or -1, depending on whether the unit vector normal to the *k*-th face of the *i*-th cell is directed outward or inward. The *t** superscript in Eq. (3.25) represents that for stability, the friction term and deposition term including the conservative variables are treated in a semi-implicit manner, while rest of the source terms are treated explicitly [*Sanders*, 2008].

Several types of boundary conditions can be imposed by either placing extrapolated quantities in a "ghost" cell adjacent to the boundary or directly specifying a given flow depth or a discharge. These extrapolated or specified quantities defined for ghost cells are employed to calculate boundary fluxes necessary in Roe's Riemann solver. At a solid slip wall boundary, water depth and concentrations are extrapolated; velocities are specified in ghost cells that require the velocity normal to the cell interface to be zero while the velocity parallel to the interface remaining unchanged. If water flows into a domain through an inflow boundary, for subcritical flow only (*I*+2) boundary conditions are needed among the (*I*+3) possible variables that include depth (*h*), two velocities (*u*, *v*), and concentrations (c_i-s, $i = 1 \ldots I$), where *I* is the number of sediment size classes. Any two flow variables and concentrations need to be specified while the remaining flow variable is extrapolated from a value adjacent to the boundary. A supercritical inflow through the boundary needs all (*I*+3) boundary conditions. For a boundary where flow leaves the domain, a subcritical flow needs one boundary condition (in this study, in

the form of free outfall or zero-depth gradient boundary condition), while no boundary condition is needed for a supercritical flow.

The proposed model is based on an explicit time integration scheme and thus a stability restriction, the Courant-Friedrichs-Lewy (CFL) condition, must be satisfied in each cell. For a triangular mesh, the time step Δt in the model is defined as [*Begnudelli and Sanders*, 2006]:

$$Cr = \Delta t \cdot max_{j=1,2,\cdots N_c}\left\{\frac{3\ max_{k=1,2,3}\left|{\lambda_{j,k}}^{\perp} l_{j,k}\right|}{A_j}\right\} \leq 1, \quad j = 1,2,\cdots N_c \tag{3.28}$$

where *Cr* is the Courant number, N_c is the number of cells, and ${\lambda_{j,k}}^{\perp}$ is the wave speed normal to the *k*-th face of the *j*-th cell. Furthermore, the restriction on the time step presented by *Heng et al.* [2009] is also considered. Specifically, negative concentrations should not be generated and an approximate estimate of the corresponding time step is

$$\Delta t \leq \frac{min_{j=1,2,\cdots N_c}(h_j)}{max_{i=1,2,\cdots I}(v_i)}\ . \tag{3.29}$$

This relation usually limits the time step because it yields estimates that are smaller than those obtained with the CFL criteria.

3.4 Model verification

3.4.1 Rainfall-induced erosion

One of the two significant contributors to the process of erosion represented in the H-R model is rainfall-induced erosion. The problem has been addressed with many methods: a steady state solution [*Hairsine and Rose*, 1991], unsteady but spatially independent solutions [*Sander et al.*, 1996; *Parlange et al.*, 1999], an event-based solution [*Hairsine et al.*, 1999], and temporally-spatially dependent solutions [*Hogarth et al.*, 2004a; *Heng et al.*, 2009]. Most of these analytical or numerical solutions were compared with experimental data by *Proffitt et al.* [1991] and demonstrated a good agreement with it. Experimental results obtained by *Proffitt et al.* [1991], specifically observations for Aridsol soil are used in this study for verification of numerical solutions of the coupled model. An approximate analytical solution developed by *Sander et al.* [1996] is also used for comparison. Although this unsteady analytical solution assumes that sediment concentration does not vary spatially and is only time dependent near the end of the flume, and thus neglects the spatial derivative terms, the effects of the assumption are minor and the accuracy of the analytical solution is trustworthy, except at very short times [*Hogarth et al.*, 2004a].

Simulation conditions and parameters giving best agreement with experimental data for the cases of Aridsol are borrowed from *Sander et al.* [1996] and listed in Table 3.2. The value of the Manning coefficient is 0.06 s/m$^{1/3}$ and for Aridsol with a slightly dispersive soil of sandy clay loam texture ten sediment sizes are used; the corresponding settling velocities, $\nu_{1,\cdots,10}$, are 0.0035, 0.07389, 0.5194, 2.1, 6.8, 20, 38, 75, 160, and 300 mm/s [*Parlange et al.*, 1999]. A shield effect factor F_w equal to 1.0 is used. The simulation domain consists of 5.8×1 m and the size of

triangular mesh elements is 0.005 m^2. The number of mesh nodes and cells are 654 and 1170, and the time step used for the simulation period of 50 min is 0.05 sec. The density of sediment material solids is 2600 kg/m^3. Hydrologic processes are not considered in this problem.

Table 3.2: Simulation conditions and parameters for Aridsol (Solonchak) after *Sander et al.* [1996].

Case	Rainfall [mm/hr]	Slope [-]	Depth [m]	a_0 [kg/m^3]	a_d [kg/m^3]	M_t^* [kg/m^2]
1	100	0.01	0.002	1233	24660	0.0493
2	100	0.04	0.005	718	14360	0.0598
3	100	0.03	0.01	412	8240	0.0515

The temporal distributions of the flow discharge, the sediment discharge, and the total concentration at the downstream end of the hillslope for the three simulation cases are shown in Figure 3.1 and Figure 3.2. Hydrographs initially show different peaks due to the differences in transient flow conditions, but eventually approach the same steady state due to the same rainfall intensity. Sedigraphs also approach a steady state, but a higher sediment discharge occurs in case 1 because of the high erodibilities of uneroded and deposited soil. In Figure 3.2, the total sediment concentrations exhibit behaviors similar to that of the sedigraphs. An overall good agreement with the experimental data by *Proffitt et al.* [1991] and the analytical solution by *Sander et al.* [1996] can be observed.

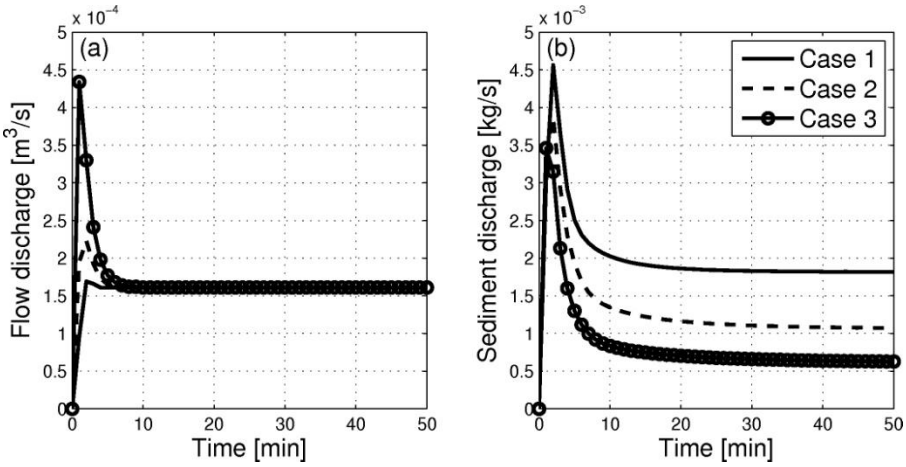

Figure 3.1: Simulated (a) hydrographs and (b) sedigraphs for three cases in the rainfall-induced erosion problem.

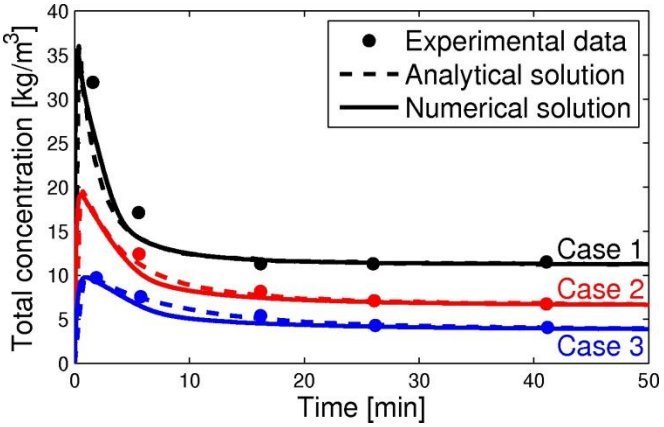

Figure 3.2: The time series of the total sediment concentration at the hillslope bottom for three cases considered in the rainfall-induced erosion problem. "Experimental data" refer to measurements by *Proffitt et al.* [1991] and the "Analytical solution" refers to *Sander et al.* [1996].

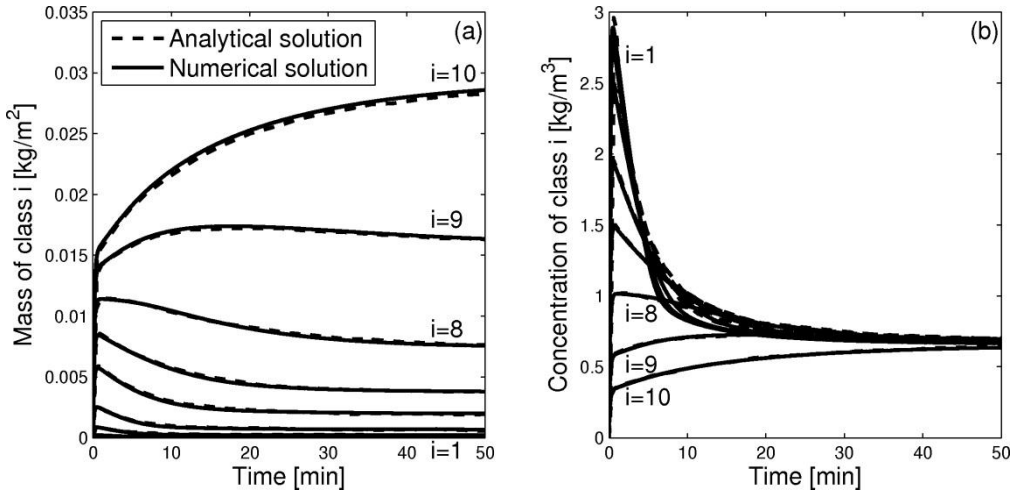

Figure 3.3: The time series of (a) deposited masses and (b) concentrations of each sediment class at the hillslope bottom for the simulation case 2 of the rainfall-induced erosion problem; *i*=1 corresponds to smallest sediment particles and *i*=10 refers to largest particles.

The time series showing size-selective characteristics at the hillslope bottom for simulation case 2 are provided in Figure 3.3. This shows how sediment particles of different size contribute to the deposited mass and water column concentration. Specifically, larger particles tend to contribute a higher fraction of the deposited mass, but comprise less sediment in water column than smaller particles. This result also agrees well with the analytical solution by *Sander et al.* [1996]. Regarding the simulated detachment and redetachment rates of each sediment class, as can be inferred from Eqs. (3.7) and (3.8), an equally-distributed ratio of each sediment class in the original soil results in uniform detachment for each sediment class while a size-selective distribution ratio of the deposited soil (Figure 3.3-(a)) results in a size-selective redetachment (not shown). After a short period of time, the original intact soil becomes almost completely covered by the deposited sediment and the shielding proportion *H* nearly approaches 1.0. As follows, most of the detachment occurs during early time period. The flowing section provides

further analysis of size-specific spatial distributions of sediment concentrations deposited mass at different simulation times.

Figure 3.4 illustrates the longitudinal distributions of sediment concentrations and the fractions of deposited mass at different times after the simulation start for simulation case 2. The amount of sediment in the water column for the smallest particle size (i=1) decreases with time, while the concentration of the largest particles (i=10) somewhat grows. Eventually, the same sediment concentration for all particle classes is achieved at steady state. At this time, the mass fractions of the deposited sediment for smaller particles are relatively small, as compared to the fractions for larger particle sizes.

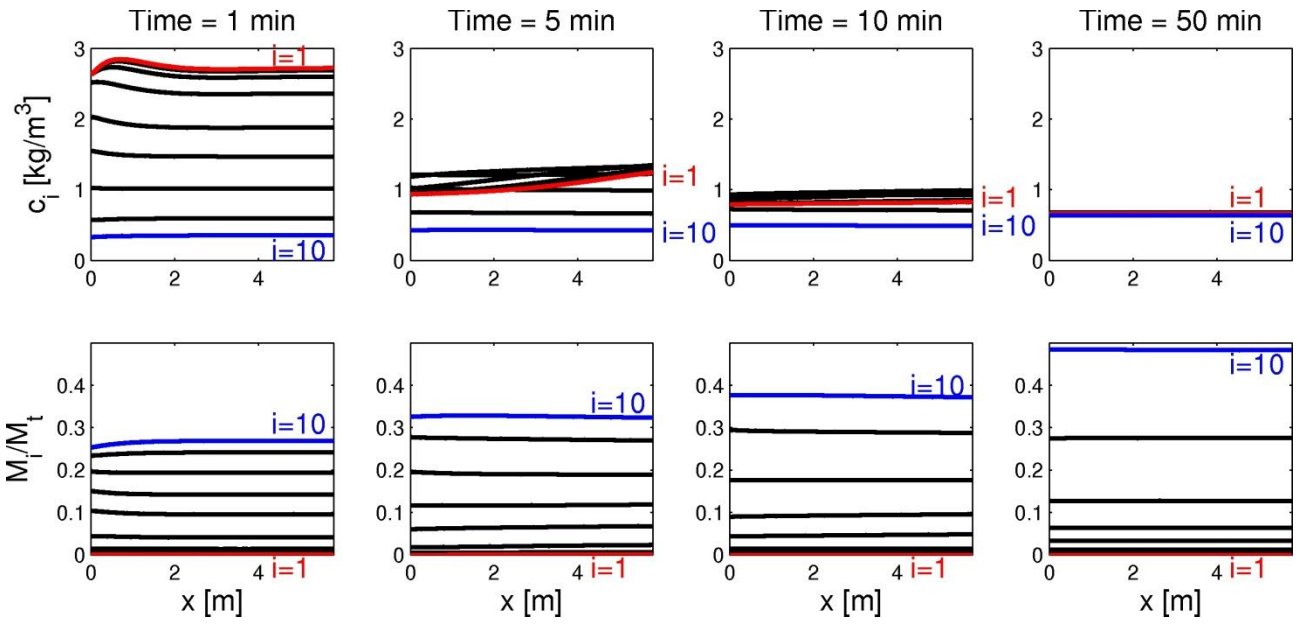

Figure 3.4: The simulated longitudinal distributions of sediment concentration (the top panel) and the fractions of deposited mass of each sediment class "i" relative to the total mass (the bottom panel) for the simulation case 2. Each column panel represents distributions for a given simulation time, i.e., 1, 5, 10, and 50 min.

3.4.2 Overland flow-induced erosion

In order to evaluate and verify the overland flow-induced erosion component of the H-R model, a sediment-laden overland flow problem [*Beuselinck et al.*, 1999; *Sander et al.*, 2002; *Heng et al.*, 2009] is presented. An overland flow rate of 0.00125 m^3/s is imposed at the hillslope upstream boundary; Concentrations of 10 kg/m^3 are specified for all sediment classes, which results in a net deposition of sediment over the domain. The parameter values are specified as follows: the Manning coefficient is 0.01 $s/m^{1/3}$, the critical stream power is 0.18639 W/m^2, the effective fraction of excess stream power is 0.01, the slope of domain is 0.02, the density of sediment is 2600 kg/m^3, and the settling velocities, $\nu_{1,\cdots,10}$, are 0.00043, 0.0037, 0.02, 0.083, 0.23, 0.46, 0.74, 1.1, 1.7, and 3.2 mm/s, respectively. The simulation domain has the dimensions of 10 $\times$ 1 m and the size of mesh elements is 0.005 m^2. The number of mesh nodes and triangular cells are 1116 and 2010, respectively. The time step used during the simulation period of 6 min is 0.005 sec. Hydrologic components are not considered in this problem.

The flow imposed as a boundary condition reaches the outlet and the system achieves steady-state nearly immediately (not shown). The total sediment yield at the outlet contains primarily finer particles as compared to coarser sediments. This is consistent with a theoretical understanding of overland flow erosion: lighter soil particles are more easily moved away from their sites of origin, as compared to slowly moving heavier particles. The spatial distributions of concentrations and mass fractions of each sediment class at steady-state are compared with an analytical solution of *Sander et al.* [2002] in Figure 3.5. Although small differences are present in the simulated concentrations of larger particles near the upstream end, an overall good agreement of the simulation results with the analytical solution can be observed. This might be because of kinematic vs. dynamic computation effect and boundary condition effect. Since only

constant q and C information are available as an inflow boundary condition from the reference, we assumed the boundary value of ghost cells for a depth as h=0.0036 m, which can be estimated from the kinematic wave solution: h=0.0036 or 0.0037 m for using the power (m) of either 1.66 or 5/3 for turbulent flow. As a result, the simulation values for h and u at steady state were 0.003697 m and 0.338122 m/s where the deviation may exist although it is small. A more significant effect may be due to the boundary effects of inflow and outflow as well as wall boundary, since slightly different value from the steady state value is observed near the boundary region.

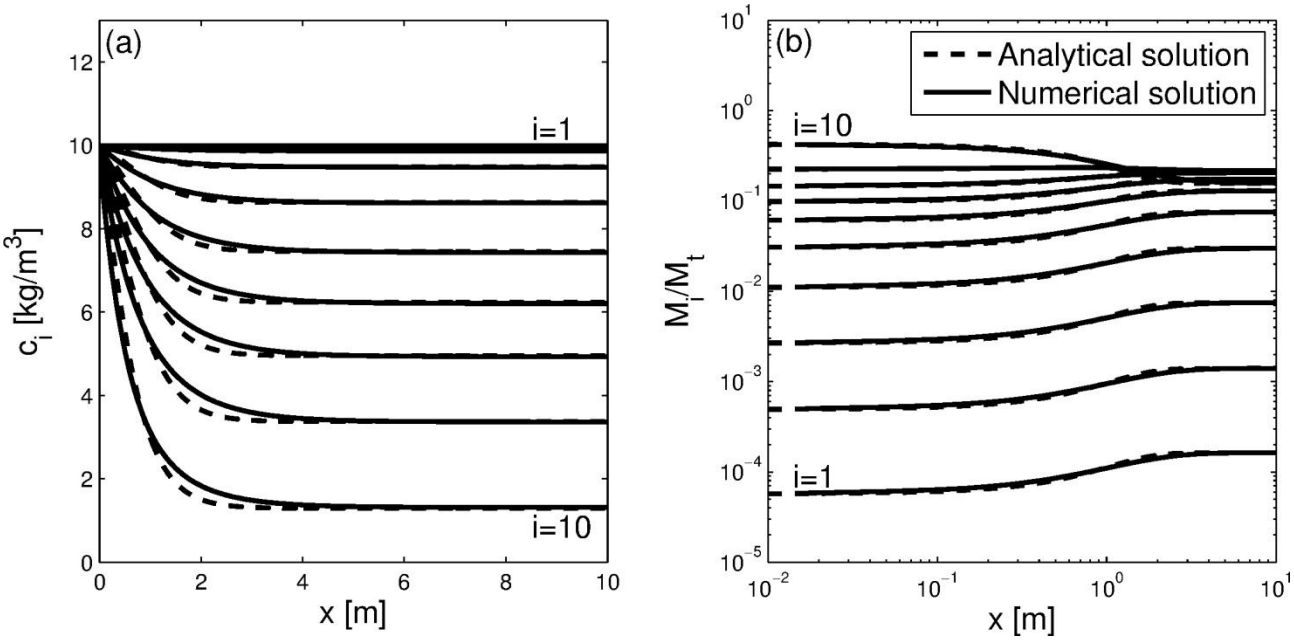

Figure 3.5: A comparison of (a) the sediment concentrations and (b) the mass fractions of each sediment class with the analytical solution of *Sander et al.* [2002]. A steady-state situation for a case of net deposition in overland flow is considered.

Figure 3.6 illustrates the spatial distributions of sediment concentrations and the fractions of deposited mass at different times after the simulation start. This temporal sequence illustrates

several interesting features of sediment movement: (1) sediment entering the domain moves continuously downstream and arrives to the outlet after about 30 sec; (2) smallest particles stay suspended over the entire duration of the domain and thus most of them flow out; (3) largest particles get deposited in the upstream area and only ~13 percent of the sediment mass given as a boundary influx flows out of the domain; (4) the concentration profiles approach steady-state, while the deposited mass continuously increases.

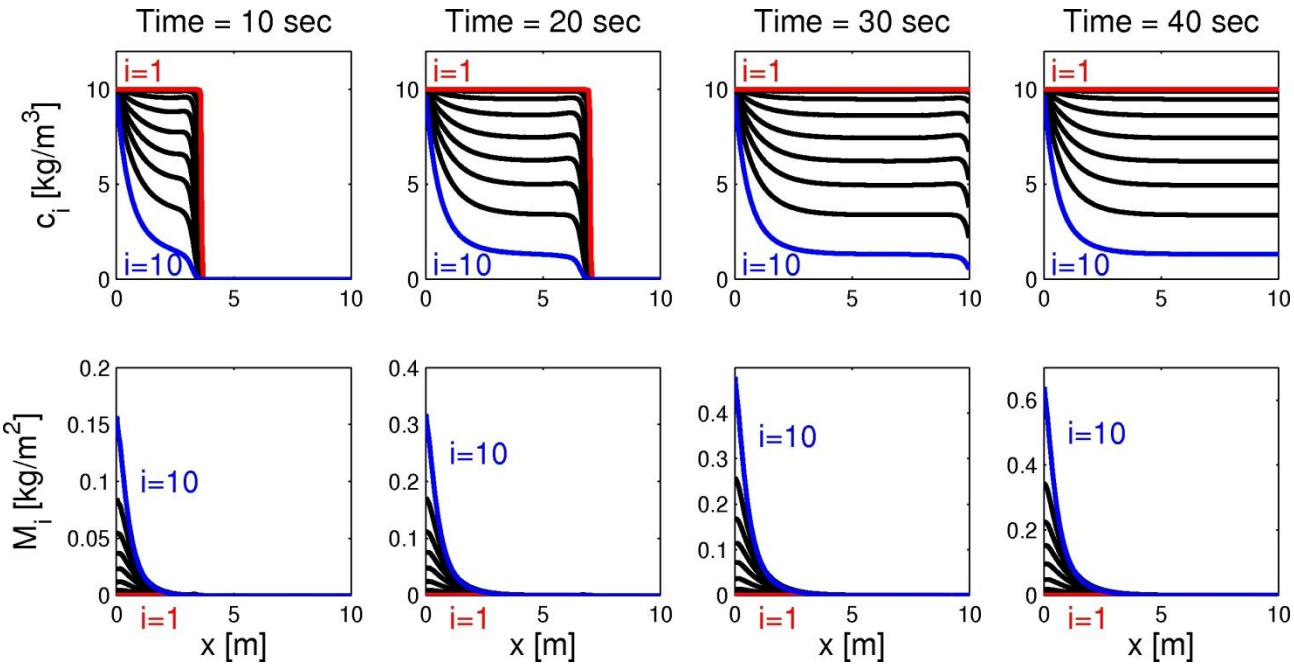

Figure 3.6: The simulated spatial distributions of sediment concentrations (the top panel) and the deposited masses (bottom panels) of each sediment class for the overland induced erosion problem. Each column panel represents distributions at a given time, i.e., 10, 20, 30, 40 sec.

3.4.3 Lucky Hills watershed

Despite their numerical formulation, the previous two simulation cases are actually one-dimensional. The perceived strength of the developed model is in the potential to represent the coupled hydrology, flow hydrodynamics, physically-based erosion, and sediment transport dynamics of more complex domain geometries. No analytical solutions or suitable laboratory observations are available for model confirmation. A real-world watershed is used as a case study for investigating the two-dimensional capabilities of the proposed model. Specifically, the Lucky Hills watershed, nested within the Walnut Gulch Experimental Watershed (WGEW), was selected because the WGEW sediment collection program provides an extensive experimental data set obtained with automatic traversing slot samplers [*Renard et al.*, 1986].

3.4.3.1 Lucky Hills watershed and its numerical representation

The Lucky Hills watershed is one of the nested watersheds within the Walnut Gulch Experimental Watershed (WGEW) in southeastern Arizona, USA. The area of the watershed is 36800 m^2 and its elevation ranges from 1364 to 1375 m above sea level. The overall slope of the basin is less than 10%; however, there are abrupt changes of elevation (~10 m) and high slopes (higher than 20%) near the center of the domain (see Figure 3.7). This morphological feature can be expected to affect the spatial variability of erosion rates and will be discussed later. Furthermore, one of the refined meshes is shown in the Figure 3.7-(c) which is defined according to the convergence of surface contributing area (CA) illustrated in the Figure 3.7-(d). This refined domain will be used to see the sensitivity of the hydrograph and sedigraph to the mesh resolution.

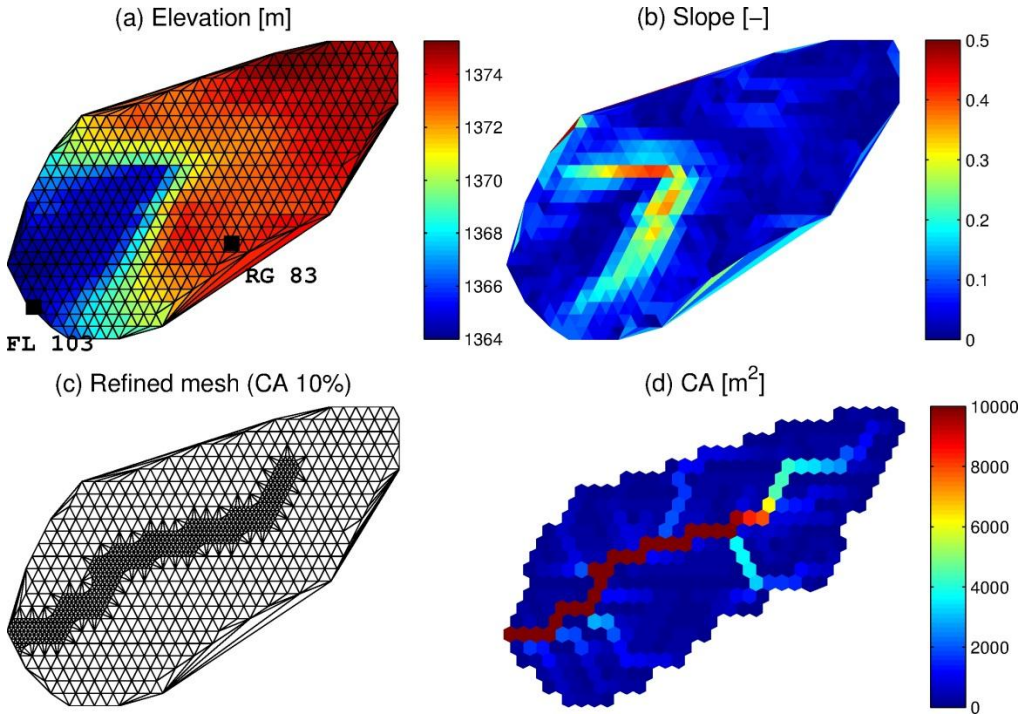

Figure 3.7: The digital elevation model (a) and the derived surface slope (b) of the Lucky Hills watershed. Precipitation is measured at the rain gauge RG83. Runoff and sediment are measured at the outlet flume FL103. Two different meshes out of 6 used in simulations: (a) Coarser mesh and (c) Refined mesh (CA 10%). The latter is refined for the channel area where the surface contributing area (d) is greater than 10 % of the total contributing area of watershed.

Average annual precipitation is about 300 mm and 70% of precipitation falls during the summer monsoon. Typical storms in the area have a short duration and a high intensity. For the calculation of the shield effect factor, the mean raindrop size is assumed to be 2 mm and the exponent *b* in Eq. (3.9) is assumed to be 1.0 [*Heng et al.*, 2011]. The dominant vegetation is desert shrub and semi-arid rangeland plants. The dominant soil type is McNeal Gravelly Sandy Loam [*Francipane et al.*, 2012]. The density of sediment is 2700 kg/m^3 and a value for the porosity of the bed equal to 0.46 is used [*Francipane et al.*, 2012].

The determination of the number of particle sizes (*I*) is of great importance for representing size-selective characteristics. For this watershed, the particle size distributions (PSDs) binned with 23 sieves (3, 6, 11, and 3 of them correspond to the range of clay, silt, sand, and gravel, respectively) were collected at 6 different locations [*Schaap and Shouse*, 2003]. To investigate the effects of the number of particle sizes on the generated sediment yields (*SY*s), the averaged distributions for 6 locations with 23 intervals are recomputed into those with 4, 8, and 12 intervals (Figure 3.8). As shown in Figure 3.9-(a), the ratio of sediment yields with respect to those obtained in the case with 23 intervals implies that the rough representation of PSD gives rise to considerable variations (e.g., up to ~60 % for *SY* of sand). However, since the ratio of *SY* of the finer particles is much greater than that of the coarser particles, the total *SY*s for 4 different *I*s do not vary significantly (e.g., up to ~5 % for $I = 4$). Consequently, the PSD with 8 intervals is, for efficiency, employed as the initial bed condition in the rest of simulations. The sediment size of each interval is 0.001191, 0.002687, 0.01555, 0.04469, 0.2876, 1.131, 3.399, and 5 mm, respectively; their corresponding fractions are 6.87, 3.33, 5.42, 4.77, 21.54, 18.39, 20.90, and 18.78 %; their settling velocities, $v_{1,\cdots,10}$, 0.0009823, 0.005001, 0.1669, 1.352, 32.89, 124.3, 252.2, and 313.6 mm/s, are calculated using the formula of *Cheng* [1997].

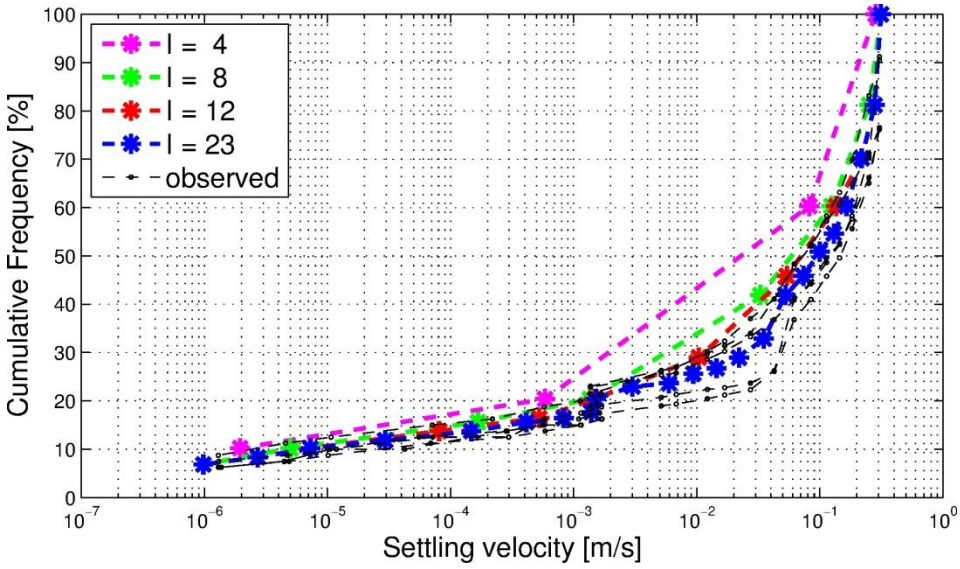

Figure 3.8: The settling velocities computed from particle size distributions at 6 different locations (black lines) and recomputed settling velocities used for simulations with different *I*s. The "*I*" denotes the number of sediment size classes.

Next, maintaining the appropriate resolution of the domain has also an important role in understanding the flood behavior. Especially, a poorly resolved mesh near the channel network gives a more significant effect on the computation of wave speed and thus, the time of concentration than in hillslope area [*Kim et al.*, 2012b]. Similarly to the previous study of *Kim et al.* [2012b], we tested the sensitivity of the hydrograph and sedigraph in terms of total volume/yield, peak rate, and time to peak for 6 different refined domains. Among 6 domains, the "coarser" domain consists of uniform mesh elements of 50 m^2; the number of mesh nodes and triangular cells are 469 and 908 (Figure 3.7-(a)) while the "finer" domain is also composed of uniform elements that are 9 times smaller (not shown). The remaining 4 domains are only refined near channel area where the flow concentration is expected according to the convergence of contributing area (Figure 3.7-(d)). Figure 3.7-(c) shows an example of the mesh refined for the area where the surface CA is greater than 10 % of the total CA (called "CA 10 %"). The time

step used for hydrologic components is 3.75 min; the time step used for the simulation of flow hydrodynamics and erosion-transport modeling components is 0.01 sec. Figure 3.9-(b) shows the sensitivity through the ratio of several variables of 6 domains with respect to the coarser mesh. CPU time is, as expected, more consumed as the number of cells/nodes increases; for the coarser mesh, it takes 15850 sec to simulate a 3 hours rainfall event with a machine having an Intel Xeon CPU (3.33 GHz, 2 processors) with 14 GB RAM. In contrast, the accuracy of the variables, i.e., total volume or total yield, peaks at hydrograph or sedigraph, and times to peaks is evaluated: for the times to peak, results of all domains are consistent; the deviations of *SY* and peak at sedigraph are up to 5 and 12 %, respectively, while those of flow volume and peak at hydrograph are up to 1 and 2 %, respectively. It implies that sediment behaviors affected by more parameters to be calibrated are more sensitive to the grid resolution than flow behaviors influenced by one friction parameter. Hereafter, due to their small deviations, we will employ the coarser domain with the time step of 0.1 sec for efficiency in the rest of simulations.

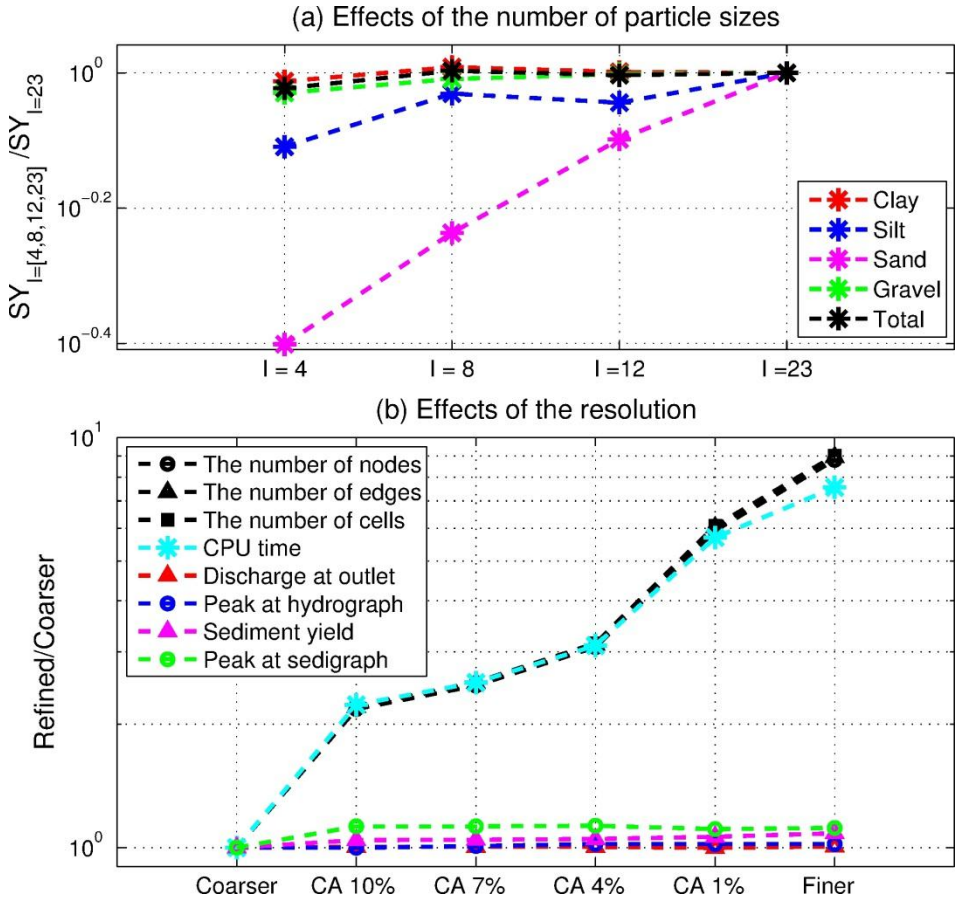

Figure 3.9: Sensitivity tests to the number of particle sizes (*I*) and the resolution of domain on hydraulic and morphologic behaviors: (a) the ratio of sediment yields of 4 different *I*s with respect to that of *I*=23; (b) the ratio of several variables (see legend) of 6 different domains with respect to those of the coarser domain.

An extensive data set on precipitation, runoff, and sediment yield has been collected at WGEW since the middle 1950s (http://www.tucson.ars.ag.gov/dap/) [*Goodrich et al.*, 2008; *Nichols et al.*, 2008; *Stone et al.*, 2008]. Data since 1999, when precipitation and runoff data collection program was updated with new sensors, are used in this study. Ten precipitation events for which runoff and sediment data exist were chosen for calibration and verification of the numerical model. These events are summarized in Table 3.3.

Table 3.3: A summary of observed rainfall, runoff, and sediment for events used in simulations for the Lucky Hills watershed. Rainfall was measured at "Gage 83". Runoff and sediment were measured at flume "FL103".

Event		Observed rainfall			Observed runoff and sediment				Simulation	
No.	Date	Start time	Duration [min]	Depth [mm]	Start time	Duration [min]	Volume [m^3]	Sediment Yield [kg]	Start time	Duration [min]
1	8/10/2000	15:40	37	26.289	15:42	53	414.736	9933	14:45	180
2	8/04/2002	12:52	34	28.956	12:54	61.25	379.04	7426	12:00	180
3	8/23/2003	14:39	16	17.780	14:42	50	230	7092	13:45	180
4	7/27/2005	18:40	169	22.987	19:07	44.5	44.528	1623	17:45	240
5	9/08/2005	12:17	73	38.735	12:15	109.25	614.56	15831	11:30	180
6	7/23/2007	13:20	14	14.224	13:21	34.75	110.032	3301	12:30	180
7*	7/31/2007	15:34	126	41.656	15:35	87.75	516.304	16027	14:45	180
8	9/09/2007	15:52	115	16.129	17:28	35.5	167.808	5244	15:00	360
9	7/19/2008	21:27	311	46.355	21:27	115	484.288	11215	20:30	360
10	7/25/2008	14:36	42	30.226	14:37	81.25	476.56	9892	13:45	180

*Event 7 is used for calibration.

3.4.3.2 Model calibration and confirmation

Calibration of any numerical model that needs parameters to represent physical phenomena is one of the most tedious works. As described in Section 3.2, there exist a large number of parameters grouped according to the usage for hydrologic (tRIBS), hydraulic (OFM), and sediment erosion-transport dynamics (H-R equations). Around 70 % of the parameters in Table 3.4 are used to represent hydrological processes that need calibration for (1) soil hydraulic properties (9 parameters in Table 3.4) associated with infiltration and runoff production. These

parameters play a key role in simulating soil moisture, flow and erosion because they control the magnitude and timing of the hydraulic and morphologic responses to precipitation. Among these 9 parameters, two principal parameters, "saturated hydraulic conductivity (K_s)" and "conductivity decay parameter (f_d)" were chosen to calibrate the model to match the flow behavior. The accepted knowledge behind this calibration is that higher value of f_d causes larger chance of infiltration-excess runoff, preclusion of groundwater exfiltration, fast basin response in time to peak, and rapid recession in hydrograph limb. More conductive soil with higher value of K_s has a tendency to generate less runoff and slower response to rainfall; (2) thermal properties for soil and vegetation (7 parameters) related to evapotranspiration and energy balance, which determines the magnitude of the surface energy fluxes such as short/long wave radiation and latent/sensible/ground heat flux, and evapotranspiration components; and (3) vegetation interception parameters (6 parameters), which influence the storage capacity and canopy dynamics of moisture in the canopy water balance model [*Rutter et al.*, 1971; *Rutter et al.*, 1975]. The latter thermal and interception parameters were not calibrated in this study because those effects might be minor in the event scale. The same values for these parameters were used since *Francipane et al.* [2012] calibrated the tRIBS model for the same watershed and showed a good agreement with the observed runoff data over a ten-year period from 1999 to 2009. A more detailed description of calibration methodology for hydrologic components refers to Section 4 of the paper by *Ivanov et al.* [2004b], which includes the relative importance of parameters and calibration efforts, and the spatiotemporal aspects of calibration. Second, for Saint-Venant equations, there exists only one parameter to be calibrated. This friction parameter is well known to influence the timing and peak of hydrograph and have a high priority in calibration. A proper value of the parameter is usually determined either by referring to literature or estimated from

regression equations such as those in *Kim et al.* [*Kim et al.*, 2012a] when the cases are of emergent vegetation or obstacles. Higher value of the friction coefficient retards the flow, making the magnitude of peak smaller and time to peak slower. In this study, the Manning resistance coefficient was manually calibrated using event 7 (Table 3.3) by matching the measured and simulated flow hydrograph characteristics at the basin outlet. Last, for parameters of H-R equations, four variables out of six major parameters (Table 3.4) were calibrated by matching the measured and simulated sediment yield for the same event. The effort of calibrating the parameters of specific energy of entrainment and critical stream power was reduced by using two relationships suggested by *Heng et al.* [2011]:

$$J = \frac{0.5\rho_w {v_R}^2}{a_0} \text{ and } \Omega_{cr} = 5.74\rho_w \left(\theta_c D_{50} g \frac{\rho_s - \rho_w}{\rho_w}\right)^{3/2} \log\left(12.3 \frac{\theta_c}{S} \frac{\rho_s - \rho_w}{\rho_w}\right), \qquad (3.30)$$

where v_R is the velocity of rainfall impact assumed to be 5.5 m/s, θ_c is the critical Shields parameter for incipient motion equal to 0.045, D_{50} is the median particle size, and S is the domain slope. The number of manually managed, replicate simulations was less than one hundred. The final values of the parameters used in simulations are presented in Table 3.4.

Table 3.4: Parameters used to represent hydrologic, hydraulic, and sediment erosion-transport dynamics of the Lucky Hills watershed. The letter "C" refers to the parameters whose values were calibrated; "L" refers to the parameters whose values were inferred from literature.

Parameter	Description	Value	Unit	Source	Usage
n	Manning coefficient	0.033	s $m^{-1/3}$	C	Flow
a_0	Detachability of original soil	80	kg m^{-3}	C	Erosion
a_d	Detachability of deposited soil	2000	kg m^{-3}	C	Erosion
F	Effective fraction of excess stream power	0.01	-	C	Erosion

Ω_{cr}	Critical stream power	0. 12	W m^{-2}	L	Erosion
J	Specific energy of entrainment	189.06	m^2 s^{-2}	L	Erosion
M_t^*	Deposited mass needed to sheild soil	2.7	kg m^{-2}	C	Erosion
K_s	Saturated hydraulic conductivity	20.0	mm hr^{-1}	C	Soil-hydraulic
θ_s	Volumetric soil moisture at saturation	0.39	m^3 m^{-3}	L	Soil-hydraulic
θ_R	Volumetric residual soil moisture	0.0463	m^3 m^{-3}	L	Soil-hydraulic
m_p	Pore-size distribution index	0.3813	-	L	Soil-hydraulic
φ_B	Air entry bubbling pressure	-63	mm	L	Soil-hydraulic
f_d	Conductivity decay parameter	0.03	mm^{-1}	C	Soil-hydraulic
A_s	Anisotropy ratio in the saturated zone	1	-	L	Soil-hydraulic
A_u	Anisotropy ratio in the unsaturated zone	1	-	L	Soil-hydraulic
η'	Bedrock depth	50	m	L	Soil-hydraulic
k_s	Volumetric heat Conductivity	0.214	J m^{-1} s^{-1} K^{-1}	L	Soil-thermal
C_s	Soil heat capacity	1209573	J m^{-3} K^{-1}	L	Soil-thermal
S_s	Canopy storage	1	mm	L	Storage
B	Interception coefficient	0.2	-	L	Storage
p	Free throughfall coefficient	0.35	-	L	Interception
S_c	Canopy field capacity	1	mm	L	Interception
K	Canopy drainage rate coefficient	0.18	mm h^{-1}	L	Interception
g_d	Canopy drainage exponent	3.9	mm^{-1}	L	Interception
alb	Surface albedo	0.22	-	L	Veg.-thermal
H_v	Vegetation height	0.46	m	L	Veg.-thermal
K_t	Optical transmission coefficient	0.7	-	L	Veg.-thermal
r_s	Canopy average stomatal resistance	200	s m^{-1}	L	Veg.-thermal
V_f	Vegetation fraction	0.5	-	L	Veg.-thermal

By using the parameter values obtained through calibration for event 7, the total watershed runoff volumes and sediment yields were calculated for ten selected events (Table 3.3). The results were compared with observations and are shown in Figure 3.10. For relatively large events, the simulated values tend to be overestimated, while for smaller events they are somewhat underestimated. Despite these discrepancies, the comparison is very satisfactory: the determination coefficients of R^2=0.86 for runoff and R^2=0.80 for sediment were obtained (Figure 3.10). The discrepancies may be due to employed assumptions and inherent uncertainties: (1) soil and land use characteristics used in tRIBS are assumed to be spatially uniform over the entire basin; (2) precipitation is also assumed to be spatially uniform and data were aggregated to a 15-minute resolution from a 1-minute resolution [*Francipane et al.*, 2012], which may affect runoff production; (3) the hydrological parameters were calibrated over a period of 10 years, with the tendency of generating a slightly higher runoff for large events.

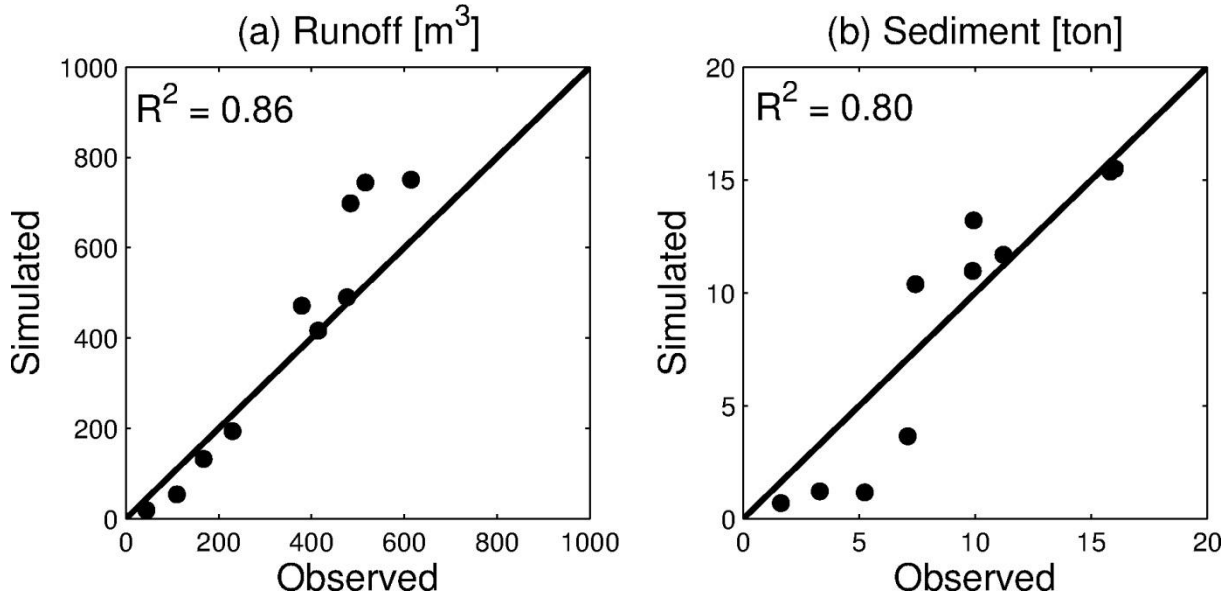

Figure 3.10: A comparison of the simulated and observed (a) runoff volumes and (b) sediment yields for ten selected events. R^2 denotes the determination coefficient, which was computed by using 9 data points (excluding data for the event 7, i.e., the calibration case).

Figure 3.11 shows the time series of flow and sediment fluxes for events 5 and 7. Since observations do not provide the actual time series of sediment flux, the observed data shown in the sedigraphs were computed using information on sediment concentration and flow volume flux. As seen, the measured and simulated flow rates at the outlet exhibit a very good match. The two sediment discharge series, however are not in perfect agreement even though the total sediment volumes are almost identical (see Figure 3.10). The reason for that could lie in the fact that concentration of sediment was measured in an intermittent manner (~10 times during an event), as compared to the flow measurements (~100 times per event); the relatively sporadic measurements of the concentration might have failed to capture an abruptly high sediment yield or the general tendency of the sedigraph. Inasmuch as a real-time measurement of a sedigraph is

difficult and errors are inevitable, the deviation between the observed and simulated sedigraphs can be comprehended.

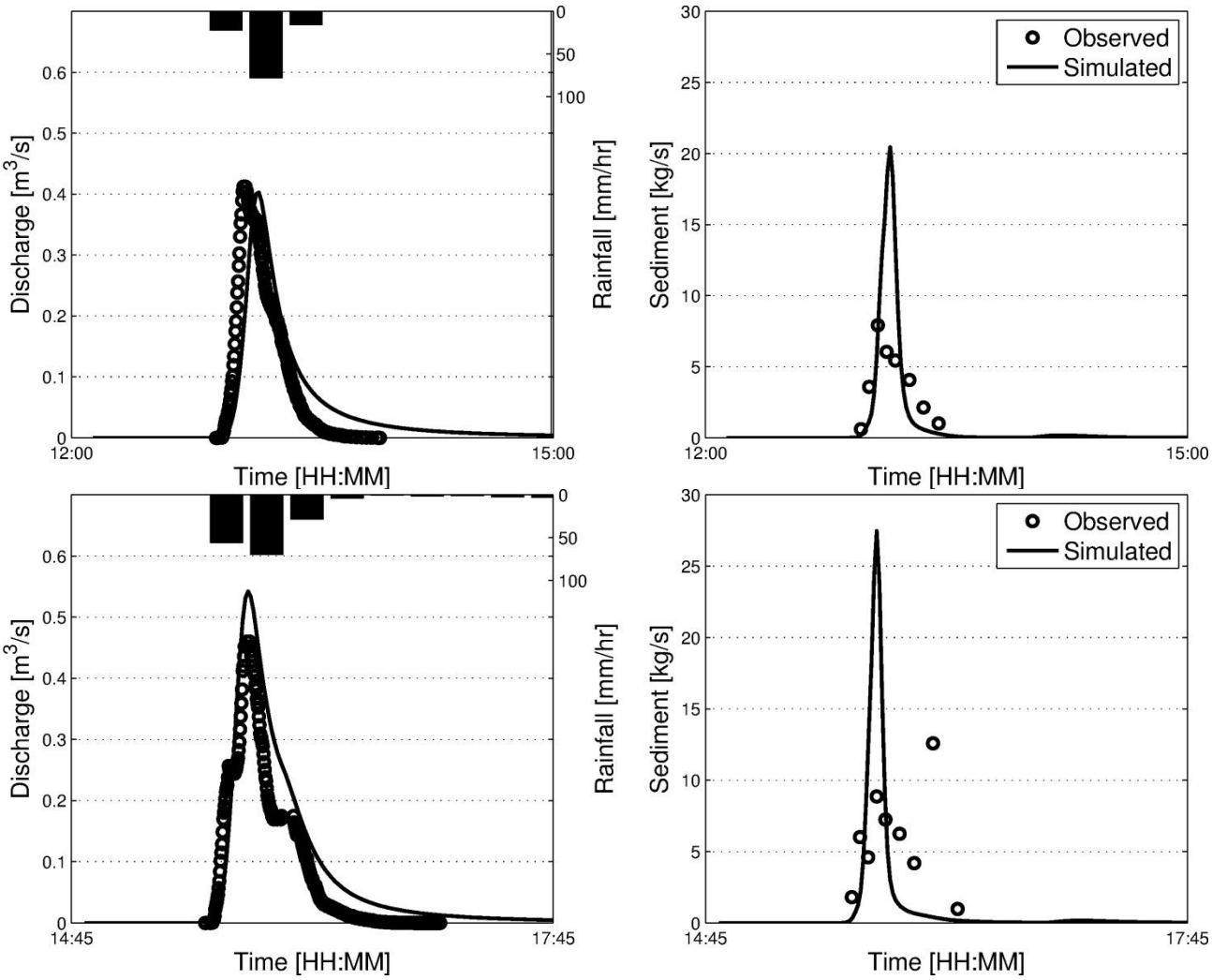

Figure 3.11: Hydrographs and sedigraphs for events 2 (the top panel) and 7 (the bottom panel).

3.4.3.3 Spatial characteristics of flow and erosion processes

Figure 3.12 illustrates the simulated spatial distributions of depth, velocity, total concentration, and elevation changes over the basin, and compares them at simulation hours 1 and 2 (event 7). The time of hour 1 corresponds to the occurrence of the observed peak and the time of hour 2 corresponds to the recession period. As expected, higher depths, velocities, and concentrations can be observed near the peak time, as compared to those during the recession period. Elevation changes are such that most of the watershed area is being eroded, except for a confluence area, where there is an abrupt morphological transition from steep to mild slopes (Figures 3.7 and 3.12). Furthermore, sharp variations in the distributions of total concentration (especially for the larger particles) and elevation change can be detected in that same area. In order to address these variations from a mechanistic point of view, an inspection of the governing equations for possible driving reasons is necessary.

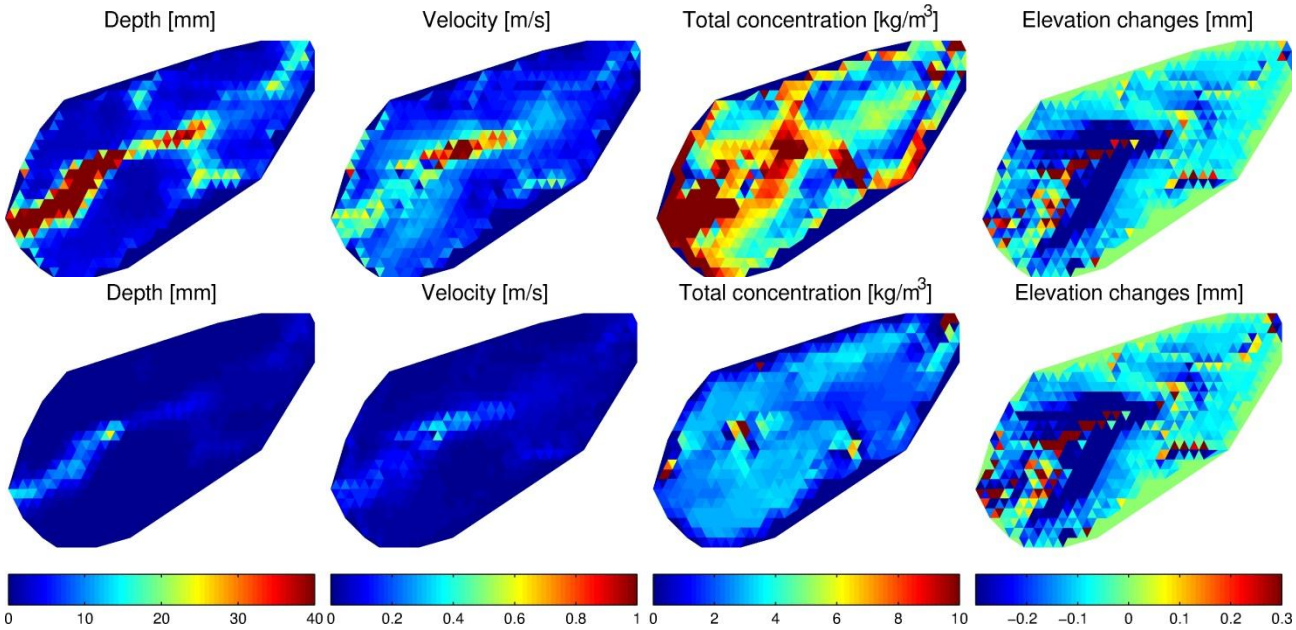

Figure 3.12: The simulated spatial distributions of depth, velocity, total concentration, and elevation changes at simulation hours 1 (the top panel) and 2 (the bottom panel) for event 7. In the plots of elevation changes, deposition is represented as positive values and erosion is represented as negative values.

Erosion processes represented by the source terms in the H-R equations indicate that major factors affecting the spatial variation of sediment variables are the two independent flow variables: depth and velocity (Eqs. (3.7), (3.8), (3.10), (3.11), and (3.12)). Since the rates of erosion in Eqs. (3.10) and (3.11) are directly proportional to flow velocity, while inversely proportional to depth, the ratio of these variables is used in Figure 3.13-(a). The figure shows change in elevation as a function of the ratio for all computational cells at hour 1. Another variable, site slope is used in Figure 3.13-(b) because the spatial variations of depth and velocity are in turn affected by the distribution of the domain slope. Theoretically, domain slope and contributing area are the dominant factors affecting spatial calculations of the flow variables under conditions in which runoff production is equal everywhere in the basin. However, the

effect of contributing area was not found to be significant in estimating the illustrated morphological changes: a relationship between the elevation changes and the topographic index exhibits a trend similar to that in Figure 3.13-(b) (not shown). Both plots in Figure 3.13 show similar patterns of erosion dependence on a prognostic variable. Specifically, erosion is higher for larger slopes (higher velocity, smaller depth). This indicates that in this zeroth-order watershed, erosion is characteristic of "diffusive" mechanism, rather than fluvial erosion [*Istanbulluoglu et al.*, 2008; *Francipane et al.*, 2012]. Specifically, diffusive erosion increases with site slope, regardless of magnitude of contributing area, while fluvial erosion occurs in channels where erosion scales with upstream contributing area. As seen in Figure 3.13-(b), erosion dependence on site slope exhibits a threshold (~0.09 for slope) beyond which the elevation changes grows significantly in a non-linear fashion. This behavior explains the substantial changes of elevation observed in Figure 3.12 in the area of steep slopes. This result indicates that topographic bed slope can be one of the most dominant factors in determining erosion process in this watershed. Conversely, deposition is more likely to occur as the ratio of flow velocity to depth or site slope decreases. But any generalization is difficult because deposition does not occur frequently in this basin (~8% of the domain).

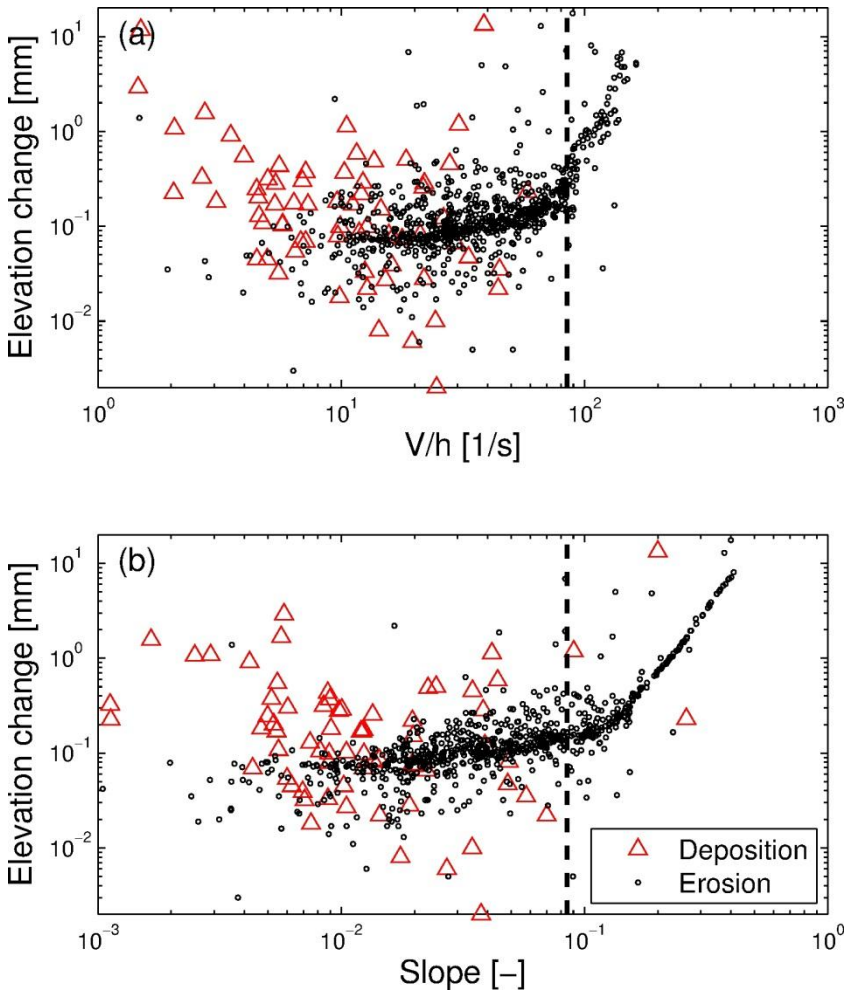

Figure 3.13: Changes in elevation the first hour of simulation as a function of (a) the ratio of local flow velocity to depth and (b) site bed slope. Data for all computational cells at simulation hour 1 are used (event 7). Red triangles correspond to deposition and black dots correspond to erosion (absolute elevation changes). The vertical dashed line depicts the threshold slope value of 8.47%.

3.4.3.4 Size-dependent characteristics and spatial variability of concentration

The simulation results that can explain how the spatial distributions of erosion variables differ depending on sediment particle size are addressed at hour 1 for event 7. First, we confirmed that similar to the previous verification cases in section 3.4, size-selective features of

erosion variables distinctly follow the inherent feature of H-R equations: similar spatial pattern of e_i between r_i, and M_i, e_{ri} between r_{ri}. However, the relative fractions of deposition rate do not follow that of concentration, i.e. the proportions of deposition for larger particles are much higher than those of concentration. This is because in the case under consideration the effect of settling velocity is one to two orders of magnitude greater than that of concentration. Second, the region with an abrupt transition from steep to mild slopes is more pronounced in spatial distributions for some particle sizes (e.g., reentrainment rates for sand and gravel), which will influence the spatial variation of concentrations. Since the first phenomena can be easily anticipated by the definition of H-R equations, we focus on the latter phenomena in later analysis.

Most interesting morphologic variables are the amount of sediment in the water column and soil bed. The latter was addressed in the previous section that the erosion is pronounced in the high-sloped area as a form of diffusive erosion. Here, size-dependent concentrations are also compared in Figure 3.14 where illustrates two distinct spatial variations and their dependence on the prognostic variables of contributing area and slope for smaller (clay and silt size) particles and larger (sand and gravel size) particles, respectively. This figure displays that the smaller particles are easily eroded, can move far from their original locations without extensive settlement, and thus their concentrations accelerate at some area (~75 % CA) where flow is anticipated to be accumulated. In contrast, the larger particles are easily deposited, take a long time to move downstream, and thus their concentrations are prominent in the area and period where/when stream power in the combination with topography is guaranteed for them to be maintained in the water column. These size-dependent spatial variations for concentration imply that dissimilarly to erosion, concentration of smaller particles follows a “fluvial” characteristic while that of larger particles behaviors as a “diffusive” characteristic. Consequently, these

inferences confirm that soil composition in both water column and bed can vary significantly according to two-dimensional morphological variations and topographical characteristics of watershed exert a crucial role on soil erosion and sediment transport processes.

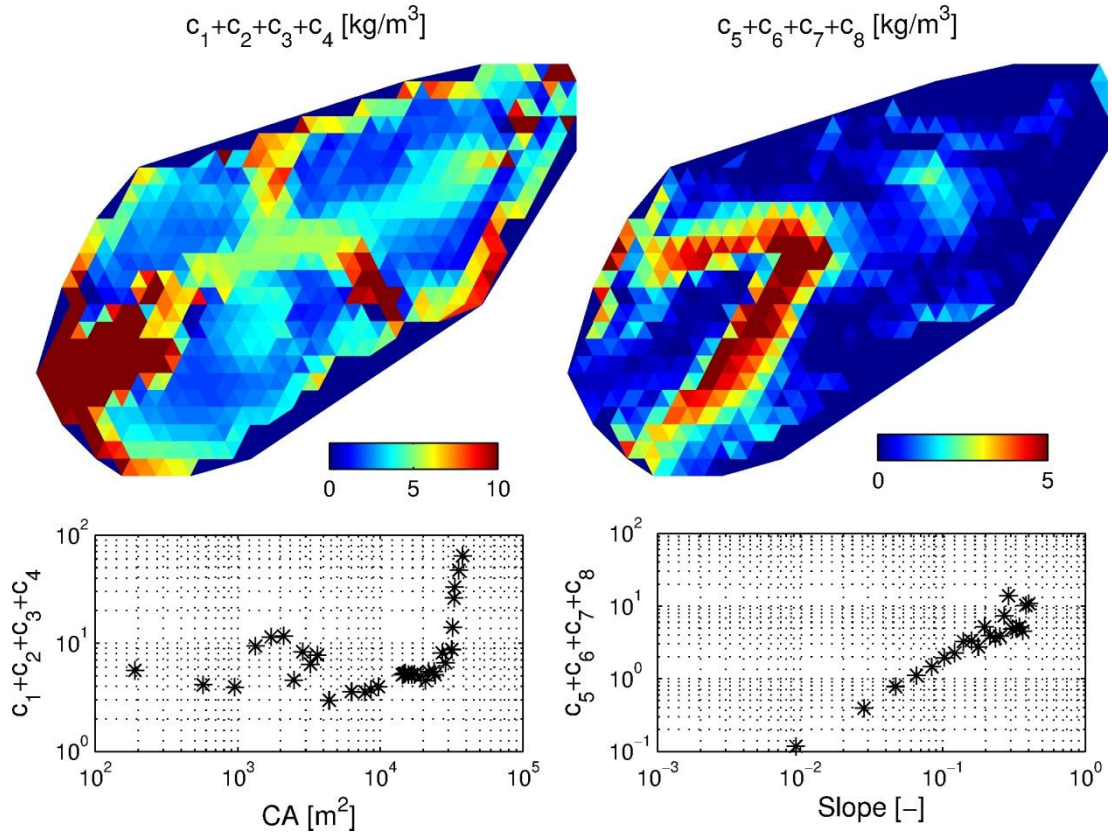

Figure 3.14: The simulated spatial distributions of summed concentrations [kg/m^3] for (a) smaller particles (i = 1, 2, 3, and 4) and (b) larger particles (i = 5, 6, 7, and 8) at simulation hour 1 (event 7). Their dependences on contributing area and domain slope are shown in two bottom plots. The contributing area and slope are binned with 100 intervals; the averaged values for each bin are used.

3.4.3.5 North- and south-facing characteristics of watershed system

Two critical features of watershed systems are their connectivity [*Michaelides and Chappell*, 2009], i.e., hydrologically mediated transfer of mass, momentum, energy, or organisms within or between basin compartments, and non-linear systems; their dynamics depend on "convective" and "dissipative" characteristics of involved processes. In this section, these connectivity and non-linearity between hydrologic processes, flow regime, erosion, and stream sedimentation are addressed by investigating how disturbances arising at eco-hydrological scale will necessarily propagate downstream. To introduce this perturbation, we used the spatial distribution of mean annual biomass obtained from the simulations. Figure 3.15-(a) evidently shows the effect of climate and slope aspect on vegetation that the north-facing elements has a higher vegetation than the south-facing elements [*Gutiérrez-Jurado et al.*, 2007]. We test two hypotheses in hydrologic and hydraulic viewpoints that the enhanced vegetation in north-facing areas gives rise to less runoff production due to more infiltration, and flow retardation caused by more obstacle effects. Two experimental heterogeneous cases as compared to the control homogeneous case (event 7) are then designed: the first one is intended to have a spatially distributed saturated conductivity ranging from 5 to 30 mm/hr such that the generated runoff for different homogeneous conductivities lies in about 20 to 25 % variations [*Gutiérrez-Jurado et al.*, 2007]. The other heterogeneous case is designed to have a spatially distributed Manning's coefficient ranging from 0.0265 to 0.0395 (note that 0.033 for the original homogeneous case). The latter values are roughly estimated from the vegetation cover fraction related to the mean annual biomass by using the Eq. (3.11) in *Kim et al.* [2012a].

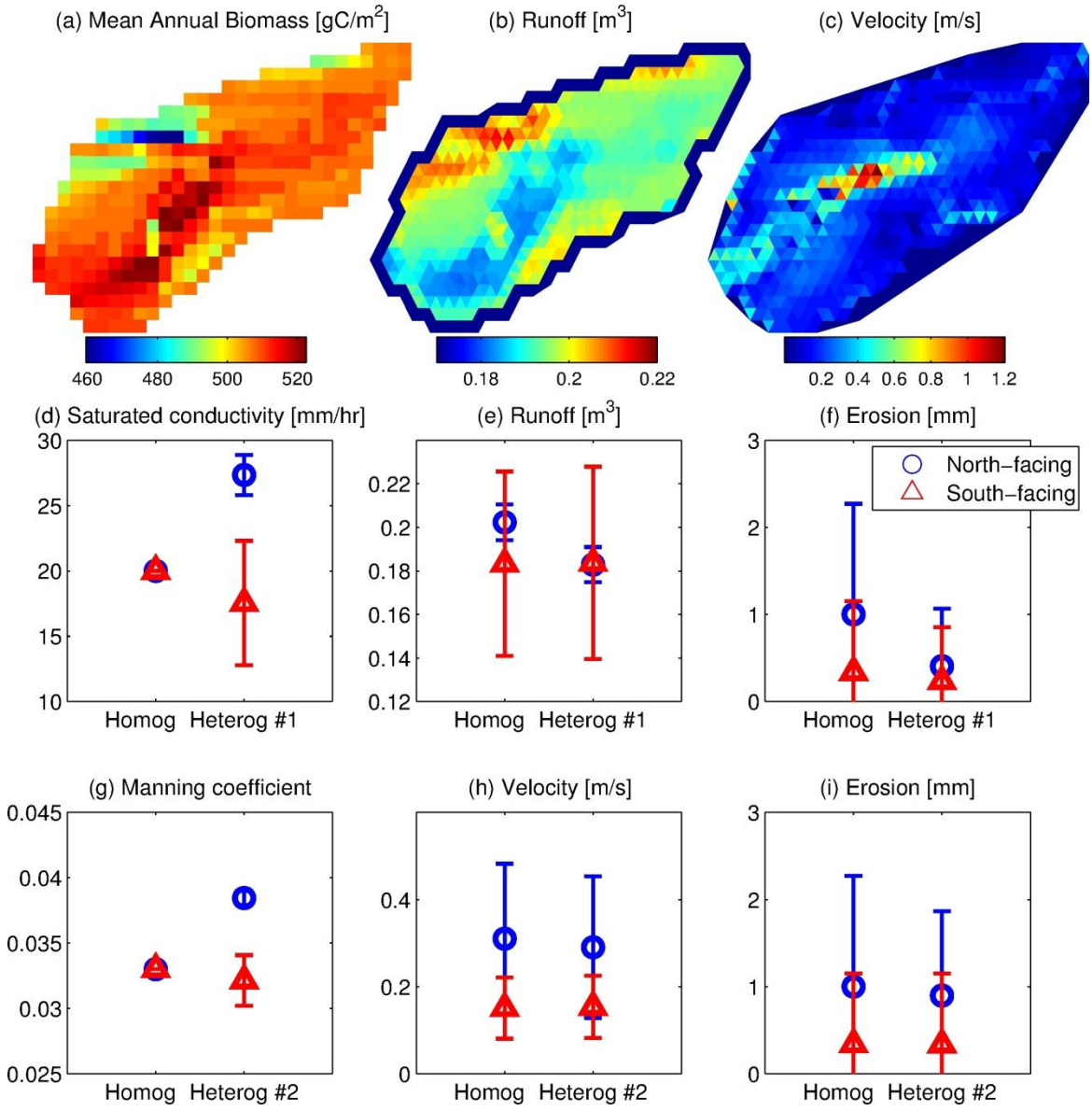

Figure 3.15: The spatial distribution of (a) mean annual biomass; (b) generated runoff; (c) computed velocity at 1 hour of Event 7. The subplot (d) and (g) represent the spatially-averaged saturated conductivity and Manning's coefficient, respectively, for the north- and south- facing elements. This division was done based on the magnitude of mean annual biomass. The subplot (e) and (h) show the simulated values of runoff and velocity caused by the perturbations. The last subplot (f) and (i) illustrate the erosion. The "Homog" denotes the spatially-homogeneous case, i.e., Event 7; the "Heterog #1" corresponds to the case where saturated conductivity is spatially varying according to the mean annual biomass; and the "Heterog #2" corresponds to the case where the friction coefficient is spatially distributed.

The hydrologic and hydraulic effects anticipated from these two heterogenetic variations are illustrated in Figure 3.15-(b) and (c), respectively where runoff productions inversely follow the biomass distribution and the velocity profile shows a slightly decrease on the north-facing elements. These phenomena can be verified by quantitatively computing the spatially-averaged values of runoff and velocity for south- and north- facing elements (Figure 3.15-(e) and (h)). The corresponding erosion in north-facing area with more vegetation generally tends to decrease resulting from reducing the runoff and velocity (Figure 3.15-(f) and (i)) while erosion in south-facing area exhibits a minor deviation. Although these results are straightforwardly obtained through two simple comparison tests, the tests are consequential in presenting a tool how the basin system can be inevitably interacted with topography, soil, and vegetation acting on the movement of flow and sediment. Another feature of this figure is non-linearity. For example, ~36 % increase of mean saturated conductivity in north-facing areas affects ~10 and 60 % of reduction on runoff and erosion, respectively; ~16 % increase of mean Manning's coefficient in the same area influences on the decrease of velocity and erosion by ~6 and 10 %. Despite of an extensive number of other significant factors affecting on erosion at watershed scale, this particular watershed addressed can sufficiently reveal a space-varying non-linearity according to the initial condition of vegetation.

3.6 Summary

A novel two-dimensional, physically-based model of soil erosion and sediment transport has been developed and coupled to a model that can simulate both hydrodynamic flow motions and hydrologic surface and subsurface processes. The erosion and transport processes are described with the Hairsine-Rose (H-R) model that accounts for size-selective sediment transport, differentiates soil of the bed into original and deposited soil layers, and tracks in time the development of the deposited area. The hydrologic and hydrodynamic model is tRIBS-OFM, Triangulated irregular network – based, Real time Integrated Basin Simulator-Overland Flow Model. For the solution of the combined two-dimensional, Saint-Venant and Hairsine-Rose equations, the finite volume method is employed based on Roe's approximate Riemann solver and resolved on an unstructured multiple resolution triangular mesh. The equations yielding space-time dynamics of flow, erosion, and sediment transport thus represent a coupled system of shallow water equations combined with advection-dominated transport equations for sediment of multiple particle sizes.

The integrated model has been verified with analytical solutions and empirical data for two one-dimensional benchmark cases dealing with rainfall-induced erosion and overland flow-induced erosion. The size-selective results of spatial distributions of sediment concentrations and deposited masses at different times, as well as temporal distributions, are presented and demonstrate a good agreement with measured data.

The model has been consequently applied at catchment scale corresponding to the Lucky Hills watershed located in southeastern Arizona, U.S.A. Before calibration, we performed a sensitivity test to a grid resolution and the number of particle size. Then, model confirmation was carried out for both flow volume and sediment yield at the basin outlet for ten different rainfall

events. As the simulation results indicate, a “diffusive” mode of erosion is characteristic of this headwater, zeroth-order catchment: erosion increases with slope and is not greatly affected by the contributing area. In particular, high elevation changes due to erosion occur over a limited hillslope area where abrupt morphological changes exist: for slopes higher than ~0.09, the elevation changes grow significantly in a non-linear fashion. In contrast, spatial, size-selective characteristics for concentrations appear to have two modes of “diffusive” for larger particles and “fluvial” for smaller particles. This tendency for concentration can also be identified in the distributions of size-selective concentrations on the prognostic variables of contributing area and domain slope. The results confirm that topographic characteristics of the basin can be one of the most dominant factors in determining the amount of sediment in water column and soil bed of this watershed, mediated by the dynamic flow regime of depth and velocity.

This study builds on and expands previous research by using a coupled framework that adapts the Hairsine-Rose model to watershed-scale simulations. The essential strengths of the combined framework are as follows. (1) Hydrological and hydraulic characteristics as well as particle size distribution, arguably the three most crucial elements among external and internal factors for modeling erosion, are all simultaneously taken into consideration. (2) The model is based on sound physical laws, which result in narrow ranges of the parameter values that are theoretically measurable; satisfactory results can thus be obtained with calibration efforts. This model attribute makes feasible a wider range of real-world, catchment-scale flow/erosion problems. (3) The spatially distributed, detailed information on soil type, land use, and topography is becoming more accurate and easily accessible. This generates the potential for making modeling of earth-surface processes more credible. By incorporating these types of information, the developed hydrologic-hydrodynamic-erosion coupled model can be used as an

assessment tool for quantitative evaluation of spatiotemporal erosion responses to imposed scenarios of climate change, variations in land-use, soil, and vegetation types in small- to medium-size basins.

CHAPTER IV

Hydraulic resistance to overland flow on surfaces with partially submerged vegetation

4.1 Introduction

Hydraulic resistance to open-channel and overland flows is an important characteristic that needs to be represented properly in modeling runoff, flood routing and inundation, and soil erosion. Resistance estimation affects not only the accurate calculation of flow variables, such as the water depth, velocity, and shear stress, but also the prediction of their derivative outcomes, such as the time of concentration, flow distribution in a basin, the transport capacity, the total sediment yield, etc. The resistance of a surface can be characterized with several hydraulic roughness coefficients. The most widely used are the Manning roughness coefficient (n), the Chezy resistance factor (C), and the Darcy-Weisbach friction factor (f). Manning's n is most popular in hydrological and soil erosion models, while using the Darcy-Weisbach f is more common than the other resistance formulations in experimental studies [*Hessel et al.*, 2003]. Theoretically, hydraulic resistance can be divided into five components: surface (grain) resistance, form resistance, wave resistance, rain resistance, and bed-mobility resistance [*Abrahams and Parsons*, 1994; *S X Hu and Abrahams*, 2006; *M W Smith et al.*, 2007].

Numerous studies have performed field or laboratory experiments and theoretical analyses seeking ways to relate hydraulic characterization of flow to roughness coefficients. These studies tried to investigate a number of dimensionless variables in an attempt to find suitable relationships using various metrics such as the Reynolds number (*Re*), the Froude number (*Fr*), the characteristic roughness length (e.g., the ratio of depth to roughness element), domain slope (*S*), and vegetation or obstacle cover fractions. Since early studies of overland flow, resistance was described by a roughness coefficient, in analogy to the resistance relations used to characterize flows in pipes. A relationship between the roughness coefficients and the Reynolds number (e.g., *f-Re*) has been well established for shallow overland flows as well as for flows in pipes and smooth channels [*Chow*, 1959; *Emmett*, 1970; *R M Li and Shen*, 1973; *Phelps*, 1975; *Savat*, 1980]. The *f-Re* relationship has a negative slope of 1.0 in the laminar flow regime [*Blasius*, 1913]; in turbulent flow, different *f* - *Re* relationships are obtained, depending on the value of the relative roughness [*Nikuradse*, 1933]. These findings indicated that among several possible dimensionless variables, *Re* has a predominant effect in quantifying the flow resistance in conditions where the flow completely submerges a plane bed with either a smooth or a rough surface. In such conditions, the roughness height is significantly smaller than the flow depth and the hydraulic resistance is dominated by the surface resistance component arising due to the presence of roughness elements beneath the flow surface.

However, in conditions where the surface is covered by stones, organic litter, or stems of vegetation that protrude through the flow, the aforementioned *f-Re* relationships are not applicable. Other dimensionless variables (e.g., *Fr*, relative roughness height, vegetation cover, etc.) may become more dominant, reflecting that the form and wave resistance can become the primary components of the total flow resistance [*Emmett*, 1970; *Roels*, 1984; *Abrahams et al.*,

1986; *Gilley and Finkner*, 1991; *Gilley et al.*, 1992b; *P Hirsch*, 1996; *Lawrence*, 1997; 2000; *Takken and Govers*, 2000; *S X Hu and Abrahams*, 2006]. For example, *Emmett* [1970] was the first to emphasize the importance of form resistance caused by microtopography, which can significantly exceed the surface resistance. *Roels* [1984] and *Abrahams et al.* [1986] stated that the standard *f-Re* relationship is not ubiquitous: the *f-Re* relationship can have a convex upward or a negatively sloping power-law relation. These relationships can be attributed to the progressive inundation of roughness elements, implying that the surface configuration of the elements, and not just the flow state, becomes dominant in quantifying the resistance. Further, *Gilley and Finkner* [1991] presented a regression equation for predicting *f* and *n* by including the characteristic length scale, i.e., a "random roughness index" as the primary variable. *Gilley et al.* [1992b] suggested that *f* is largely controlled by a measure of the gravel cover fraction. *Hirsch* [1996] developed a flow resistance model that explained flow conditions when the fraction of roughness elements was greater than 10% and *Fr* was greater than 0.5.

Recently, *Lawrence* [1997] further demonstrated the importance of other dimensionless variables in conditions of emerging vegetation and other types of obstacles protruding through the flow. Rather than using the Reynolds number, *Lawrence* [1997] advocated the use of the inundation ratio, h/k_r, as the ratio of the flow depth h to the characteristic height of roughness elements k_r. *Lawrence* [1997] identified distinct flow regimes, such as partial and marginal inundation, and well-inundated flows, with various fractions of obstacles (hemispheres) placed in the flow. Depending on whether the flow depth h was greater/smaller than the characteristic height k_r, *Lawrence* [1997] estimated f as a function of the inundation ratio by using a drag model for the partial inundation, a mixing length model for the marginal inundation, and a rough turbulent flow formula for well-inundated flows. Since the estimation of the drag model showed

an underestimation of flow resistance for the partial inundation case, *Lawrence* [2000] later modified the form drag model to obtain higher *f* values by increasing the drag coefficient, which was negatively correlated with h/k_r.

The modified model of *Lawrence* [2000] was successfully applied for the estimation of flow resistance for the case of marginal inundation, where roughness elements were randomly distributed and relatively uniform in size. However, when this model was applied under conditions differing from the setting under which the model was developed, such as complex flow geometries, the performance was not always satisfactory. *Ferro* [2003] tested the model using laboratory measurements and showed that the modified mixing length formulation provided accurate estimates, while the modified drag model resulted in a limited accuracy in estimating *f*. *Takken and Govers* [2000] also tested the partial inundation case of *Lawrence* [1997] and concluded that for situations with the complex configurations of roughness elements, a single independent variable (i.e., h/k_r) was insufficient to predict *f*. Thus, other variables, such as the flow rate, *Fr*, and *Re* need to be considered to fully characterize the flow resistance [*Takken and Govers*, 2000; *Smart et al.*, 2002; *S X Hu and Abrahams*, 2006].

In shrubland or forested hillslopes, typical flow depths are much smaller than the height of roughness elements such as vegetation stems and thus inundation ratios are very small. Such flow conditions generally prevail in hillslope hydrological dynamics. Characterization of flow for partially inundated conditions with a non-uniform distribution of roughness elements is therefore significant for modeling runoff routing and soil erosion. However, these flow conditions remain poorly characterized by empirical observations. For example, experimental data from previous studies (see Fig. 4 in *Lawrence* [1997] reporting data from eleven studies) are

limited to partial inundation cases, i.e., most of the observed inundation ratios were between 0.1 and 1.

In order to establish a general relationship applicable to a wide range of conditions, numerical modeling based on the two-dimensional shallow-water equations was carried out in this study. The numerical simulations corresponded to overland flow on hillslopes covered with shrubby or woody vegetation. An application of a numerical model, as compared to field or experimental manipulations, provides several advantages. Specifically, in the case of small depths of overland flow (few *mm* to *cm* length scale), the minimum requirement of water depth for measuring the velocity with Acoustic Doppler velocimeters or electromagnetic current meters is not satisfied [*Lawless and Robert*, 2001]. When the requirements are satisfied, small depths still represent an issue in terms of measurement accuracy [*Biron et al.*, 1998]. These difficulties result in large measurement errors in laboratory or field experiments. Furthermore, the determination of the friction (or energy) slope used in the calculation of roughness coefficients is also cumbersome. It can be normally substituted with the bed slope under uniform flow conditions, but it may not represent truthfully a spatially varying friction slope in situations with many protruding obstacles. Lastly, the difficulty of controlling conditions for high flow rates prevents empirical observations in field and laboratory studies [e.g., *Takken and Govers*, 2000; *Hessel et al.*, 2003]. For example, *Takken and Govers* [2000] used discharges ranging from 4.2×10^{-6} to 2.7×10^{-4} m^3/s.

High-resolution, hydrodynamic numerical simulations can overcome all of the above problems by specifying arbitrary flow conditions, including both high and low flow rates that occur in real world situations. Using detailed simulations performed at fine space-time scales, the properties of the resistance coefficient at larger spatial scales can be investigated. In order to

represent a system with tree/shrub stems, a sloped plane populated with "obstacle cells" that have infinitely long vertical dimension was designed. A number of scenarios with different domain slopes (S), inflow rates (Q), bed substrate roughness conditions (n_b), and vegetation cover fractions (V_f) were considered. Based on the simulation results, two methods were developed to obtain the upscaled Manning coefficient. A predictive equation was developed using multiple regression and dimensional analyses and verified with five different experimental data sets and a proposed wave resistance equation. Finally, the characteristic controls of several independent variables on the roughness coefficient are described and evaluated.

4.2 Model suitability and simulation setup

4.2.1 Model suitability

The coupled model used is able to capture the phenomena of backwater and diverging-converging thread as well as a noticeable change of flow variables (e.g., hydraulic jump). But, one logical question is whether a simplified form of the Navier-Stokes equations, the Saint-Venant shallow water equations, is an adequate approximation for simulating flows of relatively small depth and flows passing in narrow openings between vegetation stems. Specifically, the first possible concern is whether the S-V equations can accurately simulate very shallow flows. Such flows can be affected by both bottom boundary layer and free surface movement, and the vertically averaged S-V equations cannot recognize these effects of bottom/free surface boundaries. However, the major assumption in applying the S-V equations is that depth (i.e., the vertical direction scale) should be much smaller than the length scale of a flow phenomenon in the horizontal direction. In an overland flow condition with small depths and a large spatial scale

of the domain, this assumption is quite acceptable. A second concern is whether the Manning's parameterization used in the S-V equations can adequately capture the energy loss due to eddies generated around plant stems. Three-dimensional turbulence modeling would appear to be a more suitable method that can consider such effects and thus reduce the uncertainty of simplifying assumptions of the S-V model. However, the application of turbulence models presents a number of challenges. First, several parameters still need to be determined to close a system of turbulence equations, e.g., k-epsilon, k-omega, SST, etc. for RANS models or Smagorinsky constant in LES models. Second, in order to accurately resolve turbulent eddies, appropriate representation scales have to be used and very fine mesh resolutions are necessary; as a "rule of thumb", mesh resolution has to be at least one order of magnitude finer than the effective eddy scale. For example, *Stoesser et al.* [2010] used time steps satisfying the CFL condition of 0.5 and a very fine mesh with nearly 30,000,000 grid points for a simulation case with only 64 isolated stems. Although this study presented detailed results demonstrating various turbulent characteristics, extending this approach to higher Reynolds numbers and randomly distributed vegetation of a high cover fraction is not feasible. This would require much finer space-time scales of representation.

4.2.2 Simulation setup

For the estimation of Manning's *n* for overland flow, numerical simulations are carried out for an inclined plane that is 1 m wide and 2 m long, using slopes ranging from 10 to 110% (5.7 to 47.7 degrees) at the 20% resolution of the slope. Such a range of bed slopes represents possible hillslopes in a real watershed. The forcing for the domain is specified in two forms: as a spatially uniform rainfall of 10 mm/hr continuous intensity over the entire duration of the

simulation and inflow rates of 0.0001, 0.0005, 0.001, and 0.01 m^3/s uniformly distributed over the width of the upstream boundary. The inflow rates were selected so as to describe a variety of cases of hillslope hydrology. Specifically, the discharges of 0.0001, 0.001 and 0.01 m^3/s represent steady-state flow rates at different locations of a hypothetical 1-m wide planar slope at 10, 100, and 1000 m downstream of the upstream boundary, assuming 36 mm/hr excess rainfall (e.g., the kinematic wave solution yields 0.0001 m^3/s steady-state flow rate at the bottom of a 10 m hillslope as, etc.).

Manning's coefficients of 0.02, 0.03, and 0.04 were chosen so as to represent a bare, rough plane surface without vegetation. These will be referred to as "the base Manning's coefficients" and denoted by n_b. The values of n_b are used to represent various characteristics of bed, such as the particle size and distribution, the roughness height, and the degree of tillage. For example, a small value of n_b corresponds to an experimental condition of bare sand, while a larger value is a representation of the condition with irregular depressions and heavy protruding stones. These constant base Manning coefficients only explain the resistance caused by friction at the flow bottom and are within a range of values reported in literature.

Vegetation cover fractions (defined here as the fractional areas of non-submerged "stems", V_f) of 0, 5, 10, 20, 30, and 50% were used. The locations of vegetation stems were determined randomly within the simulation domain for a given V_f (see Figure 4.1). From a computational standpoint, each stem of vegetation is represented as a rigid, infinitely-long wall of hexagonal shape composed of six triangles. The shape can be fit within a circle that has a diameter of approximately 2 cm. Since for most practical situations the order of depths represented by the partial inundation is very small as compared to the stem height of plants, the assumption of a rigid, infinitely-high wall is reasonable. The free-slip boundary condition is

applied to the boundary of each stem cell, enforcing that the velocity normal to the cell interface is zero. Inside stem cells, depth and velocity are consequently forced to be zero.

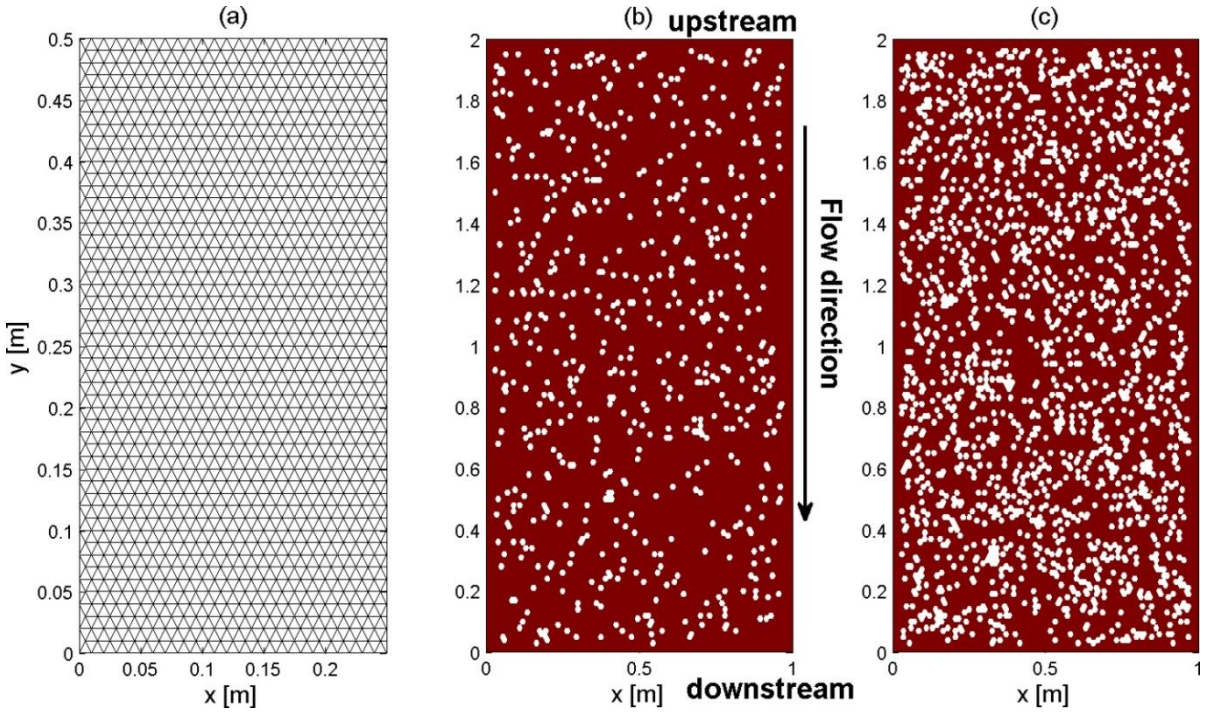

Figure 4.1: Illustrations of the simulation domain showing triangular cells ((a), zoomed-in) and locations of vegetation stems corresponding to the 10 % (b) and 30 % (c) vegetation cover cases. Each stem has a hexagonal shape consisting of six triangular cells.

The mesh spacing used to represent the simulation domain is 0.01 m and the number of mesh nodes (vertices) and triangular cells is 20,201 and 40,000, respectively. The size of mesh is appropriate for representing the shape of a vegetation stem. The time step during the simulation time of 2 min is 0.002 sec for the three low inflow rates and 0.0005 sec for the high inflow rate. The time step used is restricted by the Courant-Friedrichs-Lewy (CFL) condition that ensures the stability of the explicit numerical scheme [*Kim et al.*, 2012b]. An impervious soil surface

condition is assumed to exclude the processes of infiltration and subsurface flow. While the latter impact surface runoff generation, the aim of the study is to investigate the effects of unsubmerged obstacles on the flow process in conditions of clearly identifiable independent variables; the impact of runoff-generating processes is indirectly accounted for through the boundary inflow rate.

Simulation cases are designed so that the following characteristics are varied: vegetation cover fraction (V_f), plane slope (S), base Manning's coefficient (n_b), and inflow rate (Q). Preliminary simulations demonstrated that the effects of rainfall intensity were very minor, as compared to an inflow rate. Therefore, only a single rainfall scenario (10 mm/hr) was used.

4.3 Methods for determining a representative value of resistance coefficient

This section describes methodologies of obtaining the upscaled values of the total surface resistance (n_t) based on the results of numerical simulations. Two methods for estimating n_t, the "Equivalent Roughness Surface" (ERS) and the "Equivalent Friction Slope" (EFS), are presented in the following. The essential difference between the ERS and EFS methods is whether information at internal data points is used for the computation of roughness, and the two methods contain their advantages and disadvantages. As opposed to EFS, the ERS method does not require any computations for the internal information but relies on a relationship between the time of concentration of the flow and the Manning coefficient of a bare, rough plane surface without vegetation for a given inflow rate and plane slope. The relationship should be determined beforehand and thus additional simulations are necessary if a slope or a flow rate is changed.

4.3.1 Equivalent Roughness Surface

One method to obtain an upscaled value of roughness is by using an "Equivalent Roughness Surface" method. This method assumes that the resistance of a rough plane bed without vegetation stems is equal to the resistance of a smooth plane covered with vegetation stems. In other words, the effect of the form and wave resistances generated by internal obstacles (i.e., stems in this study) is considered to exert the same effect as the surface resistance of a rougher bed without vegetation. This method finds an equivalent resistance by analyzing the hydrographs at an outlet region; specifically, it compares the times of concentration (t_c) of the simulated hydrographs for the flow case with vegetation stems and the case of flow over a rough, bare soil plane without any unsubmerged obstacles. When t_c is matched, the two hydrographs corresponding to these flow situations are nearly identical.

The determination of t_c corresponding to the simulated hydrographs plays a crucial role in computing $n_{t.}$ In this study, t_c is defined as the time that satisfies the following two criteria:

$$\frac{dQ(t_c)}{dt} < \epsilon \ \ and \ Q(t_c) > 0.95 Q_{steady}\ , \tag{4.1}$$

where *t* is time; *Q(t)* is discharge at time *t*; Q_{steady} is the theoretical discharge at steady-state, equal to the upstream inflow rate plus the rainfall contribution; ϵ is a tolerance value assumed to be 10^{-5} in this study. The above criteria are chosen to avoid numerically unrealistic values in t_c estimation.

The derived relationship between t_c and *n* (see section 4.4.2) was assumed to be linear within intervals between the simulated cases. The relationship was used to find n_t for any arbitrary t_c through interpolation. To make the assumption of linearity valid, numerous

simulations with small increments of *n* were performed for the bare plane conditions, spanning a wide possible range of t_c values.

4.3.2 Equivalent Friction Slope

The second method used in this study uses an "Equivalent Friction Slope". It is based on information simulated at internal points and computes an average value of resistance that represents an upscaled value for the entire simulation domain. In order to obtain the value of *n*, the Manning's equation is rearranged:

$$n = \frac{{R_h}^{2/3} {S_f}^{1/2}}{V}, \tag{4.2}$$

where R_h is the hydraulic radius that can be replaced by the water depth, *h*, under the sheet flow assumption; *V* is the flow velocity, calculated as $\sqrt{u^2 + v^2}$; *u* and *v* are *x*- and *y*- directional depth-averaged velocities, respectively; S_f is the friction slope. The energy slope is typically replaced with the bottom slope for uniform flow. However, using the channel bottom slope is not appropriate in the case when protruding vegetation or other obstacles exist. Thus, the components of the friction slope are calculated as

$$S_{f,x} = -\frac{\partial}{\partial x}\left(z_b + h + \frac{u\sqrt{u^2 + v^2}}{2g}\right),$$

$$S_{f,y} = -\frac{\partial}{\partial x}\left(z_b + h + \frac{v\sqrt{u^2 + v^2}}{2g}\right), \tag{4.3}$$

where $S_{f,x}$ and $S_{f,y}$ are the *x*- and *y*- directional energy slope components; z_b is the bed elevation; g is the acceleration due to gravity; and, finally, S_f is calculated as $\sqrt{{S_{f,x}}^2 + {S_{f,y}}^2}$. The terms in the above friction slope equations represent gravitational, pressure, and inertial forces, respectively. Introducing a new variable, $E_x = z_b + h + \frac{u\sqrt{u^2+v^2}}{2g}$, its gradient can be calculated numerically from the following equation:

$$\int_{\mathrm{A}} \frac{\partial E_x}{\partial x} dA = \frac{\partial E_x}{\partial x} A \,, \tag{4.4}$$

under the assumption that the gradient of E_x is constant inside a triangle cell with an area of *A*. When Green's theorem is applied in order to transform the area integral on the left-hand side of equation (4.4) to a line integral, E_x is integrated along the cell boundaries. Thus, the *x*-directional friction slope becomes

$$\frac{\partial E_x}{\partial x} = \frac{(y_2 - y_0)\left(E_{x,1} - E_{x,0}\right) - (y_1 - y_0)\left(E_{x,2} - E_{x,0}\right)}{(\mathrm{y_2 - y_0})(\mathrm{x_1 - x_0}) - (\mathrm{y_1 - y_0})(\mathrm{x_2 - x_0})} \,, \tag{4.5}$$

where the subscripts "0", "1", and "2" are used to denote the three counter-clockwise vertices of a triangle cell [*Kim et al.*, 2012b]. The *y* - directional component is obtained in a similar fashion. Once the numerical model solves the mass and momentum equations of the flow, one can obtain the primary flow variables such as *h*, *u*, and *v* at any point of the flow domain. Then, the upscaled value of *n* for the entire domain can be computed by using the mean values of *h*, *V*, and S_f obtained at steady state:

$$n_t = \frac{\bar{h}^{2/3}\bar{S_f}^{1/2}}{\bar{V}} \tag{4.6}$$

where n_t is the upscaled value of n; $\bar{h}$ and $\overline{S_f}$ are the means of depth and friction slope for all triangle cells of the flow domain; $\bar{V}$ is calculated by dividing the unit discharge (q) by the mean depth ($\bar{h}$). This approach relies on an assumption that the representative value of S_f for the whole domain can be determined by averaging the corresponding local values. Since $\overline{S_f}$ avoids negative values because of the square root operation on the sum of its squared *x*- and *y*- components, it does not loose information on the variability of local friction slopes; this would be the case if a simple arithmetic averaging of negative and positive values were carried out.

4.4 Simulation results

4.4.1 Overall characterization of flow variables

Flow characteristics are first analyzed. Figure 4.2 shows the spatial distribution of different flow variables such as depth, velocity, and friction slope at steady-state for the case of S = 30%, n_b = 0.02, and Q = 0.001 m^3/s. The spatial distributions for the cases of bare soil and vegetated soil with V_f = 30% are compared. In the case of bare soil with these fairly large S and Q, the flow approaches a uniform state with a depth of 0.0022 m and a velocity of 0.455 m/s. These numerical values are also consistent with the results of the analytical steady uniform equation for the "turbulent rough flow", one of the four principal types of overland flow [*Julien and Simons*, 1985]. Specifically, Manning's n_b of 0.02 corresponds to a roughness height of *mm* to *cm* scale (the mean diameter of sediment). This roughness height is much larger than the thickness of the boundary sublayer, $11.6\mu/\rho\sqrt{ghS_f}$, and equal to 0.000144 m, which indicates that the flow regime of this case is "turbulent rough". Furthermore, the effects of inertia and pressure terms are minimized and the bottom friction is balanced by the gravitational force. The

friction slope under these conditions is thus almost the same as the plane slope, which is equal to 0.3.

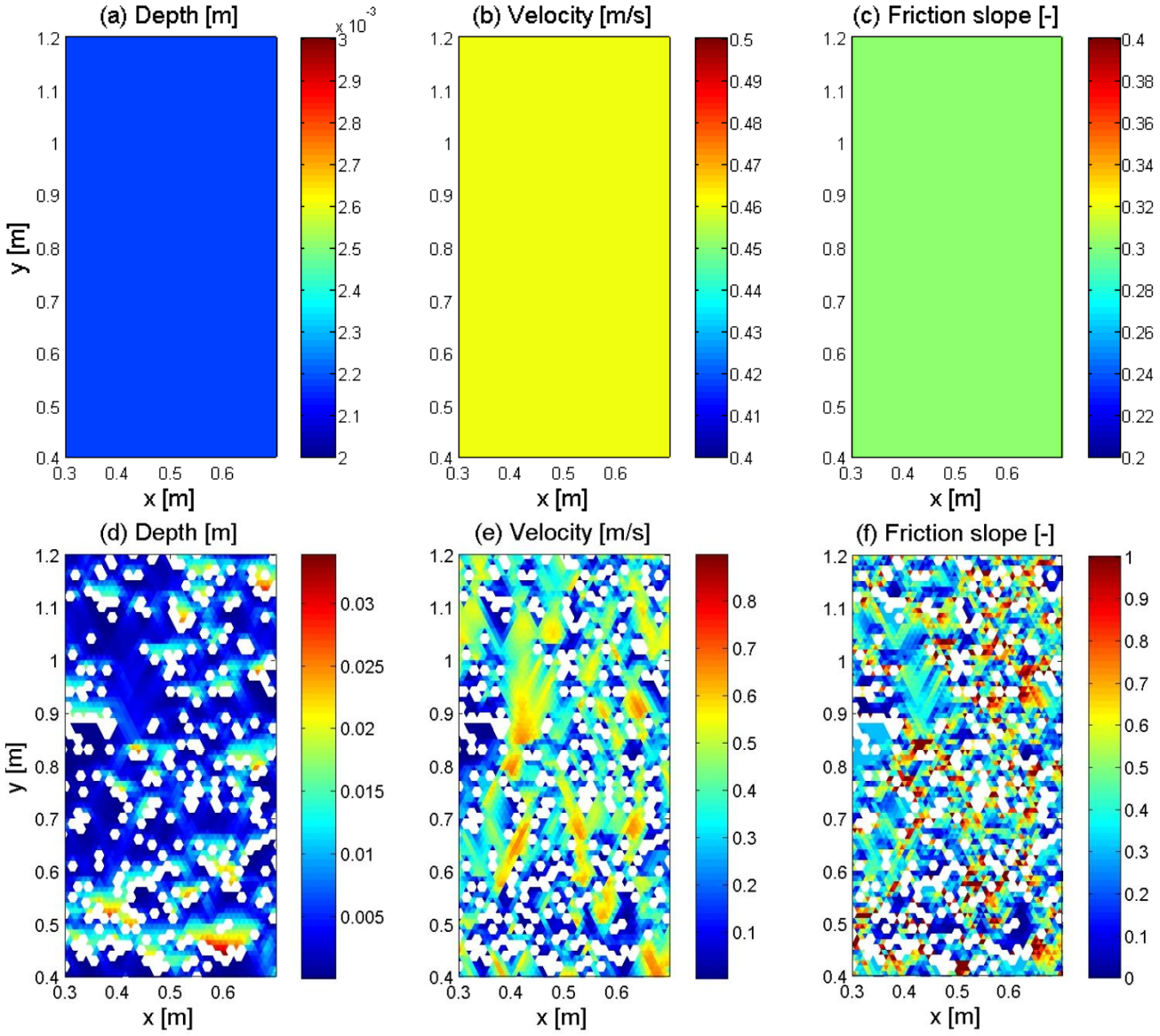

Figure 4.2: An illustration of the spatial distribution of flow variables at steady-state for the case of domain slope of 0.3 and Q = 0.001 m^3/s. The plots (a) to (c) illustrate the distributions for a bare soil surface with n_b =0.02; the plots (d) to (f) show the distributions for the case of vegetation with the stem cover fraction of 30% (n_b=0.02). Plots (a) and (d) illustrate the flow depth [m]; (b) and (e) the velocity magnitude [m/s]; and (c) and (f) the friction slope [-]. The white color refers to vegetation stems; hydraulic variables are not simulated within these areas due to the imposed boundary condition of an impermeable, rigid, infinitely-long wall.

If the flow occurs within a region with many protruding obstacles (i.e., impermeable, rigid stems of vegetation), the flow is faster between stems and retarded behind them. The flow depth and velocity vary appreciably over short distances (Figure 4.2, the bottom panel). The "spots" of white color in Figure 4.2 (the bottom panel) represent stem cells of vegetation and signify the imposed no-flow condition. The features of converging, accelerating currents between stems, and the formation of backwater upstream of the stems are well illustrated in Figure 4.2.

The friction slope S_f, a key variable for estimating the roughness coefficient, is further investigated in terms of its relation to flow variables in the vegetated case. A qualitative interpretation of Figure 4.2 indicates that backwater regions have relatively larger depths, lower velocities, and smaller friction slopes, while the converging areas have higher velocities and friction slopes. In order to verify the general applicability of such statements, three distinct intervals of S_f magnitude are considered: small (S_f < 0.233), medium (0.233 ≤ S_f < 0.548), and high (S_f ≥ 0.548). The two critical values, i.e., 0.233 and 0.548, represent the first and the fourth quartiles of the S_f spatial variability. This implies that half of the S_f magnitudes fall within the medium interval, while 25% of magnitudes fall within the intervals corresponding to small and high S_f. Statistical metrics, such as the means of h, V, and S_f and their mutual correlation coefficients, are calculated for the entire domain (the cases of V_f = 0 and V_f = 0.3), and the three sub-intervals of S_f (the case of V_f = 0.3). The results are shown in Table 4.1.

Table 4.1: The mean values and the correlation coefficients for the entire domain for the cases of both $V_f = 0$ and $V_f = 0.3$. Only a subset of cases with small, medium, and high friction slopes were selected for the case of $V_f = 0.3$. (Corr=Correlation)

	$V_f = 0$	$V_f = 0.3$			
	all S_f	all S_f	$S_f < 0.233$	$0.233 \leq S_f < 0.548$	$S_f \geq 0.548$
mean(h)	0.0022	0.0055	0.0067	0.0044	0.0064
mean(V)	0.4602	0.3293	0.2463	0.3383	0.3942
mean(S_f)	0.3000	0.4174	0.1325	0.3769	0.7830
Corr(S_f,h)	-	0.0821	-0.2942	0.0582	0.3691
Corr(S_f,V)	-	0.2969	0.4038	0.1941	-0.0639

The areas of the domain with locally small values of S_f are in good accordance with the above conceptual partition. For example, backwater regions have larger flow depths and smaller velocities, as compared to the mean conditions in the flow domain. However, using the values of h, V, and S_f (corresponding to the interval of small S_f values), the correlation coefficient between h and S_f is -0.294, while between V and S_f, it is 0.404. Such a correlation is not sufficiently high to allow any general conclusion.

The flow areas with high S_f correspond to flow convergence and generally exhibit high flow velocities. The mean velocity for such areas is 0.3942 m/s, which is about 20% larger than the mean velocity for the entire domain (0.3293 m/s). A conceptual dependence between the state of flow and S_f is that flow retardation behind obstacles makes S_f smaller, while flow acceleration in constricted areas between obstacles makes it larger, as compared to the case with a bare plane. For all domains, there is no statistically significant correlation of S_f with the variables of h and Fr (e.g., correlation coefficients between S_f and h or Fr are 0.082 and 0.14),

while weak correlation with the variables of *V* and *Re* (e.g., correlation coefficients between S_f and *V* or *Re* are 0.29 and 0.37) for vegetated hillslopes. These weak correlations make the generalization or prediction of the degree of high variability of S_f at any internal point difficult and unfeasible. Therefore, the variability should be numerically modeled with a relevant detail in estimating roughness coefficients for problems in which the value of S_f is necessarily needed for computations and plays a crucial role.

4.4.2 Results for the method of Equivalent Roughness Surface

Hydrographs at the downstream boundary of the domain were obtained for 324 simulations (as summarized in Table 4.2). They represent all possible permutations among 6 vegetation covers, 6 bed slopes, 3 base Manning coefficients, and 3 upstream boundary inflow rates. Figure 4.3 shows 18 different hydrographs for fixed *S* and n_b. Since overall trends shown in Figure 4.3 look similar to the trends in the other 17 plots (not shown) with different *S* and n_b, only one plot (Figure 4.3) out of 18 obtained plots is illustrated. The figure shows the hydrographs for six different values of V_f and three values of *Q*. The flow series with the same peak discharge correspond to the cases with the same *Q*; the series with larger times of concentration correspond to the cases with higher V_f values. Based on these simulation results, it can be concluded that as n_b and V_f increase, and *Q* and *S* decrease, flow retardation becomes more pronounced, which results in higher values of t_c.

Table 4.2: A summary of the simulation cases. Each characteristic was permutated with all other variables. The total number of simulations is 324.

Vegetation cover fraction [-]	Domain slope [-]	Manning coefficient	Inflow rate [m^3/s]	Rainfall [mm/hr]
0	0.1	0.02	0.0001	10
0.05	0.3	0.03	0.0005	
0.1	0.5	0.04	0.001	
0.2	0.7			
0.3	0.9			
0.5	1.1			

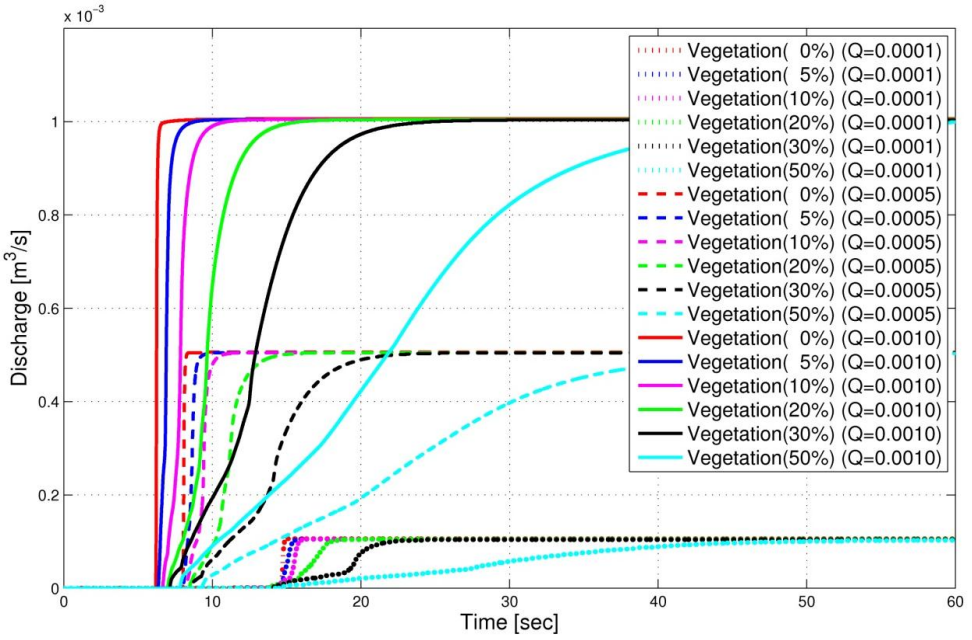

Figure 4.3: Simulated hydrographs for the cases with different vegetation covers (0 to 50 %) for the plane slope of 10 % and the base Manning's coefficient of 0.02. The highest, middle, and lowest groups of hydrographs correspond to the cases of different inflow rates.

In order to obtain a relationship between t_c and n for cases without vegetation, 144 additional simulations were carried out. These are summarized in Table 4.3. Hydrographs for the cases of S = 10% are shown in Figure 4.4, which includes 33 time series corresponding to 11 different n and 3 different Q values. It is evident that the flow is delayed and peaks occur later as the bed surface becomes rougher. The objective of these additional simulations was to develop relationships between t_c and n for exactly the same plane slopes and flow rates as those used in the scenarios with vegetation cover. For example, Figure 4.5 shows the computed (using the criteria of equation (4.1)) t_c's for two bed slopes (10% and 110%) and different inflow rates. These relationships exhibit a positive, non-linear dependence of t_c on n. Once t_c is obtained for any given case with vegetation cover, an equivalent n_t can be estimated from the t_c -n relationships obtained for bare soil plane, such as those illustrated in Figure 4.5.

Table 4.3: A summary of simulation cases used in comparisons with the equivalent roughness surface method. The total number of simulations is 144.

Vegetation cover fraction [-]	Domain slope [-]	Manning coefficient	Inflow rate [m^3/s]	Rainfall [mm/hr]
0	0.1	0.05	0.0001	10
	0.3	0.06	0.0005	
	0.5	0.07	0.001	
	0.7	0.08		
	0.9	0.09		
	1.1	0.10		
		0.15		
		0.30		

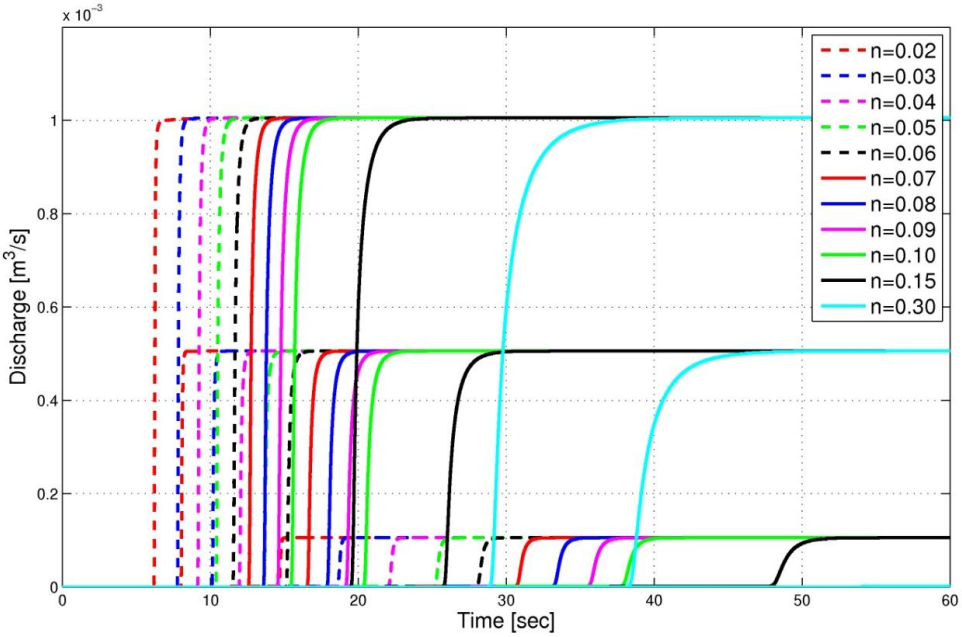

Figure 4.4: Simulated hydrographs for the cases without vegetation for the plane slope of 10 %. The highest, middle, and lowest groups correspond to the cases of different inflow rates of 0.001, 0.0005, and 0.0001 m^3/s, respectively.

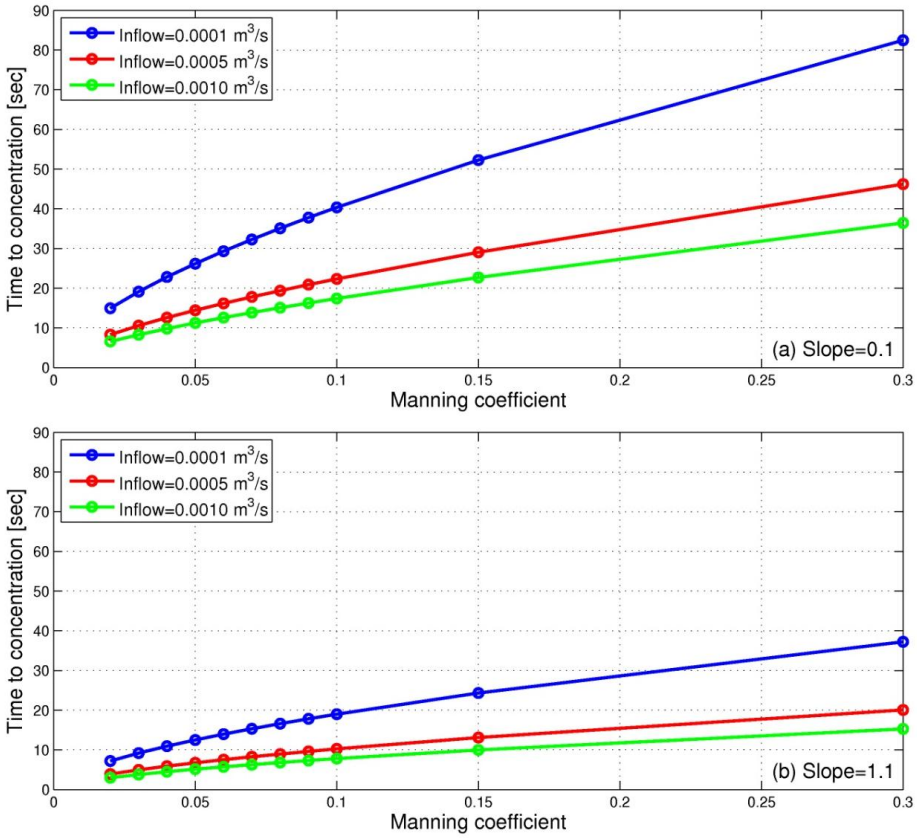

Figure 4.5: The time of concentration as a function of Manning's coefficient for the plane slopes of 10 % (a) and 110 % (b). The time of concentration was obtained using the Equivalent Roughness Surface method.

4.4.3 Results for the method of Equivalent Friction Slope

The method of Equivalent Friction Slope averages spatially-distributed flow depths and friction slopes and the upscaled, domain-representative Manning coefficient is calculated using equation (4.6). In order to investigate the difference between the upscaled coefficients obtained with the two methods, i.e., the Equivalent Roughness Surface and Equivalent Friction Slope methods, the estimates are compared in Figure 4.6. The figure indicates that both methods yield

consistent estimates of n_t with a coefficient of determination R^2 = 0.973. Values of n_t obtained with the Equivalent Friction Slope method are used for further analysis.

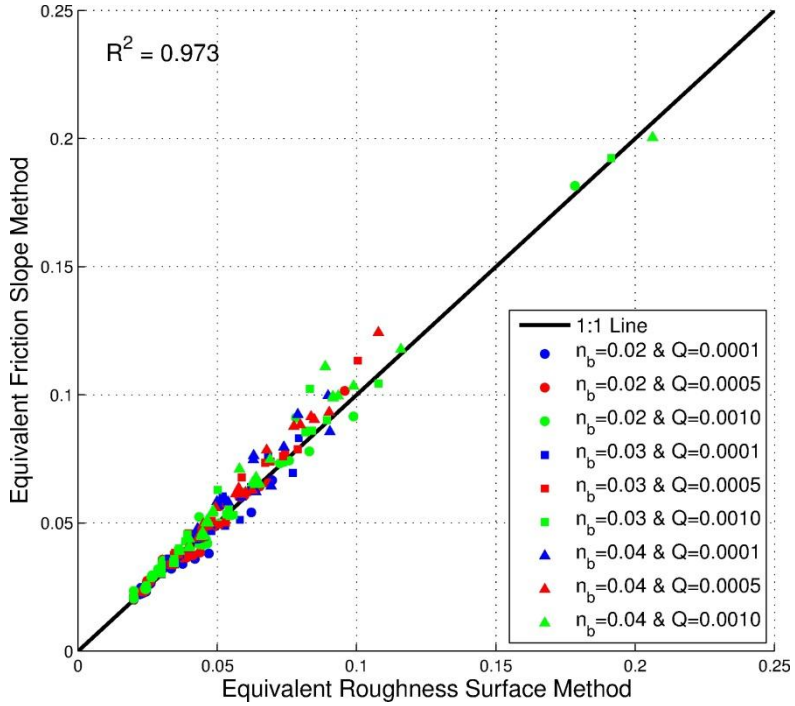

Figure 4.6: A comparison of the upscaled Manning's coefficients obtained with the hydrograph and dynamic wave analyses (Section 4.4.3). The corresponding coefficient of determination is 0.973. All simulation cases described in Table 4.2 are used.

Figure 4.7 shows n_t dependencies obtained with the Equivalent Friction Slope for all simulations summarized in Table 4.2. The figure and the table reflect variations of four independent variables: V_f, S, Q, and n_b. Figure 4.7 illustrates the general trends of effects on n_t of all independent variables used in the study. For example, the effect of V_f results in a positive dependence that is straightforward to discern. However, other effects, such as those of Q or n_b,

cannot be as clearly discerned in Figure 4.7. A discussion of the effects of these independent variables on n_t is presented in section 4.5.

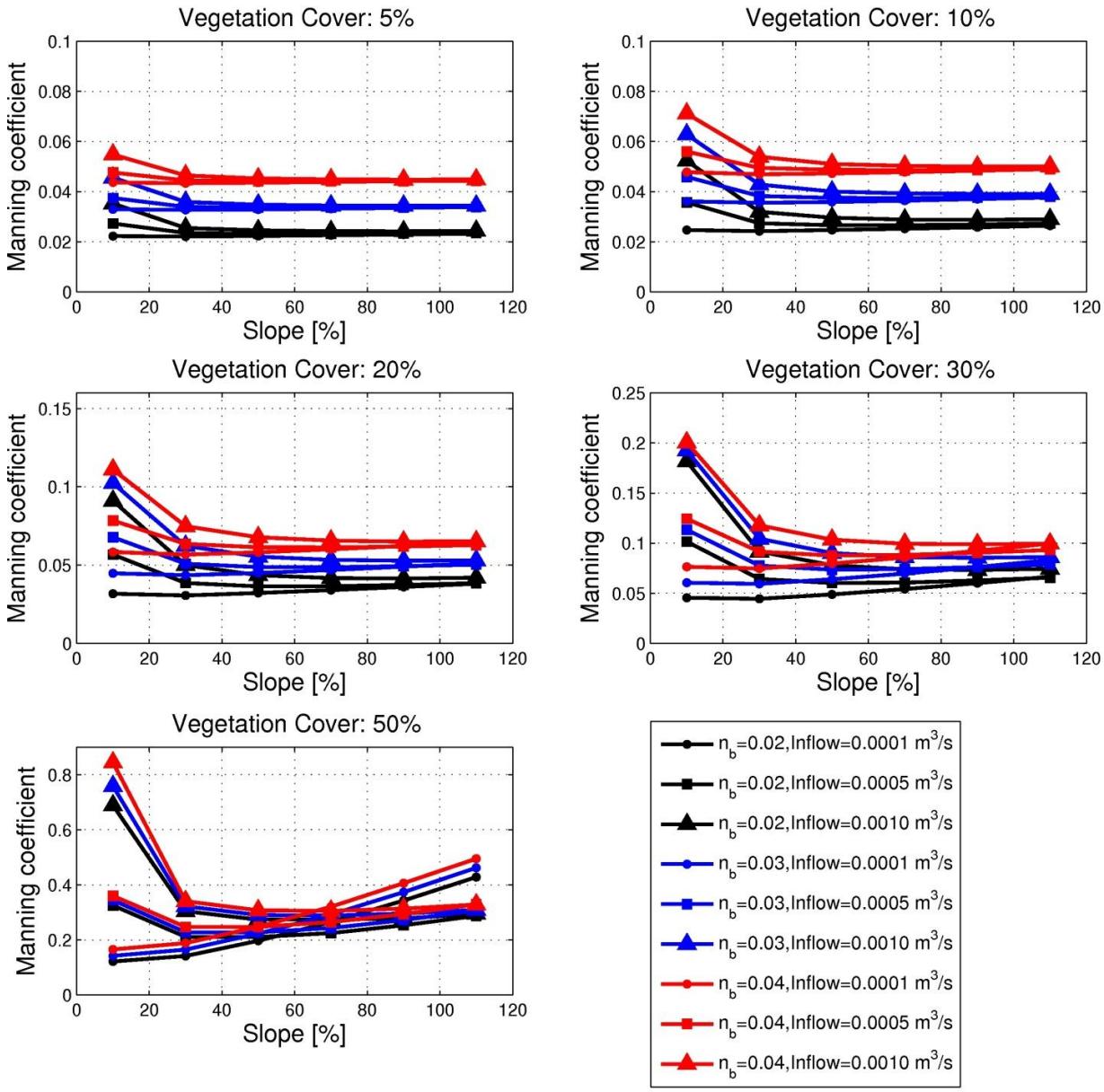

Figure 4.7: Upscaled Manning's coefficient values (n_t) obtained with the equivalent friction slope method for different vegetation fractions, slopes, inflow rates, and base Manning coefficients corresponding to the cases summarized in Table 4.2. Among the total 324 scenarios, the results of cases with non-zero vegetation cover (270 scenarios in total) are shown.

4.4.4 Predictive equations for n_t

The values of n_t obtained from the Equivalent Friction Slope are used to develop predictive equations for n_t. The relevant predictive variables and their corresponding coefficients are determined by using a dimensional analysis and a multiple linear regression.

Previous research has revealed that resistance to overland flow is influenced by many factors. Among them are the Reynolds number, the Froude number, flow depth, vegetation cover fraction, and the characteristics of roughness elements such as size, shape, spacing and pattern [*Abrahams and Parsons*, 1994]. The effect of the inflow rate on the resistance is taken into account by the Reynolds number. In this study, n_t is assumed to be a function of the following variables:

$$n_t = f\left(\rho, \mu, g, \bar{h}, \bar{V}, S, V_f, n_b\right), \tag{4.7}$$

where ρ is the density of water [ML^{-3}]; μ is the dynamic viscosity of water [$ML^{-1}T^{-1}$]; g is the acceleration due to gravity [LT^{-2}]. The Buckingham Π-theorem is used to select ρ, $\bar{h}$, and $\bar{V}$ since these are repeating variables. The relevant dimensional parameters in the functional relation are

$$n_t - n_b = f\left(\frac{\bar{h}\bar{V}}{\nu}, \frac{\bar{V}}{\sqrt{g\bar{h}}}, S, V_f\right). \tag{4.8}$$

Since this predictive equation has been previously developed in the form of a power function [*S X Hu and Abrahams*, 2006], equation (4.8) can be expressed in the following form:

$$n_t - n_b = a\left(\frac{4\bar{h}\bar{V}}{\nu}\right)^b \left(\frac{\bar{V}}{\sqrt{g\bar{h}}}\right)^c (S)^d \left(V_f\right)^e. \tag{4.9}$$

The term on the left side of this equation expresses the effect of vegetation on the total resistance coefficient, i.e., it accounts for the contributions of both the form and wave resistances. The first term on the right side is multiplied by 4 to represent the Reynolds number and the second term represents the Froude number. The domain-averaged values of depth and velocity are used in the regression. The kinematic viscosity ν is used as a constant with the value of 10^{-6} [m^2/s], which corresponds to the temperature of water of about 20 ℃. The evaluated coefficients *a*, *b*, *c*, *d*, and *e* are 0.0264, 0.2794, -0.9859, 0.3060, and 0.9591, respectively, with R^2=0.976 of the log-linear form. Note that this regression equation was developed for the cases used in the simulations that exhibit a wide range of possible scenarios of overland flow, i.e., $V_f \leq 0.5,\ 0.1 \leq S \leq 1.1$, and $0.0001 \leq Q \leq 0.001$.

As opposed to using all four dimensionless variables in Eq. (4.9), the consideration of only three dimensionless variables at a time can show the relative importance of the omitted variable in the variation of $n_t - n_b$. This procedure indicates that the exclusion of each variable *Re*, *Fr*, *S*, and V_f reduces the explained variation by 3.2, 7.2, 1.5, and 35.7%, respectively. Such a result implies that V_f is the most dominant parameter in the determination of $n_t - n_b$. Thus, in an effort of simplification, if one chooses only V_f to be present in the regression equation, the resulting form will be

$$n_t - n_b = 0.5172\left(V_f\right)^{1.7087}, \tag{4.10}$$

with R^2=0.873 (for the log-linear form), i.e., log (V_f) can account for about 87% variation in $\log(n_t - n_b)$. Alternatively, if the regression equation is represented with an exponential function, the equation is

$$n_t - n_b = 0.0033e^{8.8855V_f}\,, \tag{4.11}$$

with R^2=0.918 (for the log-linear form), which signifies a slightly better predictive power than Eq. (4.10).

A number of scenarios (Table 4.4) for the highest inflow rate, Q = 0.01 m^3/s, were introduced. The objective was to further investigate the effect of partially submerged obstacles on resistance for flow conditions that represent an extreme range for natural hillslopes, i.e., highly infrequent. Another set of regression equations including simulation data for all of the cases summarized in Tables 4.2 and 4.4 are reported. Adding simulation data for Q = 0.01 m^3/s to the regression set, Eq. (4.9) becomes

$$n_t - n_b = 0.0145\left(\frac{4\bar{h}\bar{V}}{\nu}\right)^{0.3504}\left(\frac{\bar{V}}{\sqrt{g\bar{h}}}\right)^{-1.0293}(S)^{0.3238}\left(V_f\right)^{0.8925}\,, \tag{4.12}$$

with R^2=0.969 (for the log-linear form) and has the range of applicability: $V_f \leq 0.5,\ 0.1 \leq S \leq 1.1$, and $0.0001 \leq Q \leq 0.01$ m^3/s. Additionally, Eq. (4.11) becomes

$$n_t - n_b = 0.0039e^{8.6799V_f}\,, \tag{4.13}$$

with R^2=0.831 (for the log-linear form). The regression equations (4.11) and (4.13) confirm that vegetation exerts a predominant effect on the roughness coefficient; therefore, the derived equations can be useful for estimating the degree of vegetation effects, if information on other significant variables is not readily available.

Table 4.4: A summary of simulation cases with high inflow rates. The total number of simulations is 30.

Vegetation cover fraction [-]	Domain Slope [-]	Manning's coefficient	Inflow rate [m^3/s]	Rainfall [mm/hr]
0.05	0.1	0.04	0.01	10
0.1	0.3			
0.2	0.5			
0.3	0.7			
0.5	0.9			
	1.1			

4.4.5 Verification of the regression equation

Another set of simulation was carried out to verify the proposed regression equation for flow and domain conditions that were not used in the derivation of Eqs. (4.9) and (4.12). The cases used in this verification test are described in Table 4.5. Specifically, they consist of 12 scenarios: V_f is set to 0.25, n_b is equal to 0.025, six different bed slopes range from 0.1 to 1.1, and two inflow rates of 0.0003 and 0.0007 m^3/s are used. The values are within the ranges of applicability of the regression equation (section 4.4.4). The upscaled Manning coefficients are calculated by using both the Equivalent Friction Slope and through the regression equations (4.9), (4.11), (4.12) and (4.13). The coefficients are consequently compared to verify the appropriateness of the derived equations, as shown in Figure 4.8. As seen, the differences between the coefficients obtained with the Equivalent Friction Slope and the coefficients

calculated from Eq. (4.9) and (4.12) are fairly minor. However, there are non-negligible deviations for the cases of small domain slope, when Eqs. (4.11) and (4.13) are applied. This implies that for these cases, the inclusion of only V_f is not sufficient to predict the upscaled roughness coefficients. Generally, one is cautioned against the use of Eqs. (4.11) and (4.13) for situations when other variables become significant (a relevant discussion is also provided in section 4.5.1). On the other hand, the developed regression equations (4.9) and (4.12) that include all of the variables can become a useful tool for estimating roughness of vegetated surfaces, once the primary flow variables are known. However, note that equations (4.9) and (4.12) should be used with caution for variables that are beyond the range of hydraulic, geometric, and bed conditions described in Tables 4.2 and 4.4.

Table 4.5: A summary of simulation cases used for the verification of the regression equation. The total number of simulations is 12.

Vegetation cover fraction [-]	Domain Slope [-]	Manning's coefficient	Inflow rate [m^3/s]	Rainfall [mm/hr]
0.25	0.1	0.025	0.0003	10
	0.3		0.0007	
	0.5			
	0.7			
	0.9			
	1.1			

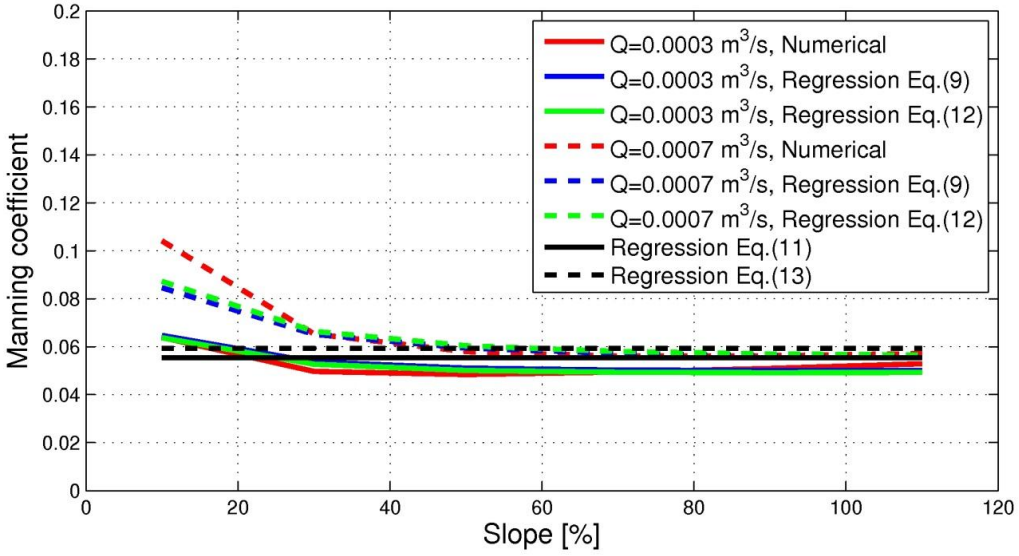

Figure 4.8: A comparison of the upscaled Manning coefficient obtained with the equivalent friction slope and the regression equations (4.9), (4.11), (4.12), and (4.13). Vegetation cover fraction of 25 % and the base Manning's coefficient of 0.025 were used for this verification set.

4.4.6 Comparison of results with previous studies

Data obtained in previous laboratory and field conditions are used in this study to provide a comprehensive validation set for the simulated effects of large-scale roughness elements. Data from five studies [*Abrahams et al.*, 1986; *Rauws*, 1988; *Gilley et al.*, 1992a; *Bunte and Poesen*, 1993; *S X Hu and Abrahams*, 2006] are summarized in Table 4.6.

Table 4.6: A summary of experimental studies used in the comparison. Notation "lab" is used for data obtained in laboratory conditions; "field" is used to denote field studies.

Publication	Macro-scale element [cm]	Micro-scale element [μm]	S [%]	Re [-]	Fr [-]	V_f [%]	No. of data points reported/used
Abrahams et al. (1986)	stones: 0.68-4.13 vegetation	loam: 500 (*assumed*)	9.2-68.7	843-4378	0.24-2.64	30.6-54.1	108/108 (field)
Bunte & Poesen (1993)	pebble: 0.86-2.10	silica flour: 90	2.2	923-5615	0.25-1.12	0-17	12/12 (lab)
Gilley et al. (1992)	gravel: 2.54-3.81 cobble: 12.7-25.4	fiberglass: 16 (*assumed*)	1.35	500-14889	0.13-1.46	4-32	100/44 (lab)
Hu & Abrahams (2006)	cylinder: 2.0 & 3.1	aluminum	11.4	1397-28380	0.51-2.81	2-24	68/68 (lab)
Rauws (1988)	hemisphere: 1.6	silica flour: 240 sand: 1180	1.7-20.8	122-2988	0.97-2.76	3.5	204/102 (lab)

In order to ensure the most proper use of the data, and to represent the same flow situations in this study, a number of assumptions had to be made. First, the effective values of V_f were re-computed for data reported in *Bunte and Poesen* [1993] and *Abrahams et al.* [1986] using auxiliary information reported in these studies. Specifically, in the former study, rock fragments, regardless of submerged conditions, were reported to range from 0 to 99% but some of the rocks were submerged by the flow, and thus the fragments did not contribute to V_f. This study specified the effective widths by considering only portions of protruding rocks; thus, we used the fraction of protruding rocks to obtain an effective fraction of V_f, which resulted in the V_f range of 0-17%. These values of V_f are used for computation with the regression Eq. (4.12) and

the results are shown in Figure 4.9. The uncertainty bounds are also shown, which indicate 10% of variability for the used V_f.

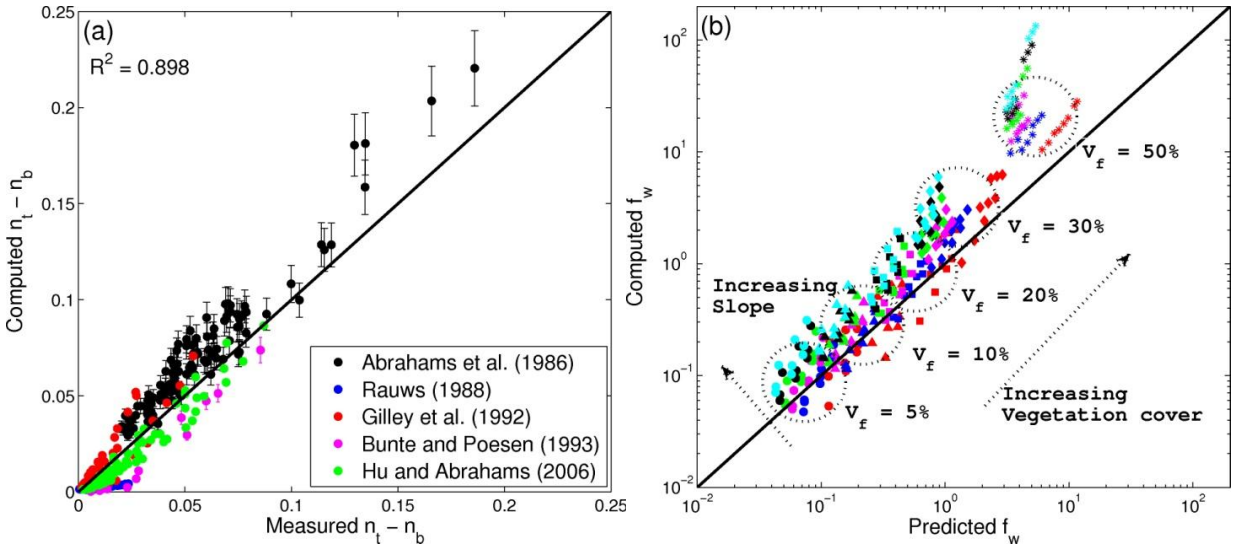

Figure 4.9: Plot (a): A comparison of $n_t - n_b$ values computed from the regression Eq. (4.12) (y-axis) and obtained from the measured data (x-axis) reported in five different studies (R^2 = 0.90). Plot (b): A comparison of the computed f_w from Eq. (4.15) and predicted f_w from Eq. (4.14). In plot (b), the coefficient of determination R^2 = 0.72 in log-transformed units for all of the values; R^2 = 0.90 in log-transformed units for data corresponding to S = 0.1 and 0.3. The circle, triangle, square, and diamond symbols represent the cases with V_f = 5, 10, 20, 30, and 50 %, respectively. The red, blue, magenta, green, black, and cyan symbols represent the cases with S = 0.1, 0.3, 0.5, 0.7, 0.9, and 1.1, respectively. All of the 270 scenarios (excluding the 54 scenarios with zero vegetation fraction) summarized in Table 4.2 were used.

Further, *Abrahams et al.* [1986] did not provide any detailed information on submerged gravel fractions by specifying only the fractions greater than 2 mm. Therefore, an assumption was made that only half of the gravel fraction in *Abrahams et al.* [1986] could be considered as large elements (i.e., partially-submerged condition). The determination of the effective V_f was done through a summation of fraction for the two types of partially-submerged elements: the reported vegetation fraction and half of the total gravel fraction. As a result, V_f changed from the

originally reported range of 56.5-88.2% to 30.6-54.1%. Choosing the 50% ratio in order to get an effective V_f is an unavoidable assumption and thus it influences the computation of the resistance coefficient. The sensitivity of estimates to this ratio is shown in the left plot of Figure 4.9: the black dots correspond to the ratio of 50%, while the lower and upper bounds correspond to the ratios of 40 and 60%, respectively. It is found that the effective rock ratio between 30% and 60% shows a reasonable match with the predicted values with limited deviations from the one-to-one regression line.

Further, *Gilley et al.* [1992b) specified flow depths that were larger than the dimension of the gravel material; consequently, 36 data points for the gravel bed and 20 data points for the cobble bed are excluded to avoid the submerged condition.

In the study by *Rauws* [1988], the depth range of 0.5 to 1.5 mm for the sub-experiment performed over the sand bed has a similar order of magnitude as the dimensions of the micro-scale sand bed (1.18 mm). In conditions of shallow flow over the sand bed, the effect of the surface resistance induced by the sand bed may be much larger than that of the form/wave resistances induced by the macro-scale roughness (only 3.5% of V_f), and thus data of the sand bed experiment are also excluded from this analysis.

The objective of this study is to investigate the effects of large-scale elements on the total resistance to flow. One way to carry out an analysis is to explore the fraction of the total resistance (n_t) in reference to the resistance caused by small-scale elements, i.e., with respect to the surface resistance n_b. The left plot in Figure 4.9 illustrates a comparison of $n_t - n_b$ computed from the regression Eq. (4.12) and obtained from the reported data. It should be noted that in all of the experimental studies, the value of n_t was given, but the value of n_b was not

provided in most studies, except for the work of *Hu and Abrahams* [2006]. Thus, the surface resistance was derived based on auxiliary information provided for the small-scale roughness elements. In order to derive reasonable approximations, the Strickler formula [*Chow*, 1959] $n_b = 0.041{D_r}^{1/6}$ is used, where D_r is the diameter of roughness elements in meters. We assumed the diameter of micro-scale elements: 500 μm for loam in *Abrahams et al.* [1986] and 16 μm for fiberglass in *Gilley et al.* [1992]. We further found that the choice of the size of roughness elements does not influence the determination of n_b appreciably. Note that even though several assumptions are made in the predicted $n_t - n_b$, the overall deviations in this plot are relatively minor (R^2 = 0.898).

A comparison of data points computed based on the results of this study with the estimates of the prognostic equation proposed by *Hu and Abrahams* [2006] is also presented. Specifically, these authors computed flow resistance from their experimental data and proposed a wave resistance (f_w) formula for a fixed or mobile bed. The experiments were performed on a flume that had the following characteristics: 0.5 m wide, 4.9 m long, slope of 0.114, covered with cylinders with the diameters of 0.02 or 0.031 m (served as large-scale roughness elements). The concentrations of cylinders ranged from 2 to 24%, and flows ranged from 0.000185 to 0.0034 m^3/s. *Hu and Abrahams* [2006] first calculated the total roughness (f_t), the surface roughness (f_s), and the form roughness (f_f); they subsequently obtained f_w by subtracting f_s and f_f from f_t. They presented a regression equation for a fixed bed as follows

$$f_w = 79.38\left(\frac{\bar{h}}{D_r}\right)^{0.25} Fr^{-0.5}{R_r}^{-0.33}V_f \,, \tag{4.14}$$

where R_r is the roughness Reynolds number, $R_r = VD_r/\nu$.

Using the flow variables obtained in this study, we can compute f_w. Specifically, since the effects of resistance due to rainfall and mobile bed on the total resistance are neglected, the latter can be divided into three components assumed to be additive. Therefore, f_w is calculated with the following equation:

$$f_w = f_t - f_s - f_f \,, \tag{4.15}$$

where the above three components on the right side of the equation are obtained from hydraulic results based on the numerical simulations: $f_t = 8g\bar{h}\bar{S}_f/\bar{V}^2$; f_s can be substituted with f_t calculated for the case of a domain without vegetation; and f_f is calculated by using the modified drag model [*Lawrence*, 2000] for the case of partial inundation:

$$f_f = \frac{2f_v C_D \boldsymbol{A}(\bar{h}/k)}{[1 - f_v \boldsymbol{V}(\bar{h}/k)]^3} \,, \tag{4.16}$$

where $\boldsymbol{A}(\bar{h}/k)$ accounts for the change in the frontal area with inundation, $\boldsymbol{V}(\bar{h}/k)$ accounts for the occluded volume of the roughness elements, and C_D is the drag coefficient equal to 1.2, which is the value used by *Hu and Abrahams* [2006]. The above formulation was originally developed for roughness elements with a hemispheric shape. Thus, if we apply this for the elements with the hexagonal column shape used in this study, we obtain $\boldsymbol{A}(\bar{h}/k) = 2D_r\bar{h}/A_r$ and $\boldsymbol{V}(\bar{h}/k) = 1$. Then, equation (4.16) becomes:

$$f_f = \frac{4D_r V_f C_D \bar{h}}{A_r[1 - V_f]^3} \tag{4.17}$$

where A_r is the area of the roughness element with the hexagonal shape. In order to verify the simulated results, we compared f_w computed from Eq. (4.15) (the y-axis in Figure 4.9b) with f_w

predicted from Eq. (4.14) using the characteristics of flow scenarios of this study (the *x*-axis in Figure 4.9b).

As Figure 4.9b shows, the results of applying Eq. (4.15) for $V_f \leq 0.3$ and $0.1 \leq S \leq 0.3$ are fairly consistent with the results obtained with Eq. (4.14) (R^2=0.90 in log-transformed units), while the results outside of these ranges are not, especially for the data with larger S and $V_f = 0.5$. This can be partially attributed to the fact that the predictive equation (4.14) was derived for the conditions of $0.02 \leq V_f \leq 0.24$ and $S = 0.114$, while this numerical study used a much larger range of slope magnitudes and vegetation cover fractions. The plot exhibits two discernible characteristics: first, an increasing vegetation cover implies an increase in wave resistance (a straightforward and consistent conclusion following from Eq. (4.14)); second, the higher the domain slope, the higher the differences between the compared f_w values. The effect of slope was not included in Eq. (4.14) developed by *Hu and Abrahams* [2006] because they used a fixed domain slope, but, in general, it should be accounted for in the computation of f_w.

4.5 Discussion

4.5.1 Effects of vegetation cover fraction

It is apparent from the simulation results that as V_f increases, n_t also grows. This statement is also supported by the high values of the determination coefficient resulting from the estimates obtained with Eqs. (4.11) and (4.13). Since in general hillslope flows have relatively small discharges, (e.g., see *Abrahams et al.* [1986] for Walnut Gulch Experimental Watershed), the results in cases presented in Table 4.2 are used in the following analysis. Figure 4.10 shows

54 ensemble lines that correspond to 6 domain slopes, 3 inflow rates, and 3 bed roughness coefficients. If the mean and the standard deviation of these ensemble lines are computed, the absolute contributions of protruding vegetation stems to n_t are as high as 0.0047, 0.0098, 0.0242, 0.0563, and 0.2787 for 5, 10, 20, 30, and 50% vegetation cover fractions, respectively (see also Table 4.7). The effect of V_f is generally insignificant for vegetation covers less than 10% but becomes more pronounced for higher fractions. This observation is also consistent with the results of *Hirsch* [1996]. Furthermore, an increase in $n_t - n_b$ for V_f less than 20% is well aligned with a thesis of *Einstein and Banks* [1950] and *Cowan* [1956] who proposed that an effect of isolated roughness elements without mutual interference should be additive; or, in other words, $n_t - n_b$ should assume a linear growth. Conversely, a non-linear increase of $n_t - n_b$ in the interval of V_f from 30 to 50% is also observed. It is argued that a large portion of roughness elements forms clumps of obstacles, where a mutual interference of individual stem effects can be observed. This leads to a relatively higher retardation of the flow, as compared to the case with nearly no interference for V_f less than 20%.

Table 4.7 The means and the standard deviations of the difference between the upscaled and base Manning's coefficient $\boldsymbol{n_t - n_b}$. Results for all simulations are presented. (SD=Standard deviation)

n_b	Statistics	V_f =0	V_f =0.05	V_f =0.1	V_f =0.2	V_f =0.3	V_f =0.5
0.02	Mean	0.0006	0.0043	0.0090	0.0220	0.0526	0.2645
	SD	0.0008	0.0030	0.0065	0.0138	0.0309	0.1236
0.03	Mean	0.0005	0.0047	0.0098	0.0241	0.0561	0.2780
	SD	0.0009	0.0030	0.0063	0.0134	0.0299	0.1344
0.04	Mean	0.0005	0.0052	0.0108	0.0266	0.0601	0.2935
	SD	0.0009	0.0026	0.0056	0.0124	0.0281	0.1481
All	Mean	0.0005	0.0047	0.0098	0.0242	0.0563	0.2787
	SD	0.0008	0.0028	0.0060	0.0131	0.0292	0.1337

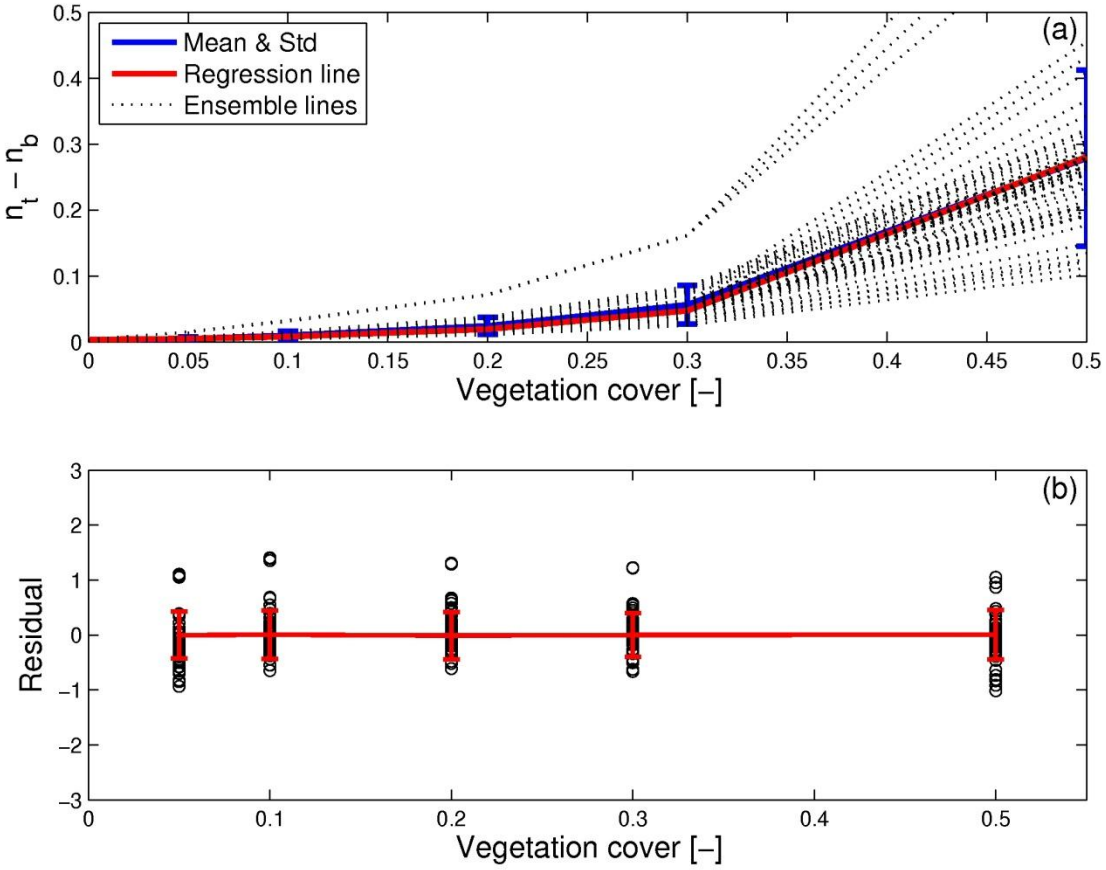

Figure 4.10: The effect of vegetation cover fraction on Manning's coefficient. The dotted lines in the plot (a) show the results of 54 simulation cases (3 inflow rates, 3 base Manning coefficients, and 6 domain slopes were permutated); the solid blue line illustrates the mean of simulations for a given V_f, while the vertical bars show the standard deviation; and the red line illustrates the regression line based on Eq. (4.11) with R^2=0.918 (log-transformed). The plot (b) illustrates the regression residuals (circles), their mean values (red line), and the standard deviations (red vertical bars). The residuals are calculated as the difference between the natural logarithms of $n_t - n_b$ obtained from Eq. (4.11) and from the equivalent friction slope method.

The residuals computed as the difference between the ensemble lines and the predicted values from the regression equation (4.11) are calculated as the difference between the natural logarithms of $n_t - n_b$ obtained from Eq. (4.11) and from the Equivalent Friction Slope method. In the bottom plot of Figure 4.10, the mean of residuals at each V_f is nearly zero and the standard deviation of the residuals (in units of natural log-transform) is nearly constant. This ensures that the regression equation (4.11) is a consistent estimator.

Equations (4.11) and (4.13) are derived only by considering the effects of vegetation fraction. Regardless of what the values of the other variables are (e.g., *Q* or *S*), the values of $n_t - n_b$ predicted with these equations are the same. Predictions may therefore contain large errors in cases where the effects of *Q* and *S* become significant, and thus a caution should be used in using these equations. In particular, cases with small *S* or high V_f exhibit large effects of *Q* and *S*, respectively. These are addressed in the following section.

4.5.2 Effects of bed slope

As Figure 4.7 shows, it is difficult to infer a unique trend of the resistance coefficient relative to changes in *S* because n_t may exhibit both negative and positive variations. The negative trend of n_t with growing *S* is characteristic for high flow rates, while a positive trend of n_t with increasing *S* can be discerned at low flow rates. These changes are relatively minor for the cases with small vegetation cover. A positive trend with the domain slope at low flow rates also emerged in the experimental study by *Hessel et al.* [2003], who used a discharge of about $6.67 \cdot 10^{-5}$ m^3/s. Their study used bed slopes less than 64%, a relatively small inflow rate, and

vegetation cover fractions smaller than ~30%. For a cropland area, they found an increase in Manning's coefficient with increasing slope.

To further investigate possible trends, a set of simulation scenarios summarized in Table 4.4 were considered in addition to the cases described in Table 4.2. These included extreme cases with a higher inflow rate of 0.01 m^3/s. Flow rates reaching or exceeding such a magnitude are unlikely to occur in real-world hillslopes, except for most extreme hydrologic events. The four considered inflow rates, i.e., 0.0001, 0.0005, 0.001, and 0.01 m^3/s, therefore span the likeliest possible range and extend the analysis to "limiting" flow conditions. Similar to previous results in Figure 4.7, the set of simulation cases for Q = 0.01 m^3/s exhibit a decreasing trend of n_t with growing slope (not shown).

The effects of the difference in possible trends can be explained by using the Manning's equation. For a given inflow rate, the spatial variability of n_t is influenced by both friction slope and depth:

$$n_t = \bar{h}^{\frac{5}{3}} \bar{S}_f^{\frac{1}{2}} / q \, . \tag{4.18}$$

If the plane slope is increased, the friction slope will also grow, and the flow depth will decrease. These two effects exert a conflicting impact on the determination of n_t and thus are the reason of the two trends observed in the simulation results for changes in the bed slope. A specific trend (i.e., the growth or decay of n_t with S) is observed depending on whether the contribution of one effect overwhelms the contribution of the other. Selecting 10% bed slope as a "reference" slope and deriving the ratio of n_t at any slope with respect to $n_{t,10\%}$ at this reference slope yields an equation in a logarithmic form:

$$\log\left(\frac{n_t}{n_{t,10\%}}\right) = \frac{5}{3}\log\left(\frac{\bar{h}}{\bar{h}_{10\%}}\right) + \frac{1}{2}\log\left(\frac{\bar{S}_f}{\bar{S}_{f,10\%}}\right) \ , \tag{4.19}$$

which implies that n_t varies according to its controlling variables $\bar{h}$ and $\bar{S}_f$. The three terms of Eq. (4.19) are shown in Figure 4.11 for three different vegetation cover fractions of 0, 10, and 30%. For $V_f = 0$, the effects of $\bar{h}$ and $\bar{S}_f$ are nearly identical in the absolute magnitude and thus n_t is almost constant. However, for larger stem fractions (e.g., $V_f = 0.3$), the gradient $\partial n_t / \partial S$ is less than zero for larger inflow rates and nearly always positive for the smallest flow rate. The latter effect is because the relative rate of increase of $\bar{S}_f$ with respect to $\bar{S}_{f,10\%}$ is higher than the rate of decrease of $\bar{h}$ with respect to $\bar{h}_{10\%}$; the opposite holds true for the higher flow rates. One can consequently infer that the gradient $\partial n_t / \partial S$ becomes zero or, equivalently, exhibits a local minimum, where the two effects are balanced.

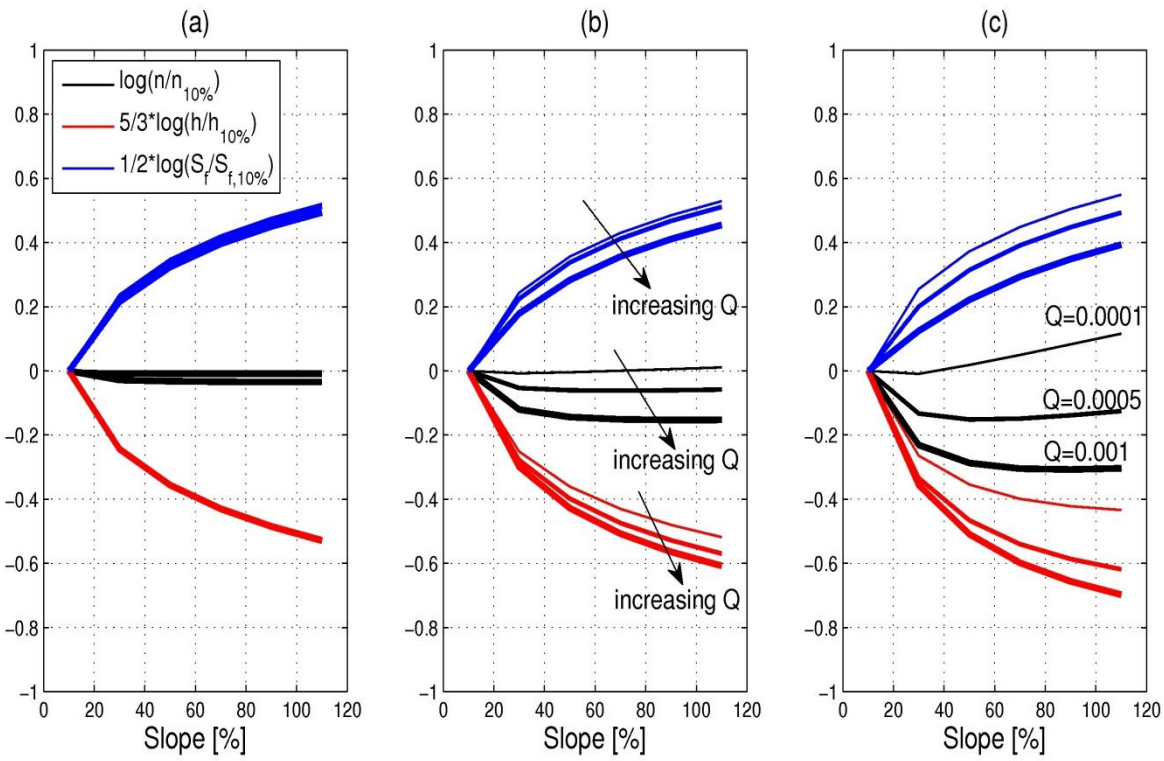

Figure 4.11: The log-ratio of n, h, and S_f to their respective magnitudes at 10% bed slope. The thin, the medium, and the thick lines correspond to the inflow rates Q of 0.0001, 0.0005 and 0.001 m^3/s. Vegetation covers are (a) 0%, (b) 10%, and (c) 30%.

In order to address these trends mathematically and verify the condition of existence of a point of local minimum, the regression equation (4.12) including *Re* and *Fr* is rewritten through the unit discharge and flow depth, as follows:

$$n_t - n_b = 9.6580(q)^{-0.6789}\left(\bar{h}\right)^{1.544}(S)^{0.3238}\left(V_f\right)^{0.8925}. \tag{4.20}$$

Given constant q and V_f, the derivative of $\partial n_t / \partial S$ is

$$\frac{\partial n_t}{\partial S} = 9.658(q)^{-0.6789}\left(V_f\right)^{0.8925}\left(\bar{h}\right)^{0.544}(S)^{0.3238}\left[1.544\frac{\partial \bar{h}}{\partial S} + 0.3238\frac{\bar{h}}{S}\right]. \tag{4.21}$$

The first four terms in Eq. (4.21) are always positive. The gradient $\partial n_t / \partial S$ therefore depends on the sign of the expression in the brackets. To find a minimum point at which the sign of dependency of n_t on slope is changed, the above equation is set to zero:

$$\frac{\partial \bar{h}}{\partial S} + 0.2097 \frac{\bar{h}}{S} = 0, \tag{4.22}$$

from this one obtains:

$$\bar{h} S^{0.2097} = constant. \tag{4.23}$$

Because $\bar{h}/S$ is always positive, the variability of n_t on S is determined by the magnitude of $\partial \bar{h} / \partial S$. The expression in Eq. (4.22) shows that n_t decreases only when the gradient of depth with respect to the bed slope ($\partial \bar{h} / \partial S$) is large enough (absolute of negative value), as compared to the ratio of depth and bed slope ($\bar{h}/S$); conversely, n_t increases when $\partial \bar{h} / \partial S$ has only a relatively small negative value. If the integration constant is known, the trend of n_t on S can be explicitly determined from Eq. (4.23). Although the above equations are derived from an empirical regression equation, they indicate that the variability of $\bar{h}$ with respect to S plays a key role in determining the shape of n_t on S.

4.5.3 Effects of inflow rate

Implications of the change of the flow rate are such that n_t slightly increases with Q. An increase of the wetted projected area of vegetation stems with growing Q can explain this phenomenon [*Abrahams et al.*, 1986]. However, for all cases, this trend does not represent a statistically meaningful result since Q is not highly correlated with n_t, and the standard deviation

of the latter for each flow rate is high, as compared to its mean. The coefficient of determination, R^2 of the regression equation between Q and n_t is less than 0.1 regardless of the selected equation type, such as linear or log-transformed power, exponential, or logarithmic functions.

As seen in Figure 4.7, the effects of Q on n_t are conveyed in two ways: an increasing trend of n_t with Q, when the domain slope is small, and a decreasing trend for a steeply-sloped plane. This effect of Q on n_t can be addressed in a fashion similar to the one used in Section 4.5.2. Given constant S and V_f, the derivative of $\partial n_t / \partial q$ is

$$\frac{\partial n_t}{\partial q} = 9.658(q)^{-0.6789}\left(V_f\right)^{0.8925}\left(\bar{h}\right)^{0.544}(S)^{0.3238}\left[1.544\frac{\partial \bar{h}}{\partial q} - 0.6789\frac{\bar{h}}{q}\right]. \qquad (4.24)$$

Since the first four terms in Eq. (4.24) are always positive, the gradient $\partial n_t / \partial q$ depends on the sign of the expression in the brackets:

$$\frac{\partial \bar{h}}{\partial q} - 0.4397\frac{\bar{h}}{q} = 0. \qquad (4.25)$$

Since $\partial \bar{h} / \partial q$ is positive, n_t can increase or decrease with q depending on whether the gradient of depth with respect to inflow rate ($\partial \bar{h} / \partial q$) is larger than their ratio ($\bar{h}/q$). Given constant S and V_f, the variability of $\bar{h}$ with respect to q plays a key role in determining the shape of n_t on q.

4.5.4 Effects of bed surface roughness condition

When overland flow occurs in areas with emerging vegetation, characteristics of original soil, expressed here as the base Manning's resistance coefficient n_b, may also affect the domain-representative roughness coefficient n_t. Various conditions of the bed surface are represented

with different values of n_b, e.g., a larger n_b corresponds to a rougher condition of the bed. The effect of n_b on n_t is illustrated in Figure 4.12 in which $n_t - n_b$ is used as the variable for the *y*-axis. This difference can be also recognized as the net total contributions of the form and wave resistances, which need to be accounted for in the presence of obstacles. Note that an analysis of the effect of n_b should be carried by mutually comparing the sets of lines of different color: red (n_b=0.04), black (n_b=0.02), and blue (n_b=0.03) lines (see Figure 4.12). The red lines are mostly above the black lines, which implies that the rougher the surface of the plane, the larger the effect of the form/wave resistances due to vegetation. As compared to the smoother bed corresponding to n_b of 0.02, the rougher bed with n_b of 0.04 leads to increasing contributions of the form/wave resistances to n_t by about 21, 20, 21, 14, 11% for the vegetation cover of 5, 10, 20, 30, 50%, respectively (Table 4.7).

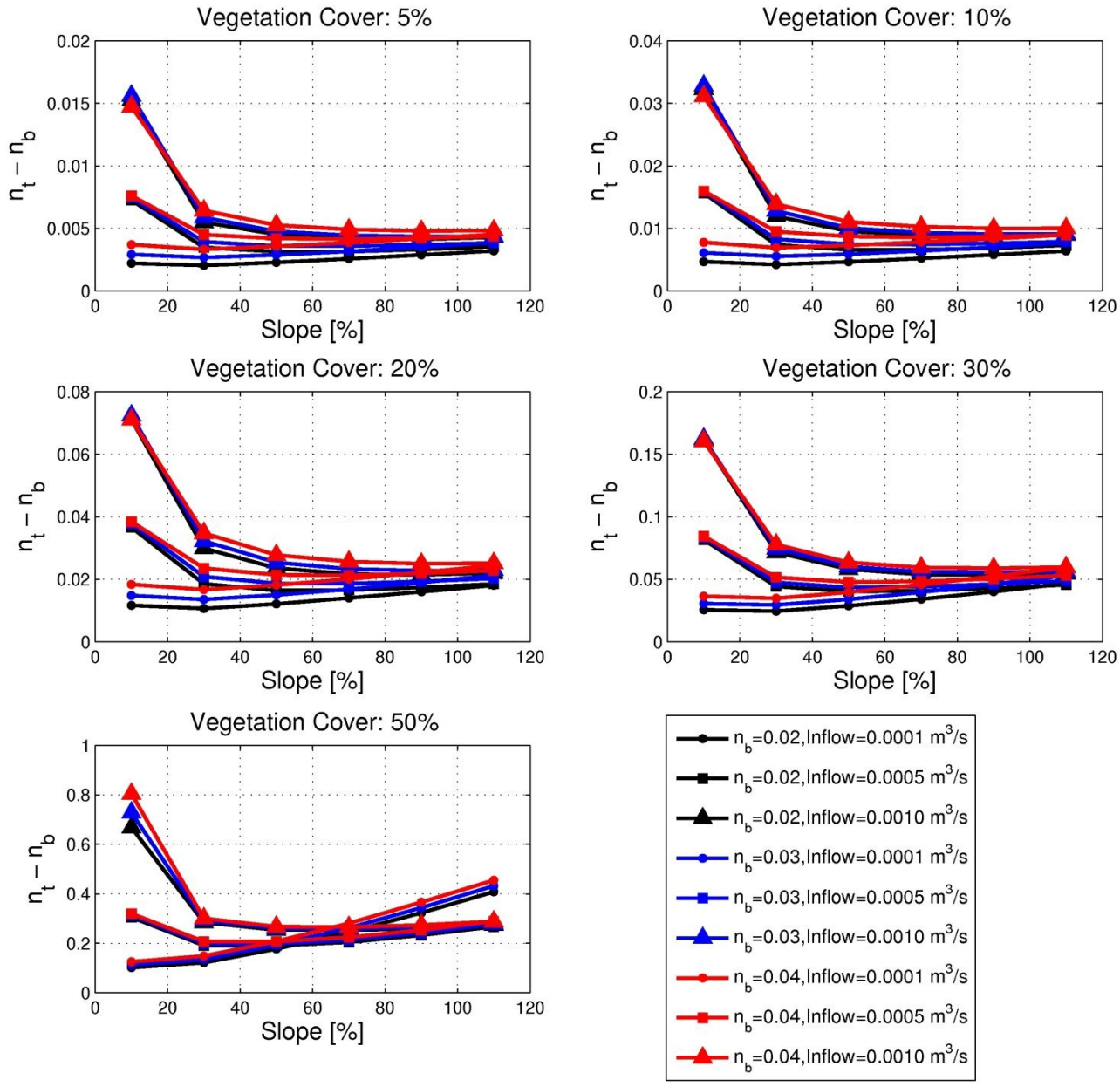

Figure 4.12: The effects of the base Manning's coefficient $\boldsymbol{n_b}$ on upscaled $\boldsymbol{n_t}$ for different vegetation fractions. The results were obtained using the equivalent friction slope method. Note that while Figure 4.7 illustrates the total resistance, this figure shows the sum of the form and wave resistances, which implies the net total contribution of resistances due to partially submerged vegetation to the total resistance.

4.5.5 Relationship between flow depth or velocity and the Manning coefficient

Patterns of a relationship between the upscaled Manning's coefficient n_t and main flow variables (h and V) are illustrated in Fig. 13. For a fixed S and Q, n_t is positively related to h and is negatively related to V. These relationships are consistent with the previous discussion of relationships between n_t and independent variables and corroborate the results of studies by *Fathi-Moghadam* [2006].

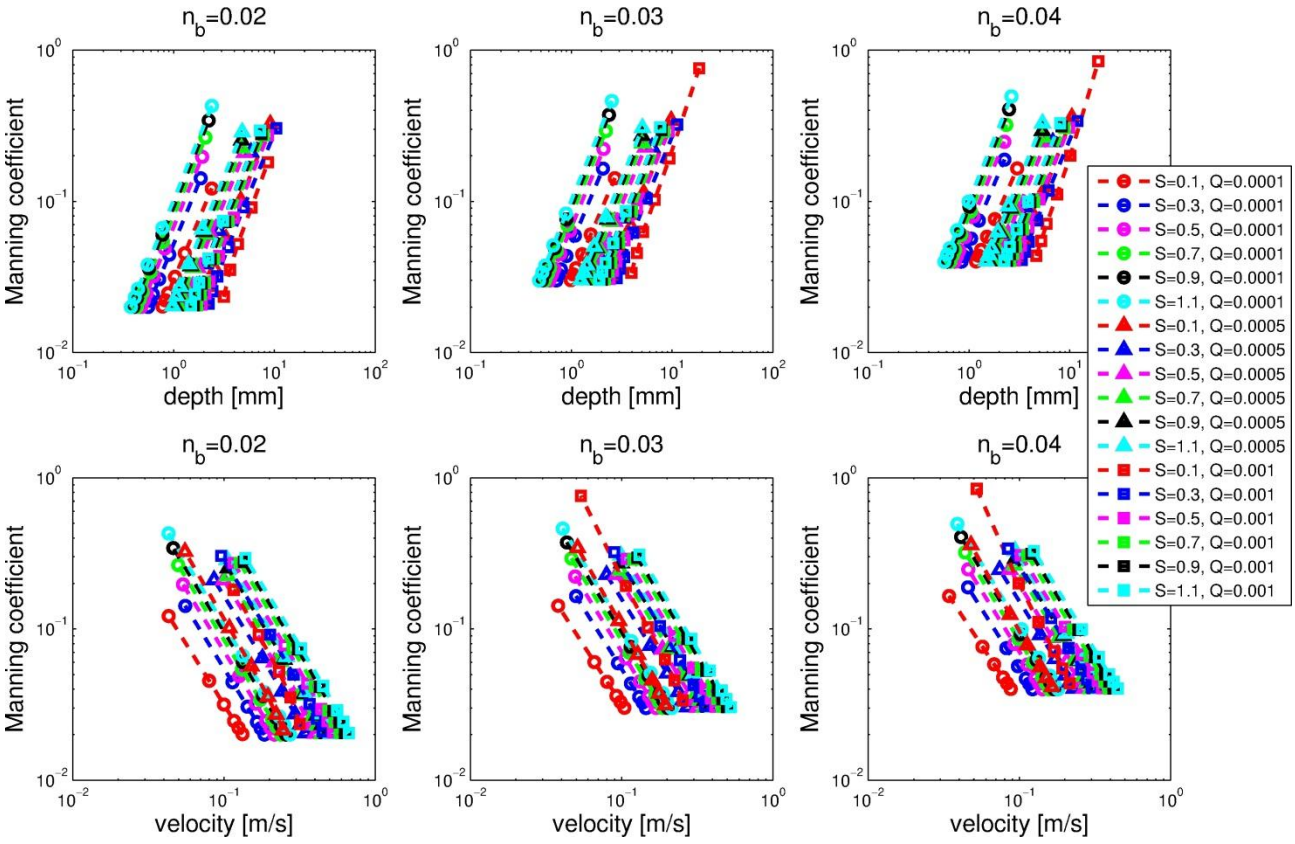

Figure 4.13: Upscaled Manning's coefficients ($\boldsymbol{n_t}$) shown with respect to average flow depth and velocity. The results were obtained using the equivalent friction slope method for different slopes, inflow rates, and base Manning coefficients corresponding to the cases summarized in Table 4.2. Six points in each line correspond to six vegetation fractions.

4.5.6 Validity of performance skill

Despite the simplified nature of the S-V equations and the implications of underlying assumptions, the results of this study are consistent with a broad range of data from five experimental studies. While some of the reported data required additional interpretations and thus resulted in a larger uncertainty, no assumptions were made when recent data by *Hu and Abrahams* [2006] were used (see Section 4.4.6) and the obtained results showed an excellent skill. Furthermore, the reported simulation results confirmed a regression equation for the wave resistance proposed by *Hu and Abrahams* [2006] (see Section 4.4.6) and relationships between resistance and depth/velocity proposed by *Fathi-Moghadam* [2006] (see Section 4.5.5). One possible reason of why the application of the S-V equations has demonstrated such a good performance could be due to a relatively minor role that obstacle-induced eddies play in affecting larger-scale characteristics of the flow. As *Stoesser et al.* [2010] illustrated, the time-averaged streamwise (horizontal) velocities resulting from their 3-D LES model show similar patterns to those obtained in this study: higher velocity between stems and smaller velocities behind stems. Although there can be no exact comparison between the two studies, one important inference from *Stoesser et al.* [2010] is that the size/region of wake behind a vegetation stem is relatively small as compared to the stem diameter. This indicates that a possible uncertainty region, due to inability to explicitly resolve eddies with the S-V model, may be restricted to a single triangle cell behind any given stem represented in this study.

4.6 Conclusions

Using high-resolution, hydrodynamic numerical simulation results performed at very fine space-time scales, two methods were developed to obtain the upscaled Manning coefficient, specifically, "the Equivalent Roughness Surface" (ERS) and "the Equivalent Friction Slope" (EFS) methods. The former approach assumes that the resistance of a rough plane bed without vegetation is equal to the resistance of a smooth plane covered with vegetation stems or other obstacles. The latter method obtains the upscaled resistance by using information on flow depth, velocity, and friction slope simulated at steady state in internal points of a domain. The values obtained with these two methods yield nearly identical estimates of n_t; the coefficient of determination of the relationship between them is $R^2 = 0.973$.

The values of n_t obtained in the simulation scenarios described in Tables 4.2 and 4.4 were used to develop a predictive equation. The relevant variables and their corresponding coefficients were determined by using the dimensional analysis and a multiple linear regression analysis. A general relation accounting for the effect of four independent variables (i.e., S, Q, n_b, and V_f) is given by Eq. (4.12), which is applicable to conditions with $V_f \leq 0.5$, $0.1 \leq S \leq 1.1$, and $0.0001 \leq Q \leq 0.01$.

We compared $n_t - n_b$ computed from the general regression Eq. (4.12) with data reported in five different studies, as presented in Table 4.6. Although certain assumptions had to be made, so as to derive representative values of n_b and V_f, the overall deviations were minor (R^2 = 0.898). Also, the wave resistance coefficients obtained with the Equivalent Friction Slope method were compared with estimates from a predictive equation of *Hu and Abrahams* [2006]. We found that the estimates are quite consistent with the numerical results obtained in this study

within the range of experimental conditions for which the equation of *Hu and Abrahams* [2006] was developed. Overall, it follows that the predictive equation derived in this study is well corroborated by reported experimental data and a previously developed formulation for wave resistance. Thus, this framework can become a suitable tool for predicting roughness coefficient for vegetated hillslopes.

Furthermore, the effects of independent variables on n_t were investigated. First, the effect of V_f on n_t is that as V_f increases, n_t also grows. This positive trend is represented by Eq. (4.11) and Eq. (4.13) with high values of the determination coefficient of the log-transform linear relationships. These equations can be useful in estimating the degree of vegetation effects on resistance, when other variables required by equations (4.9) or (4.12) are not available. However, they cannot be used in cases where effects of other independent variables become significant: for example, the effects of Q are significant in cases with small S values, and the effects of S are non-negligible for the cases with high V_f values. Second, in terms of effects of S on n_t for a fixed V_f and Q, two distinct trends exist: a positive dependence at low flow rates and a decreasing trend at high flow rates. These two trends are due to two conflicting impacts determining n_t: when S is increased, the friction slope S_f grows, while the same is true for cases when the flow depth h decreases. On the other hand, for a fixed V_f and S, two distinct modes of the relationship between Q and n_t emerge: a positive dependence at mild slopes, and a negative dependence at steep slopes. A regression analysis shows that these two conflicting trends can happen depending on whether the variability of flow depth with respect to S (or Q) is greater than the ratio of h and S (or Q). Third, a rougher bed with larger n_b implies an increase of the form/wave resistances due to vegetation. Last, this study corroborates earlier research that n_t grows as h increases and decreases with higher V [*Fathi-Moghadam*, [2006].

CHAPTER V

On the non-uniqueness of sediment yield: effects of initialization and surface shield

5.1 Introduction

Estimation of sediment yield (*SY*) the catchment scale, defined here as the total sediment mass discharged by a basin at an outlet section and corresponding to a given duration, e.g., a hydrological 'event', plays a significant role for optimal design of hydraulic structures, such as bridges, culverts, reservoirs, canals, harbors, and detention basins, as well as making informed decisions in environmental and ecological management. Prior experimental studies focused on obtaining flow and sediment data in a search of unique relationships between runoff (specifically, volume and peak) and characteristics of basin sediment yield [*Pierson et al.*, 2001; *Harmel et al.*, 2006; *Nearing et al.*, 2007]. These relationships were employed to predict sediment yield from flow information due to relatively larger difficulties in measuring sediment. Generally, sediment yield is assumed to increase with flow volume (*FV*) for a given basin area. However, there are substantial nonlinearities in the basin response that can trigger remarkable variations in any perceived unique relationship, thus making the estimation of *SY* very uncertain. Indeed, actual event-scale sediment yield produced by a river basin can vary significantly for the same metric

of the hydrological response (e.g., see for example Fig. 2 in *Nearing et al.* [2007] reporting data from real watersheds).

Such non-uniqueness of sediment yield is common for many locations around the world and can be attributed to nonlinearities associated with several possible contributing factors. (1) Given the same rainfall, sediment output at a basin outlet is non-linear with respect to the size of a watershed. Drainage basins of higher orders have lower delivery ratios (defined as the ratio between *SY* and the total eroded material), as compared to smaller watersheds, due to larger watershed storage capacities, such as floodplains [*Lane et al.*, 1997; *Phillips*, 2003]. (2) Sediment dynamics strongly depend on land use, land cover, and conservation management practices [*Harmel et al.*, 2007; *Ward et al.*, 2009; *Notebaerta et al.*, 2011; *Defersha and Melesse*, 2012]. As an example, for two major cropping systems in Texas Blackland Prairies, annual soil loss in regions producing small grain (wheat or oat) is significantly lower than that of areas with row crop production (corn or sorghum) [*Harmel et al.*, 2006]. In watersheds with either shrub or grass vegetative cover in southeastern Arizona, the mean erosion rates in shrubby areas are higher than those in grassy sites [*Nearing et al.*, 2005]. (3) Erosion is higher at sites with steeper and longer slopes [*Defersha et al.*, 2011]. This phenomenon is particularly pronounced in regions where gravity plays a significant role in sediment release and movement. However, the relationship between site slope and erosion rate is subject to substantial variations in areas of mild topography, where the processes related to flow characteristics (e.g., the development of narrower and faster flow threads) and flow patterns (e.g., connectivity between soil surfaces with broader or narrower flows) are predominant over the gravity-related processes [*Armstrong et al.*, 2011]. (4) Precipitation characteristics (intensity, frequency, duration, and volume) substantially affect the temporal variability of sediment yield. Only several extreme storms can be responsible

for most of the total erosion loss over a long term period [*Edwards and Owens*, 1991; *Nearing et al.*, 2007]; the temporal sequence of rainfall events may also impact the amount of erosion [*Romkens et al.*, 2001]. (5) Surface conditions such as soil moisture contents, crust formation, sealing, slaking and organic matter contents influence runoff and erosion generating processes [*Bissonnais et al.*, 1995; *Mamedov et al.*, 2006; *Wuddivira et al.*, 2009].

In addition to these aforementioned reasons, the type of soil and its particle size distribution (PSD) may result in selective erosion and transport of sediment that depend on a grain size and the corresponding settling velocity [*Hairsine et al.*, 1999]. Specifically, smaller particles have low settling velocities and prone to move far from their original position of detachment. Conversely, larger particles can settle quickly near their source locations because of their heavier immersed weight. Larger particles can also form a shield on soil bed and protect underlying material from rainfall detachment and runoff entrainment [*Kinnell*, 1993; *Hairsine et al.*, 1999] and experimental research on the formation and temporal development of a shielding layer has demonstrated a range of relevant phenomena [*Heilig et al.*, 2001; *Walker et al.*, 2007; *Armstrong et al.*, 2012]. *Heilig et al.* [2001] first confirmed the existence of a shielding layer through a simple experimental setup under rainfall-induced erosion. *Walker et al.* [2007] examined the role of infiltration on soil erosion, and argued that increased infiltration makes the formation of a shielding layer faster by increasing the vertical deposition rate. *Armstrong et al.* [2012] further investigated the effects of slope, ponding depth, and infiltration. In their experiments, the first two variables were found to be significant factors controlling shield development, while the effects of infiltration were minor.

These experimental studies corroborated the formation of a shielding layer through video image processing and statistical analyses and presented the implications of several parameters on

the process. The studies primarily focused on relatively simple, small-scale experiments over a short term (hourly time scales) by using plot-scale domains: a small horizontal soil surface ($7 \times 7 \times 7$ cm^3) [*Heilig et al.*, 2001], a soil chamber with a diameter of 7.5 cm [*Walker et al.*, 2007], and Perspex soil boxes ($25 \times 25 \times 15$ cm^3) [*Armstrong et al.*, 2012]. None of these studies however could address the effects of relevant variables on the formation and break down of a shielding layer and its impact on the erosion process and sediment loss at larger (e.g., hillslope), spatial scales and over the long-term.

The overarching goal of this study is to further explore why watersheds can produce non-unique sediment yield for the same runoff volume in the context of size-selective erosion phenomena. The specific objectives are (1) to investigate the effects of various rainfall patterns on sediment yield, (2) to elucidate the occurrence of unsteady phenomena in the process of erosion under steady-state hydraulic flow condition, and (3) to describe unsteady patterns and attribute them to critical time scales in the dynamics of morphologic variables. The study is based on a numerical investigation of sediment yield response from a zeroth-order watershed (the total area is 14×28 m^2) forced by a number of synthetic rainfall events. The modeling scenarios are constructed such that perturbations caused by prior rainfall affect the initial condition for a succeeding storm event in terms of either (i) flow (smaller/larger depth) or (ii) soil bed (intact/loose). The various initial conditions lead to the non-uniqueness of basin sediment yield with respect to the same runoff. The numerical model used in this study is the two-dimensional Hairsine-Rose erosion/sediment transport model coupled to a fully distributed hydrology and hydrodynamic model (tRIBS-OFM: Triangulated irregular network - based Real time Integrated Basin Simulator-Overland Flow Model).

5.2 Model appropriateness and simulation design

5.2.1 Model appropriateness

The basic premise of this study is that soil bed with multiple particle sizes can form a shield by relatively larger particles, which can lead to a non-unique sediment response with respect to the same forcing. The appropriate formulation of erosion and sediment transport model capable of incorporating features required for a numerical exploration of the above assertion is the Hairsine-Rose (H-R) model [*Hairsine and Rose*, 1991; 1992; *Sander et al.*, 2007a]. It represents a mechanistic erosion and sediment transport model that can describe the formation and development of surface shield. Since the original research in 1990s, a significant amount of research on the Hairsine-Rose formulation has confirmed its appropriateness; it has been addressed analytically [*Sander et al.*, 1996; *Hairsine et al.*, 1999; *Hairsine et al.*, 2002; *Sander et al.*, 2002; *Hogarth et al.*, 2004b], numerically [*Hogarth et al.*, 2004a; *Heng et al.*, 2009; *Kim et al.*, 2013], and experimentally [*Proffitt et al.*, 1991; *Heilig et al.*, 2001; *Rose et al.*, 2007; *Walker et al.*, 2007; *Armstrong et al.*, 2011; *Heng et al.*, 2011; *Armstrong et al.*, 2012]. Further, these unsteady, two-dimensional, advection-dominated sediment transport equations have been successfully combined with flow mass and momentum equations, such as the two-dimensional Saint-Venant equations [*Anderson*, 1995] using the Finite Volume framework [*Heng et al.*, 2009; *Papanicolaou et al.*, 2010; *Kim et al.*, 2013].

5.2.2 Modeling erosion processes

Soil erosion and sediment transport are very complex phenomena and all relevant processes are extremely difficult to describe at a high detail in a numerical model. The

advantages of the employed model are as follows. First, two-dimensional flow motions caused by variations in topography and meteorological forcing, as well as hydrologic partition related to vegetation cover, landuse, and subsurface processes can be well captured in a spatiotemporally manner in this coupled model. Next, the Hairsine-Rose formulation can render the phenomena of detachment, deposition, and sediment transport in a more physically consistent fashion [*Sander et al.*, 2007b], as compared to numerical models using the transport capacity concept, such as KINEROS [*Woolhiser et al.*, 1990] and WEPP [*Nearing et al.*, 1989]. The latter models employ two different erosion source equations depending on whether flow conditions are under net eroding or net depositional regimes and therefore, under a given flow condition, only a single erosional regime can occur. However, empirical evidence on detachment and deposition processes testifies that each process occurs simultaneously and continuously. *Polyakov and Nearing* [2003] pointed out that models based on a single, prescribed transport capacity fail to simulate soil conditions with multiple particle sizes and evolving composition of the bed, because the transport capacity is not unique during simulations in such conditions [*Polyakov and Nearing*, 2003; *Sander et al.*, 2007b]. The coupled model adopting the Hairsine-Rose formulation can satisfactorily resolve such challenging effects caused by both preferential deposition in a water column and a physical protection by the deposited layer.

In contrast, the processes that are not or cannot be fully addressed by the formulation used in this study are as follows. (1) The erosion phenomena related to subsurface water content and the effect of negative or positive soil matric pore pressures are not considered [*Simon and Collison*, 2001]. For instance, as soil becomes saturated, erosion can increase due to the growth of pore water pressure that reduces soil cohesive strength [*Simon and Collison*, 2001]. (2) Erosion enhancement due to increasing aggregate breakdown and slaking, which is attributed to

air burst within the pores of aggregates during rapid wetting [*Le Bissonnais et al.*, 1989; *Rudolph et al.*, 1997]. The process of slaking is more pronounced in soils where organic matter that contributes to binding mineral particles is low. (3) Repelling of soil particles in condition of wet soil. This process is due to an interaction between a layer of positive charges composed of chemical cations (e.g., sodium, calcium, and magnesium) surrounding clayey soil particles that carry negative electrical charge. (4) Drying of slaked clayey soil that leads to crusting and sealing and may result in a reduction of infiltration and growth of runoff and erosion [*Le Bissonnais et al.*, 1989]. (5) The employed model cannot represent "sub-grid" processes, such as a flow motion occurring in narrower, faster flow threads of the assumed planar surface of a computational cell (i.e., a triangle). Specifically, the numerical model does not require a "rill" or a "stream parameterization", provided the resolution of computational cells is small enough to capture the scale and the actual representation of a rill or a stream. If the resolution is coarser, however, the model formulation assumes sheet flow within a cell. In summary, all of the above processes related to a degree of soil saturation, slaking by trapped air, repelling between chemical cations (dispersion), crusting, and rill formation are excluded in this study. Better parameterizations or exact mathematical theories associated with these processes are needed for a more complete numerical treatment of the erosion process.

5.2.3 Simulation setup

5.2.3.1 Domain and modeling configuration

Sediment yield at an outlet of a zero-order catchment [*Ivanov et al.*, 2010] is simulated for different precipitation patterns. The domain is 14 m wide and 28 m long and is resolved with a mesh of about 1 m spacing. Local slopes range from 7.3 to 32.8% (see Figure 5.1). Such a relatively small catchment, as compared to most instrumented, real-world watersheds, is nonetheless significantly larger than domains used in experimental studies exploring size-selective erosion processes. It is selected to take into account mechanisms operating in real topographies exhibiting a range of slopes and to permit computational feasibility. Another reason is to exclude the effects of perennial channels, where substantial flow depths can influence the process of rainfall (re)detachment [*Laws and Parsons*, 1943; *Mutchler and McGregor*, 1983; *Proffitt et al.*, 1991]. Therefore, as compared to higher order watersheds, this zero-order domain can help identify whether shielding is caused by flow depth or shielding layer of soil particles.

The number of mesh nodes and triangular cells are 435 and 812 (Figure 5.1). The time step used for runoff generation routine is 7.5 min. The time step used for the simulation of flow hydrodynamics and erosion-transport modeling components is 0.2 sec.

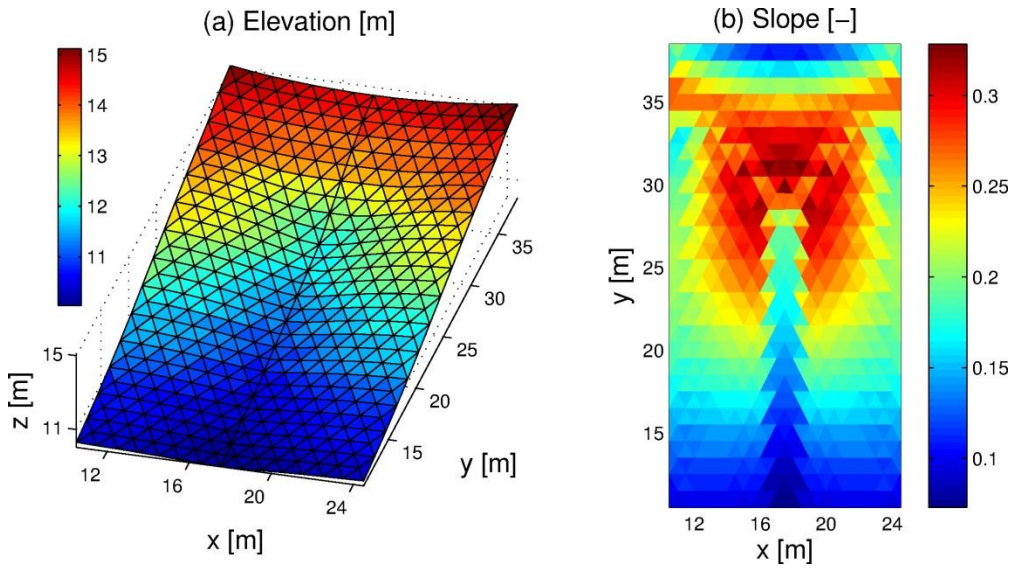

Figure 5.1: Illustrations of (a) elevation and (b) slope fields of the simulation domain.

5.2.3.2 Rainfall forcing

Five synthetic simulation cases with different rainfall patterns are designed (see Table 5.1 and Figure 5.2). The generated rainfall forcing for the domain is spatially uniform, while temporally variable and defined by the rainfall intensity (*RI*), duration (T_r), and lag time between events (T_b). The first case of forcing (Case 1) represents a composition of two rectangular "pulses" of rainfall (E_1 and E_2), both of which have the same intensity and duration of 1 hour ($RI_1 = RI_2$, $T_{r,1} = T_{r,2}$ =1). Variables that are varied in the Case 1 are the magnitude of rainfall intensity (*RI*) and the lag time between the two events (T_b). As a result of permutation of 5 rainfall intensities ($RI_1 = RI_2$ = 10, 30, 50, 70, and 90 mm/hr) and 7 different lag times (T_b = 0, 2, 4, 6, 8, 10, and 12 hr), Case 1 includes 35 sub-cases. The varying lag times between the two rainfall pulses imply different initial states of overland flow within the domain for the second rainfall event.

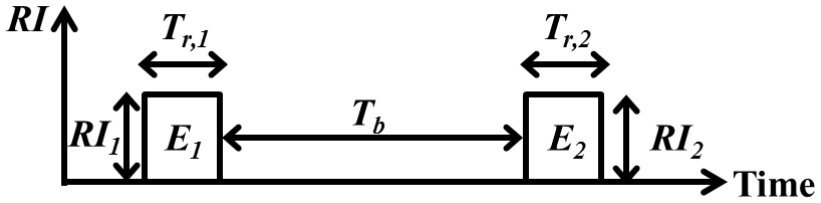

Figure 5.2: A schematic diagram of characteristic variables describing precipitation patterns used in this study: *E* denotes an event, i.e., a rectangular "pulse" of rainfall; *RI* is the corresponding rainfall intensity; T_r is the event duration; T_b is the time lag between two events. Subscripts '1' and '2' refer the first and second rainfall events, respectively.

In the second and third rainfall forcing cases (Case 2 and Case 3), two rainfall pulses are also used. They have the same duration of 1 hour but may have different rainfall intensities ($RI_1 \neq RI_2$, $T_{r,1} = T_{r,2} = 1$). Both cases consist of 25 sub-cases that correspond to permutations of 5 rainfall intensities for the first event (RI_1 = 10, 30, 50, 70, and 90 mm/hr) and for the second event (RI_2 = 10, 30, 50, 70, and 90 mm/hr). The only difference between Cases 2 and 3 is the time lag between the two pulses: T_b = 12 hr for Case 2 and T_b = 0 for Case 3. The reason for the chosen T_b set to 12 hr (Case 2) is because this time period was determined to be sufficiently long to exclude the effects of overland flow initialization for the second event; different rainfall intensities during the first rainfall pulse target the generation of different initial conditions of soil bed for the subsequent event. In contrast, Case 3 uses T_b = 0, which generates different initial conditions in terms of both flow and sediment for the second simulation event.

The Case 4 corresponds to 5 different scenarios with a single rainfall event such that the total precipitation depth of 300 mm is imposed. The rainfall intensities, RI_1 = 20, 40, 60, 80, and 100 mm/hr, therefore define the rainfall duration ($T_{r,1}$): 15.0, 7.5, 5.0, 3.75, and 3.0 hr,

respectively. The Case 4 is useful for identifying how rainfall events of the same volume but different intensities affect sediment erosion.

The last set of rainfall forcing scenarios (Case 5) is designed to have a single rainfall event that has a duration of 60 days. Five rainfall intensities are used: RI_1 = 10, 30, 50, 70, and 90 mm/hr. Such a long event duration is of course entirely hypothetical but this long-term simulation can be helpful in identifying how unsteady sediment dynamics occur and temporally transform, even though flow motion exhibits steady state most of the simulation period.

Table 5.1: A summary of five principal simulation cases. The total number of simulations is 95.

Name	# of events	# of sub-cases	Duration, T_r [hr]	Intensity RI [mm/hr]	Lag time T_b [hr]
Case 1	2	35	$T_{r,1} = T_{r,2}$ =1	$RI_1 = RI_2$ = 10, 30, 50, 70, 90	0, 2, 4, 6, 8, 10, 12
Case 2	2	25	$T_{r,1} = T_{r,2}$ =1	$RI_1 \neq RI_2$ = 10, 30, 50, 70, 90	12
Case 3	2	25	$T_{r,1} = T_{r,2}$ =1	$RI_1 \neq RI_2$ = 10, 30, 50, 70, 90	0
Case 4	1	5	$T_{r,1}$ = 15, 7.5, 5, 3.75, 3	RI_1 = 20, 40, 60, 80, 100	-
Case 5	1	5	$T_{r,1}$ = 1440	RI_1 = 10, 30, 50, 70, 90	-

5.2.3.3 Soil characterization

In this study, silty sand soil that has four different particle fractions, each contributing an equal fraction of 25 %, is considered as an initial bed condition for all simulation cases (i.e., at time equal to zero). The sediment sizes of considered soil particle types are assumed to be 0.02, 0.05, 0.1, and 0.5 mm, respectively. The smallest particle type is called S1, the second smallest and progressively larger particle types are respectively called S2, S3, and S4 types. Their corresponding settling velocities, $\nu_{1,\cdots,4}$, are 0.000276, 0.0017, 0.0062, and 0.0619 m/s. They are calculated using a formula of *Cheng* [1997].

Note that when fine-sized dry clayey soil is subjected to wetting, aggregate slaking and breakdown will occur; conversely, crust on soil is formed when slaked soil dries. Additionally, clay particles containing chemical elements (particularly, sodium) are prone to separate themselves from soil aggregates in wet conditions. Since these structural (slaking) and chemical (dispersion) mechanisms can only be implicitly incorporate in the parameters related to erodibility, fine-sized particles are excluded from the presented numerical analysis.

An impervious soil surface condition is assumed for all simulation scenarios to exclude the processes of infiltration and subsurface flow. While the latter certainly affects surface runoff generation, the aim of the study is to investigate the effects of the dynamic evolution of a shielding layer on the erosion and sediment processes in conditions of clearly identifiable precipitation patterns. The impact of runoff-generating processes is however indirectly accounted for through magnitudes of rainfall intensity.

5.2.3.4 Model parameterization

Every model that involves a description of physical phenomena faces a challenge of parameter identification. Choosing proper values for these parameters is a necessary step before exploratory simulations and they are usually determined either by referring to previous research described in literature or through the process of manual/automated calibration. In this synthetic study, the parameters summarized in Table 5.2 refer to previous research [*Heng et al.*, 2011; *Francipane et al.*, 2012; *Kim et al.*, 2013]. In the calculation of the shield effect factor by water flow, the mean raindrop size is assumed to be 2 mm and the exponent is assumed to be 1.0 [*Heng et al.*, 2011]. Since the study essentially focuses on the movement of flow and sediment, the values of landuse and soil parameters are inherited from previous studies applied for the Lucky Hills watershed in southeastern Arizona, U.S.A. [*Francipane et al.*, 2012; *Kim et al.*, 2013]. The density of sediment (ρ_s) and water (ρ_w) is 2,700 and 1000 kg/m^3 respectively, and the porosity of the bed is 0.46. Manning's coefficient of 0.03 is chosen for a representation of shear resistance.

Table 5.2: The model parameters used to represent hydrologic, hydraulic, and sediment erosion-transport dynamics.

Parameter	Description	Value	Unit	Usage
n	Manning coefficient	0.03	$s/m^{1/3}$	Flow
a_0	Detachability of original soil	20.0	kg/m^3	Erosion
a_d	Detachability of deposited soil	2000	kg/m^3	Erosion
F	Effective fraction of excess stream power	0.01	-	Erosion
Ω_{cr}	Critical stream power	0.1053	W/m^2	Erosion
J	Specific energy of entrainment	750	m^2/s^2	Erosion
M_t^*	Deposited mass needed to sheild original soil	2.7	kg/m^2	Erosion
D_r	Mean raindrop size	2.0	mm	Erosion
b	An exponent in power law by *Proffitt et al.* [1991]	1.0	-	Erosion
K_s	Saturated hydraulic conductivity	0.0	mm/hr	Soil

5.3 Simulation results

Simulation cases addressed in this study are designed (Section 5.2.3.2) so that several rainfall characteristics are varied: rainfall intensity (*RI*), duration (T_r), and lag time between events (T_b). Different precipitation patterns are employed to investigate the effects of the frequency of rainfall events (Case 1), the arrangement and sequence of events (Cases 2 and 3), and the long-term duration of rainfall (Cases 4 and 5) on the non-uniqueness of basin sediment yield.

5.3.1 Case 1

While Case 1 was designed to permit different initial conditions in terms of flow depth distribution, the generated runoff flows out of the domain rapidly and hydraulic effects of the first rainfall event on the second one are very limited. Simulated sedigraphs for the rainfall intensity of 50 mm/hr are shown in Figure 5.3-(a) for different values of T_b. As seen, while the sedigraphs for the first and second events are always different, the time series of sediment yield for the second event are nearly indistinguishable with respect to variations in T_b. Even for a very small lag between the two events (~15min), the sediment rates do not change considerably (not shown). This result implies that while the initial conditions of overland flow within the domain might somewhat differ, they do not significantly influence the amount of sediment yield for the second rainfall event.

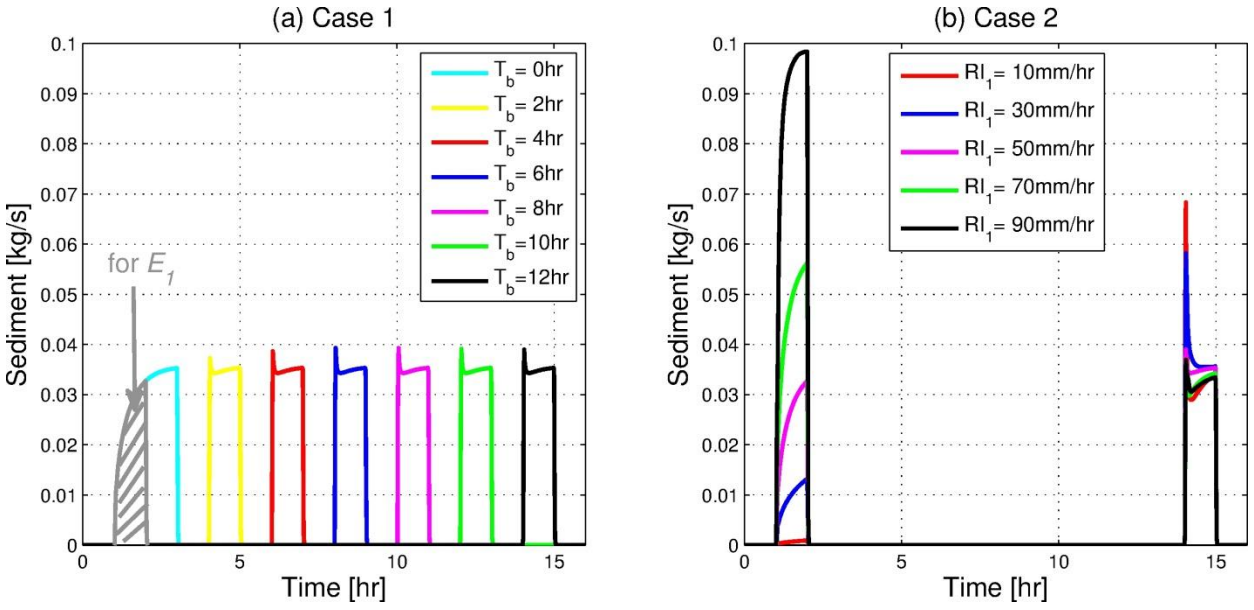

Figure 5.3: The simulated sedigraphs: (a) for the rainfall intensities RI_1 = RI_2 = 50 mm/hr (Case 1; note that sedigraph corresponding to the first event is denoted with the gray line, hour 1-2); (b) for different rainfall intensities during the first rainfall event RI_1 =10, 30, 50, 70, 90 and the second rainfall event with an intensity of RI_2 = 50 mm/hr (Case 2).

5.3.2 Case 2

Figure 5.3-(b) illustrates sedigraphs for five sub-cases of Case 2 (among the total 25). Specifically, five rainfall events of different magnitudes are followed by a rainfall event that has an intensity of 50 mm/hr. In contrast to the previous results, the varying rainfall intensities of the first event generate different conditions of the deposited sediment layer that serves as initialization for the second event. This results in non-unique sedigraph series for the second event, in spite of the same rainfall input of 50 mm at the same intensity.

5.3.3 Case 3

All simulated hydrographs and sedigraphs for the Case 3 are displayed in Figure 5.4. As seen, the hydrographs peak very rapidly, near the beginning of all rainfall events, implying that the times of concentration are very small. The flow remains at steady state, unless rainfall input changes. In this small impermeable domain, the flow response to a given rainfall is linear: the relationship between the rainfall input and the flow is always identical regardless of the configurations of rainfall events. However, the response of sediment to the rainfall forcing is apparently nonlinear: a notable feature is that sedigraphs may not peak within the duration of a rainfall event and may not approach the steady state. Depending on the magnitude of the first rainfall event, the second rainfall event can be highly affected. For example, for varying magnitudes of the first event and a fixed subsequent rainfall, there are considerable changes in the sediment rate series corresponding to the second event. Note that there is no change in the flow series (see any set of five column-wise sub-plots in Figure 5.4).

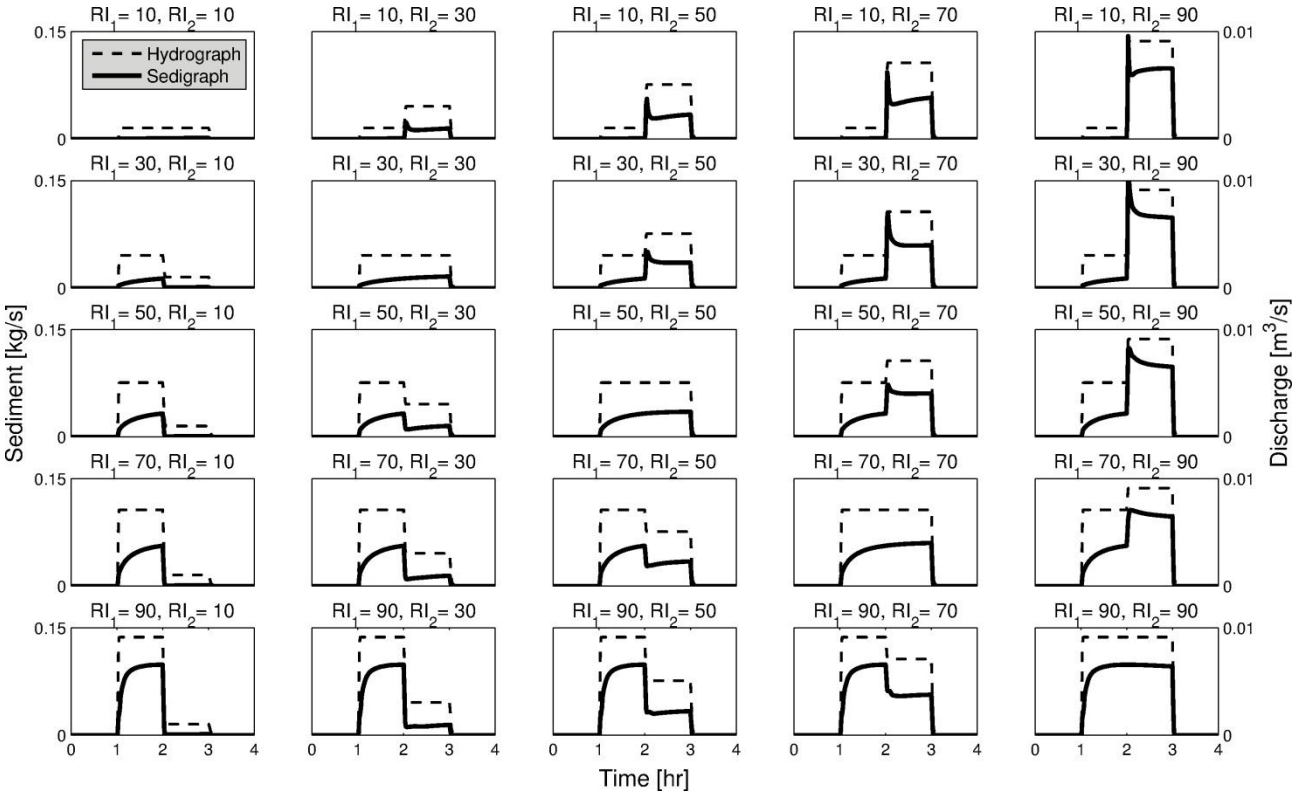

Figure 5.4: The simulated hydrographs and sedigraphs for Case 3. The left axis in all sub-plots corresponds to a sedigraph (solid line), while the right axis corresponds to a hydrograph (dashed line).

5.3.4 Cases 4 and 5

Figure 5.5 shows the simulated sedigraphs for the Case 4 (sub-plots (a) and (b)) and the Case 5 (sub-plots (c) and (d)). The obtained sedigraphs for these fairly long-term simulations emphasize the unsteady dynamics of erosion processes. For a given rainfall intensity and duration, sediment rate quickly increases and peaks early; after that, the series exhibit a gradual decrease and an asymptotic approach to the steady state. For higher rainfall intensities, the peak of sediment rate as well as the steady state are achieved relatively faster (the associated time scales will be addressed in the discussion section). Also shown is the partition of sediment yield

into absolute (Figure 5.5-(b)) or relative (Figure 5.5-(d)) fractions corresponding to the four particle sizes (S1 through S4). The notable feature in the Case 4 is that despite the same runoff volume, the total sediment yield for RI_1 = 100 mm/hr is almost three times higher than that for RI_1 = 20 mm/hr (specifically, 431.65 vs. 1146.2 kg). Such a large difference is mainly attributable to the high erosion loss of large-sized particles. Similarly, the results in Figure 5.5-(d) show that higher rainfall intensities result in a progressively larger flow rate sufficient to entrain and move larger particles, giving rise to very high nonlinearities of the total (and relative, partitioned) sediment yields.

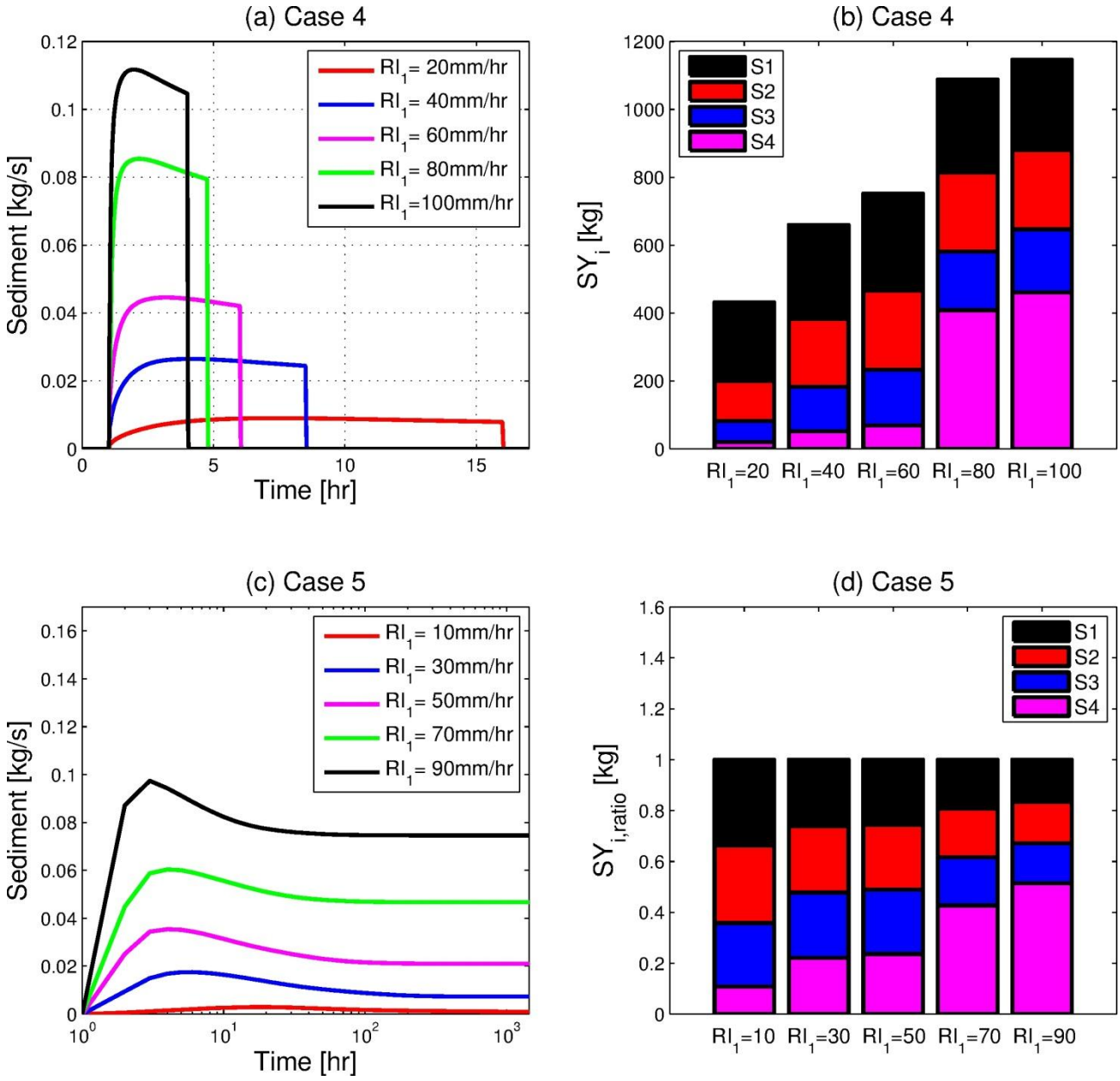

Figure 5.5: The simulated sedigraphs for (a) Case 4 and (c) Case 5. The sub-plot (b) shows the partition of sediment yield into relative fractions corresponding to the four particle sizes (S1 through S4) for Case 4. The sub-plot (d) illustrates the ratio of sediment yields corresponding to the four particle sizes (S1 through S4) for the total sediment yield for Case 5.

Selected spatial distributions of hydraulic variables (depth, velocity, and stream power) and morphologic variables (total concentration, total sediment yield, and elevation changes) for RI_1=50 mm/hr of Case 5 are presented in Figure 5.6. Sub-plots (a) to (c) correspond to the time at flow steady state. A similar pattern in the spatial distribution of all of the flow variables, i.e., higher magnitudes in the channel network and lower values in the headwater areas, are characteristic for the steady-state period, that is, from the time of concentration until the rainfall cessation. More specifically, in most regions of the domain, except for the flow convergence trough, the stream power barely exceeds a predefined threshold value needed to trigger overland flow induced erosion. Thus, the predominant controller in such upland areas is raindrop impact [*Kinnell*, 1982].

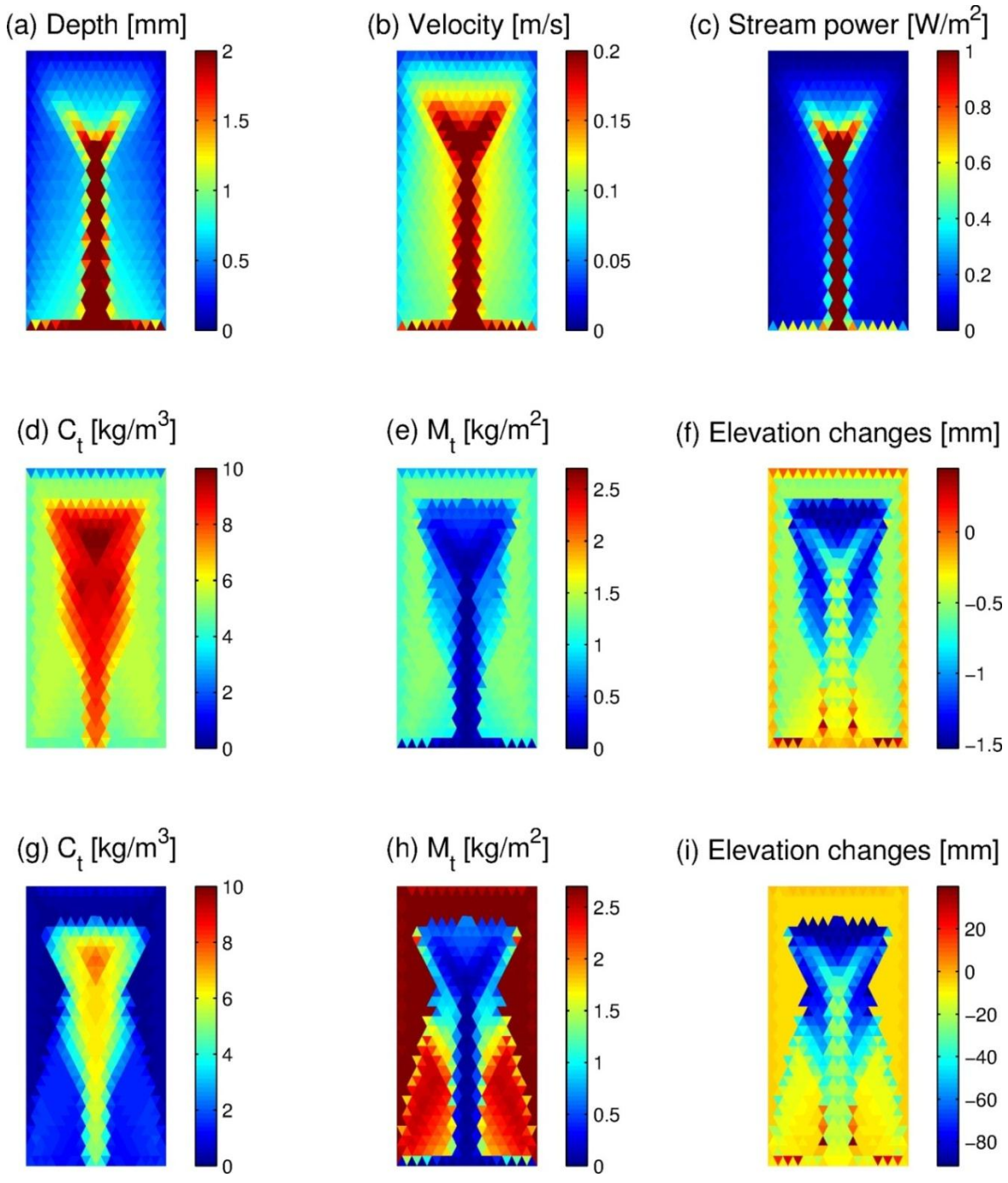

Figure 5.6: Spatial distributions of depth, velocity, stream power, total concentration, total sediment yield, and elevation changes for RI_1=50 mm/hr of Case 5. Plots (a) to (c) correspond to the time at flow steady state; plots (d) to (f) correspond to the time at sediment yield peak (hour 4); plots (g) to (i) correspond to time at sediment yield steady state (hour 163). In sub-plot (i), positive values denote deposition; negative values imply erosion. C_t is the total sediment concentration; M_t is the total deposited mass.

Conversely to the temporal invariance of the flow state, the spatial pattern of morphologic variables continuously changes until the steady-state is reached. The simulated morphologic variables are compared for two time instants: sub-plots (d) to (f) correspond to the peak of sediment yield, and sub-plots (g) to (i) correspond to the sediment yield steady-state (these two critical times will be further compared in the discussion section). As seen from these two sets of sub-plots, sediment concentrations decrease from the peak yield time to the steady state, and they are particularly high in the area of flow convergence. In contrast, the deposited mass temporally increases and is higher in the headwater areas due to their low stream power. Last, the elevation changes are computed to investigate regions where the domain has eroded (negative magnitudes) or sediment deposition has occurred (positive magnitudes). Overall, extensive areas have eroded with especially high erosion rates in steeper regions; the amount of erosion has consistently increased with the rainfall duration (sub-plot (f) vs. sub-plot (i)).

5.4 Discussion

5.4.1 Variations of sediment yield for the same flow volume

Several of the presented simulation results vividly demonstrate that there can be a considerable variation in sediment yield despite the same rainfall volume. While the dependence on rainfall rate has been long discussed in literature [*Edwards and Owens*, 1991; *Romkens et al.*, 2001; *Abu Hammad et al.*, 2006; *Ahmadi et al.*, 2010; *Svoray and Ben-Said*, 2010], the results of this study address the importance of additional mechanisms that can cause similar conditions of non-uniqueness. Figure 5.7 summarizes the addressed variability by displaying event runoff volume versus the corresponding sediment yield for all of the considered Cases. The initial

condition of soil bed at the simulation start is “intact”, i.e., the soil has not yet been disturbed. This results in a low erodibility of the soil bed, leading to relatively low erosion. This is opposite to the effect of a looser soil condition at the onset of subsequent rainfall event (Cases 1-3, 5). Thus, the sediment yields for two events can be different, while corresponding to the same flow volume (Figure 5.7-(a), (b), and (c)).

Using the above inference (and results shown in Figure 5.7-(a) to (c)), the eroded material generated during the first hour should be progressively smaller than sediment flux leaving the basin during later hours. However, a notable result in Figure 5.7-(f) is that *SY* corresponding to later hours can be smaller than that for the first hour. This result is of interest because in conditions of a relatively loose soil bed material, the erosion loss can become smaller than that for soil in initial, intact condition exhibiting low detachability. Such an outcome indicates that there exists a mechanism that hampers progressively higher erosion. This study argues that the mechanism is mainly attributed to the development of a shielding layer that protects underlying soil, counteracting the effect of an increasing amount of loose material.

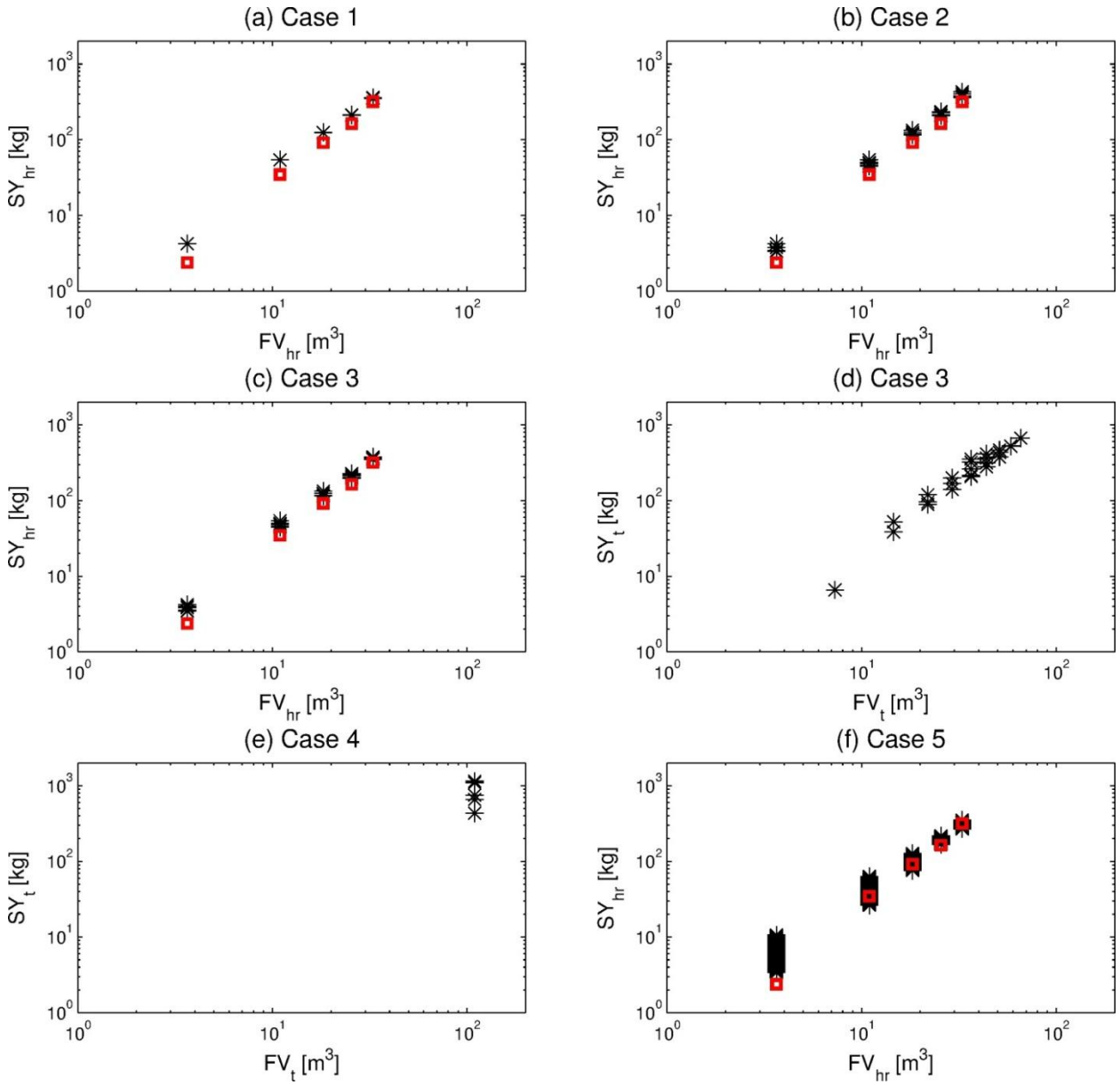

Figure 5.7: Flow volume (*FV*) versus sediment yield (*SY*) for all simulation cases. *FV* and *SY* are computed by integrating the flow and the sediment rates of the corresponding hydrographs and sedigraphs. The red squares correspond to the first rainfall event (1 hour duration, Cases 1, 2, and 3) or simply the first simulation hour (Case 5), for which the initial condition of soil bed was not 'disturbed' (i.e., intact soil bed condition). Black stars correspond to either the second event (Cases 1, 2, and 3 in sub-plots (a)-(c)), the entire single event (Cases 3 and 4, sub-plots (d)-(e)), or hourly volumes (Case 5, sub-plot (f)). Specifically, sub-plots (d) and (e) illustrate FV_t and SY_t that were computed for the entire simulation period of Cases 3 and 4 to ensure the same runoff volume. Sub-plot (f) illustrates a regression between hourly sediment yield (SY_{hr}) and flow (FV_{hr}) of Case 5.

For all of the simulated Cases, a statistical metric is introduced to illustrate how a given precipitation scenario affects the variation of eroded sediment mass. Given the same rainfall volume, the variation of sediment yield mass V_{SY} (in percent) is defined as

$$V_{SY} = \frac{SY_{max} - SY_{min}}{SY_{min}} \times 100\,, \tag{5.1}$$

where the subscripts "*max*" and "*min*" refer to maximum and minimum values among sediment yields (depicted as black stars in Figure 5.7, i.e., excluding the red squares) for the same flow volume. Table 5.3 shows the computed values of V_{SY} for all Cases shown in Figure 5.7. According to these estimates, the range of non-uniqueness caused by the effects of time lag between two successive events of the same magnitude is extremely small (less than 3 %, Case 1). Conversely, sediment dynamics, as affected by magnitude of a previous rainfall event, can result in *SY* variations ranging from 7.88 to 26.6 % (Cases 2 and 3). Even larger variations in the total or hourly *SY* can occur in Cases 4 and 5, implying that longer intervals of coupled flow-sediment dynamics are likely to exhibit a more pronounced non-unique behavior in response to the same input.

Table 5.3: Variations of sediment yield V_{SY} [%] for all Cases shown in Figure 5.7 with respect to the same volume of rainfall corresponding to either the second event (Cases 1, 2, and 3 in sub-plots (a)-(c)), the entire single event (Cases 3 and 4, sub-plots (d)-(e)), or hourly volumes (Case 5, sub-plot (f)).The last two columns represent variations illustrated in Figure 5.7-(d).

Rain Volume [mm]	Case 1	Case 2	Case 3	Case 4	Case 5	Rain Volume [mm]	Case 3
10	0.36	26.64	21.20	-	214.23	40	35.97
30	0.15	21.59	21.41	-	140.88	60	34.32
50	0.44	15.50	15.24	-	68.74	80	42.62
70	1.15	13.79	14.52	-	29.34	100	69.21
90	3.05	18.98	7.88	-	30.55	120	47.79
300	-	-	-	165.53	-	140	24.02
						160	0.97

The last two columns of Table 5.3 illustrate the erosion response based on estimates in Figure 5.7-(d), which show the total sediment yields associated with two-hour rainfall periods; *SY* variations were subsequently computed for the same rainfall volume (Case 3). Additionally, if one separately examines sequences of either increasing or decreasing rainfall magnitude in Case 3, the total *SY* corresponding to the sequence with an increasing trend is always greater than that for a sequence of events with decreasing magnitude. The corresponding variability of the total yield for the same rainfall volume was computed by comparing ten sub-case sets with both increasing and decreasing trends (e.g., one of the sets consists of two sub-cases, i.e., RI_1 = 10, RI_2 = 30 and RI_1 = 30, RI_2 = 10 mm/hr, etc.), which resulted in the range from 1.0 to 36 % (not shown). This variability indicates that depending on whether a storm interval with a higher erosive power occurs at the beginning or the end and depending on how significantly soil bed is perturbed during or prior to it, the prediction of the total sediment loss is strongly affected. In the context of the considered scenario of a continuous 2-hour storm (Case 3), a higher rainfall during the second hour (applied in conditions of soil that was perturbed by the rainfall of the first hour) implies a larger erosion capacity. A similar conclusion was obtained experimentally by *Romkens et al.* [2001] for the case of 2% slope. However, an opposite result was obtained for the other two slopes used by *Romkens et al.* [2001]: a decreasing precipitation rate yielded a larger sediment loss. This was primarily attributed to the surface rilling, which was more severe for a decreasing storm rate, and to the surface sealing, which is unlikely to occur for an initial rainfall of a higher intensity. Although the numerical model used here does not consider the processes of sealing or rill formation, another considerable issue associated with this disparity is in the fact that the study of *Romkens et al.* [2001] did not use particles of larger sizes, being only constrained to 98%

of clay and silt. Due to the imposed short time scale of the experiment (~6 hr) and the used particle sizes, the development of a shielding layer was unlikely to occur.

5.4.2 Initialization effects on the non-uniqueness of sediment yield

The presented results suggest that the initial states of the domain in terms of distributions of flow characteristics and deposited mass can contribute to explaining the processes of sediment dynamics and inferred non-uniqueness of SY. Specifically, Cases 1, 2, and 3 were designed so that first rainfall event generates varying initializations of hydraulic and morphologic variables for the second event. For Case 1, these were flow depth, velocity, and stream power; for Case 2, different distributions of deposited mass were generated; and for Case 3, different flow characteristics as well as sediment concentration and deposited mass were targeted. Basin geomorphic response only to the second event will be therefore emphasized in the analysis.

In Case 1, the total sediment yields generated by the second event ($SY_{t,2}$) for the same rainfall magnitude of the first event (i.e., individual values on the x-axis in Figure 5.7-(a)) are almost unique (less than 3% variations). The sediment partition into the fractions corresponding to the four particle sizes for the second event ($SY_{i,2}$) also does not vary significantly, despite the wide range of initial states of flow depth or velocity (not shown). Specifically, the initial flow depth averaged over the domain before the commencement of the second event ranges between 10^{-3} m, for smaller T_b magnitudes (less than 15 min), and 10^{-6} m, for larger T_b. The general agreement of rainfall or overland flow-driven erosion processes is that the flow depth plays two conflicting roles: it positively impacts fluvial erosion through enhanced stream power; however, by forming a water shield, deeper flow hampers erosion by rainfall detachment [*Gao et al.*, 2003].

The obtained outcome of Case 1 is because the effects of depth are very minor: the domain is of zero-order and therefore there is no sufficient flow accumulation. While the domain conditions represent an idealized simulation case, the same phenomenon can be expected in headwater areas of complex topography exhibiting a small fraction of surface runoff detention.

In Cases 2 and 3, different spatial compositions of bed in terms of original, 'intact' soil and non-local sediment material transported and deposited locally prior to the second event were obtained. In order to capture the differences between the corresponding composition states, particle size distributions of the deposited mass prior to the second event ($M_{i,2}^{ini}$) are averaged spatially and presented in Figure 5.8 (for RI_2=50 mm/hr only). Higher magnitudes of $M_{i,2}^{ini}$ represent a larger proportion of the deposited, loose material. Depending on preceding rainfall (i.e., the magnitude of RI_1), the local surface condition of soil can be partially altered; 5 (smallest rainfall rate) to 20 % (highest rainfall rate) of intact soil was changed to the deposited soil. The deposited sediment also exhibits spatially varying PSDs, which can be very different from the uniform distribution of sizes in the original, intact soil. As seen in Figure 5.8-(b) and (d), a smaller rainfall intensity of the first event leads to a PSD similar to that of the original soil. Conversely, larger magnitudes of the first event transform the composition of the surface soil dramatically, which can become composed of predominantly coarser particles (see Figure 5.8-(b) and (d)). It can be also inferred that as $M_{i,2}^{ini}$ increases, sediment yield ($SY_{i,2}$) also grows initially because the deposited soil material has higher erodibility, as compared to the original soil. However, $SY_{i,2}$ exhibits a maximum at lower magnitudes of the deposited soil material and shows a decay for larger $M_{i,2}^{ini}$ (for both Cases 2 and 3, Figure 5.8-(a) and (c)). A similar pattern of dependence is obtained for other magnitudes of RI_2 (not shown). Such a peculiar behavior is explained by the growing fraction of coarser particles that have high settling velocities: through

their deposition, a surface shield is created. Since large particles (which are otherwise 'loose') cannot be easily entrained, the formation of such a shielding layer protects the underlying intact soil and impedes the process of erosion.

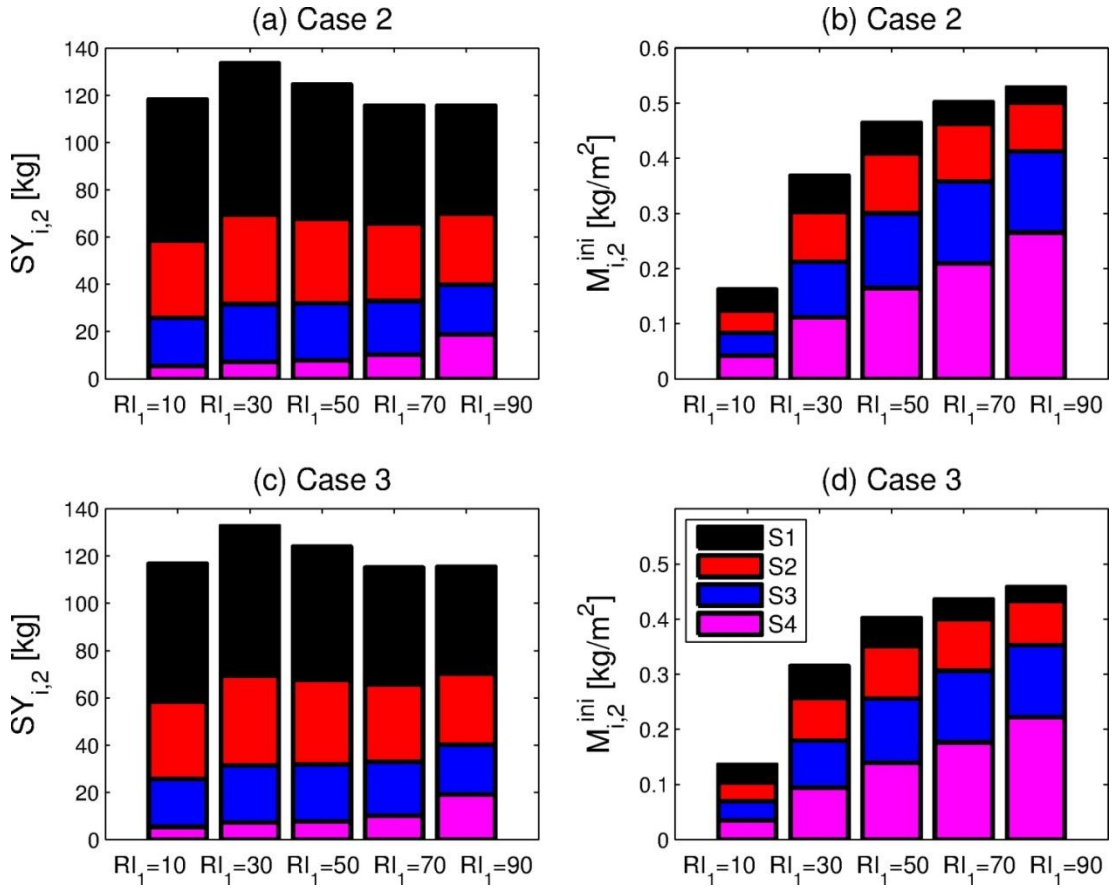

Figure 5.8: The partition into relative fractions corresponding to the four particle sizes (S1 to S4) of sediment yield ($SY_{i,2}$) generated by the second event for (a) Case 2 and (c) Case 3; and the partition of spatially-averaged deposited mass immediately prior to the second event ($M_{i,2}^{ini}$) for (b) Case 2 and (d) Case 3. All sub-plots correspond to the results of RI_2=50 mm/hr.

5.4.3 Patterns of evolution of sediment yield and critical time scales

Morphologic variables characterizing sediment content in water column and deposited area are key indicators for inspecting the variation of sediment yield. The long-term simulation of Case 5 is used to detect phases of non-uniqueness of erosion and deposition processes, relate them to morphologic variables, and find the time scales describing characteristic transitions of sediment generation within a watershed.

The non-unique property of erosion and sediment transport of this particular simulation case has already been illustrated by the sedigraph in Figure 5.5-(c). During the continuous rainfall, water flow achieves steady state early (~4 to 7 minutes after the start) and maintains it over an entire simulation period, as seen in Figure 5.9-(a). Initially, the eroded materials yielded by the catchment are represented by smaller, silt-size sediments that lead to a peak in sediment yield rate at an early stage (~ 4 hours after the start). After the peak, the sediment rate is decreasing and asymptotically approaches the steady state. This dynamic, unsteady evolution is illustrated in Figure 5.9-(b) for RI_1 = 50 mm/hr. As seen, both $SY_{t,hr}$ and $C_{t,hr}^{ini}$ follow the described increasing-decreasing-steady state trend, while $M_{t,hr}^{ini}$ exhibits an increasing-steady state trend. The transitions to the steady state for these three metrics are in general accordance and the determination of the transient time scales thus should play a crucial role in understanding the non-unique property of the erosional response.

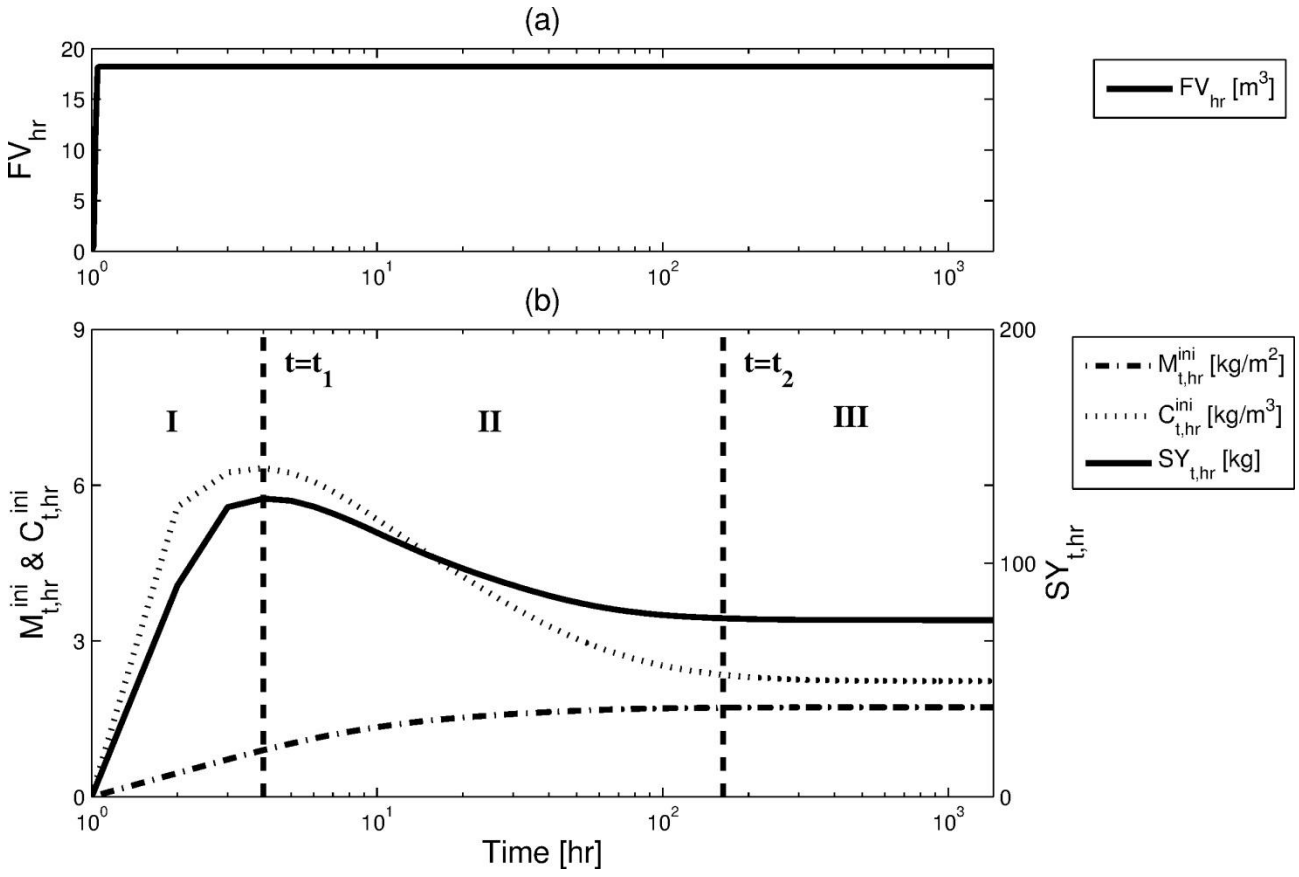

Figure 5.9: An illustration of dynamic, unsteady evolution of erosion and sediment transport response to a continuous rainfall of RI_1 = 50 mm/hr simulated in Case 5. The temporal evolution of (a) the hourly flow volume (FV_{hr}) and (b) the hourly instantaneous, spatially-averaged total concentrations ($C_{t,hr}^{ini}$) and total deposited mass ($M_{t,hr}^{ini}$) as well as the total sediment yield ($SY_{t,hr}$). The left axis is used for $M_{t,hr}^{ini}$ and $C_{t,hr}^{ini}$, while the right axis is used for $SY_{t,hr}$. The two time scales, t_1 and t_2, are identified with the two vertical dashed lines; the three corresponding phases (I, II, and III) are also illustrated. The results obtained for the other rainfall intensities and also specific for each particle size are provided in Figure 5.10.

Two critical characteristic periods, the time to peak (t_1) and the time to steady state (t_2) are defined here by using the simulated sediment yield series. The interval t_1 is defined as the period to a maximum value of SY_{hr} and t_2 is defined as the largest time that satisfies the following two criteria:

$$\frac{dSY_{hr}(t_2)}{dt} < \epsilon \ \ and \ SY_{hr}(t_2) > 1.01 SY_{hr}(t_{end}) \,, \tag{5.2}$$

where t is time; $SY_{hr}(t)$ is the hourly sediment yield at time t; t_{end} is the time at the end of simulation (60 days) at which steady state is achieved for most simulations except for the case with RI_1 = 10 mm/hr in which a much longer rainfall is needed; ϵ is a tolerance value assumed to be 10^{-4} in this study. The above criteria are chosen so as to avoid numerically unrealistic large values in t_2 estimation.

Based on these criteria, both the time to peak (t_1) and the time to steady state (t_2) are computed and illustrated in Figure 5.9 as well as Figure 5.10. The two time scale values are qualitatively related to a given precipitation input and sediment size: the smaller the rainfall rate and the heavier a given particle, the longer it takes to reach t_1 and t_2. This observation can be explained by introducing the dimensionless Shields parameter (τ_*). The Shields parameter, defined as the ratio of the drag force to the submerged weight of a particle, describes the extent of forcing to resistance for sediments:

$$\tau_* = \frac{\tau}{(\rho_s - \rho_w) g D} \,, \tag{5.3}$$

where τ is the shear stress; g is the acceleration constant due to gravity; D is the diameter of a particle. The t_1 and time t_2 time scales are log-linearly and negatively related to the spatially-averaged Shields parameters for both S1 to S4 (Figure 5.11). The obtained relationships confirm

that a higher rainfall forcing will perturb soil bed more rapidly, achieving earlier peak time and steady state. The following section provides further analysis of the two time scales with respect to the rainfall intensities and particle sizes.

For five rainfall intensities and four particle sizes, Figure 5.10 illustrates the dynamic unsteady evolution of three morphologic variables: sediment concentration (C_{hr}^{ini}) and deposited mass (M_{hr}^{ini}) averaged over the basin at every hour as well as hourly sediment yield (SY_{hr}) for the entire simulation period. A qualitative interpretation of this figure reveals that similarly to the results for the total concentration and deposited mass (subplots in column (a)), the hourly, size-specific series of SY_{hr} are in accordance with the series of C_{hr}^{ini} and M_{hr}^{ini} for S1, S2, and S3 particle sizes, while they are dissimilar for S4. Additionally, higher contributions of either concentration or deposited mass to their total can be detected for either smaller or larger particles, respectively.

Based on the criteria formulated in Eq. (5.2), both the time to peak (t_1) and the time to steady state (t_2) were computed and illustrated in all sub-plots (see the two vertical dotted lines in most of the sub-plots). The characteristics associated with these critical times are as follows. (1) The larger the rainfall forcing, the shorter the time intervals to peak and the steady state. (2) The results for the smallest RI_1=10 mm/hr show that the steady state is not reached within the simulation period of 60 days. (3) The patterns of temporal dynamics of sediment variables vary depending on the particle size; specifically, as the size of soil particle increases, t_1 and t_2 also increase. (4) For S4, SY_{hr} approaches the steady state magnitude coincides with the peak, which implies that the values of t_1 and t_2 are equal.

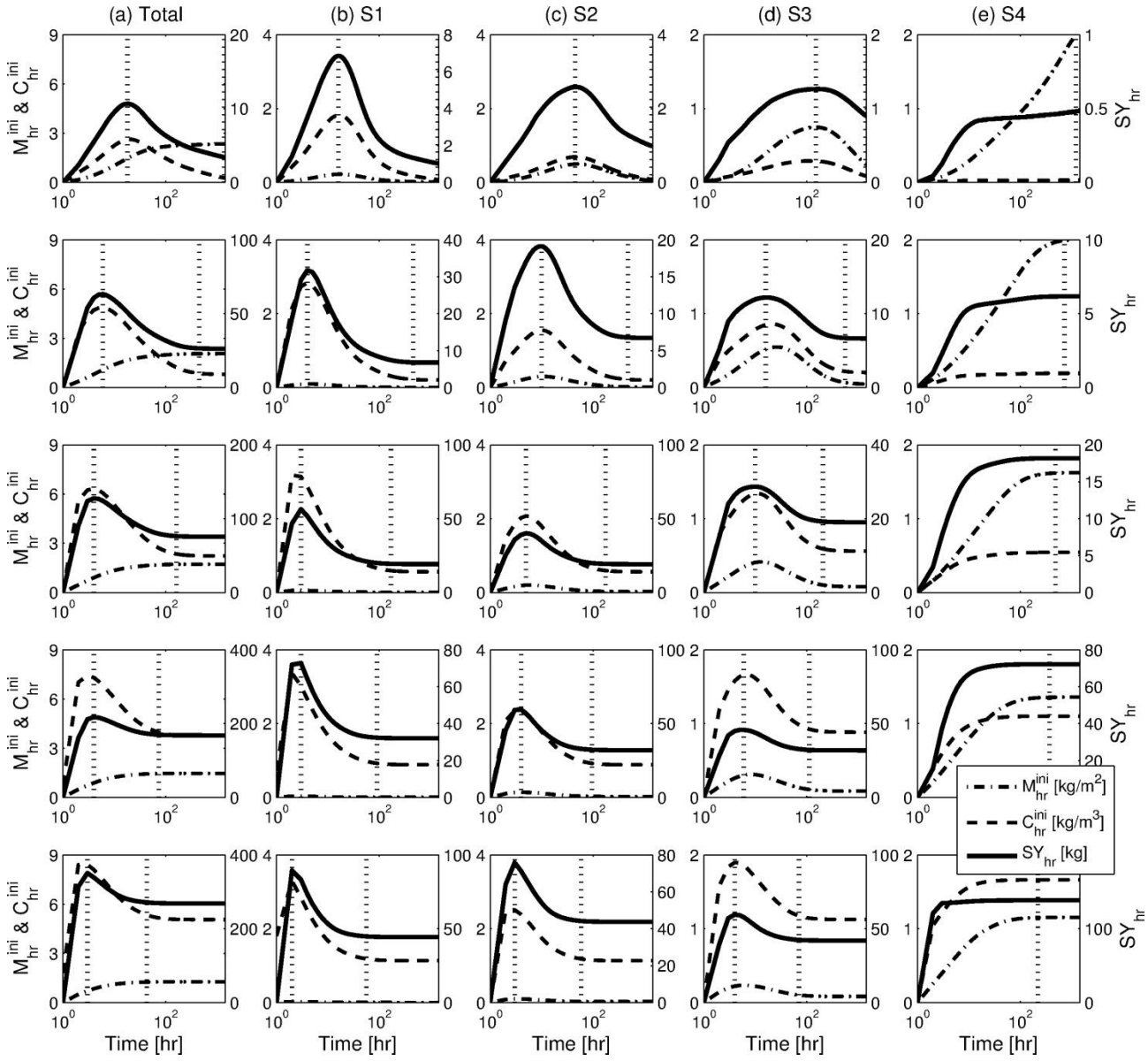

Figure 5.10: The time series of spatially-averaged concentration (C_{hr}^{ini}), deposited mass (M_{hr}^{ini}), and the outlet sediment yield (SY_{hr}) as bulk characteristics (column a) and specific for each particle size (columns b, c, d, and e). Simulation results are for Case 5. The five sub-plots in the same row correspond to the same rainfall intensity: from 10 mm/hr in the top row, to 90 mm/hr in the bottom row. In each sub-plot, the left axis is used for M_{hr}^{ini} and C_{hr}^{ini}, while the right axis is used for SY_{hr}. Two vertical dotted lines represent the time to peak (t_1) and the time at steady state (t_2), respectively.

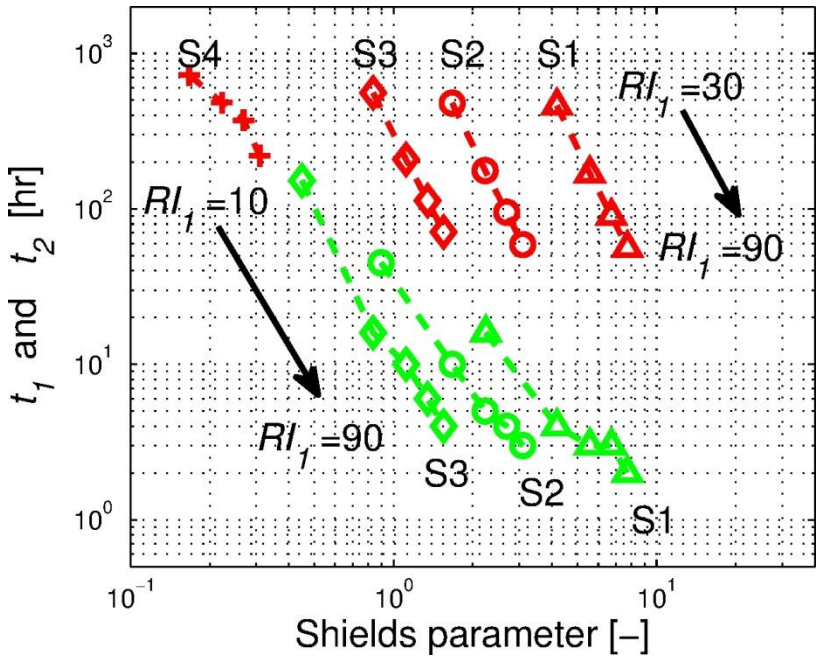

Figure 5.11: The Shields parameter related to the two time scales, the time to peak (t_1) and the time to steady state (t_2): the green dashed lines correspond to t_1, while the red dashed lines correspond to t_2. For S4 ('+' symbol), t_1 and t_2 are overlapped and for RI_1=10 mm/hr, steady state is not reached.

A physical interpretation of the two time scales leads to identification of three characteristic regimes of geomorphic response: flow-limited, source-limited, and steady-state.

I. The flow-limited regime, time $\leq t_1$. At an early stage of rainfall, there is an increase of loose sediments that are likely to be eroded and transported by the flow. As it rains continuously, the sediment contained in the deposited layer and water column also grows, resulting in larger local erosion and yield at the basin outlet. In this regime, the sediment source is always sufficient and does not limit entrainment into the water column. Larger runoff or flow would cause higher erosion and the basin yield.

II. The source-limited regime, t_1 < time ≤ t_2. Continuing rain keeps driving the processes of detachment, entrainment, and deposition, but the geomorphic response changes. Even though the total deposited mass is continuously increasing, the basin sediment yield no longer grows after t_1. This is because of the dynamic evolution of a shielding layer formed by larger, heavier particles. The yield of smaller-sized particles that can be easily eroded and transported is becoming constrained by their availability across the domain, as these particles had been mostly flushed out of the basin prior to the occurrence of t_1. The yield therefore would not respond positively to an increase in runoff/flow depth.

III. The steady-state regime, time > t_2. The ratio between sediment originating from the initially 'intact' soil and deposited mass as well as the partition of each particle size within the deposited soil become time-invariant, reflecting 'stabilization' of the soil bed. For any subsequent hours of the same rainfall forcing, the unit response will be identical. An increase in the rainfall forcing will however drive an unsteady regime that will cause the occurrence of all three phases of sediment dynamics, albeit with different characteristic time scales.

5.4.4 Patterns of temporal evolution specific to particle sizes

Figure 5.12 is intended to facilitate understanding of the temporal evolution of the spatially-averaged concentration of individual particle size $C_{i,hr}^{ini}$ and deposited mass $M_{i,hr}^{ini}$ (the subscript '*i*' denoting the four particle sizes, S1 to S4). The occurrence of the three characteristic regimes for these variables is also illustrated. The cumulative SY_{hr} are shown with respect to $C_{i,hr}^{ini}$ and deposited mass $M_{i,hr}^{ini}$. Overall, the evolution patterns of $C_{i,hr}^{ini}$ and $M_{i,hr}^{ini}$ are contrasting: as a particle size increases, smaller concentrations and higher deposited masses are

simulated; a wide range of concentrations occurs during an early simulation period and a nearly uniform magnitude is reached at steady state. An opposite evolution pattern takes place for the deposited mass. The particle-size specific characteristics of the three regimes can be described as follows. (1) Over the period near the simulation start, $M_{i,hr}^{ini}$ corresponds to the particle size distribution of the original soil. Such a period is longer for smaller *RI* (see Figure 5.13) because the limited erosion or transport capacities resulting from smaller rainfall/runoff rates lead to a delayed initiation of selective erosion processes. Over the same period, a similar mass of each particle size on the bed becomes entrained but heavier materials are deposited at a larger rate, resulting in higher concentrations of smaller particles. In contrast, the sediment sources for all particle types in the bottom and the water column are seamlessly increasing until the timing of peak sediment yield. (2) After the peak time, lighter particles are still preferably eroded and transported within the domain without a significant deposition, as compared to heavier particles. But heavier particles start covering the underlying the original ('intact') soil and thus, the availability of lighter sediment becomes restricted by the deposition of heavier sediment material. This phenomenon is graphically represented as the abrupt decrease of availability of lightest particles ($C_{i,hr}^{ini}$ and $M_{i,hr}^{ini}$), while a gradual increase of the heaviest type (Figure 5.12). At this period, most of particles that are available for erosion are the largest particle type that results in retardation of all relevant erosion processes. The temporal variation of $C_{i,hr}^{ini}$ and $M_{i,hr}^{ini}$ is more significant for smaller *RI* (Figure 5.13). (3) During the steady-state regime, the variations of the morphologic variables stabilize: an almost uniform concentration for all particle sizes in the flow water column is attained; the fractions in the deposited mass however vary by several orders of magnitude (Figure 5.12). These stable morphologic conditions define the continuing steady state

response of the basin. The following section provides an additional analysis of the effects of rainfall intensity on the particle-size specific dynamics.

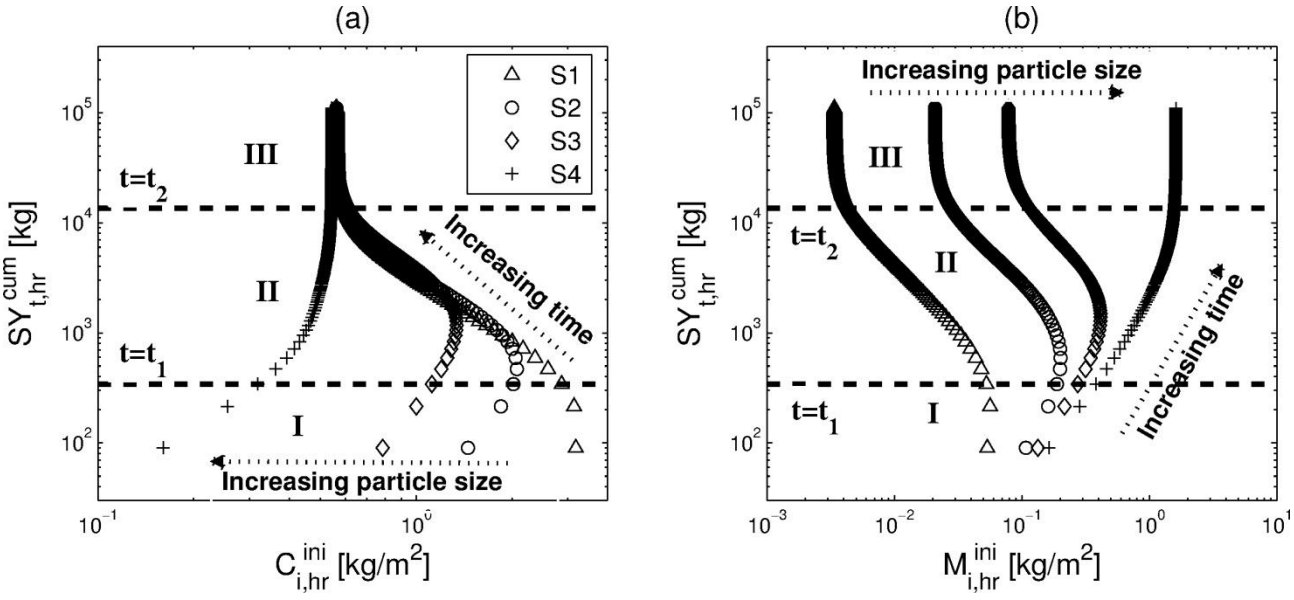

Figure 5.12: An illustration of dynamic, unsteady evolution of erosion and sediment transport response to a continuous rainfall of RI_1 = 50 mm/hr simulated in Case 5. The cumulative total sediment yield resolved at the hourly scale $SY_{t,hr}^{cum}$ plotted against the spatially-averaged, species-specific (for the four particle sizes, S1 to S4) (c) concentration $C_{i,hr}^{ini}$ and (d) deposited mass $M_{i,hr}^{ini}$. The two time scales, t_1 and t_2, are identified with the two horizontal dashed lines; the three corresponding phases (I, II, and III) are also illustrated. The results obtained for the other rainfall intensities and also specific for each particle size are provided in Figure 5.13.

For five rainfall intensities of 10, 30, 50, 70, and 90 in Case 5, the cumulative SY_{hr}^{cum} is illustrated with respect to the spatially-averaged C_{hr}^{ini} (Figure 5.13-(a)) and M_{hr}^{ini} (Figure 5.13-(b)) corresponding to four particle sizes (S1 to S4). Interesting features associated with different rainfall intensities are: (1) the maximum absolute deviation between concentrations or deposited masses corresponding to different particle sizes (i.e., $|C_{4,hr}^{ini} - C_{1,hr}^{ini}|$ or $|M_{4,hr}^{ini} - M_{1,hr}^{ini}|$)

occurs for the smallest rainfall intensity. This signifies that smaller runoff rate allows a wide range of particle size distributions, either near the beginning of runoff generation (for concentrations) or in the steady state (for deposited mass). Conversely, a nearly uniform PSD occurs initially for $M_{i,hr}^{ini}$, resembling the PSD of the original, 'intact' soil; this is more pronounced for the smaller *RI*. Such an effect occurs because smaller eroding or transporting power of smaller *RI* takes a longer time to alter the original soil into 'loose' soil and to initiate size-selective erosion processes. Similarly, a uniform PSD for $C_{i,hr}^{ini}$ is observed when the steady state is achieved.

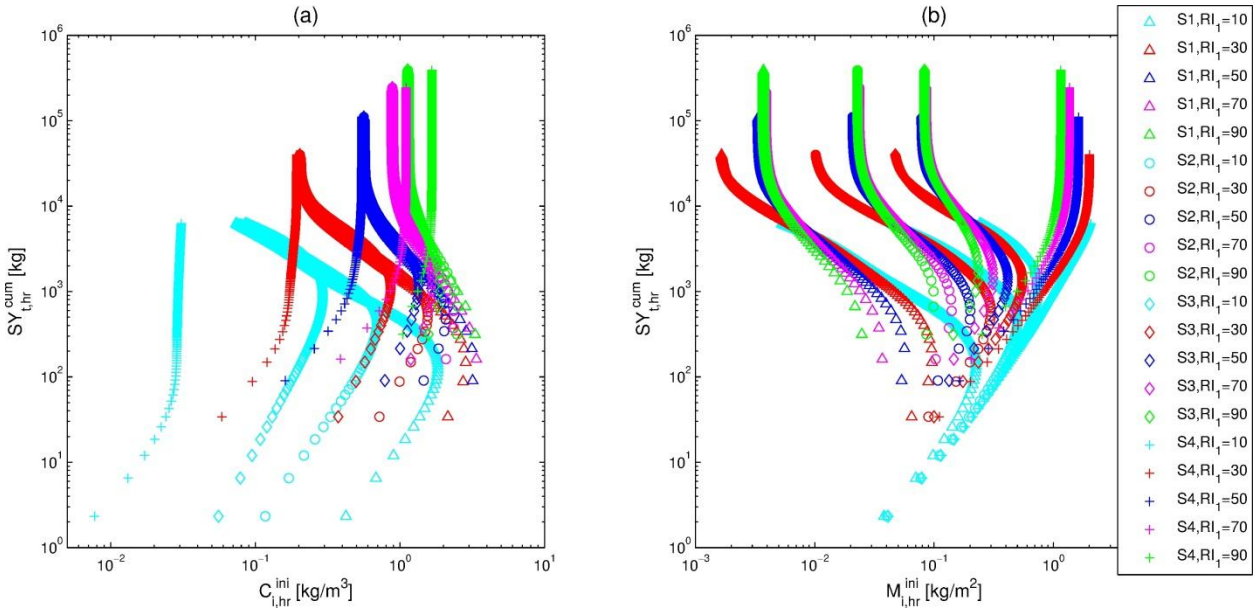

Figure 5.13: The cumulative total sediment yield resolved at the hourly scale ($SY_{t,hr}^{cum}$) versus the hourly instantaneous, spatially-averaged (a) concentrations ($C_{i,hr}^{ini}$) and (b) deposited mass ($M_{i,hr}^{ini}$) corresponding to four particle sizes (S1 to S4) and five rainfall intensities ($RI_{1,}$) of 10, 30, 50, 70, and 90 for Case 5.

5.5 Conclusions

This study develops a series of modeling scenarios for a zeroth-order watershed to generate an ensemble of runoff and sediment responses simulated in a controlled fashion, i.e., without an explicit representation of the processes of infiltration and subsurface moisture dynamics. The series of simulation cases are designed so that rainfall intensity, duration, and lag time between successive events are varied. The anticipated outcome of such a design is that a 'perturbation' of soil substrate by an initial rainfall event influences the conditions of flow and sediment prior to the onset of a subsequent rainfall event. Specifically, in Cases 1, 2, and 3, the first rainfall event generates varying initializations of hydraulic and morphologic variables. For Case 1, these are flow depth, velocity, and stream power; for Case 2, different distributions of deposited mass are generated; and for Case 3, different flow characteristics as well as sediment concentration and deposited mass are produced. Cases 4 and 5 represent simulations of response to relatively long-term precipitation to resolve continuously varying morphologic bed conditions for a steady-stated hydraulic flow regime.

The generated different initial conditions change the particle size distribution of the soil substrate, which may form a shielding layer composed of larger particles. One of the outcomes is that unless the initial condition of flow and sediment is identical, the same volume of runoff (produced at the same rate) can generate different total sediment yields. For example, the variation of sediment yield in Case 1 is nearly zero (less than 3 %), because of the limited change in the initial condition. Conversely, the variations exhibited by the rest of the simulation cases reach up to ~200%. In Case 3, the sediment yield is greater for a sequence of rainfall events with increasing magnitudes, as compared to decreasing magnitudes. This is in contrast to a subset of results by *Romkens et al.* [2001], which can be attributed to their smaller experimental domain

and soil type dominated by finer fractions (98% of clay and silt) as well as an insufficient monitoring period (~6 hr) to observe the development of a shielding layer.

The shield formation by relatively larger particles can be one of the significant controllers of erosion and net sediment transport at the event scale; the cycle of shield formation and destruction is likely to be a strong contributor to the non-uniqueness of erosion dependence on runoff. The temporal development of the shielding layer determines the amount of sediments in the flow water column and areas of deposition, resulting in the dynamic, unsteady variation of sediment yield. For a long-term simulation with continuous rainfall, the peculiar feature of sediment yield is the existence of maximum before steady-state of yield is reached. The two identified time scales, i.e., the time to peak (t_1) and the time to steady-state (t_2) distinguish the corresponding transitions that help addressing the non-uniqueness property of sediment yield from a physical standpoint. Specifically, the time scales imply the existence of three characteristic periods which correspond to flow-limited, source-limited, and steady-state regimes. The flow-limited regime occurs during early stages of rainfall. Continuous forcing leads to an increase of watershed areas where sediment is detached from the soil surface by rainfall or entrained by the flow, resulting in a net increase of erosion. In this regime, the sediment source is sufficient and thus a larger forcing would lead to higher erosion. The source-limited regime corresponds to the time period between t_1 and t_2. During this time, the total deposited mass that has higher erodibility than the original, 'intact' soil is continuously increasing but the domain sediment yield diminishes after t_1. This occurs because of the dynamic evolution of a shielding layer formed by larger particles – they cause a concurrent reduction of availability of lighter sediment because heavier particles cover the underlying intact soil. During the steady-state after t_2, soil bed conditions, i.e., the ratio of the amount of intact and loose materials, and the

component substrates inside the deposited area become stabilized and time-invariant. The stabilized initial condition always provides the identical response to the same forcing. Therefore, a unique relationship between rainfall forcing and generated sediment yield is attained at this phase.

Soil erosion and sediment transport are complex phenomena and it has been practically impossible to fully incorporate all relevant details in numerical models. This study addressed only those erosion processes that are perceived to be essential: rainfall-induced detachment and overland flow-induced entrainment of soil particles, their deposition due to gravity, and shield effects by both larger particles and flow depth. These processes are simultaneously computed responding to a detailed representation of flow motion. Other related processes depending on a degree of soil saturation, slaking, dispersion, crusting, and rill formation are not taken into account because of the intricacies of relevant theories and existing parameterizations. Despite the simplified nature of the erosion processes and the implications of underlying assumptions, the obtained results simulated for a zero-order catchment that represent headwater areas of natural watersheds appear to be physically sound. Two major conflicting effects due to the existence of the shielding layer have been captured: a positive contribution to erosion because of supply of highly erodible sediment and erosion impediment because of constrain on availability of lighter particles. One of implications of this study is that a short-term prediction of geomorphic events from headwater areas may never become a tractable problem. The latter would require an unrealistically detailed spatial characterization of particle size distribution prior to precipitation events.

CHAPTER VI

Research summary and perspectives for future studies

6.1 Summary of research

Watershed systems supply services and goods to human society. They should be sustainable, maintain natural structure and function, and continue to meet societal needs in the long-term. Watersheds however are under the impact of rapid climate change, rarely experienced in the past. In recent years, numerous research efforts investigated the effects of climate change on watershed components. However, comprehensive studies of climate impacts relevant to the scale of human decisions, such as an agricultural field, a stream reach, or a flood-control structure, have been extremely limited. For example, global and regional scale studies have examined the impact of projected climate change on a number of large-scale hydrologic variables [*Barnett et al.*, 2005; *Milly et al.*, 2005]. They however lacked the propagation of this information through watershed systems to seek a more detailed level of flow characteristics (i.e., those that extend beyond the traditional metrics of bulk, area-integrated runoff) that can be directly responsible for major impacts on water quality and aquatic habitat characteristics. At the other end of research spectrum, hydraulic engineers carried out stream-reach scale studies addressing flow regimes and details of flow dynamics. However, by assuming artificial boundary conditions these studies have failed to connect to catchment- and larger-scale (e.g., climate)

information. This has essentially "disengaged" channel flow from watershed processes [*Milly et al.*, 2002; *Arnell*, 2003; *Cherkauer and Sinha*, 2010]. As a result, at present we entirely lack assessments of climate impacts on spatially-distributed flow characteristics, water quality, and aquatic systems through a holistic, multi-scale approach.

One of the primary goals of this dissertation is to develop a holistic, multi-scale watershed model that describes essential physical processes of hydrology, hydrodynamics, and erosion and sedimentation. Such a holistic approach can be the only option to fully consider prominent features of connectivity and nonlinearity in the watershed systems. Disturbances arising at any scale within these systems will necessarily propagate downstream, e.g., large-scale climate perturbations will affect local-scale hydrologic processes, flow regime, erosion, and stream sedimentation. Local-scale effects can be responsible for further damages to aquatic habitats and disruption of ecological services [*Mooney et al.*, 2009]. Due to the tremendous disparity of involved spatiotemporal scales, we currently lack assessment tools that explicitly consider connectivity of watershed processes and are relevant to the "scales of human decisions" and ecosystem services. Further, watersheds are non-linear systems; their dynamics depend on 'convective' and 'dissipative' characteristics of involved processes. The latter are inevitably time- and space- varying and depend on forcings, initial, and boundary conditions. The developed tRIBS-OFM-HRM model is one of the most comprehensive, process-scale tools required for evaluations of climate signals that propagate through a non-linear hydrological system.

In this dissertation, a coupling framework between a hydrologic model, a hydrodynamic model, and soil erosion and sediment transport was developed. A previously existing model describing hydrological processes (tRIBS) has been integrated with a solution of the Saint-

Venant shallow water equations (OFM) and the Hairsine-Rose formulation of erosion and deposition processes (HRM) with multiple particle sizes. The system of equations is resolved using the finite volume method based on the Roe's approximate Riemann solver on an unstructured grid. The Saint-Venant equations are appropriate for simulating flows of relatively small depth and flows passing in narrow openings between vegetation stems in hillslope and channel. The Hairsine-Rose equations allow one to account for size-selective sediment transport and differentiate bed material into original and deposited soil layers. In the flow model, a numerical problem, the "no-flow phenomenon", was observed and resolved by applying a new method of reconstruction of variables. This problem is not generally experienced with hydrodynamic models that rely on 'partially-submerged' cell conceptualization and target typical hydraulic applications. Modifications of the hydrodynamic model were described in Chapter II.

The essential strengths of the combined model described in Chapter III are as follows. (1) Hydrological and hydraulic characteristics as well as the particle size distribution, arguably the three most crucial elements among external and internal factors for modeling erosion, are all simultaneously taken into consideration. (2) The model is based on sound physical laws, which result in narrow ranges of parameter values that are theoretically measurable; satisfactory results can thus be obtained with less calibration efforts. This feature makes feasible a wider range of real-world, catchment-scale flow/erosion problems. (3) The model can solve the overland flow problem in all situations that cannot be addressed with traditional hydrologic models. These include hydraulic jumps, backwater conditions, control structure effects, and simulations for flow converging-diverging effects due to microtopographic disturbances and vegetation features at both micro- (cm) and macro- (km) scales. (4) The model is especially valuable in hydraulic problems related to stream or river domains (e.g., flood inundation), where upstream or

downstream boundary conditions of a river cannot be easily specified and need to be computed independently with a hydrologic model. (5) The spatially distributed, detailed information on soil type, land use, and topography is becoming more accurate and easily accessible. This generates the potential for making modeling of earth-surface processes and aquatic habitat more credible. By incorporating these types of information, the developed hydrologic-hydrodynamic-erosion coupled model can be used as an assessment tool for quantitative evaluation of spatiotemporal erosion responses to imposed scenarios of climate change, variations in land-use, soil, and vegetation in small- to medium-size basins.

Furthermore in Chapter III, the driving role of topography in erosion processes was discussed: an overall "diffusion-like" type of erosion is characteristic of this headwater, zeroth-order catchment: erosion increases with slope and is not greatly affected by the contributing area. In particular, large elevation changes due to erosion occur over a limited hillslope area with abrupt morphological changes: for slopes higher than a particular threshold, erosion grows significantly and in a non-linear fashion. When sediment concentration in surface flow is partitioned according to particle sizes, the spatial distributions exhibit two types of dependencies: with site slope, for larger particles, and with contributing area, for smaller particles. The results emphasize the importance of different basin topographic characteristics in determining the amount of sediment in water column, as mediated by the dynamic flow regime of depth and velocity.

Chapter IV proposed two methods termed "Equivalent Roughness Surface (ERS)" and "Equivalent Friction Slope (EFS)" for computing the upscaled Manning coefficient for areas covered with partially submerged vegetation elements, such as shrub or tree stems. Several predictive equations with four different prognostic variables of the additional resistance caused

by partially submerged vegetation representing the sum of the form and wave resistances were developed. The equations were successfully verified with data reported in five different studies as presented in Table 4.6, and compared with estimates from a predictive equation of *Hu and Abrahams* [2006]. Overall, it follows that the predictive equation derived in this Chapter is well corroborated by reported experimental data and a previously developed formulation for wave resistance. The prognostic regression equation can therefore become a useful tool for upscaling roughness coefficient for vegetated hillslopes.

Further, the effects of four independent variables on the total Manning coefficient were investigated. First, the effect of V_f on n_t is that as V_f increases, n_t also grows. This positive trend is represented by Eq. (4.11) and Eq. (4.13) with high values of the determination coefficient of the log-transform linear relationships. Second, in terms of effects of S on n_t for a fixed V_f and Q, two distinct trends exist: a positive dependence at low flow rates and a decreasing trend at high flow rates. On the other hand, for a fixed V_f and S, two distinct modes of the relationship between Q and n_t emerge: a positive dependence at mild slopes, and a negative dependence at steep slopes. Third, a rougher bed with larger n_b implies an increase of the form/wave resistances due to vegetation. Last, this study corroborates earlier research that n_t grows as h increases and decreases with higher V [*Fathi-Moghadam*, 2006].

In Chapter V, the coupled model has been used to address a possible mechanism leading to the non-uniqueness of soil erosion. The results indicate that unless the initial condition of flow and sediment spatial distribution is identical, the same volume of runoff can generate different total sediment yields even in conditions of identical rainfall forcing. The range of variation can reach up to ~200%. The effect was attributed to two major conflicting effects exerted by the

shielding layer: erosion enhancement, because of supply of highly erodible sediment, and erosion impediment, because of constraint on the availability of lighter particles by heavier sediment. The reasons for non-uniqueness are attributed to two major conflicting effects occurring during the erosion process: erosion enhancement, because of supply of highly erodible sediment from upstream areas, and erosion impediment, because of formation of a shielding layer that constrains the availability of lighter particles due to heavier sediment. Long-term simulations with continuous rainfall also show that a peculiar feature of sediment yield series is the existence of maximum before the steady-state is reached. Two characteristic time scales, the time to peak and the time to steady-state, are eventually presented to separate three characteristic periods that correspond to flow-limited, source-limited, and steady-state regimes. These time scales are demonstrated to be log-linearly and negatively related to the spatially averaged Shields parameter: the smaller the rainfall input and the heavier a given particle is, the larger the two scales are. Despite the simplified representation of the erosion process, the results indicate that a short-term prediction of geomorphic events from headwater areas may never become a tractable problem because the latter would require a detailed spatial characterization of particle size distribution prior to precipitation events.

6.2 Critical assumptions and limitations of the research

Any modeling work inherently contains a number of assumptions or limitations. The most critical assumptions and processes that are not or cannot be fully addressed by the formulation used in this research are summarized as follows.

- *Governing equations*: The first assumption of the study was that a simplified form of the Navier-Stokes equations, the Saint-Venant (S-V) shallow water equations, can be an adequate approximation for simulating flows of relatively small depth and flows passing in narrow openings between vegetation stems. Specifically, the S-V equations can accurately simulate very shallow flows. Although such flows can be affected by both bottom boundary layer and free surface movement, and the vertically averaged S-V equations cannot recognize these effects of bottom/free surface boundaries, this assumption is quite acceptable in an overland flow condition with small depths and a large spatial scale of the domain. The requirement in application of the S-V formulation is that the depth (i.e., the vertical direction scale) should be much smaller than the length scale of a flow phenomenon in the horizontal direction. This is certainly the case here. The relevant discussion is presented in Chapter IV.
- *Passive admixture of sediment load*: This study assumed that sediment concentrations are small enough and do not affect the movement of the fluid. This assumption is acceptable because the relative time scale between the flow and deformation time scales [*Cao et al.*, 2002] is always above 10^4, a threshold advocated by *Cao et al.* [2002], who suggested the magnitude as the relative time scale. However, for torrent flow conditions with high particle concentrations (e.g., dam-break or debris flow), where sediment cannot be considered to be a passive admixture, a simultaneous solution of the S-V equations and H-R equations is preferable [*Cao et al.*, 2002]. A possible flow and morphologic condition satisfying such criteria occurs in the Yellow River, China, where typical

concentrations are very high, at approximately 10 %, i.e., ~265 kg/m^3 [*Cao et al.*, 2002].

- *Representation of friction*: The estimation of friction terms has been one of the most difficult issues. A concern of the study was whether the Manning's parameterization used in the S-V equations can adequately capture the energy loss due to eddies generated around plant stems. Three-dimensional turbulence modeling would appear to be a more suitable method that can consider such effects and thus reduce the uncertainty of simplifying assumptions of the S-V model. However, the application of turbulence models presents a number of challenges. First, several parameters still need to be determined to close a system of turbulence equations, e.g., k-epsilon, k-omega, SST, etc. for RANS models or Smagorinsky constant in LES models. Second, in order to accurately resolve turbulent eddies, appropriate representation scales have to be used and very fine mesh resolutions are necessary; as a "rule of thumb", mesh resolution has to be at least one order of magnitude finer than the effective eddy scale.
- *Representation of deposition rate*: Two implicit assumptions of Eq. (3.12) were employed. One is that the suspended load in the water column is completely mixed in the vertical direction [*Hairsine and Rose*, 1992], and the other is that infiltration rate does not affect settling velocities [*Tromp-van Meerveld et al.*, 2008]. The former assumption cannot be avoided because the two-dimensional H-R erosion model coupled with the vertically-averaged S-V equations indeed cannot recognize the non-uniform vertical distribution, although the sediment concentration adjacent to the soil bed should be used. The latter assumption is

additionally employed in applications at the watershed scale because current deposition equations including infiltration rates are not univeral and are only appropriate for limited experimental conditions. A universal relationship at watershed scale where infiltration rate is really time-dependent and varies with soil moisture condition should be required.

- *Effects of matric pore pressure*: The erosion phenomena related to subsurface water content and the effect of negative or positive soil matric pore pressures were not considered [*Simon and Collison*, 2001]. For instance, as soil becomes saturated, erosion can increase due to the growth of pore water pressure that reduces soil cohesive strength [*Simon and Collison*, 2001], but this phenomena cannot be taken into account in this model.
- *Slaking effects*: The model does not consider erosion enhancement due to increasing aggregate breakdown and slaking, which is attributed to air burst within the pores of aggregates during rapid wetting [*Le Bissonnais et al.*, 1989; *Rudolph et al.*, 1997]. The process of slaking is more pronounced in soils where organic matter that contributes to binding mineral particles is low.
- *Dispersion effects*: One of the repelling phenomena of soil particles in condition of wet soil is dispersion. This process is due to an interaction between a layer of positive charges composed of chemical cations (e.g., sodium, calcium, and magnesium) surrounding clayey soil particles that carry negative electrical charge.
- *Crusting and sealing effects*: Drying of slaked clayey soil that leads to crusting and sealing and may result in a reduction of infiltration and growth of runoff and erosion [*Le Bissonnais et al.*, 1989] was also not considered.

- *Representation of rill*: The employed model cannot represent "sub-grid" processes, such as the flow motion occurring in narrower, faster flow threads of the assumed planar surface of a computational cell (i.e., a triangle surface). Specifically, the numerical model does not require a "rill" or a "stream parameterization", provided the resolution of computational cells is small enough to capture the scale and the actual representation of a rill or a stream. If the resolution is coarser, however, the model formulation assumes sheet flow within a cell.

In summary, several assumptions in terms of process representation or parameterization of the friction terms and the deposition rates were applied; a number of processes related to a degree of soil saturation, slaking by trapped air, repelling between chemical cations (dispersion), crusting, and rill formation were excluded in this study. Better parameterizations or exact mathematical theories associated with these processes are needed for a more complete numerical treatment of the erosion process.

6.3 Uncertainties in the multi-scale modeling

6.3.1 Verification of the coupled model

Since all numerical models are developed to mimic real world systems, yet they are never expected to exactly reproduce the behavior of a real system, any numerical model must be verified to the degree that the model is deemed to be credible and accurate in its prediction. Thus, the verification or validation process is a necessary step in the development of a model before users or policy makers can employ it in providing simulation results and making a decision from

its outputs. Verification is usually carried out by comparing numerical results with analytical solutions, other numerical results obtained from previously developed, credible models, and observation data obtained in laboratory and field. Among these comparison methods, the field data are most valuable because the model can be validated in conditions that are most similar to real watershed systems. However, obtaining a sufficiently detailed field data that can be used for comparisons with results describing two-dimensional spatial flow and sediment fields is very difficult, expensive, labor intensive, and time consuming.

For the verification of the proposed model, analytical solutions for flow and sediment behaviors, numerical results obtained from commercial models, and observation data measured in real watersheds were used. However, these comparisons mostly focused on observations at a single outlet point. For confirming the simulated spatial variability within watersheds, a large array of relevant data including topography, soil and landuse, spatial varying flow and morphologic distributions, etc. is needed; however, it is very difficult to obtain all of the required information. Sediment-related data are available from experimental studies in several watersheds: Walnut Gulch Experimental Watershed (WGEW) at Tombstone, Arizona; watersheds at Heks, Kinderveld, Huldenberg, and Nethen located in Belgium. However, even in these experimental watersheds, data have a number of limitations and are insufficient to completely verify the spatial results of the developed model. For instance, the sediment data for WGEW, Heks, and Kinderveld were measured only at the outlet location. The short period of point observations and unavailability of all required data indicate that a complete validation of a two-dimensional model may never be possible, and model predictions will always contain poorly quantified uncertainties. In order to reduce these uncertainties, intensive observations sets that include spatially and temporally varying sediment fields in both water column and soil bed will be required.

6.3.2 Calibration of the coupled model

Calibration of a numerical model that uses multiple input parameters to represent physical phenomena is a challenging task. This is especially true for a coupled model that involves a description of a variety of physical processes. Depending on how the calibration process is carried out, which parameters are chosen as primary for a calibration analysis, their covariance properties, and what range of values is inferred for non-calibrated parameters from previous references, the outcome can have plausible ranges of variations, which would imply different physical behaviors. In this study, the parameters are grouped according to their primary effect in simulating hydrologic, hydraulic, or sediment erosion-transport dynamics. Approximately 70 % of the parameters are used to represent hydrological processes that are further categorized as three sub-groups representing soil hydraulic properties (9 parameters) associated with processes of infiltration and runoff production, soil thermal properties and vegetation characteristics (7 parameters) related to evapotranspiration and energy balance, and vegetation interception (6 parameters), which influence the storage capacity and canopy dynamics of moisture in the canopy water balance model.

In the presented case studies, the first calibration effort was devoted to the hydrologic component. The saturated hydraulic conductivity and the conductivity decay parameter were selected as the primary variables significantly affecting the processes of infiltration and runoff production. Thus, only a limited number of these two parameters were calibrated, while the remaining seven parameters were fixed because of narrow plausible range of values as inferred from literature. This is acceptable because previous studies have shown that the calibration effort related to the latter parameters is not high. In terms of the model hydraulic component, only a single parameter used for computing the friction force needed to be calibrated. The Manning

roughness coefficient was calibrated using flow information observed at the event scale by matching the measured and simulated flow hydrograph characteristics at the basin outlet. The last parameter group used in this study is for simulating erosion and sediment transport. In this group, four out of six major parameters were calibrated by matching the measured and simulated event sediment yield, while the effort of calibrating the remaining two parameters was reduced by using existing relationships.

An extensive analysis of the relative importance of parameters, sensitivities of parameters under various experimental conditions, and uncertainties related to calibration has not been fully performed in this study. It is noted however that in no way this research neglects the need to understand why uncertainties occur and how uncertainties in parameter values may affect the representation of hydrologic, hydraulic, and morphologic systems. The analysis of uncertainty and sensitivity of parameters is addressed in the next section by using a large-scale database.

6.4 An feasibility study of soil loss assessment

This section addresses a feasibility of a national soil loss assessment by using the physically-based, coupled model described in Chapter III. The soil loss assessment has been of great interest because soil erosion plays a pivotal role in understanding and managing negative implications on cropland productivity or sustainability (on-site impacts) and on water quality and biological activity (off-site impacts). The U.S. national erosion assessment using the National Resources Inventories (NRI-s), i.e., a statistical survey of the national resource conditions and trends, [*Nusser and Goebel*, 1997], has been performed by the U.S. Department of Agriculture-Natural Resources Conservation Service (USDA-NRCS) every five years since 1982 [*USDA*-

NRCS, 2009; 2010]. At the core of the assessment methodology is the Universal Soil Loss Equation (USLE) empirical equation, which was developed using plot-scale observations that covered a wide range of long-term historical climate conditions, soil properties, site characteristics and cropping and management practices [*USDA*, 1965; 1978]. Specifically, USLE equation has the following form:

$$U_A = U_R \times U_K \times U_{LS} \times U_C \times U_P \,, \tag{6.1}$$

where U_A represents the long term average annual soil loss [tons/acre/year]; U_R is the rainfall and runoff factor; U_K is the soil erodibility factor; U_{LS} is the slope length-gradient factor; U_C is the crop and management factor; U_P is the support practice factor.

Soil erosion rates have been estimated in the form of average annual rates, which showed a moderate success of implemented practices and delivered credible knowledge about the status, conditions, and trends of erosion on non-federal cropland. One of the key findings was that due to introduction of conservation practices, such as specific tillage methods, landuse conversions, and erosion protection enforced by the Food Security Act of 1989 to mitigate erosion, soil loss caused by flow and wind processes decreased by 43 % between 1982 and 2007 [*USDA-NRCS*, 2010].

However, this assessment based on USLE and its 6 principal parameters (rainfall, soil erodibility, topography, cover and management, and support practice factors) is not entirely adequate to capture the high nonlinearity of erosion phenomena in changing climate conditions and address connectivity between watershed components. This is because of USLE's inherent nature of an empirical equation involving lumped parameters that cannot be directly measured in the field, thus inducing an ad-hoc selection of parameter values. It is also because of region-

specific characterization that the parameters cannot easily take non-linearities between sites into account, thus limiting transferability of parameters from one location to another. At present, we entirely lack assessments of climate impacts on erosion using physically-based approaches. To address this question, the coupled model should be verified with extensive data and then corresponding parameter sets for various conditions should be generated. A feasibility attempt is carried out in the following Section by using the USLE database, where 3195 plot-years (310 plots) at 14 sites are available.

6.4.1 USLE database and rainfall disaggregation

The collection of data that contributed to the USLE database was initiated in 1940 in the Corn Belt States. The procedure developed in this region is known as the 'slope-practice method'. In 1946, a national committee attempted to extend this method to cropland in other regions by modifying the Corn Belt factor and a rainfall factor, resulting in the development of the Musgrave equation. From this region-specific soil erosion equation, USLE was developed at the National Runoff and Soil Loss Data Center established in 1954, where a collection of data files containing over 11,000 plot-years of observations at 47 locations in 24 states were used. Only 3195 plot-years (310 plots) at 14 field sites are available from the website: http://topsoil.nserl.purdue.edu/usle. The database consists of three data sets of storm, soil loss and runoff, and site-specific data for crop rotations, special practices, and management. Furthermore, it provides a variety of soil conditions, slope magnitudes, climate conditions, landuse cover, farming and conservation practices, management information (crops in rotation). Table 6.1 summarizes the locations of USLE database for which all storm, runoff, and soil loss data are accessible.

Table 6.1: A summary of USLE field locations and WebMET database climate stations used for rainfall disaggregation. The "Lat." and "Lon." denote the latitude of longitude of the USLE locations; the "mi" denotes the distances in miles between original locations and WebMET meteorological stations. The last column reports the period for which the hourly time series of precipitation in WebMET stations are available.

No.	USLE Location	Lat.	Lon.	WebMET location	mi	hourly
1	Batesville, AR	35.8306	-91.7944	Memphis Intl AP, TN	115	61-90
2	Tifton, GA	31.4461	-83.4767	Macon Middle GA Regional	86	61-90
3	Watkinsville, GA	33.8628	-83.4081	Athens Ben Epps	7	61-90
4	Joliet, IL	41.5033	-88.1027	Chicago Ohare	35	61-90
5	Urbana, IL	40.084	-88.2404	Springfield Capital	78	61-90
6	Clarinda, IA	40.7244	-95.0191	Des Moines intl	90	61-90
7	Seymour, IA	40.6667	-93.1167	Des Moines intl	67	61-90
8	Hays, KS	38.8586	-99.3358	Goodland Municipal	131	61-90
9	Presque Isle, ME	46.6540	-68.0089	Caribou Municipal	15	61-90
10	State College, MS					
11	Bethany, MO	40.2575	-94.0269	Kansas City	76	61-90
12	Beemerville, NJ	41.2096	-74.6930	Newark	43	61-90
13	Arnot, NY	42.2632	-76.6278	Binghamton Broome County	33	61-90
14	Temple, TX	31.0957	-97.3452	Waco Blackland Field	36	61-90

Although the database provides storm characteristics, their use is limited in performing a numerical simulation because rainfall monitoring was not carried out in a continuous fashion; storm information contains storm date, duration, total depth, 5, 15, 30, and 60 minute interval peak intensities. In order to perform a numerical simulation, one needs rainfall series obtained by disaggregation of rainfall information provided at the event scale. In this section, the multiplicative, microcanonical model, one of the available stochastic disaggregation techniques [*Menabde and Sivapalan*, 2000; *Molnar and Burlando*, 2005; *Fatichi*, 2010], is used to generate continuous, high-resolution rainfall time series. The procedure generating disaggregated precipitation series involves (1) estimation of the parameters illustrated in Figure 6.1, (2)

carrying out the multiplicative process using information on the total amount and duration of a storm event, (3) re-aggregation to the fine-scale rainfall series obtained in the previous step into the series with 5, 15, 30, and 60 minute intervals, and (4) determination of the proper disaggregated time series by checking that storm characteristics satisfy the given 5, 15, 30, and 60 minute peak intensities. A large number of rainfall series satisfying all of the requirements can be attained. For example, 15 different rainfall series are used for the simulation described below and one of the series is illustrated in Figure 6.2.

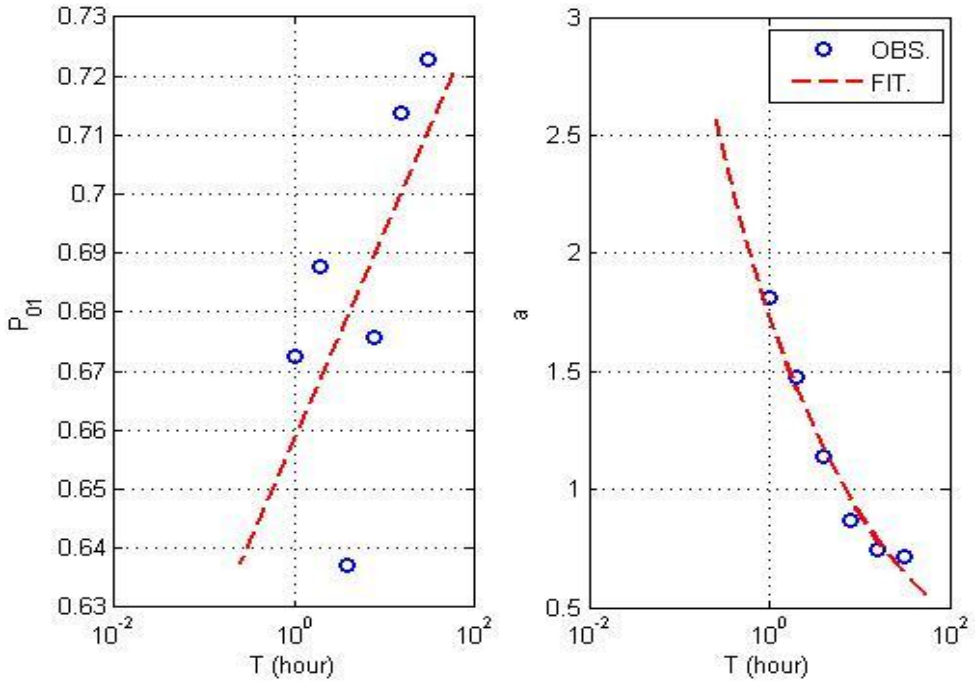

Figure 6.1: Parameters of the microcanonical disaggregation model for the location of Watkinsville, GA. The rainfall data for a station at the Athens airport are used. The left plot shows the probability that the cascade weight is 0 or 1 against the time scale, while the right plot shows the parameter of Beta distribution for the cascade weights. The dashed lines are a fitted logarithmic function (left plot) and a fitted power law (right plot). The blue circles indicate the time scales over which the models disaggregate rainfall.

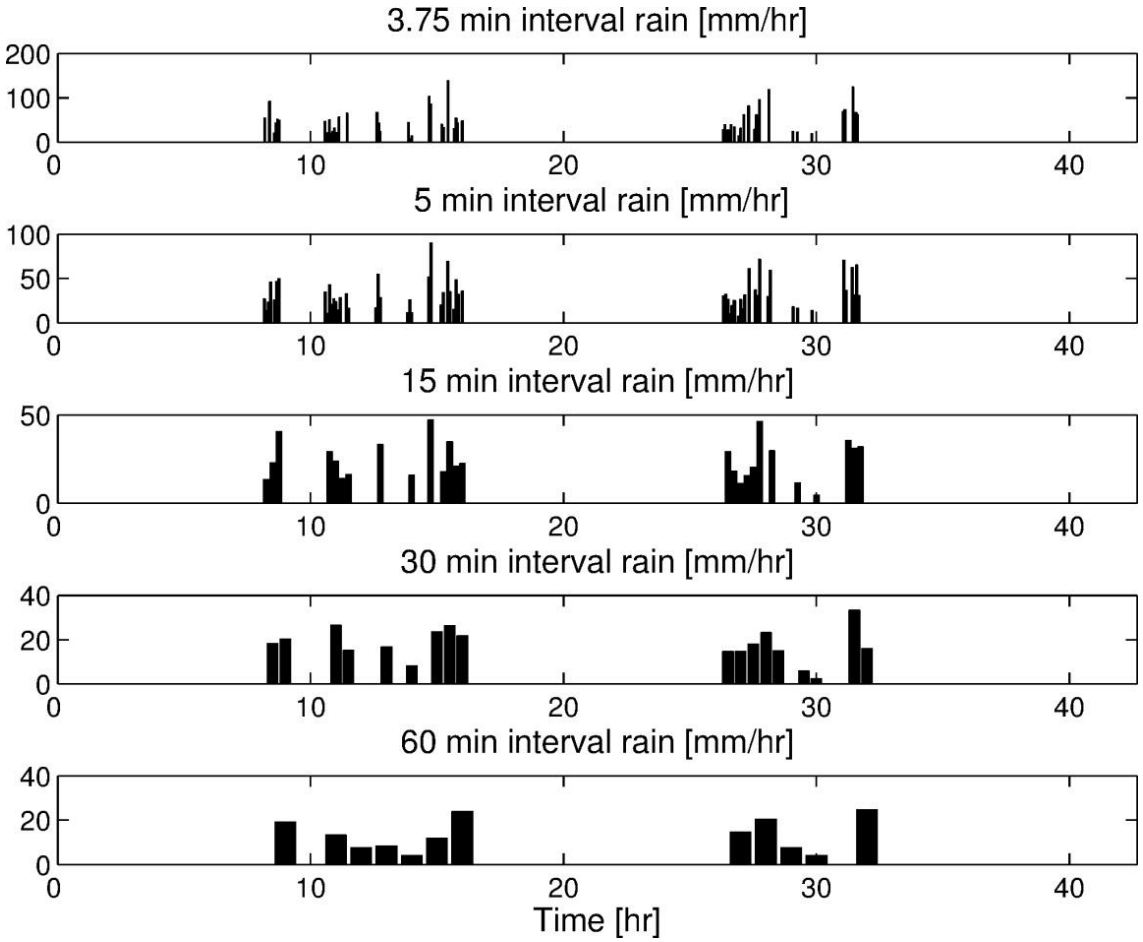

Figure 6.2: An example of generated rainfall series. The top plot is first based on the total amount and duration of storm and then aggregated into rainfall series with 5, 15, 30, and 60 minute intervals in order to verify that the disaggregated storm characteristics satisfy the peak intensities over these intervals.

6.4.2 Numerical representation and results

The location of Watkinsville, GA is chosen because detailed rainfall data are available for a nearby location (the Athens airport). Since the soil texture at this site is sandy clay loam (clay=25%; silt=25%; sand=50%), four different particle fractions (each contributing an equal mass fraction of 25 %) are considered as an initial bed condition. The sediment size of each soil particle type is assumed to be 0.005, 0.05, 0.1, and 0.5 mm, respectively. The smallest particle type is called S1, the second smallest and progressively larger particle types are respectively called S2, S3, and S4 types. Their corresponding settling velocities, $v_{1,\ldots,4}$, are 0.0000173, 0.0017, 0.0062, and 0.0619 m/s. They are calculated using a formula of *Cheng* [1997]. Also, a sloped plane with a length of 21.4 m and a width of 6.4 m is used for representing the experimental design of plots that formed the empirical USLE database. The slope of the domain is 7 %; the area of smallest triangular cell is 0.032 m^2; the number of nodes and cells are 4374 and 8559, respectively; the time step used for flow and erosion equations is 0.1 sec; the Manning's coefficient of 0.03 is calibrated. Table 6.2 summarizes the rest of parameters and their calibrated values.

Figure 6.3 illustrates the results of comparison of the observed and simulated runoff and sediment loss at Watkinsville, GA for a storm event on October 19, 1950. As seen, the computed runoff and soil loss show a satisfactory comparison. An interesting feature of this figure is that variability of data observed at five different plots is greater than that of the simulation results that only incorporated the uncertainty of precipitation forcing. This result underlines the uncertainty inherent to the process of erosion and sediment transport.

Table 6.2: Parameters used to represent hydrologic, hydraulic, and sediment erosion-transport dynamics for the location of Watkinsville, GA. The letter "C" refers to the parameters whose values were calibrated; "L" refers to the parameters whose values were inferred from literature.

Parameter	Description	Value	Unit	Source	Usage
n	Manning coefficient	0.033	$s/m^{1/3}$	C	Flow
a_0	Detachability of original soil	41.3	kg/m^3	C	Erosion
a_d	Detachability of deposited soil	2000	kg/m^3	C	Erosion
F	Effective fraction of excess stream power	0.01	-	C	Erosion
Ω_{cr}	Critical stream power	0.00012	W/m^2	L	Erosion
J	Specific energy of entrainment	366.22	m^2/s^2	L	Erosion
M_t^*	Deposited mass needed to sheild original soil	2.7	kg/m^2	C	Erosion
K_s	Saturated hydraulic conductivity	7.93	mm/hr	L	Soil
θ_s	Volumetric soil moisture at saturation	0.414	$m^3\ m^{-3}$	L	Soil
θ_R	Volumetric residual soil moisture	0.0463	$m^3\ m^{-3}$	L	Soil
m_p	Pore-size distribution index	0.1426	-	L	Soil
φ_B	Air entry bubbling pressure	-63	mm	L	Soil
f_d	Conductivity decay parameter	0.032	mm^{-1}	L	Soil
A_s	Anisotropy ratio in the saturated zone	1	-	L	Soil
A_u	Anisotropy ratio in the unsaturated zone	1	-	L	Soil
η'	Bedrock depth	50	M	L	Soil
k_s	Volumetric heat Conductivity	0.214	J/m/s/K	L	Soil
C_s	Soil heat capacity	1209573	J/m^3K	L	Soil
S_s	Canopy storage	1	mm	L	Landuse
B	Interception coefficient	0.2	-	L	Landuse
p	Free throughfall coefficient	0.35	-	L	Landuse
S_c	Canopy field capacity	1	mm	L	Landuse
K	Drainage coefficient	0.18	mm/h	L	Landuse
g_d	Drainage exponent parameter	3.9	mm^{-1}	L	Landuse
alb	Albedo	0.22	-	L	Landuse
H_v	Vegetation height	0.46	-	L	Landuse
K_t	Optical transmission coefficient	0.7	-	L	Landuse
r_s	Reference canopy stomatal resistance	200	s/m	L	Landuse
V_f	Vegetation fraction	0.5	-	L	Landuse

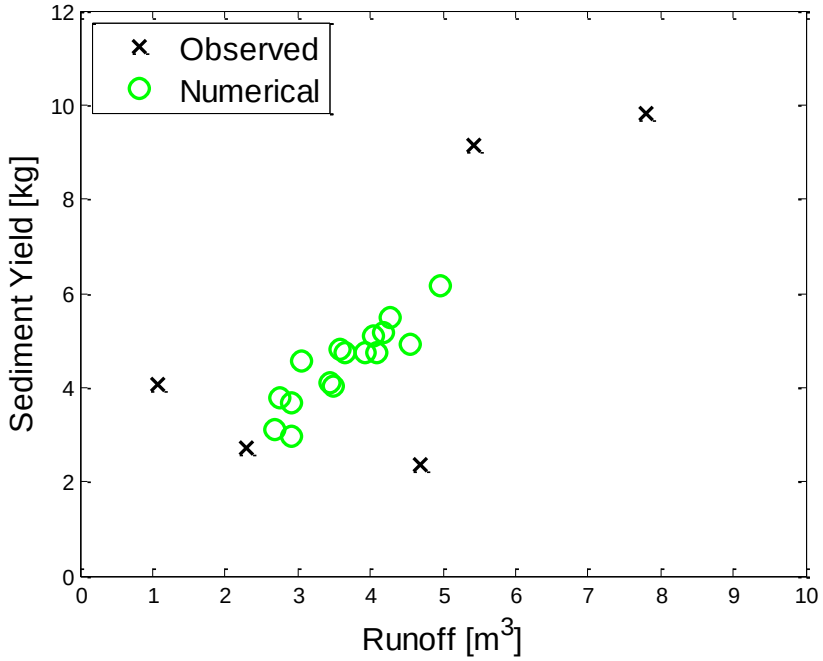

Figure 6.3: A comparison of runoff and sediment yield obtained from observed date and simulations. The five observed data values correspond to observations at 5 plots at the Watkinsville, GA, for a storm event starting on 19th of October in 1950. The green circles indicate the simulation results for 15 different disaggregation rainfall inputs.

6.5 Future studies

6.5.1 Eco-hydrologic-hydraulic-morphologic modeling and their interactions

The USLE database offers extensive availability of historical observations. At present, only a single parameter set corresponding to the event at a specific location was derived, while more detailed research is needed for complex farming conditions that exhibit random variations of surface roughness, ridge height, bulk density, effective hydraulic conductivity, tillage date/depth, surface disturbance level, vegetation growth, and residue burial amounts. The use of USLE database regarding the varying farming conditions enables us to investigate and quantify

the soil-terrain-vegetation interactions of watershed systems. However, numerical representation of such conditions is very challenging because it is involved with feasibilities of several processes of flow, subsurface, and vegetation; thus can only become a reality under the multi-scale, coupled approach proposed in this dissertation. In the future study, numerical simulations with all eco-hydrological-hydraulic-morphologic components will be addressed as one of the most fruitful topics. How important is a fully consideration of connected watershed systems in quantifying the response of the morphologic variations in future climates? What is the role of vegetation in the sedimentary dynamics? Does vegetation influence hydrologic partitioning of water and energy, converging and diverging flow and sediment movements, and their accumulation behind a clump of vegetation? Also, how can topographic characteristics of domain affect morphologic features? Do north-facing hillslopes increase erosion or deposition? Is this phenomenon because of different vegetation due to opposing climate conditions?

6.5.2 Future assessment studies with uncertainty analyses under climate change

Another prospective of the future studies is to investigate the uncertainty and non-linearities of morphologic responses for the climatologic signals given in a watershed system. Due to feedback and compensatory processes as well as the dissipative nature of watersheds, the key to a breakthrough in predictive capabilities lies in an integrated, interdisciplinary approach, whereby the physically-based model can be used for climate impact evaluations. The processes involved in the propagation of climate signals are characterized by such vastly different spatial and temporal scales with high non-linearities. As mentioned previously, any response to the forcings such as precipitation and temperature showed a highly varying, sometimes contradictory result, but sufficient explanations for the result were not discussed yet. How can we characterize

uncertainty and non-linearities associated with projections of climate change impact on watershed systems? How do large-scale processes affect variables at the scales relevant to human actions and ecosystem services? To answer the questions, the following elements will be explicitly addressed in future assessment studies: (1) the uncertainty of climate projections, as inferred from an ensemble of GCM realizations [Note: the current generation of Global Circulation Models (GCMs) exhibits a large degree of uncertainty in simulation of precipitation, the primary hydrological driver; the typical ad hoc selection of a given GCM for impact evaluations introduces subjectivity into the assessment process]; (2) the uncertainty of hydrological simulation [Note: a single hydrological model is typically used in assessments because of lack of standardized physically-based models; uncertainty estimation has to accompany inferences of a single-model assessment]; (3) when precipitation extremes are concerned, alternative approaches to their projection into future need to be accounted for [Note: both GCMs and Regional Climate Models (RCMs) do not capture extremes well]; (4) the dynamic nature of vegetation has to be accounted for [Note: currently, hydrological assessments do not represent the physiological response of vegetation to longer growing seasons, warmer conditions, and atmosphere enriched with CO2, a potentially important feedback from the land-surface]; and, importantly, (5) the hydrological impacts of climate change need to be represented at a range of spatiotemporal scales (multi-scale), in particular, at those relevant to the scales of human actions and ecosystem services [Note: similar to the concept of a using a finer-resolution RCM forced with boundary conditions of a coarser-scale GCM, a nested, multi-scale approach to assessments in hydrological modeling will generate features emerging from atmosphere-vegetation-soil-streamflow processes, which will be dynamically consistent with boundary

conditions generated by a coarser watershed-scale model. All these elements will be addressed in the future studies.

6.5.3 A longer time simulation with a parallel mode

This study was one of the first who addressed the interactions between the watershed components. Chapter III was to identify the effects of topography on morphologic behaviors; Chapter IV was to quantify the interactions between flow and vegetation; Chapter V was to investigate the effects of climatological forcing on morphologic variations. These Chapters, by assuming the bed condition as impermeable and considering vegetation growths as static, focused on a short-term response between the processes and did not fully take hydrological effects or vegetation dynamics into account at long-term scales due to the constrained time step. Since a longer time simulation helps us to understand valuable information on the seasonal patterns or cycles of hydrologic, morphologic, hydraulic variables, we need to extend feasibility of the model to the longer time simulation. However, unfortunately, the long-term simulations in serial mode are not currently feasible because of a limited computing power and the inherent feature of the adopted numerical scheme. Therefore, for attempting to trade off the accuracy of the numerical model against the efficiency, a promising alternative is to perform the model with a parallel mode. One of the future directions will be focused on overcoming the constraint of temporal scale by means of a parallelized code.

APPENDIX A

Error Indices

A.1 Error Indices

1. Peak flow error (PFE, [%])

$$PFE = \frac{\left|{Q_{max}}^{obs} - {Q_{max}}^{sim}\right|}{{Q_{max}}^{obs}} \times 100 \quad \text{(A. 1)}$$

2. Phase error (PE, [hour])

$$PE = \tau^{obs} - \tau^{sim} \quad \text{(A. 2)}$$

3. Volume error (VE, [%])

$$VE = \frac{\left|V^{obs} - V^{sim}\right|}{V^{obs}} \times 100 \quad \text{(A. 3)}$$

4. Root mean square error (RMSE, [m^3/s])

$$RMSE = \sqrt{\frac{\sum_{i=1}^{N}\left({Q_i}^{obs} - {Q_i}^{sim}\right)^2}{N}} \quad \text{(A. 4)}$$

5. Coefficient of correlation (CC, [-])

$$CC = \frac{\sum_{i=1}^{N}\left[\left(Q_i^{obs} - Q_{mean}^{obs}\right)\left(Q_i^{sim} - Q_{mean}^{sim}\right)\right]}{\sqrt{\sum_{i=1}^{N}\left(Q_i^{obs} - Q_{mean}^{obs}\right)^2}\sqrt{\sum_{i=1}^{N}\left(Q_i^{sim} - Q_{mean}^{sim}\right)^2}} \quad (A.5)$$

6. Explained variance (EV, [-])

$$EV = 1 - \frac{\sum_{i=1}^{N}\left[\left(Q_i^{sim} - Q_i^{obs}\right) - 1/N \times \sum_{i=1}^{N}\left(Q_i^{sim} - Q_i^{obs}\right)\right]^2}{\sum_{i=1}^{N}\left(Q_i^{obs} - Q_{mean}^{obs}\right)^2} \quad (A.6)$$

7. Nash and Sutcliffe [1970] Efficiency (NSE, [-])

$$NSE = 1 - \frac{\sum_{i=1}^{N}\left(Q_i^{obs} - Q_i^{sim}\right)^2}{\sum_{i=1}^{N}\left(Q_i^{obs} - Q_{mean}^{obs}\right)^2} \quad (A.7)$$

8. Percent bias (PBIAS, [%])

$$PBIAS = \frac{\sum_{i=1}^{N}\left(Q_i^{obs} - Q_i^{sim}\right)}{\sum_{i=1}^{N}\left(Q_i^{obs}\right)} \times 100 \quad (A.8)$$

9. RMSE-observations standard deviation ratio (RSR, [-])

$$RSR = \frac{RMSE}{STDEV_{obs}} = \frac{\sqrt{\sum_{i=1}^{N}\left(Q_i^{obs} - Q_i^{sim}\right)^2}}{\sqrt{\sum_{i=1}^{N}\left(Q_i^{obs} - Q_{mean}^{obs}\right)^2}} \quad (A.9)$$

where, the superscripts '*obs*' and '*sim*' denote observation and simulation series, respectively; Q_i is the discharge at each time step [m^3/s]; Q_{mean} and Q_{max} are the average and maximum discharges; V denotes the total volume contained in the hydrograph for an event period; τ

denotes the time when the peak discharge is reached; *N* is a total number of values within the time period of an event.

APPENDIX B

Eigenvalues and eigenvectors of Jacobian

B.1 Jacobian

For the purpose of evaluating the flux using the Roe's approximate Riemann solver, the Jacobian of the normal flux (**F** · **n**) can be first computed as

$$\mathbf{J}_n = \frac{\partial(\mathbf{F}\cdot\mathbf{n})}{\partial\mathbf{U}} = \frac{\partial\mathbf{E}}{\partial\mathbf{U}}n_x + \frac{\partial\mathbf{G}}{\partial\mathbf{U}}n_y \tag{B.1}$$

The conservative variable vector, **U** and *x*- and *y*- directional flux vectors, **E** and **G** can be explicitly written as

$$\mathrm{U}_1 = h\ ;\ \mathrm{U}_2 = u\mathrm{U}_1\ ;\ \mathrm{U}_3 = v\mathrm{U}_1\ ;\ \mathrm{U}_{i+3} = c_i\mathrm{U}_1$$

$$\mathrm{E}_1 = \mathrm{U}_2\ ;\ \mathrm{E}_2 = \frac{\mathrm{U}_2^2}{\mathrm{U}_1} + \frac{g}{2}\mathrm{U}_1^2\ ;\ \mathrm{E}_3 = \frac{\mathrm{U}_2\mathrm{U}_3}{\mathrm{U}_1}\ ;\ \mathrm{E}_{i+3} = \frac{\mathrm{U}_2\mathrm{U}_{i+3}}{\mathrm{U}_1}$$

$$\mathrm{G}_1 = \mathrm{U}_3\ ;\ \mathrm{G}_2 = \frac{\mathrm{U}_2\mathrm{U}_3}{\mathrm{U}_1}\ ;\ \mathrm{G}_3 = \frac{\mathrm{U}_3^2}{\mathrm{U}_1} + \frac{g}{2}\mathrm{U}_1^2\ ;\ \mathrm{G}_{i+3} = \frac{\mathrm{U}_3\mathrm{U}_{i+3}}{\mathrm{U}_1} \tag{B.2}$$

Then, the derivatives of **E** and **G** with respect to **U** are

$$\frac{\partial \mathbf{E}}{\partial \mathbf{U}} = \begin{pmatrix} \frac{\partial \mathrm{E}_1}{\partial \mathrm{U}_1} & \frac{\partial \mathrm{E}_1}{\partial \mathrm{U}_2} & \frac{\partial \mathrm{E}_1}{\partial \mathrm{U}_3} & \frac{\partial \mathrm{E}_1}{\partial \mathrm{U}_4} & \cdots & \frac{\partial \mathrm{E}_1}{\partial \mathrm{U}_{I+3}} \\ \frac{\partial \mathrm{E}_2}{\partial \mathrm{U}_1} & \frac{\partial \mathrm{E}_2}{\partial \mathrm{U}_2} & \frac{\partial \mathrm{E}_2}{\partial \mathrm{U}_3} & \frac{\partial \mathrm{E}_2}{\partial \mathrm{U}_4} & \cdots & \frac{\partial \mathrm{E}_2}{\partial \mathrm{U}_{I+3}} \\ \frac{\partial \mathrm{E}_3}{\partial \mathrm{U}_1} & \frac{\partial \mathrm{E}_3}{\partial \mathrm{U}_2} & \frac{\partial \mathrm{E}_3}{\partial \mathrm{U}_3} & \frac{\partial \mathrm{E}_3}{\partial \mathrm{U}_4} & \cdots & \frac{\partial \mathrm{E}_3}{\partial \mathrm{U}_{I+3}} \\ \frac{\partial \mathrm{E}_4}{\partial \mathrm{U}_1} & \frac{\partial \mathrm{E}_4}{\partial \mathrm{U}_2} & \frac{\partial \mathrm{E}_4}{\partial \mathrm{U}_3} & \frac{\partial \mathrm{E}_4}{\partial \mathrm{U}_4} & \cdots & \frac{\partial \mathrm{E}_4}{\partial \mathrm{U}_{I+3}} \\ \vdots & \vdots & \vdots & \vdots & \ddots & \vdots \\ \frac{\partial \mathrm{E}_{I+3}}{\partial \mathrm{U}_1} & \frac{\partial \mathrm{E}_{I+3}}{\partial \mathrm{U}_2} & \frac{\partial \mathrm{E}_{I+3}}{\partial \mathrm{U}_3} & \frac{\partial \mathrm{E}_{I+3}}{\partial \mathrm{U}_4} & \cdots & \frac{\partial \mathrm{E}_{I+3}}{\partial \mathrm{U}_{I+3}} \end{pmatrix} \tag{B.3}$$

$$= \begin{pmatrix} 0 & 1 & 0 & 0 & \cdots & 0 \\ -\frac{\mathrm{U}_2^2}{\mathrm{U}_1^2} + g\mathrm{U}_1 & \frac{2\mathrm{U}_2}{\mathrm{U}_1} & 0 & 0 & \cdots & 0 \\ -\frac{\mathrm{U}_2\mathrm{U}_3}{\mathrm{U}_1^2} & \frac{\mathrm{U}_3}{\mathrm{U}_1} & \frac{\mathrm{U}_2}{\mathrm{U}_1} & 0 & \cdots & 0 \\ -\frac{\mathrm{U}_2\mathrm{U}_4}{\mathrm{U}_1^2} & \frac{\mathrm{U}_4}{\mathrm{U}_1} & 0 & \frac{\mathrm{U}_2}{\mathrm{U}_1} & \cdots & 0 \\ \vdots & \vdots & \vdots & \vdots & \ddots & \vdots \\ -\frac{\mathrm{U}_2\mathrm{U}_{I+3}}{\mathrm{U}_1^2} & \frac{\mathrm{U}_{I+3}}{\mathrm{U}_1} & 0 & 0 & \cdots & \frac{\mathrm{U}_2}{\mathrm{U}_1} \end{pmatrix} = \begin{pmatrix} 0 & 1 & 0 & 0 & \cdots & 0 \\ gh - u^2 & 2u & 0 & 0 & \cdots & 0 \\ -uv & v & u & 0 & \cdots & 0 \\ -uc_1 & c_1 & 0 & u & \cdots & 0 \\ \vdots & \vdots & \vdots & \vdots & \ddots & \vdots \\ -uc_I & c_I & 0 & 0 & \cdots & u \end{pmatrix}$$

$$\frac{\partial \mathbf{G}}{\partial \mathbf{U}} = \begin{pmatrix} \frac{\partial \mathrm{G}_1}{\partial \mathrm{U}_1} & \frac{\partial \mathrm{G}_1}{\partial \mathrm{U}_2} & \frac{\partial \mathrm{G}_1}{\partial \mathrm{U}_3} & \frac{\partial \mathrm{G}_1}{\partial \mathrm{U}_4} & \cdots & \frac{\partial \mathrm{G}_1}{\partial \mathrm{U}_{I+3}} \\ \frac{\partial \mathrm{G}_2}{\partial \mathrm{U}_1} & \frac{\partial \mathrm{G}_2}{\partial \mathrm{U}_2} & \frac{\partial \mathrm{G}_2}{\partial \mathrm{U}_3} & \frac{\partial \mathrm{G}_2}{\partial \mathrm{U}_4} & \cdots & \frac{\partial \mathrm{G}_2}{\partial \mathrm{U}_{I+3}} \\ \frac{\partial \mathrm{G}_3}{\partial \mathrm{U}_1} & \frac{\partial \mathrm{G}_3}{\partial \mathrm{U}_2} & \frac{\partial \mathrm{G}_3}{\partial \mathrm{U}_3} & \frac{\partial \mathrm{G}_3}{\partial \mathrm{U}_4} & \cdots & \frac{\partial \mathrm{G}_3}{\partial \mathrm{U}_{I+3}} \\ \frac{\partial \mathrm{G}_4}{\partial \mathrm{U}_1} & \frac{\partial \mathrm{G}_4}{\partial \mathrm{U}_2} & \frac{\partial \mathrm{G}_4}{\partial \mathrm{U}_3} & \frac{\partial \mathrm{G}_4}{\partial \mathrm{U}_4} & \cdots & \frac{\partial \mathrm{G}_4}{\partial \mathrm{U}_{I+3}} \\ \vdots & \vdots & \vdots & \vdots & \ddots & \vdots \\ \frac{\partial \mathrm{G}_{I+3}}{\partial \mathrm{U}_1} & \frac{\partial \mathrm{G}_{I+3}}{\partial \mathrm{U}_2} & \frac{\partial \mathrm{G}_{I+3}}{\partial \mathrm{U}_3} & \frac{\partial \mathrm{G}_{I+3}}{\partial \mathrm{U}_4} & \cdots & \frac{\partial \mathrm{G}_{I+3}}{\partial \mathrm{U}_{I+3}} \end{pmatrix} \tag{B.4}$$

$$= \begin{pmatrix} 0 & 0 & 1 & 0 & \cdots & 0 \\ -\frac{\mathrm{U}_2\mathrm{U}_3}{\mathrm{U}_1^2} & \frac{\mathrm{U}_3}{\mathrm{U}_1} & \frac{\mathrm{U}_2}{\mathrm{U}_1} & 0 & \cdots & 0 \\ -\frac{\mathrm{U}_3^2}{\mathrm{U}_1^2} + g\mathrm{U}_1 & 0 & \frac{2\mathrm{U}_3}{\mathrm{U}_1} & 0 & \cdots & 0 \\ -\frac{\mathrm{U}_3\mathrm{U}_4}{\mathrm{U}_1^2} & 0 & \frac{\mathrm{U}_4}{\mathrm{U}_1} & \frac{\mathrm{U}_3}{\mathrm{U}_1} & \cdots & 0 \\ \vdots & \vdots & \vdots & \vdots & \ddots & \vdots \\ -\frac{\mathrm{U}_3\mathrm{U}_{I+3}}{\mathrm{U}_1^2} & 0 & \frac{\mathrm{U}_{I+3}}{\mathrm{U}_1} & 0 & \cdots & \frac{\mathrm{U}_3}{\mathrm{U}_1} \end{pmatrix} = \begin{pmatrix} 0 & 0 & 1 & 0 & \cdots & 0 \\ -uv & v & u & 0 & \cdots & 0 \\ gh - v^2 & 0 & 2v & 0 & \cdots & 0 \\ -vc_1 & 0 & c_1 & v & \cdots & 0 \\ \vdots & \vdots & \vdots & \vdots & \ddots & \vdots \\ -vc_I & 0 & c_I & 0 & \cdots & v \end{pmatrix}$$

To sum up, we can finally obtain the Jacobian following as

$$\mathbf{J}_n = \tag{B.5}$$

$$\begin{pmatrix} 0 & n_x & n_y & 0 & \cdots & 0 \\ (-u^2 + gh)n_x - uvn_y & 2un_x + vn_y & un_y & 0 & \cdots & 0 \\ -uvn_x + (-v^2 + gh)n_y & vn_x & un_x + 2vn_y & 0 & \cdots & 0 \\ -uc_1n_x - vc_1n_y & c_1n_x & c_1n_y & un_x + vn_y & \cdots & 0 \\ \vdots & \vdots & \vdots & \vdots & \ddots & \vdots \\ -uc_In_x - vc_In_y & c_In_x & c_In_y & 0 & \cdots & un_x + vn_y \end{pmatrix}$$

B.2 Eigenvalues and Eigenvectors

To obtain the eigenvalue of the square matrix, Jacobian, we need to find numbers satisfying the following relation:

$$|\mathbf{J}_n - \lambda \mathbf{I}| = 0 \tag{B.6}$$

This determinant shows the order of I+3 so that it has the same number of roots. The computed roots corresponding to eigenvalues are:

$$\lambda_1 = un_x + vn_y - a\,;\ \lambda_2 = un_x + vn_y\,;\lambda_3 = un_x + vn_y + a\,;\ \lambda_{i+3} = un_x + vn_y$$

$$|\hat{\Lambda}| = \begin{pmatrix} |\hat{u}_\perp - \hat{a}| & & & & & \\ & |\hat{u}_\perp| & & & & \\ & & |\hat{u}_\perp + \hat{a}| & & & \\ & & & |\hat{u}_\perp| & & \\ & & & & \ddots & \\ & & & & & |\hat{u}_\perp| \end{pmatrix} \tag{B.7}$$

The introduction of matrices with a single column can be used for the computation of right-eigenvector (**R**). From the following definition

$$(\mathbf{J}_n - \lambda \mathbf{I}) \cdot \mathbf{R} =$$

$$\begin{pmatrix} -\lambda R_1 + n_x R_2 + n_y R_3 \\ \left((a^2 - u^2)n_x - uvn_y\right) R_1 + \left(2un_x + vn_y - \lambda\right) R_2 + un_y R_3 \\ \left((a^2 - v^2)n_y - uvn_x\right) R_1 + \left(un_x + 2vn_y - \lambda\right) R_3 + vn_x R_2 \\ -\left(un_x + vn_y\right) c_1 R_1 + c_1 n_x R_2 + c_1 n_y R_3 + (un_x + vn_y - \lambda) R_4 \\ \vdots \\ -\left(un_x + vn_y\right) c_I R_1 + c_I n_x R_2 + c_I n_y R_3 + (un_x + vn_y - \lambda) R_{I+3} \end{pmatrix} = 0 \tag{B.8}$$

$$\hat{R} = \begin{pmatrix} 1 & 0 & 1 & 0 & \cdots & 0 \\ \hat{u} - \hat{a}\cos\emptyset & -\sin\emptyset & \hat{u} + \hat{a}\cos\emptyset & 0 & \cdots & 0 \\ \hat{v} - \hat{a}\sin\emptyset & \cos\emptyset & \hat{v} + \hat{a}\sin\emptyset & 0 & \cdots & 0 \\ \hat{c}_1 & 0 & \hat{c}_1 & 1 & \cdots & 0 \\ \vdots & \vdots & \vdots & \vdots & \ddots & \vdots \\ \hat{c}_I & 0 & \hat{c}_I & 0 & \cdots & 1 \end{pmatrix} \tag{B.9}$$

Left eigenvector is necessarily needed to calculate the derivation of wave strength described in Eq. (3.20). The left-eigenvector is simply computed as a form of inverse matrix of the right-eigenvector.

$$\mathbf{L} = \mathbf{R}^{-1} = \frac{1}{|\mathbf{R}|}\begin{pmatrix} C_{11} & C_{21} & C_{31} & C_{41} & \cdots & C_{I+31} \\ C_{12} & C_{22} & C_{32} & C_{42} & \cdots & C_{I+32} \\ C_{13} & C_{23} & C_{33} & C_{43} & \cdots & C_{I+33} \\ C_{14} & C_{24} & C_{34} & C_{44} & \cdots & C_{I+34} \\ \vdots & \vdots & \vdots & \vdots & \ddots & \vdots \\ C_{1I+3} & C_{2I+3} & C_{3I+3} & C_{4I+3} & \cdots & C_{I+3I+3} \end{pmatrix} \tag{B.10}$$

where $|\mathbf{R}|$ is the determinant of right eigenvector; C_{I+3I+3} is the matrix of cofactors. The specific values of these two variables are

$$|\mathbf{R}| = -\sin\theta\,(v + a\sin\theta) - \cos\theta\,(u + a\cos\theta)$$

$$+\cos\theta\,(u - a\cos\theta) + \sin\theta\,(v - a\sin\theta) = -2a$$

$$C_{11} = -\sin\theta\,(v + a\sin\theta) - \cos\theta\,(u + a\cos\theta) = -(a + u_{\perp})$$

$$C_{12} = -[(u - a\cos\theta)(v + a\sin\theta) - (u + a\cos\theta)(v - a\sin\theta)] = 2au_{\parallel}$$

$$C_{13} = \sin\theta\,(v - a\sin\theta) + \cos\theta\,(u - a\cos\theta) = -(a - u_{\perp})$$

$$C_{1i+3} = -c_i[-\sin\theta\,(v + a\sin\theta) - \cos\theta\,(u + a\cos\theta)$$
$$+ \cos\theta\,(u - a\cos\theta) + \sin\theta\,(v - a\sin\theta)] = 2ac_i$$

$$C_{21} = \cos\theta$$

$$C_{22} = v + a\sin\theta - (v - a\sin\theta) = 2a\sin\theta$$

$$C_{23} = -\cos\theta$$

$$C_{2i+3} = c_i(-\cos\theta + \cos\theta) = 0$$

$$C_{31} = \sin\theta$$

$$C_{32} = -[(u + a\cos\theta) - (u - a\cos\theta)] = -2a\cos\theta$$

$$C_{33} = -\sin\theta$$

$$C_{3i+3} = -c_i[\sin\theta - \sin\theta] = 0$$

$$C_{i+31} = C_{i+32} = C_{i+33} = C_{i+3j+3} = 0 \quad for\ i \neq j$$

$$C_{i+3i+3} = -\sin\theta\,(v + a\sin\theta) - \cos\theta\,(u + a\cos\theta)$$
$$+ \cos\theta\,(u - a\cos\theta) + \sin\theta\,(v - a\sin\theta) = -2a$$

The final form of the left eigenvector is

$$\mathbf{L} = \frac{1}{2a}\begin{pmatrix} a + u_\perp & -\cos\theta & -\sin\theta & 0 & \cdots & 0 \\ -2au_\parallel & -2a\sin\theta & 2a\cos\theta & 0 & \cdots & 0 \\ a - u_\perp & \cos\theta & \sin\theta & 0 & \cdots & 0 \\ -2ac_1 & 0 & 0 & 2a & \cdots & 0 \\ \vdots & \vdots & \vdots & \vdots & \ddots & \vdots \\ -2ac_I & 0 & 0 & 0 & \cdots & 2a \end{pmatrix} \tag{B.11}$$

By using the left eigenvector, we can finally obtain the wave strength used in Roe's approximate Riemann solver as:

$$\Delta\hat{V} = \hat{L}\Delta U = \frac{1}{2a}\begin{pmatrix} a+u_\perp & -\cos\theta & -\sin\theta & 0 & \cdots & 0 \\ -2au_\parallel & -2a\sin\theta & 2a\cos\theta & 0 & \cdots & 0 \\ a-u_\perp & \cos\theta & \sin\theta & 0 & \cdots & 0 \\ -2ac_1 & 0 & 0 & 2a & \cdots & 0 \\ \vdots & \vdots & \vdots & \vdots & \ddots & \vdots \\ -2ac_I & 0 & 0 & 0 & \cdots & 2a \end{pmatrix}\begin{pmatrix} \Delta h \\ \Delta(uh) \\ \Delta(vh) \\ \Delta(c_1 h) \\ \vdots \\ \Delta(c_I h) \end{pmatrix} \quad \text{(B. 12)}$$

$$= \frac{1}{2a}\begin{pmatrix} (a+u_\perp)\Delta h - \cos\theta\Delta(uh) - \sin\theta\Delta(vh) \\ -2au_\parallel\Delta h - 2a\sin\theta\Delta(uh) + 2a\cos\theta\Delta(vh) \\ (a-u_\perp)\Delta h + \cos\theta\Delta(uh) + \sin\theta\Delta(vh) \\ -2ac_1\Delta h + 2a\Delta(c_1 h) \\ \vdots \\ -2ac_I\Delta h + 2a\Delta(c_I h) \end{pmatrix}$$

$$= \begin{pmatrix} \frac{h_R - h_L}{2} - \frac{((uh)_R - (uh)_L)\cos\emptyset + ((vh)_R - (vh)_L)\sin\emptyset - (\hat{u}\cos\emptyset + \hat{v}\sin\emptyset)(h_R - h_L)}{2\hat{a}} \\ ((vh)_R - (vh)_L)\cos\emptyset - ((uh)_R - (uh)_L)\sin\emptyset - (-\hat{u}\sin\emptyset + \hat{v}\cos\emptyset)(h_R - h_L) \\ \frac{h_R - h_L}{2} + \frac{((uh)_R - (uh)_L)\cos\emptyset + ((vh)_R - (vh)_L)\sin\emptyset - (\hat{u}\cos\emptyset + \hat{v}\sin\emptyset)(h_R - h_L)}{2\hat{a}} \\ (c_1 h)_R - (c_1 h)_L - \hat{c}_1(h_R - h_L) \\ \vdots \\ (c_I h)_R - (c_I h)_L - \hat{c}_I(h_R - h_L) \end{pmatrix}$$

NOTATION

Parameter	**Description**
A	area of triangular cell
A_r	area of roughness element
$\boldsymbol{A_s}$	anisotropy ratio in the saturated zone
$\boldsymbol{A_u}$	anisotropy ratio in the unsaturated zone
a	celerity
a_0	detachability of original soil
a_d	detachability of deposited soil
alb	surface albedo
B	interception coefficient
b	exponent used in Eq. (3.9)
C	Chezy resistance factor
C_D	bed drag coefficient
C_r	Courant number
$\boldsymbol{C_s}$	soil heat capacity
c_i	sediment concentration
D	erosion rates vector
D_R	mean raindrop size
D_r	diameter of roughness element
D_{50}	median particle size
d_i	deposition rate
E	x-directional flux vector
E_x	summation of bed elevation, depth, and velocity head
e_i	rainfall driven detachment rate
e_{ri}	rainfall driven redetachment rate
F	flux vector
F	effective fraction of excess stream power
F_w	shield effect factor

f	Darcy-Weisbach friction factor
f_d	conductivity decay parameter
f_f	form Darcy-Weisbach friction factor
f_s	surface Darcy-Weisbach friction factor
f_t	total Darcy-Weisbach friction factor
f_w	wave Darcy-Weisbach friction factor
$\mathbf{G}$	y-directional flux vector
g	acceleration constant due to gravity
g_d	canopy drainage exponent
H	shielding proportion
H_v	vegetation height
h	flow depth
h_0	threshold used in Eq. (3.9)
$\overline{\boldsymbol{h}}$	spatially averaged flow depth
I	the number of sediment size classes
i	particle size class
J	specific energy of entrainment
j	cell index
K	canopy drainage rate coefficient
$\boldsymbol{K_s}$	saturated hydraulic conductivity
K_t	optical transmission coefficient
k	face index
k_r	characteristic height of roughness element
$\boldsymbol{k_s}$	volumetric heat Conductivity
L	left side of the cell interface
$\hat{\boldsymbol{L}}$	left eigenvector
l	length of triangular edge
$\mathbf{M}$	sediment mass vector
M_i	deposited mass of each sediment size
M_t	total deposited mass
M_t^*	deposited mass needed to sheild original soil
m	a fuction that has 1 or -1 depending on the unit vector's directions
m_p	pore-size distribution index
N_c	the number of triangular cells
$\mathbf{n}$	outward-directed unit vector normal to the boundary
n	manning coefficient
n_b	base Manning roughness coefficient
n_t	total Manning roughness coefficient
P	precipitation intensity
p	free throughfall coefficient

p_i	ratio of sediment class *i*
Q	inflow rate
Q_{steady}	discharge at steady state
$Q(t)$	discharge at time t
q	discharge per unit width
R	right side of the cell interface
$\widehat{\boldsymbol{R}}$	right eigenvector
R_h	hydraulic radius
R^2	coefficient of determination
Re	Reynolds number
R_r	roughness Reynolds number
r_i	flow induced entrainment rate
r_{ri}	flow induced reentrainment rate
r_s	canopy average stomatal resistance
$\mathbf{S}$	source vector
S	domain slope
S_c	canopy field capacity
S_f	friction slope
S_{fx}	*x*-directional friction slope
S_{fy}	*y*-directional friction slope
$\overline{\boldsymbol{S_f}}$	spatially averaged friction slope
S_r	net runoff production rate
S_s	canopy storage
t	time
t_c	time of concentration
$\mathbf{U}$	conservative variable vector
U_A	long term average annual soil loss in Eq. (6.1)
U_C	crop and management factor in Eq. (6.1)
U_K	soil erodibility factor in Eq. (6.1)
U_{LS}	slope length-gradient factor in Eq. (6.1)
U_P	support practice factor in Eq. (6.1)
U_R	rainfall and runoff factor in Eq. (6.1)
u	*x*-directional velocity
V	velocity magnitude
$\overline{\boldsymbol{V}}$	spatially averaged velocity magnitude
V_f	vegetation cover fraction
v	*y*-directional velocity
z_b	bed elevation at cell center
Γ	boundary of the control volume
$\widehat{\boldsymbol{\Lambda}}$	eigenvalue
Ω	stream power

Ω_{cr}	critical stream power
Ω_x	*x*-directional stream power
Ω_y	*y*-directional stream power
$\emptyset$	angle between the face normal vector and the *x* axis
β	porosity of bed
$\boldsymbol{\theta_c}$	critical Shields parameter for incipient motion
$\boldsymbol{\theta_R}$	volumetric residual soil moisture
$\boldsymbol{\theta_s}$	volumetric soil moisture at saturation
$\boldsymbol{\varphi_B}$	air entry bubbling pressure
$\boldsymbol{\eta'}$	bedrock depth
v_R	rainfall impact velocity
μ	dynamic viscosity of water
ρ_s	density of sediment
ρ_w	density of water
λ	eigenvalue
ϵ	a tolerance value used in Eq. (4.1)
Δ	finite difference across the interface
$\Delta\widehat{\boldsymbol{V}}$	wave strength

BIBLIOGRAPHY

Abbott, M. B. (1974), Continuous flows, discontinuous flows and numerical analysis, *Journal of Hydraulic Research*, *12*(4), 417-467.

Abrahams, A. D., and A. J. Parsons (1994), Hydraulics of interrill overland-flow on stone-covered desert surfaces, *Catena*, *23*(1-2), 111-140.

Abrahams, A. D., A. J. Parsons, and S. H. Luk (1986), Resistance to overland-flow on desert hillslopes, *J. Hydrol.*, *88*(3-4), 343-363.

Abu Hammad, A. H., T. Børresen, and L. E. Haugen (2006), Effects of rain characteristics and terracing on runoff and erosion under the Mediterranean, *Soil and Tillage Research*, *87*(1), 39-47.

Ahmadi, A., M. R. Neyshabouri, H. Rouhipour, H. Asadi, and M. Irannajad (2010), Factors and mechanisms influencing interrill erodibility at different rainfall intensities, *Journal of Food, Agriculture & Environment*, *8*(2), 996-999.

Akanbi, A. A., and N. D. Katopodes (1988), Model for flood propapation on initially dry land, edited, pp. 689-706, Journal of Hydraulic Engineering-ASCE.

Aksoy, H., and M. L. Kavvas (2005), A review of hillslope and watershed scale erosion and sediment transport models, *CATENA*, *64*(2-3), 247-271.

Alonso, R., M. Santillana, and C. Dawson (2008), On the diffusive wave approximation of the shallow water equations, *European Journal of Applied Mathematics*, *19*, 575-606.

Anderson, J. D. (1995), *Computational Fluid Dynamics*, McGraw–Hill, New York.

Armstrong, A., J. N. Quinton, B. C. P. Heng, and J. H. Chandler (2011), Variability of interrill erosion at low slopes, *Earth Surface Processes and Landforms*, *36*(1), 97-106.

Armstrong, A., J. N. Quinton, B. C. P. Heng, and G. C. Sander (2012), Processes controlling the development of a shielding layer on natural soil, *European Journal of Soil Science*, *63*(1), 54-64.

Arnell, N. W. (2003), Effects of IPCCSRES emissions scenarios on river runoff: a global perspective, *Hydrology and Earth System Sciences*, *7*(5), 619-641.

Bagnold, R. A. (1966), An approach to the sediment transport problem for general physics, *Geological Survey Professional Paper (U.S.)*, 442-I.

Bai, Z. G., D. L. Dent, L. Olsson, and M. E. Schaepman (2008), Proxy global assessment of land degradation, *Soil Use and Management*, *24*, 223-234.

Baird, W. F. (2001), Muskegon river delta - Role of the cobb plant discharge channel structure, *Report to Consumers Energy*.

Barnett, T. P., J. C. Adam, and D. P. Lettenmaier (2005), Potential impacts of a warming climate on water availability in snow-dominated regions, *Nature*, *438*, 303-309.

Begnudelli, L., and B. F. Sanders (2006), Unstructured grid finite-volume algorithm for shallow-water flow and scalar transport with wetting and drying, *Journal of Hydraulic Engineering-ASCE*, *132*(4), 371-384.

Begnudelli, L., and B. F. Sanders (2007), Simulation of the St. Francis dam-break flood, *Journal of Engineering Mechanics-ASCE*, *133*, 1200-1212.

Begnudelli, L., B. F. Sanders, and S. F. Bradford (2008), Adaptive Godunov-based model for flood simulation, *Journal of Hydraulic Engineering-ASCE*, *134*(6), 714-725.

Beuselinck, L., G. Govers, A. Steegen, and P. B. Hairsine (1998), Experiments on sediment deposition by overland flow, *Modelling Soil Erosion, Sediment Transport and Closely Related Hydrological Processes*(249), 91-96.

Beuselinck, L., G. Govers, A. Steegen, and T. A. Quine (1999), Sediment transport by overland flow over an area of net deposition, *Hydrological Processes*, *13*(17), 2769-2782.

Biron, P. M., S. N. Lane, A. G. Roy, K. F. Bradbrook, and K. S. Richards (1998), Sensitivity of bed shear stress estimated from vertical velocity profiles: the problem of sampling resolution., *Earth Surface Processes and Landforms*, *23*, 133-139.

Bissonnais, Y. L., B. Renaux, and H. Delouche (1995), Interactions between soil properties and moisture content in crust formation, runoff and interrill erosion from tilled loess soils, *CATENA*, *25*(1-4), 33-46.

Bixio, A. C., M. Putti, S. Orlandini, and C. Paniconi (2000), Physically-based distributed model for coupled surface runoff and subsurface flow simulation at the catchment scale, *Computational Methods in Water Resources*, 1115-1122.

Blasius, H. (1913), Das Ähnlichkeitsgesetz bei Reibungsvorgängen in Flüssigkeiten, *Forschungs-Arbeit des Ingenieur-Wesens*, *131*, 1-41.

Bradford, S. F., and N. D. Katopodes (1999), Hydrodynamics of turbid underflows. I: Formulation and numerical analysis, *Journal of Hydraulic Engineering-ASCE*, *125*(10), 1006-1015.

Bradford, S. F., and N. D. Katopodes (2001), Finite volume model for nonlevel basin irrigation, *Journal of Irrigation and Drainage Engineering-ASCE*, *127*(4), 216-223.

Bradford, S. F., and B. F. Sanders (2002), Finite-volume model for shallow-water flooding of arbitrary topography, *Journal of Hydraulic Engineering-ASCE*, *128*(3), 289-298.

Bras, R. L. (1990), Hydrology: an Introduction to Hydrologic Science., *Addison-Wesley/Longman, Reading, MA/London.*

Brown, L. R. (1984), *Conserving soils., State of the world, L. R. Brown, ed., Norton, New York*, 53-75.

Brufau, P., and P. Garcia-Navarro (2003), Unsteady free surface flow simulation over complex topography with a multidimensional upwind technique, *Journal of Computational Physics*, *186*(2), 503-526.

Brufau, P., P. Garcia-Navarro, and M. E. Vazquez-Cendon (2004), Zero mass error using unsteady wetting-drying conditions in shallow flows over dry irregular topography, *International Journal of Numerical Methods in Fluids*, *45*(10), 1047-1082.

Bunn, S. E., and A. H. Arthington (2002), Basic principles and ecological consequences of altered flow regimes for aquatic biodiversity, *Environmental Management*, *30*(4), 492-507.

Bunte, K., and J. Poesen (1993), Effects of rock fragment covers on erosion and transport of noncohesive sediment by shallow overland flow, *Water Resources Research*, *29*, 1415-1424.

Buringh, P. (1981), An assessment of losses and degradation of productive agricultural land in the world, *FAO Working Group on Soils Policy, Rome*.

Cabral, M. C., L. Garrote, R. L. Bras, and D. Entekhabi (1992), A kinematic model of infiltration and runoff generation in layered and sloped soils, *Advances in Water Resources*, *15*, 311-324.

Camporese, M., C. Paniconi, M. Putti, and S. Orlandini (2010), Surface-subsurface flow modeling with path-based runoff routing, boundary condition-based coupling, and assimilation of multisource observation data, *Water Resources Research*, *46, W02512, doi:10.1029/2008WR007536.*

Cao, Z., R. Day, and S. Egashira (2002), Coupled and decoupled numerical modeling of flow and morphological evolution in alluvial rivers, *Journal of Hydraulic Engineering-ASCE*, *128*(3), 306-321.

Cao, Z., G. Pender, S. Wallis, and P. Carling (2004), Computational dam-break hydraulics over erodible sediment bed, *Journal of Hydraulic Engineering-ASCE*, *130*(7), 689-703.

Chen, X., J. Wu, and Q. Hu (2008), Simulation of climate change impacts on streamflow in the Bosten lake basin using an artificial neural network model, *Journal of Hydrologic Engineering*, *13*(3), 180-183.

Cheng, N. (1997), Simplified settling velocity formula for sediment particle, *Journal of Hydraulic Engineering-ASCE*, *123*(2), 149-152.

Cherkauer, A., and T. Sinha (2010), Hydrologic impacts of projected future climate change in the Lake Michigan region, *Journal of Great Lakes Research*, *36*, 33-50.

Chow, V. T. (1959), *Open-channel Hydraulics, McGraw-Hill Book Co., New York, N.Y., 680 pp.*

Cowan, W. L. (1956), Estimating hydraulic roughness coefficients, *Agricultural Engineering*, *37*(7), 473-475.

Dankers, R., and L. Feyen (2008), Climate change impact on flood hazard in Europe: An assessment based on high-resolution climate simulations, *Journal of Geophysical Research-Atmospheres*, *113*(D19).

De Roo, A. P. J., L. Hazelhoff, and P. A. Burrough (1989), Soil erosion modelling using 'ANSWERS' and geographical information systems, *Earth Surface Processes and Landforms*, *14*, 517-532.

Deardorff, J. W. (1978), Efficient prediction of ground surface temperature and moisture, with inclusion of a layer of vegetation, *Journal of Geophysical Research*, *83*(C4), 1889-1903.

Defersha, M. B., and A. M. Melesse (2012), Field-scale investigation of the effect of land use on sediment yield and runoff using runoff plot data and models in the Mara River basin, Kenya, *CATENA*, *89*, 54-64.

Defersha, M. B., S. Quraishi, and A. Melesse (2011), The effect of slope steepness and antecedent moisture content on interrill erosion, runoff and sediment size distribution in the highlands of Ethiopia, *Hydrology and Earth System Sciences*, *15*, 2367-2375.

DiGiammarco, P., E. Todini, and P. Lamberti (1996), A conservative finite elements approach to overland flow: The control volume finite element formulation, *J. Hydrol.*, *175*(1-4), 267-291.

Downer, C. W., and F. L. Ogden (2004), GSSHA: Model to simulate diverse stream flow producing processes, *Journal of Hydrologic Engineering*, *9*(3), 161-174.

Du, J. K., S. P. Xie, Y. P. Xu, C. Y. Xu, and V. P. Singh (2007), Development and testing of a simple physically-based distributed rainfall-runoff model for storm runoff simulation in humid forested basins, *J. Hydrol.*, *336*(3-4), 334-346.

Dunne, T., and R. D. Black (1970), An experimental investigation of runoff production in permeable soils, *Water Resources Research*, *6*(2), 478-490.

Edwards, W. M., and L. B. Owens (1991), Large storm effects on total soil erosion, *Journal of Soil and Water Conservation*, *46*(1), 75-78.

Einstein, H. A., and R. B. Banks (1950), Fluid resistance of composite roughness, *Transactions of the American Geophysics Union*, *31*(4), 603-610.

Eltahir, E. A. B., and R. L. Bras (1993), A description of rainfall interception over large areas, *Journal of Climate*, *6*, 1002-1008.

Emmett, W. W. (1970), The hydraulics of overland flow on hillslopes, *U.S. Geological Survey, Prof. Paper 662-A*, 68 pp.

Entekhabi, D. (2000), Land Surface Processes: Basic Tools and Concepts., *Department of Civil and Environmental Engineering, MIT, Cambridge, MA.*

Fathi-Moghadam, M. (2006), Effects of Land Slope and Flow Depth on Retarding Flow in Non-submerge Vegetated Lands, *Journal of Agronomy*, *5*, 536-540.

Fatichi, S. (2010), The Modeling of Hydrological Cycle and its Interaction with Vegetation in the Framework of Climate Change, *ph.D dissertation*, University of Firenze.

Ferro, V. (2003), Flow resistance in gravel-bed channels with large-scale roughness, *Earth Surface Processes and Landforms*, *28*, 1325-1339.

Fiener, P., G. Govers, and K. Van Oost (2008), Evaluation of a dynamic multi-class sediment transport model in a catchment under soil-conservation agriculture, *Earth Surface Processes and Landforms*, *33*(11), 1639-1660.

Francipane, A., V. Y. Ivanov, L. V. Noto, E. Istanbulluoglu, E. Arnone, and R. L. Bras (2012), tRIBS-Erosion: A parsimonious physically-based model for studying catchment hydro-geomorphic response, *CATENA*, *92*(0), 216-231.

Gao, B., M. T. Walter, T. S. Steenhuis, J. Y. Parlange, K. Nakano, C. W. Rose, and W. L. Hogarth (2003), Investigating ponding depth and soil detachability for a mechanistic erosion model using a simple, *J. Hydrol.*, *277*(1-2), 116-124.

Gilley, J. E., and S. C. Finkner (1991), Hydraulic roughness coefficients as affected by random roughness, *Transactions of American Society of Agricultural Engineers*, *34*(3), 897-903.

Gilley, J. E., E. R. Kottwitz, and G. A. Wieman (1992a), Darcy-Weisbach roughness coefficients for gravel and cobble surfaces, *Journal of Irrigation and Drainage Engineering-ASCE*, *118*, 104-112.

Gilley, J. E., D. Flanagan, E. R. Kottwitz, and M. A. Weltz (1992b), Darcy-Weisbach roughness coefficients for overland flow, *In Parsons, A. J. and Abrahams, A.D., editors, Overland flow, London: UCL Press*, 25-52.

Goderniaux, P., S. Brouyere, H. J. Fowler, S. Blenkinsop, R. Therrien, P. Orban, and A. Dassargues (2009), Large scale surface–subsurface hydrological model to assess climate change impacts on groundwater reserves, *J. Hydrol.*, *373*, 122-138.

Goodrich, D. C., T. O. Keefer, C. L. Unkrich, M. H. Nichols, H. B. Osborn, J. J. Stone, and J. R. Smith (2008), Long-term precipitation database, Walnut Gulch Experimental Watershed, Arizona, United States, *Water Resources Research*, *44*(5).

Gottardi, G., and M. Venutelli (2008), An accurate time integration method for simplified overland flow models, *Advances in Water Resources*, *31*(1), 173-180.

Govindaraju, R. S., M. L. Kavvas, and S. E. Jones (1990), Approximate analytical solutions for overland flows, *Water Resources Research*, *26*(12), 2903-2912.

Gutiérrez-Jurado, H. A., E. R. Vivoni, E. Istanbulluoglu, and R. L. Bras (2007), Ecohydrological response to a geomorphically significant flood event in a semiarid catchment with contrasting ecosystems, *Geophysical Research Letters 34*, L24S25.

Hairsine, P. B., and C. W. Rose (1991), Rainfall detachment and deposition: Sediment transport in the absence of flow-driven processes, *Soil Science Society of America Journal*, *55*(2), 320-324.

Hairsine, P. B., and C. W. Rose (1992), Modeling water erosion due to overland flow using physical principles: 1. Sheet flow, *Water Resources Research*, *28*(1), 237-243.

Hairsine, P. B., L. Beuselinck, and G. C. Sander (2002), Sediment transport through an area of net deposition, *Water Resources Research*, *38*(6).

Hairsine, P. B., G. C. Sander, C. W. Rose, J. Y. Parlange, W. L. Hogarth, I. Lisle, and H. Rouhipour (1999), Unsteady soil erosion due to rainfall impact: a model of sediment sorting on the hillslope, *J. Hydrol.*, *220*(3-4), 115-128.

Harmel, R. D., J. V. Bonta, and C. W. Richardson (2007), The original USDA-ARS experimental watersheds in Texas and Ohio: contributions from the past and visions for the future, *Transactions of the American Society of Agricultural and Biological Engineers*, *50*(5), 1669-1675.

Harmel, R. D., C. W. Richardson, K. W. King, and P. M. Allen (2006), Runoff and soil loss relationships for the Texas Blackland Prairies ecoregion, *J. Hydrol.*, *331*, 471-483.

HEC (1998), HEC-1 Flood Hydrograph Package User's Manual version 4.1, *US ARMY CORPS OF ENGINEERS, Hydrologic Engineering Center*.

Heilig, A., D. DeBruyn, M. T. Walter, C. W. Rose, J. Y. Parlange, T. S. Steenhuis, G. C. Sander, P. B. Hairsine, W. L. Hogarth, and L. P. Walker (2001), Testing a mechanistic soil erosion model with a simple experiment, *J. Hydrol.*, *244*(1-2), 9-16.

Heng, B. C. P., G. C. Sander, and C. F. Scott (2009), Modeling overland flow and soil erosion on nonuniform hillslopes: A finite volume scheme, *Water Resources Research*, *45*.

Heng, B. C. P., G. C. Sander, A. Armstrong, J. N. Quinton, J. H. Chandler, and C. F. Scott (2011), Modeling the dynamics of soil erosion and size-selective sediment transport over nonuniform topography in flume-scale experiments, *Water Resources Research*, *47*.

Hessel, R., V. Jetten, and Z. Guanghui (2003), Estimating Manning's n for steep slopes, *Catena*, *54*, 77-91.

Hirsch, C. (1990), Numerical computation of internal and external flows, *John Wiley & Sons, New York*.

Hirsch, P. (1996), Hydraulic resistance to overland flow on semiarid hillslopes: A physical simulation, *Ph.D. thesis, State University of New York at Buffalo*.

Hogarth, W. L., C. W. Rose, J. Y. Parlange, G. C. Sander, and G. Carey (2004a), Soil erosion due to rainfall impact with no inflow: a numerical solution with spatial and temporal effects of sediment settling velocity characteristics, *J. Hydrol.*, *294*(4), 229-240.

Hogarth, W. L., J. Y. Parlange, C. W. Rose, G. C. Sander, T. S. Steenhuis, and A. Barry (2004b), Soil erosion due to rainfall impact with inflow: an analytical solution with spatial and temporal effects, *J. Hydrol.*, *295*(1-4), 140-148.

Horritt, M. S. (2002), Evaluating wetting and drying algorithms for finite element models of shallow water flow, *International Journal for Numerical Methods in Engineering*, *55*(7), 835-851.

Horton, R. E. (1933), The role of infiltration in the hydrological cycle, *Transactions, American Geophysical Union*, *14*, 446-460.

Howes, D. A., A. D. Abrahams, and E. B. Pitman (2006), One- and two-dimensional modelling of overland flow in semiarid shrubland, Jornada basin, New Mexico, *Hydrological Processes*, *20*(5), 1027-1046.

Hromadka, T. V., and A. J. Nestlinger (1985), Technical note - Estimating watersheds-graphs using a diffusion flow model, *Advances in Water Resources*, *8*(4), 214-218.

Hromadka, T. V., C. E. Berenbrock, J. R. Freckleton, and G. L. Guymon (1985), A two-dimensional dam-break flood-plain model, *Advances in Water Resources*, *8*(1), 7-14.

Hu, S. X., and A. D. Abrahams (2006), Partitioning resistance to overland flow on rough mobile beds, *Earth Surface Processes and Landforms*, *31*(10), 1280-1291.

Hu, Z., and S. Islam (1995), Prediction of ground surface temperature and soil moisture content by the force-restore method., *Water Resources Research*, *31*(10), 2531-2539.

Huang, C., L. K. Wells, and L. D. Norton (1999), Sediment transport capacity and erosion processes: Model concepts and reality, *Earth Surface Processes and Landforms*, *24*(6), 503-516.

Huang, J. K., and K. T. Lee (2009), Influences of spatially heterogeneous roughness on flow hydrographs, *Advances in Water Resources*, *32*(11), 1580-1587.

Hunter, N. M., P. D. Bates, M. S. Horritt, and M. D. Wilson (2007), Simple spatially-distributed models for predicting flood inundation: A review, *Geomorphology*, *90*(3-4), 208-225.

Hursh, C. R., and E. F. Brater (1941), Separating storm-hydrographs from small drainage-areas into surface and subsurface flow, *Transactions, American Geophysical Union*, *22*, 863-870.

IPCC (Intergovernmental Panel on Climate Change) (2001), Climate Change 2001: The Scientific Basis, *Contribution of Working Group I to the Third Assessment Report of the Intergovernmental Panel on Climate Change*, [Houghton, J.T.,Y. Ding, D.J. Griggs,4 M. Noguer, P.J. van der Linden, X. Dai, K. Maskell, and C.A. Johnson (eds.)]. Cambridge University Press, Cambridge, United Kingdom and New York, NY, USA, 881pp.

IPCC (Intergovernmental Panel on Climate Change) (2007), Climate Change: The Physical Science Basis. In: Solomon, S., Qin, D., Manning, M., Chen, Z., Marquis, M., Avery, K.B., Tignor, M., Miller, H.L. (Eds.), *Contribution of Working Group 1 to the Fourth Assessment Report of the Intergovernmental Panel on Climate Change*, Cambridge Univ. Press, Cambridge, UK.

Istanbulluoglu, E., O. Yetemen, E. R. Vivoni, H. A. Gutierrez-Jurado, and R. L. Bras (2008), Eco-geomorphic implications of hillslope aspect: Inferences from analysis of landscape morphology in central New Mexico, *Geophysical Research Letters*, *35*(14).

Ivanov, V. Y., E. R. Vivoni, R. L. Bras, and D. Entekhabi (2004a), Catchment hydrologic response with a fully distributed triangulated irregular network model, *Water Resources Research*, *40*(11).

Ivanov, V. Y., E. R. Vivoni, R. L. Bras, and D. Entekhabi (2004b), Preserving high-resolution surface and rainfall data in operational-scale basin hydrology: a fully-distributed physically-based approach, *J. Hydrol.*, *298*(1-4), 80-111.

Ivanov, V. Y., S. Fatichi, G. D. Jenerette, J. F. Espeleta, P. A. Troch, and T. E. Huxman (2010), Hysteresis of soil moisture spatial heterogeneity and the "homogenizing" effect of vegetation, *Water Resources Research*, *46*, W09521, doi:09510.01029/02009WR008611.

Johanson, R. C., J. C. Imhoff, and H. H. Davis (1980), Users Manual for the Hydrologic Simulation Program-Fortran (HSPF) version No. 5.0, EPA-600/9-80-105, *US EPA Environmental Research Laboratory, Athens, GA*

Jones, J. P., E. A. Sudicky, and R. G. McLaren (2008), Application of a fully-integrated surface-subsurface flow model at the watershed-scale: A case study, *Water Resources Research, 44, W03407, doi:10.1029/2006WR005603*.

Julien, P. Y., and D. B. Simons (1985), Sediment transport capacity of overland flow, *Transactions of the American Society of Agricultural Engineers*, *28*(3), 755-762.

Katopodes, N. D. (1982), On zero inertia and kinematic waves, *Journal of Hydraulic Engineering, ASCE*, *108*, 1380-1387.

Katopodes, N. D., and S. F. Bradford (1999), Mechanics of overland flow, *International Workshop on Numerical Modeling of Hydrodynamic Systems, Zaragoza, Spain* 1-23.

Kawahara, M., and T. Yokoyama (1980), Finite element method for direct runoff flow, *Journal of the Hydraulics Division-ASCE, 106*(4), 519-534.

Kay, A. L., H. N. Davies, V. A. Bell, and R. G. Jones (2009), Comparison of uncertainty sources for climate change impacts: flood frequency in England, *Climatic Change*, *92*(1-2), 41-63.

Keskin, M. E., and N. Agiralioglu (1997), A simplified dynamic model for flood routing in rectangular channels, *J. Hydrol.*, *202*(1-4), 302-314.

Kim, J., V. Y. Ivanov, and N. D. Katopodes (2012a), Hydraulic resistance to overland flow on surfaces with partially submerged vegetation, *Water Resources Research*, *48*, W10540, doi:10510.11029/12012WR012047.

Kim, J., V. Y. Ivanov, and N. D. Katopodes (2013), A physically based model of flow and erosion processes at watershed scale, *Water Resources Research*, in Review.

Kim, J., A. Warnock, V. Y. Ivanov, and N. D. Katopodes (2012b), Coupled modeling of hydrologic and hydrodynamic processes including overland and channel flow, *Advances in Water Resources*, *37*, 104-126.

Kinnell, P. I. A. (1982), Laboratory studies on the effect of drop size on splash erosion, *Journal of Agricultural Engineering Research*, *27*(5), 431-439.

Kinnell, P. I. A. (1993), Interrill erodibilities based on the rainfall intensity flow discharge erosivity factor, *Australian Journal of Soil Research*, *31*(3), 319-332.

Kollet, S. J., and R. M. Maxwell (2006a), Integrated surface-groundwater flow modeling: A free-surface overland flow boundary condition in a parallel groundwater flow model, *Advances in Water Resources*, *29*(7), 945-958.

Kollet, S. J., and R. M. Maxwell (2006b), Integrated surface–groundwater flow modeling: A free-surface overland flow boundary condition in a parallel groundwater flow model, *Advances in Water Resources*, *29*, 945-958.

Lane, L. J., M. Hernandez, and M. Nichols (1997), Processes controlling sediment yield from watersheds as functions of spatial scale, *Environmental Modelling and Software*, *12*(4), 355-369.

Lawless, M., and A. Robert (2001), Scales of boundary resistance in coarse-grained channels: turbulent velocity profiles and implications, *Geomorphology*, *39*, 221-238.

Lawrence, D. S. L. (1997), Macroscale surface roughness and frictional resistance in overland flow, *Earth Surface Processes and Landforms*, *22*(4), 365-382.

Lawrence, D. S. L. (2000), Hydraulic resistance in overland flow during partial and marginal surface inundation: Experimental observations and modeling, *Water Resources Research*, *36*(8), 2381-2393.

Laws, J. O., and D. A. Parsons (1943), The relation of raindrop size to intensity, *Transactions of the American Geophysics Union*, *24*, 452-460.

Le Bissonnais, Y., A. Bruand, and M. Jamagne (1989), Laboratory experimental study of soil crusting: Relation between aggregate breakdown mechanisms and crust stucture, *CATENA*, *16*(4-5), 377-392.

Leendertse, J. J. (1967), Aspects of a computational model for long-period water wave propagation, Memorandum RM-5294-PR. Santa Monica, California: The Rand Corporation.

Li, L. H., H. G. Xu, X. Chen, and S. P. Simonovic (2010), Streamflow Forecast and Reservoir Operation Performance Assessment Under Climate Change, *Water Resources Management*, *24*(1), 83-104.

Li, R. M., and H. W. Shen (1973), Effect of tall vegetations on flow and sediment, *Journal of the Hydraulics Division-ASCE*, *99*(5), 793-814.

Liggett, J. A. (1968), Mathematical flow determination in open channels, *Journal of the Engineering Mechanics Division - ASCE*, *94*(EM4), 947-963.

Lin, J. D. (1980), On the force-restore method for prediction of ground surface temperature., *Journal of Geophysical Research*, *85(C6)*, 3251-3254.

Loague, K., C. S. Heppner, B. A. Ebel, and J. E. VanderKwaak (2010), The quixotic search for a comprehensive understanding of hydrologic response at the surface: Horton, Dunne, Dunton, and the role of concept-development simulation, *Hydrological Processes*, *24*, 2499-2505.

Makkeasorn, A., N. B. Chang, and X. Zhou (2008), Short-term streamflow forecasting with global climate change implications - A comparative study between genetic programming and neural network models, *J. Hydrol.*, *352*(3-4), 336-354.

Mamedov, A. I., C. Huangb, and G. J. Levy (2006), Antecedent moisture content and aging duration effects on seal formation and erosion in smectitic soils, *Soil Science Society of America Journal*, *70*, 832-843.

Mantua, N., I. Tohver, and A. Hamlet (2010), Climate change impacts on streamflow extremes and summertime stream temperature and their possible consequences for freshwater salmon habitat in Washington State, *Climatic Change*, *102*(1-2), 187-223.

Menabde, M., and M. Sivapalan (2000), Modeling of rainfall time series and extremes using the bounded random cascades and Levy-stable distributions, *Water Resources Research*, *36*(11), 3293-3300.

Merritt, W. S., R. A. Letcher, and A. J. Jakeman (2003), A review of erosion and sediment transport models, *Environmental Modelling & Software*, *18*(8-9), 761-799.

Meyer, J. L., and W. M. Pulliam (1992), Modifications of Terrestrial aquatic Interactions by a Changing Climate. In: *Global Climate Change and Freshwater Ecosystems*, P. Firth and S. G. Fisher (Editors). Springer Verlag. New York, New York, 177-191.

Michaelides, K., and A. Chappell (2009), Connectivity as a concept for characterising hydrological behaviour, *Hydrological Processes*, *23*, 517-522.

Milly, P. C. D., K. A. Dunne, and A. V. Vecchia (2005), Global pattern of trends in streamflow and water availability in a changing climate, *Nature*, *438*(7066), 347-350.

Milly, P. C. D., R. T. Wetherald, K. A. Dunne, and T. L. Delworth (2002), Increasing risk of great floods in a changing climate, *Nature*, *415*(6871), 514-517.

Molnar, P., and P. Burlando (2005), Preservation of rainfall properties in stochastic disaggregation by a simple random cascade model, *Atmospheric Research*, *77*, 137-151.

Monteith, J. L. (1965), Evaporation and environment., *Symposia of the Society for Experimental Biology*, *19*, 205-234.

Mooney, H., A. Larigauderie, M. Cesario, T. Elmquist, O. Hoegh-Guldberg, S. Lavorel, G. M. Mace, M. Palmer, R. Scholes, and T. Yahara (2009), Biodiversity, climate change, and ecosystem services, *Current Opinion in Environmental Sustainability*, *1*(1), 46-54.

Moramarco, T., and V. P. Singh (2000), A practical method for analysis of river waves and for kinematic wave routing in natural channel networks, *Hydrological Processes*, *14*(1), 51-62.

Morgan, R. P. C., J. N. Quinton, R. E. Smith, G. Govers, J. W. A. Poesen, K. Auerswald, G. Chisci, D. Torri, and M. E. Styczen (1998), The European Soil Erosion Model (EUROSEM): A dynamic approach for predicting sediment transport from fields and small catchments, *Earth Surface Processes and Landforms*, *23*(6), 527-544.

Moriasi, D. N., J. G. Arnold, M. W. Van Liew, R. L. Bingner, R. D. Harmel, and T. L. Veith (2007), Model Evaluation Guidelines for Systematic Quantification of Accuracy in Watershed Simulations, *Transactions of the ASABE*, *50*(3), 885-900.

Morita, M., and B. C. Yen (2002), Modeling of Conjunctive Two-Dimensional Surface-Three-Dimensional Subsurface Flows, *Journal of Hydraulic Engineering-ASCE*, *128*(2), 184-200.

Morris, E. M., and D. A. Woolhiser (1980), Unsteady one-dimensional flow over a plane - Partial equilibrium and recession hydrographs, *Water Resources Research*, *16*(2), 355-360.

Murillo, J., P. Garcia-Navarro, P. Brufau, and J. Burguete (2008), 2D modelling of erosion/deposition processes with suspended load using upwind finite volumes, *Journal of Hydraulic Research*, *46*(1), 99-112.

Mutchler, C. K., and K. C. McGregor (1983), Erosion from low slopes, *Water Resources Research*, *19*(5), 1323-1326.

Nash, J. E., and J. V. Sutcliffe (1970), River flow forecasting through conceptual models part I - A discussion of principles, *J. Hydrol.*, *10*(3), 282-290.

Nearing, M. A., G. R. Foster, L. J. Lane, and S. C. Finkner (1989), A process-based soil erosion model for USDA-water erosion prediction project technology, *Transactions of the ASAE*, *32*(5), 1587-1593.

Nearing, M. A., A. Kimoto, M. H. Nichols, and J. C. Ritchie (2005), Spatial patterns of soil erosion and deposition in two small, semiarid watersheds, *Journal of Geophysical Research*, *110*, F04020.

Nearing, M. A., M. H. Nichols, J. J. Stone, K. G. Renard, and J. R. Simanton (2007), Sediment yields from unit-source semiarid watersheds at Walnut Gulch, *Water Resources Research*, *43*, *W06426*, *doi:10.1029/2006WR005692*.

Nichols, M. H., J. J. Stone, and M. A. Nearing (2008), Sediment database, Walnut Gulch Experimental Watershed, Arizona, United States, *Water Resources Research*, *44*(5).

Nikuradse, J. (1933), Strömungsgesetze in rauhen Rohren., *Forschungs-Arbeit des Ingenieur-Wesens*, *361*, 1-22.

Noel, D. U. (2001), A note on soil erosion and its environmental consequences in the United States, *Water Air & Soil Pollution*, *129*(1), 181-197.
Nord, G., and M. Esteves (2005), PSEM_2D: A physically based model of erosion processes at the plot scale, *Water Resources Research*, *41*(8).
Notebaerta, B., G. Verstraetena, P. Wardb, H. Renssenb, and A. V. Rompaey (2011), Modeling the sensitivity of sediment and water runoff dynamics to Holocene climate and land use changes at the catchment scale, *Geomorphology*, *126*(1-2), 18-31.
Noto, L. V., V. Y. Ivanov, R. L. Bras, and E. R. Vivoni (2008), Effects of initialization on response of a fully-distributed hydrologic model, *J. Hydrol.*, *352*(1-2), 107-125.
Nusser, S. M., and J. J. Goebel (1997), The National Resources Inventory: a long-term multi-resource monitoring programme, *Environmental and Ecological Statistics*, *4*, 181-204.
Odai, S. N. (1999), Nonlinear kinematic-wave model for predicting open-channel flow rate, *Journal of Hydraulic Engineering-Asce*, *125*(8), 886-889.
Oldeman, L. R., R. T. A. Hakkeling, and W. G. Sombroek (1991), *World map of the status of human-induced soil degradation, 2nd edition, ISRIC, Wageningen*.
Orlandini, S., and R. Rosso (1998), Parameterization of stream channel geometry and the distributed modeling of catchment dynamics, *Water Resources Research*, *34*(8), 1971-1985.
Panday, S., and P. S. Huyakorn (2004), A fully coupled physically-based spatially-distributed model for evaluating surface/subsurface flow, *Advances in Water Resources*, *27*(4), 361-382.
Papanicolaou, A. N., J. T. Sanford, D. C. Dermisis, and G. A. Mancilla (2010), A 1-D morphodynamic model for rill erosion, *Water Resources Research*, *46*.
Parlange, J. Y., C. W. Rose, and G. Sander (1981), Kinematic flow approximation of runoff on a plane - An exact analytical solution, *J. Hydrol.*, *52*(1-2), 171-176.
Parlange, J. Y., W. L. Hogarth, C. W. Rose, G. C. Sander, P. Hairsine, and I. Lisle (1999), Addendum to unsteady soil erosion model, *J. Hydrol.*, *217*(1-2), 149-156.
Penman, H. L. (1948), Natural evaporation from open water, bare soil and grass., *Proceedings of the Society of London Series A193*, 120-145.
Phelps, H. O. (1975), Shallow laminar flows over rough granular surfaces, *Journal of the Hydraulics Division-ASCE*, *101*(3), 367-384.
Phillips, J. (2003), Alluvial storage and the long-term stability of sediment yields, *Basin Research*, *15*, 153-163.
Pierson, F. B., C. W. Slaughter, and Z. K. Cram (2001), Long-term stream discharge and suspended-sediment database, Reynolds Creek Experimental Watershed, Idaho, United States, *Water Resources Research*, *37*(11), 2857-2861.
Pimentel, D., et al. (1995), Environmental and economic costs of soil erosion and conservation benefits, *Science*, *267*(5201), 1117-1123.
Poff, N. L., and J. D. Allan (1995), Functional organization of stream fish assemblages in relation to hydrological variability, *Ecology*, *76*(2), 606-627.
Poff, N. L., and J. K. H. Zimmerman (2010), Ecological responses to altered flow regimes: a literature review to inform the science and management of environmental flows, *Freshwater Biology*, *55*(1), 194-205.
Polyakov, V. O., and M. A. Nearing (2003), Sediment transport in rill flow under deposition and detachment conditions, *CATENA*, *51*, 33-43.

Prestininzi, P. (2008), Suitability of the diffusive model for dam break simulation: Application to a CADAM experiment, *J. Hydrol.*, *361*(1-2), 172-185.

Proffitt, A. P. B., C. W. Rose, and P. B. Hairsine (1991), Rainfall detachment and deposition: Experiments with low slopes and significant water depths, *Soil Science Society of America Journal*, *55*(2), 325-332.

Rauws, G. (1988), Laboratory experiments on resistance to overland flow due to composite roughness, *J. Hydrol.*, *103*, 37-52.

Renard, K. G., J. R. Simanton, and C. E. Fancher (1986), Small watershed automatic water quality sampler, edited, pp. 1-51 to 51-58, Proceedings of the 4th Federal Interagency Sedimentation Conference, Las Vegas, NV.

Rihani, J. F., R. M. Maxwell, and F. K. Chow (2010), Coupling groundwater and land surface processes: Idealized simulations to identify effects of terrain and subsurface heterogeneity on land surface energy fluxes, *Water Resources Research, 46, W12523, doi:10.1029/2010WR009111*.

Rinehart, A. J., E. R. Vivoni, and P. D. Brooks (2008), Effects of vegetation, albedo, and solar radiation sheltering on the solution of snow in the Walles Caldera, New Mexico., *Ecohydrology*, *1*, 253-270.

Roe, P. L. (1981), Approximate Riemann solvers, parameter vectors, and difference-schemes, *Journal of Computational Physics*, *43*(2), 357-372.

Roels, J. M. (1984), Flow resistance in concentrated overland flow on rough slope surfaces., *Earth Surface Processes and Landforms*, *9*, 541-551.

Romkens, M. J. M., K. Helming, and S. N. Prasad (2001), Soil erosion under different rainfall intensities, surface roughness, and soil water regimes, *CATENA*, *46*(2-3), 103-123.

Rose, C. W., B. Yu, H. Ghadiri, H. Asadi, J. Y. Parlange, W. L. Hogarth, and J. Hussein (2007), Dynamic erosion of soil in steady sheet flow, *J. Hydrol.*, *333*(2-4), 449-458.

Rudolph, A., K. Helming, and H. Diestel (1997), Effect of antecedent water content and rainfall regime on microrelief changes, *Soil Technology*, *10*, 69-81.

Rutter, A. J., A. J. Morton, and P. C. Robins (1975), A predictive model of interception in forests. 2. Generalization of the model and comparison with observations in some coniferous and hardwood stands., *Journal of Applied Ecology*, *12*, 367-380.

Rutter, A. J., K. A. Kershaw, P. C. Robins, and A. J. Morton (1971), A predictive model of rainfall interception in forests. 1. Derivation of the model from observation in a plantation of Corsican pine., *Agricultural Meteorology*, *9*, 367-384.

Sander, G. C., T. Zheng, and C. W. Rose (2007a), Update to "Modeling water erosion due to overland flow using physical principles: 1. Sheet flow", *Water Resources Research*, *43*(4).

Sander, G. C., P. B. Hairsine, L. Beuselinck, and G. Govers (2002), Steady state sediment transport through an area of net deposition: Multisize class solutions, *Water Resources Research*, *38*(6).

Sander, G. C., J. Y. Parlange, D. A. Barry, M. B. Parlange, and W. L. Hogarth (2007b), Limitation of the transport capacity approach in sediment transport modeling, *Water Resources Research*, *43*(2).

Sander, G. C., P. B. Hairsine, C. W. Rose, D. Cassidy, J. Y. Parlange, W. L. Hogarth, and I. G. Lisle (1996), Unsteady soil erosion model, analytical solutions and comparison with experimental results, *J. Hydrol.*, *178*(1-4), 351-367.

Sanders, B. F. (2008), Integration of a shallow water model with a local time step, *Journal of Hydraulic Research*, *46*(4), 466-475.

Sanders, B. F., J. E. Schubert, and H. A. Gallegos (2008), Integral formulation of shallow-water equations with anisotropic porosity for urban flood modeling, *J. Hydrol.*, *362*(1-2), 19-38.

Savat, J. (1980), Resistance to flow in rough supercritical sheet flow, *Earth Surface Processes and Landforms*, *5*(2), 103-122.

Schaap, M. G., and P. J. Shouse (2003), A description of the procedures followed for the determination of water retention and particle size distribution for samples taken from SAHRA's San Pedro watershed.

Schreiber, D. L., and D. L. Bender (1972), Obtaining overland flow resistance by optimization, *Journal of the Hydraulics Division-Asce*, *98*, 8773-8781.

Shen, C., and M. S. Phanikumar (2010), A process-based, distributed hydrologic model based on a large-scale method for surface–subsurface coupling, *Advances in Water Resources*, *33*, 1524-1541.

Simon, A., and J. C. Collison (2001), Pore-water pressure effects on the detachment of cohesive streambeds: Seepage forces and matric suction, *Earth Surface Processes and Landforms*, *26*, 1421-1442.

Simpson, G., and S. Castelltort (2006), Coupled model of surface water flow, sediment transport and morphological evolution, *Computers & Geosciences*, *32*(10), 1600-1614.

Smart, G. M., M. J. Duncan, and J. M. Walsh (2002), Relatively rough flow resistance equations, *Journal of Hydraulic Engineering-ASCE*, *128*(6), 568-578.

Smith, M. B., V. I. Koren, S. M. Reed, Z. Zhang, D. J. Seo, F. Moreda, and Z. Cui (2006), The Distributed Model Intercomparison Project: Phase 2, Science Plan, http://www.weather.gov/oh/hrl/dmip/2/science_plan.html.

Smith, M. B., D. J. Seo, V. I. Koren, S. M. Reed, Z. Zhang, Q. Duan, F. Moreda, and S. Cong (2004), The distributed model intercomparison project (DMIP): motivation and experiment design, *J. Hydrol.*, *298*(1-4), 4-26.

Smith, M. W., N. J. Cox, and L. J. Bracken (2007), Applying flow restistance equations to overland flows, *Progress in Physical Geography*, *31*, 363-387.

Stoesser, T., S. J. Kim, and P. Diplas (2010), Turbulent Flow through Idealized Emergent Vegetation, *Journal of Hydraulic Engineering-Asce*, *136*(12), 1003-1017.

Stone, J. J., M. H. Nichols, D. C. Goodrich, and J. Buono (2008), Long-term runoff database, Walnut Gulch Experimental Watershed, Arizona, United States, *Water Resources Research*, *44*(5).

Sulis, M., C. Paniconi, and M. Camporese (2011), Impact of grid resolution on the integrated and distributed response of a coupled surface–subsurface hydrological model for the des Anglais catchment, Quebec, *Hydrological Processes*, *25*, 1853-1865.

Sulis, M., S. B. Meyerhoff, C. Paniconi, R. M. Maxwell, M. Putti, and S. J. Kollet (2010), A comparison of two physics-based numerical models for simulating surface water-groundwater interactions, *Advances in Water Resources*, *33*(4), 456-467.

Svoray, T., and S. Ben-Said (2010), Soil loss, water ponding and sediment deposition variations as a consequence of rainfall intensity and land use: a multi-criteria analysis, *Earth Surface Processes and Landforms*, *35*(2), 202-216.

Takken, I., and G. Govers (2000), Hydraulics of interrill overland flow on rough, bare soil surfaces, *Earth Surface Processes and Landforms*, *25*(13), 1387-1402.

Titov, V. V., and C. E. Synolakis (1995), Modeling of breaking, and nonbreaking long-wave evolution and runup using VTCS-2, *Journal of Waterway Port Coastal and Ocean Engineering-Asce*, *121*(6), 308-316.

Tromp-van Meerveld, H. J., J. Y. Parlange, D. A. Barry, M. F. Tromp, G. C. Sander, M. T. Walter, and M. B. Parlange (2008), Influence of sediment settling velocity on mechanistic soil erosion modeling, *Water Resources Research*, *44*(6).

Tsai, T. L., and J. C. Yang (2005), Kinematic wave modeling of overland flow using characteristics method with cubic-spline interpolation, *Advances in Water Resources*, *28*(7), 661-670.

USDA-NRCS (2009), Summary Report 2007 National Resources Inventory, Natural Resources Conservation Service, U.S. Department of Agriculture.

USDA-NRCS (2010), 2007 National Resources Inventory, *2007 annual NRI - Soil Erosion*, Natural Resources Conservation Service, U.S. Department of Agriculture.

USDA (1965), Predicting rainfall-erosion losses from cropland east of the rocky mountains: Guide for selection of practices for soil and water conservation, *Agriculture Handbook*, *282*.

USDA (1978), Predicting rainfall erosion losses: A guide to conservation planning, *Agriculture Handbook*, *537*.

VanderKwaak, J. E., and K. Loague (2001), Hydrologic-response simulations for the R-5 catchment with a comprehensive physics-based model, *Water Resources Research*, *37*(4), 999-1013.

Walker, J. D., M. T. Walter, J. Y. Parlange, C. W. Rose, H. Meerveld, B. Gao, and A. M. Cohen (2007), Reduced raindrop-impact driven soil erosion by infiltration, *J. Hydrol.*, *342*(3-4), 331-335.

Wang, G. T., S. L. Chen, B. Jan, C. O. Stockle, and D. K. McCool (2002), Modelling overland flow based on Saint-Venant equations for a discretized hillslope system, *Hydrological Processes*, *16*(12), 2409-2421.

Ward, P. J., R. T. v. Balen, G. Verstraeten, H. Renssen, and J. Vandenberghe (2009), The impact of land use and climate change on late Holocene and future suspended sediment yield of the Meuse catchment, *Geomorphology*, *103*(3), 389-400.

Weyman, D. R. (1970), Throughflow on hillslopes and its relation to the stream hydrograph, *Bulletin of the International Association of Scientific Hydrology*, *15*, 25-33.

Woolhiser, D. A., R. E. Smith, and D. C. Goodrich (1990), KINEROS, A kinematic runoff and erosion model: Documentation and user manual, *Rep. ARS-77, Agricultural Research Service, USDA, Washington, D. C.*, 130.

Wuddivira, M. N., R. J. Stone, and E. I. Ekwue (2009), Clay, organic matter, and wetting effects on splash detachment and aggregate breakdown under intense rainfall, *Soil Science Society of America Journal 73*, 226-232.

Xia, J., R. A. Falconer, B. Lin, and T. G. (2010), Modelling flood routing on initially dry beds with refined treatment of wetting and drying, *International Journal of River Basin Management*, *8*(3-4), 225-243.

Yu, D., and S. N. Lane (2006), Urban fluvial flood modelling using a two-dimensional diffusion-wave treatment, part 1: mesh resolution effects, *Hydrological Processes*, *20*(7), 1541-1565.

Zokagoa, J., and A. Soulaimani (2010), Modeling of wetting-drying transitions in free surface flows over complex topographies, *Computer Methods in Applied Mechanics and Engineering*, *199*, 2281-2304.